Investigating the cardioprotective potential of exosomes from different cellular sources

PhD thesis written by student: Miroslava Katsur

Supervisors: Prof Sean Davidson and Prof Derek Yellon

Hatter Cardiovascular Institute, London, UK

Aug 1, 2022

Declaration

I, Miroslava Katsur, confirm that the work presented in this thesis is my own. Where information has been derived from other sources, I confirm that this has been indicated in the thesis.

Katšur

Signature

Abstract

Myocardial infarction is the leading cause of mortality worldwide. Reperfusion is the primary therapy for myocardial infarction. Paradoxically, reperfusion causes further cell death beyond the injury caused by ischaemia alone. Exosomes are a type of extracellular vesicles released from cells. Exosomes from stem cells have been reported to confer cardioprotection from ischaemia and reperfusion injury. However, since it is currently challenging to obtain exosomes of high purity and quantity, it is difficult to know whether exosomes or residual contaminants are responsible for cardioprotection. In this thesis, I report my studies comparing different techniques to isolate exosomes and developing a novel affinity method to isolate more pure exosomes. I show that exosomes separated by size-exclusion chromatography are not as pure as affinity-purified exosomes. I found that exosomes obtained from a commercial collaborator using a combination of by size exclusion chromatography and tangential flow filtration were highly variable. Therefore, a novel isolation method was established in which exosomes were affinity purified by immune-pulldown of an epitope tag transiently expressed in cells in culture. This method allows the collection of more pure exosomes. Exosomes purified by this method could be used to understand the role of exosomes in cardioprotection. Finally, I investigated several previously published cell models of cardiac ischaemia and reperfusion injury focusing on mitochondrial injury, but these had low replicability.

Impact statement

A novel method presented in this thesis, of exosome purification by affinity isolation of an expressed tag may bring benefits both inside and outside academia. First, it allows separation of high purity exosomes. If the cell quantity for exosome collection is increased, this method could produce large quantities of pure exosomes. These can be used for comprehensive studies to determine if exosomes can be used as a treatment for various diseases, such as myocardial infarction, neurodegeneration, and cancer. Second, exosomes obtained by this method could be used to establish the characteristics of highly pure exosomes, including protein/lipid ratio. Finally, protein and RNA cargo of exosomes subsets from various cells could be studied to elucidate their role in healthy and diseased conditions.

COVID impact on this PhD

Just before COVID outbreak, I worked on mPTP assays and another project, which is not presented in this thesis. Specifically, I was investigating if a phospholipid LBPA, (S,S) Bisoleoyl-lysobisphosphatidic acid, which is found in the internal membrane of multivesicular bodies, could be used as a marker of exosomes. The work with LBPA required regular use of an electron microscope. Additionally, I was about to do proteomics of affinity purified exosomes with our research collaborator. During the first lockdown, I was at home for ~6 months. At first, I focused analysing old data, conducting tutorials for UCL Bachelor and Medical students, assessing their reports and essays, and doing courses offered by UCL Doctoral Training programme. Then, I wrote two chapters of this thesis and a research paper as the first author.

I was lucky to return to my laboratory earlier than other students as my colleagues started to do COVID research, meaning that we had a special permission to go to work. At that time, there was a severe shortage of basic goods, such as gloves and ethanol, which was needed for NHS and care homes. Also, there was severe disruption of delivering laboratory items including cell media, pipette tips, and plates. This meant that it took many weeks before my work returned to the same speed as it was during pre-COVID times.

Unfortunately, the person who agreed to do proteomics with me passed away during COVID lockdown. Moreover, the electron microscope was broken and stayed broken for almost a year as strict COVID rules delayed its servicing. This meant that the pilot data I accumulated before COVID was not usable anymore as I had limited time to finish my PhD.

In the first and consequent lockdowns, I developed a severe back pain which required medical treatment, even though I did my best to stay active. This made me unable to work many weeks during or after lockdowns.

Because of all issues I faced, I applied for PhD extension and, luckily, I was awarded six months of extra work. It was enough for me to develop a novel method of exosome purification.

Overall, COVID outbreak meant that my work was severely disrupted. I estimate that I lost one year of work due to COVID lockdowns, COVID-associated disruptions such as stock shortage and discontinued projects, and health issues. If not COVID, I could have achieved the goal of my PhD, which is evaluating highly pure cell exosomes in the models of myocardial infarction.

Acknowledgements

I would like to thank here many people who helped me during my PhD and made this work possible. My PhD supervisor, Prof Sean Davidson, did everything what a supervisor is meant to do. He was the one who gave me these projects, taught me to use several instruments, to design and troubleshoot my experiments, and interpret my data. Thanks to his open-door policy and flexibility, I was always able to obtain his advice promptly. He also supported my professional development and helped me to learn how to cope with results which did not meet my expectations. Prof Davidson has helped me to structure my thesis, improve my writing, analyse data, and he proofread my thesis several times. Prof Davidson went beyond his role and supported me during difficult times I had. I attribute my personal growth and growth as a scientist to him. I am enormously grateful for his patience and kindness and grateful for being his student.

My secondary supervisor, Prof Derek Yellon, has been an amazing example of what a great scientist should be. He is well invested into making sure that our lab members are aware of work of each other and other scientists in the same field, learn to scrutinize the papers, have a good work ethic while juggling numerous commitments. He helped me to get new ideas for my project when something did not work, and he was there to increase my confidence in myself as a student.

Many our current and former lab members helped me with my research. Dr Kaloyan Takov was the final year PhD student when I came to the lab. He helped me to improve my cell work, learn some exosome characterization methods and use various software. Dr Pelin Golforoush helped me to learn a better way to perform molecular biology techniques and designed a plasmid for me. Elias Sulaiman was a great person to teach exosome techniques, improve them together, and some of his data is included in this thesis. Dr Sapna Arjun always was there to help if I was unsure how to troubleshoot my experiment. Dr Siavash Beikoghli Kalkhoran was helping me to maintain the order in the tissue culture room, which was particularly helpful when we had new students. All these people and other students who I worked with helped me to become a better person as well as supported me when my high expectations of what I should achieve during my PhD were not met.

There are other people who helped me. Mark Turmaine and Elizabeth Slavik-Smith taught me how to use a transmission electron microscope. Dr David He allowed me to use his *in vivo* data from an experiment where cardioprotective effect of exosomes which I characterized was investigated. He also helped me to be a more responsible lab member. He and Jill Jarvis helped me to order anything I needed, and I ordered the most items than anyone in the lab! ReNeuron company kindly supplied me with exosomes and allowed us to publish paper about them. NanoView Diagnostics taught me how to use ExoView Tetraspanin kits and helped me to analyse my samples more extensively. I have been also lucky to teach many bright students who helped me to understand that I enjoy teaching and that I possess some knowledge and skills. Those students also taught me to improve my time management skills and reflect more on my work, which improved my methods and results.

I am grateful for the UCL for providing doctoral training and other opportunities to learn new skills. I am grateful for the opportunities I got here such as becoming a postgraduate teaching assistant, being a student representative, sitting on a disability committee, and being a moderator for Age Innovation Hub where I gathered ideas from the public on how to improve the lives of older generation. All these opportunities helped me to develop new skills, make a change in lives of others, and made my time in the UCL even more enjoyable.

I am deeply grateful for the selection committee for this programme. I thought I performed very poorly on the interview, yet they saw something in me and gave me this lifechanging chance. I doubt I would understand why they chose me. However, thanks to these people, I was able to fulfil my dreams of becoming a scientist, finding a field I enjoy working in, meeting the amazing people, grow as a person, and finding a job which ticks all my boxes. It all started with them, and their decision was life changing for me.

There are many others who played a role in my life during my PhD. Dr Dezso Modos, has been my emotional support. As a double doctor, he was able to teach me about cardiac physiology and biomedical research.

This has been an experience of a lifetime I would never forget.

Table of contents

Abbreviations

Δψm, mitochondrial membrane potential.

ACTN4, actinin alpha 4.

AKT, protein kinase B.

ANOVA, analysis of variance.

AM, acetoxymethyl ester.

AMI, acute myocardial infarction.

ANT, adenine nucleotide translocator.

ApoB, apolipoprotein.

ATP, adenosine triphosphate.

a.u., arbitrary units.

BCA, bicinchoninic acid assay.

BM, bone marrow.

BrdU, bromodeoxyuridine.

BSA, bovine serum albumin.

CAP, catabolite activator protein.

CCCP, carbonyl cyanide m-chlorophenyl hydrazone.

CCD, charge-coupled device.

CCV, clathrin-coated vesicle.

CD, cluster of differentiation.

CIP, calf-intestinal alkaline phosphatase.

CMOS, complementary metal-oxide-semiconductor.

CMV, cytomegalovirus.

CsA, cyclosporin A.

CsH, cyclosporine H.

CVDs, cardiovascular diseases.

CY5, cyanine (dye).

Da, daltons.

Dox/Dex, doxycycline, and dexamethasone.

DELFIA, dissociation-enhanced lanthanide fluorescence immunoassay.

DMEM/F-12, Dulbecco's Modified Eagle Medium/Nutrient Mixture F-12.

DMSO, dimethyl sulfoxide.

DNA, deoxyribonucleic acid.

DOPC, 1,2-Dioleoyl-sn-glycero-3-phosphocholine.

DTSSP, 3,3'-dithiobis(sulfosuccinimidylpropionate).

DTT, dithiothreitol.

EB, Evan’s blue.

EE, early endosome.

EGF, epidermal growth factor.

ERK1/2, extracellular signal-regulated protein kinase ½.

ESCRT, endosomal sorting complexes required for transport machinery.

ETC, electron transport chain.

EVs, extracellular vesicles.

ExoDiff, exosomes from differentiating CTX0E03 cells.

ExoPr0, exosomes from proliferating CTX0E03 cells.

FADH, reduced form of flavin adenine dinucleotide.

FBS, foetal bovine serum.

FITC, fluorescein isothiocyanate.

FSC, forward scatter.

G418, Geneticin.

GAPDH, glyceraldehyde 3-phosphate dehydrogenase.

GBD, mutated glucocorticoid-binding domain.

GFP, green fluorescent protein.

GMP, good manufacturing practice.

GP96, heat shock protein 96.

HEK293, Human embryonic kidney 293

HIF-1, hypoxia-inducible factor 1.

HLA-DR, major histocompatibility complex (MHC) II cell surface receptor.

HSP, heat shock protein.

HUVEC, human umbilical vein endothelial cells.

IDL, intermediate-density lipoprotein.

IgG1-3, immunoglobulin G 1-3.

ILVs, intraluminal vesicles.

I/R, ischaemia/reperfusion.

IRES, EMCV internal ribosome entry site.

irtTA, reverse tetracycline-controlled transcriptional activator.

ISEV, International Society for Extracellular Vesicles.

Kd, dissociation constant.

LAMP2, lysosomal associated membrane protein 2.

LDL, low-density lipoprotein.

LDS, lithium dodecyl sulfate.

LE, late endosome.

LED, light-emitting diode.

MIC60, inner membrane mitochondrial protein.

MISEV2018, Minimal Information for Studies of Extracellular Vesicles.

MitoPQ, MitoParaquat.

mPTP, mitochondrial permeability transition pore.

MSC, mesenchymal stromal cell.

MVB, multivesicular bodies (same as MVE).

MVE, multivesicular endosomes (same as MVB).

NADH, reduced form of nicotinamide adenine dinucleotide.

NTA, nanoparticle tracking analysis.

4-OHT, 4-hydroxy-tamoxifen.

P2Y12, chemoreceptor for adenosine diphosphate.

PBS, phosphate-buffered saline.

PCR, polymerase chain reaction.

PGK, phosphoglycerate kinase.

PEI, polyethyleneimine.

PET, positron emission tomography.

PI, propidium iodide.

Rb, retinoblastoma.

RCGM, rat cardiac myocyte growth media.

RISK, reperfusion injury salvage kinase.

RNA, ribonucleic acid.

ROS, reactive oxygen species.

SD, standard deviation.

SEC, size exclusion chromatography.

SEM, standard error of the mean.

SP-IRIS, single particle interferometric reflectance imaging.

SR, sarcoplasmic reticulum.

SSC, side scatter.

STEMI, ST-segment elevation myocardial infarction.

SV40, Simian virus 40.

TAE, Tris-acetate-EDTA.

TBS, Tris-buffered saline.

TE, Tris-EDTA.

TEM, transmission electron microscopy.

TetA, tetracycline resistance protein.

TetO(p), tetracycline operator.

TetR, tetracycline repressor protein.

TFF, tangential flow filtration.

TGFβ1, transforming growth factor beta 1.

TLR4, toll-like receptor 4.

TMRM, tetramethylrhodamine.

TRITC, tetramethylrhodamine.

TSA, trichostatin A.

TTC, triphenyl tetrazolium chloride.

UV, ultraviolet.

VEGFA, vascular endothelial growth factor A.

VH, variable domain of the heavy chain.

VHH, single variable domain on a heavy chain.

VL, variable domain of the light chain.

VLDL, very low-density lipoprotein.

Chapter 1

The societal impact of cardiovascular diseases

Cardiovascular diseases (CVDs) accounted for 863 billion US$ in health spending in 2010 worldwide, which included treatment cost and productivity loss due to the resultant disabilities (Bloom *et al.*, 2011). Around 30% of all deaths per year due to CVDs, or more than 17 million deaths. The incidence of CVDs is expected to increase by 40% by 2030 (Mendis *et al.*, 2011). Importantly, ischaemic heart disease accounts for around half of the deaths due to CVDs (Naghavi *et al.*, 2017).

Atherosclerosis is an underlying cause of ischaemic heart disease

Ischaemic heart disease is characterised by reduced or restricted cardiac perfusion. It typically occurs due to atherosclerosis affecting the coronary arteries. Atherosclerosis starts with the accumulation of low-density lipoproteins (LDLs) in the arterial intima with the compromised integrity, i.e. the layer of endothelial cells inside the blood vessel which is in direct contact with blood (Figure 1, pre-lesion) (Skålén *et al.*, 2002). Damaged endothelial cells produce high levels of reactive oxygen species (ROS) that oxidise underlying lipoproteins (Steinbrecher, 1988). The modified LDLs induce endothelial and smooth muscle cells to express chemoattractants, growth factors such as macrophage colony-stimulating factors, and adhesion molecules that attract circulating monocytes (Libby, Ridker and Hansson, 2011) (Figure 1, stage I). Monocytes adhere to the damaged endothelium and migrate into the subendothelial space where they acquire macrophage characteristics. These monocytes internalise LDLs and become “foam-like” cells (Chistiakov *et al.*, 2017) (Figure 1, stage II/III). Foam cells aggregate to form the fatty streak of the plaque. Damaged endothelial cells attract other inflammatory cells, e.g. T cells, mast cells, and dendritic cells, to the lesion site (Bot *et al.*, 2007; Gil-Pulido and Zernecke, 2017; Tabas and Lichtman, 2017). Recruited cells produce proinflammatory stimuli and promote lesion development (Figure 1, stage IV/V). Necrotic cells, calcium deposits, and cholesterol accumulate in the lesion, forming its necrotic core (Otsuka *et al.*, 2014). Smooth muscle cells migrate to form a fibrous cap to protect the plaque.

Infiltrating immune cells and accumulating cell debris contribute to the growth of the plague causing stenosis, or narrowing, of the blood vessel. If the fibrous cap thins enough to cause the plaque to rupture, exposed necrotic core attracts platelets that facilitate thrombus formation (Virmani *et al.*, 2002). This thrombus may block the blood vessel or detach to become an embolus and block it further down the bloodstream. Stenosis, thrombi, and emboli can each cause ischaemia of the heart and result in cell death, called myocardial infarction.

Acute myocardial infarction

Acute myocardial infarction (AMI), commonly known as a “heart attack”, predominantly occurs due to the blockage of a coronary artery (Thygesen *et al.*, 2012). Total or partial occlusion of a coronary artery can lead to a STEMI (ST-segment elevation myocardial infarction) and unstable acute coronary syndrome without ST elevation, respectively (Anderson and Morrow, 2017). The occlusion produces an “area at risk” or ischaemic zone. Cardiomyocytes start to die within 20min of ischaemia in the “area at risk”, first in the subendocardium and then progressively towards the epicardium (Jennings and Ganote, 1974; Algranati, Kassab and Lanir, 2011). Necrosis of cardiomyocytes in the ischaemic zone begins after 2-4h and depends on the extent of the collateral circulation, the type of the occlusion, and individual demand in energy (Thygesen *et al.*, 2007). The dead cardiomyocytes release creatine kinase and troponin in the blood, which are used as diagnostic markers (Thygesen *et al.*, 2007).

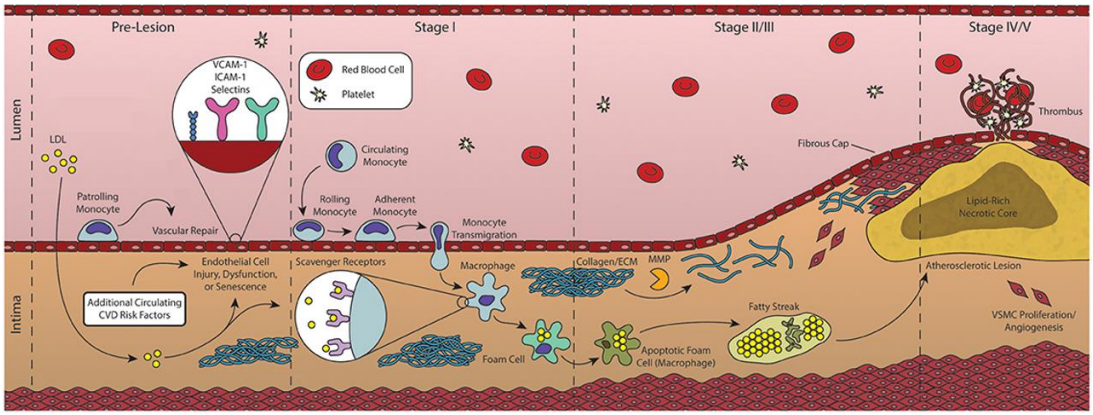

Figure 1. Development stages of the atherosclerotic plaque.

The stages of atherosclerosis, illustrating LDL infiltration of the vessel wall during the pre-lesion stage, monocyte attraction and their change into foam cells during Stage I, following by their apoptosis leading to the formation of a fatty streak and fibrous cap during stage II/III and rupture during stage IV leading to an occlusive thrombus. The picture is adapted from (Head, Daunert and Goldschmidt-Clermont, 2017).

It is crucial to restore the blood flow to the ischaemic area rapidly since the size and location of the infarction determine ventricular remodelling and cardiac dysfunction post-AMI. Typically, reperfusion of the ischaemic area is restored by a stent inserted into the site of the blockage (primary percutaneous coronary intervention), medication (e.g. antithrombotic therapy), and/or diversion of the blood around the blocked artery (coronary artery bypass surgery) (Anderson and Morrow, 2017). Early reperfusion and advances in drug discovery have improved patient survival (French *et al.*, 2010; Schmidt *et al.*, 2012). However, reperfusion kills around 50% more cells compared to ischaemia alone (Hausenloy and Yellon, 2007; Kalogeris *et al.*, 2016). Various pathogenic processes, such as peroxidation of the cell membrane and DNA damage, altered expression of genes (e.g. those involved in cell survival, cardiac metabolism, and inflammation), vascular endothelial dysfunction, infiltration of neutrophils that release ROS and proteinases, all contribute to the cardiac injury post-AMI (Virág *et al.*, 2003; Schofield *et al.*, 2013; Yang *et al.*, 2016; Perrino *et al.*, 2017). The resultant oedema and haemorrhage make the extracellular space in the infarct region to increase. Later, the necrotic heart tissue is replaced by a fibrotic scar tissue when macrophages finish with the digestion of the necrotic zone (Richardson *et al.*, 2015). This process leads to “infarct shrinkage” until the infarct size reaches its final size after one month. The infarct size stays of similar size between one month and six months post-infarction (Ripa *et al.*, 2007). Since electrical conduction in the post-infarction area is altered, the heart may undergo re-entrant arrhythmias, ventricular tachycardia, and may cause sudden cardiac death (Zaman and Kovoor, 2014). With the increasing world population, cases of complications and mortality due to AMI steadily increase. Currently, 22% and 7% of patients develop heart failure or die within one year of post-STEMI, exerting an ever-increasing burden of economic resources of the healthcare system (Roger *et al.*, 2010; Moran *et al.*, 2014).

Prospects of heart regeneration after myocardial infarction

The capability of the human heart to regenerate spontaneously post-infarction is limited because adult cardiomyocytes typically do not proliferate (Bergmann *et al.*, 2009). Therefore, the potential of stem cells to replace the scar tissue with new cardiomyocytes was evaluated in many pre-clinical and clinical studies over the last two decades. Different stem cells, such as mesenchymal stem cells and cardiac stem cells, had shown promise in studies where they contributed to the reduction of the scar size, replenished lost cardiomyocytes, promoted pre-existing cardiomyocyte survival, improved contractility, and ejection fraction after myocardial infarction, in both animals and humans (Orlic *et al.*, 2001; Makkar *et al.*, 2012; Williams *et al.*, 2013; Nigro *et al.*, 2018).

However, the results of studies about the use of stem cells in post-myocardial infarction are largely inconsistent (Tendera *et al.*, 2009; Wöhrle *et al.*, 2010; Hirsch *et al.*, 2011). Also, stem cells exhibit a low level of survival and are poorly retained in the hostile necrotic tissue. Furthermore, they have only a small chance of differentiating into cardiomyocytes (Smith, Marbán and Marbán, 2013; Madonna *et al.*, 2016). Moreover, stem cell engraftment cannot easily be controlled to ensure that they are electrically synchronous with other cardiomyocytes, and therefore the patient may develop life-threatening arrhythmias (Smit and Coronel, 2014; Mount and Davis, 2016). Finally, stem cells can form teratomas as shown by Adamiak and colleagues: induced pluripotent stem cells became tumours in half of the treated mice (Adamiak *et al.*, 2018). Yet, since some studies showed that beneficial effects of stem cells persisted after they were no longer present in the heart, it was hypothesised that stem cells release factors that favourably affect the infarcted area. Indeed, the cell media of stem cells was later found to confer the same cardioprotective properties as the parent stem cell to the injured heart. Specifically, treatment with this media increased cardiomyocyte survival post-infarction, enhanced angiogenesis, reduced heart remodelling, and inflammation, all without causing teratomas and arrhythmias (Mirotsou *et al.*, 2011; Khanabdali *et al.*, 2016; Adamiak *et al.*, 2018).

Extracellular vesicles including exosomes mediate cardioprotection of stem cells

The secretome of cells, which was determined to be the active component of stem cell media, contains cytokines, RNAs, growth factors, and extracellular vesicles that are implicated in mediating cardioprotective effects to the injured hearts (Caplan and Dennis, 2006; Haider *et al.*, 2008; Tang *et al.*, 2010; Marote *et al.*, 2016; Phelps *et al.*, 2018). Extracellular vesicles (EVs) are heterogeneous nanoparticles (around 30-2000nm in diameter) that are released by most cells, if not all, including cardiomyocytes, endothelial cells, blood cells, and stem cells (Wang *et al.*, 2014; Hromada *et al.*, 2017; Davidson and Yellon, 2018). The International Society for Extracellular Vesicles (ISEV) proposed to categorise them into groups. There are two groups of vesicles with possibly overlapping sized, microvesicles (100-1000nm) and exosomes (50-150nm). These vesicles differ by the mechanisms of biogenesis and release: microvesicles are formed by outward budding of the cell membrane whereas exosomes are produced by intraluminal vesiculation within endosomal multivesicular bodies and released by fusion of these bodies with the cell membrane (Figure 2) (Chen, Li and Liu, 2018; Hessvik and Llorente, 2018). Microvesicles can be considered like a “liquid biopsy” of the parent cells and are produced in response to stimuli (Cocucci, Racchetti and Meldolesi, 2009). In contrast, exosomes are constitutively formed and released from the cell, and their composition is tightly controlled by the cellular machinery. Biogenesis and transport of EVs, their source, and the growing conditions of the parent cell affect the membrane composition and cargo of EVs (Genneback *et al.*, 2013; Malik *et al.*, 2013; Lopatina *et al.*, 2014; Meldolesi, 2018). The membrane constituents and cargo, in turn, may determine the cardioprotective potential of EVs. When administered to hearts undergoing ischaemia/reperfusion, EVs are equally effective or outperform their parent stem cells e.g. they improve the left ventricular function, reduce cardiomyocyte apoptosis and increase vascularity of the infarct area (Table 1) (Adamiak *et al.*, 2018). Importantly, exosomes may confer cardioprotection rapidly within ~15min. For example, when plasma exosomes were administered to rats, HSP70 on the membrane of the exosomes activated the cardioprotective p38 kinase signalling pathway in cardiomyocytes by interacting with toll-like receptor 4 on the cell membrane, resulting in a smaller infarct size (Vicencio *et al.*, 2015).

However, it is hard to be certain which specific bioactive molecules in EVs or their membranes are responsible for cardioprotective effects. The reason is that current isolation protocols allow enrichment of exosomes, but not complete purification (Konoshenko *et al.*, 2018). Frequently, exosomes are co-isolated with microvesicles that have various bioactive molecules inside them and on the membrane. Additionally, numerous cardioprotective proteins and their aggregates may co-isolate with exosomes.

Hypothesis

The overall hypothesis of my study was that functional exosomes derived from stem cells of high purity can confer cardioprotection in the cell models of myocardial injury.

Aims

The overarching aim of this thesis was to develop a method of studying exosomes in a cell model of myocardial infarction. This thesis consists of three sections. Chapter 2 describes the complete characterization of stem cell exosomes which were collected from cells grown according to the good manufacturing practice regulations. Since these exosomes are purified by two different methods, they were expected to be of relatively high purity. Chapter 3 presents a novel method of exosome purification using a recombinant protein tag. Chapter 4 describes an extensive investigation of *in vitro* models of myocardial injury which is simulated by using mitotoxic drugs in cardiac cells.

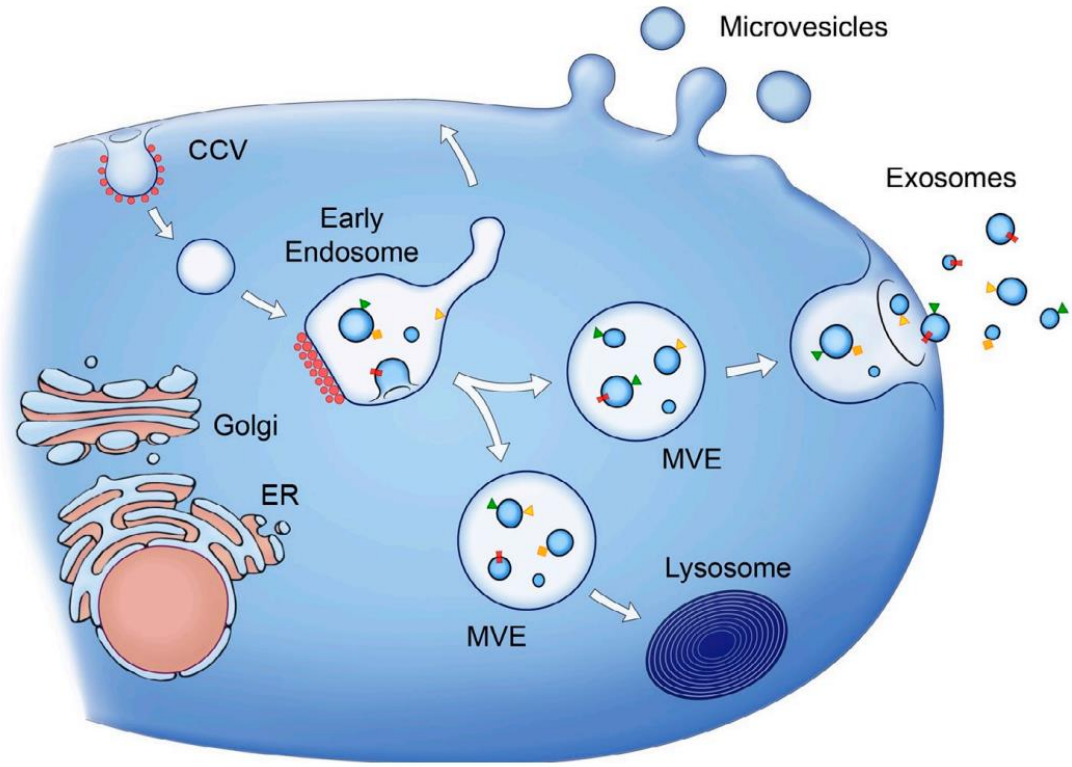

Figure 2. Biogenesis of exosomes and microvesicles.

Microvesicles are released from cells by outward blebbing and shedding of the cell membrane whereas exosomes production starts with endocytosis. The cell membrane buds inwards forming a clathrin-coated vesicle (CCV). CCV eventually becomes an early endosome (EE). Membrane proteins are usually rapidly recycled back to the membrane from the EE, but certain proteins accumulate in the EE over time. As endosomes mature, they form intraluminal vesicles (ILVs, 50-100nm) inside them by inward vesiculation, thus capturing a small volume of cytosol. Endosomes with intraluminal bodies are called multivesicular endosomes (MVE; or bodies, MVB). The endosomal sorting complex required for transport (ESCRT) and clathrin on the EE membrane select certain ubiquitinated cell membrane proteins into ILVs. One role of ILVs is to collect cell membrane proteins and lipids which later will be degraded in lysosomes. With an increased number of ILVs, MVE becomes a late endosome (LE) which is more acidic and larger than MVE. LE does not recycle proteins anymore. Instead, LE becomes a lysosome by the accumulation of lysosomal components and removal of LE components, or LE transfer their cargo to a lysosome, or fuse with a lysosome. Proteins from LE then either undergo degradation in the lysosomal environment or maintain the lysosome structure and function. Alternatively, LE fuses with the cell membrane instead and release their ILVs. Once released by cells, these vesicles are called exosomes. The figure is obtained from (Raposo and Stoorvogel, 2013).

Source of exosomes	Exosome action *in vivo* and *in vitro* models of myocardial ischaemia/reperfusion injury
Mesenchymal stem/stromal cells	• Reduction of infarct size (Lai *et al.*, 2010) • Improvement of cardiac function and protection from oxidative stress (Arslan *et al.*, 2013) • Angiogenesis, reduction of fibrosis, and decrease of cardiac cell apoptosis (Zhao *et al.*, 2015) • Improved cardiac contractility (Mayourian *et al.*, 2017) • Immunomodulation (Monguió-Tortajada *et al.*, 2017)
Cardiac stem cells	• Angiogenesis, reduction of fibrosis, a decrease of cardiac cell apoptosis, and improvement of cardiac function (L Barile *et al.*, 2014)
Embryonic stem cells	• Angiogenesis, reduction of fibrosis, and decrease of cardiac cell apoptosis (Khan *et al.*, 2015) • Improvement of cardiac function (Kervadec *et al.*, 2016)
Hematopoietic stem cells	• Angiogenesis (Sahoo *et al.*, 2011)
Cardiospheres	• Reduction of infarct size, improvement of cardiac function, reduction of fibrosis, and microvascular obstruction (Gallet, Dawkins, Valle, Simsolo, De Couto, *et al.*, 2017) • Angiogenesis and decrease of cardiac cell apoptosis (Tseliou *et al.*, 2015)

Induced pluripotent stem cells	• Angiogenesis, a decrease of cardiac cell apoptosis, and inhibition of hypertrophy (Adamiak *et al.*, 2018) • Protection from oxidative stress (Wang *et al.*, 2015) • Reduction of fibrosis and immunomodulation (Yang, 2018)

Table 1. Cardioprotection against ischaemia/reperfusion injury by exosomes.

Exosome-rich secretome of various stem cells were shown to protect the heart against ischaemia/reperfusion injury by suppressing different pathological processes and promoting heart healing (Davidson and Yellon, 2018; Yuan *et al.*, 2018)**.**

Chapter 2

Introduction

CTX0E03 neuroepithelial cells as a source of exosomes for myocardial ischaemia/reperfusion injury

Exosomes from many stem cells, irrespective of which cell types they can differentiate into, have been shown to confer cardioprotection in the setting of cardiac ischaemia/reperfusion (I/R) injury (Davidson and Yellon, 2018). However, only some types of stem cells are readily produced on a large scale as reproducible stocks. For example, primary MSCs such as amniotic fluid mesenchymal stromal cells, which are cardioprotective, have limited proliferative capacity of several weeks (Takov *et al.*, 2020). Considering that long-term expansion of stem cells increases the risk of their genetic and phenotypic instability, this increases the risk that their exosome quality and safety vary over time (Oliveira, da Silva and Cabral, 2014).

To address these problems of stem cell safety and scalability, a UK-based stem cell research company ReNeuron established large-scale and cGMP-standardized (current good manufacturing practice regulations) production of genetically modified somatic stem cells. In 2006, they first reported their methods (Pollock *et al.*, 2006). Plasmid DNA encoding the *c*-mycER^{TAM} sequence was cloned into a retroviral vector. The construct encoding for a transcription factor, *c*-myc, enhances transcription of a human growth-promoting gene. The transcription factor was conjugated to a modified mouse oestradiol receptor. This monomeric complex is inactive in the cytosol until tamoxifen is added to the culture medium and converted to its metabolite 4-hydroxy-tamoxifen (4-OHT) by the cell. Then, the complex dimerises, translocates to the nucleus, and initiates cell proliferation (Littlewood *et al.*, 1995). The *c*-mycER^{TAM} sequence also carries a neo$^{R\text{-selectable}}$ marker which allows the selection of transduced cells by conferring resistance to neomycin.

After the retrovirus was generated, neuroepithelial cells, stem cells that differentiate into neurons and glia, were isolated from a 12-week-old foetal human cortex. ReNeuron chose these cells because of their interest in stroke. Neuroepithelial cells were infected with the virus and then the transduced cells were selected with neomycin. A neomycin-resistant 4-OHT-positive colony named CTX0E03 was confirmed to be genetically stable (Pollock *et al.*, 2006). It can be successfully grown in the presence of 4-OHT or differentiated into neurons and a smaller amount of glia in the absence of 4-OHT. Importantly, ReNeuron states that the CTX0E03 stem cell line will not be re-derived because they have sufficient cell stocks which would enable almost limitless manufacture.

After ReNeuron established large-scale automated cell expansion, they sought to investigate CTX0E03 cells as a treatment against cerebral I/R injury (Thomas *et al.*, 2009). Ischaemic stroke and acute myocardial infarction have similar aspects of I/R injury. During cerebral ischaemia, cellular energy levels are rapidly depleted. This is followed by cellular lactic acidosis, sodium/potassium pump failure, excessive ROS production, and abnormal glutamate release that causes excitotoxicity (Stonesifer *et al.*, 2017). As in myocardial infarction, cerebral ischaemic stroke requires rapid reperfusion which contributes to the eventual overall infarct size. Reperfusion promotes further oxidative stress, mitochondrial permeability transition pore (mPTP) opening, and deleterious inflammation (Bowler *et al.*, 1998). The resultant disruption of the blood-brain barrier ultimately leads to brain tissue loss, neurological dysfunction, and even death of the patient (Lin, Wang and Yu, 2016). Currently, stroke patients are treated with a tissue plasminogen activator, which has inconsistent efficacy and a narrow therapeutic window. Alternatively, surgical interventions are used, and their purpose is to remove the cause of ischaemia and allow reperfusion. Yet, there is no adequate treatment to address the consequences of the I/R injury, namely the loss of neurons.

The CTX0E03 cell line has been investigated to address this problem. Stroke was induced in rodents by occluding the middle cerebral artery, which is commonly affected in clinical ischaemic stroke. This causes paresis and sensory dysfunction (Shahjouei *et al.*, 2016). CTX0E03 cells were engrafted close to the infarcted area in these rodents. The cells were found to enhance functional and behavioural recovery, improve cerebral blood flow, modulate the immune response, promote neurogenesis and angiogenesis (Pollock *et al.*, 2006; Eve *et al.*, 2009; Stroemer *et al.*, 2009; Hassani *et al.*, 2012). Then, ReNeuron proceeded with small clinical trials. The PISCES I and II trials suggested that engrafting CTX0E03 cells were feasible and safe (Kalladka *et al.*, 2016; Muir *et al.*, 2020). Interestingly, CTX0E03 neuroepithelial cells were also protective in a rodent model of hindlimb ischaemia, suggesting that they may be useful in other ischaemia/reperfusion models (Katare *et al.*, 2014).

Early on, however, ReNeuron discovered that very few cells survived *in vivo* and even fewer differentiated into neurons or glia (Stevanato *et al.*, 2009; Stroemer *et al.*, 2009). Therefore, they hypothesised that CTX0E03 cells may release paracrine factors which mediate the observed improvements (Stroemer *et al.*, 2009). Indeed, the cells were later discovered to promote angiogenesis by releasing angiogenic factors (Hicks *et al.*, 2013). Yet, those factors alone could not explain the multitude of the effects observed with the cell treatment. Other laboratories reported that EVs are important in mediating the effects of stem cells (Drago *et al.*, 2013). There are numerous ways to isolate and characterise exosomes (Davidson *et al.*, 2022). Yet, it is not feasible to isolate completely pure exosomes, especially the large quantities that are required for functional studies (Table 2). Commonly, exosomes are co-isolated with lipoproteins, proteins and microvesicles. Therefore, ReNeuron developed procedures to isolate large quantities of GMP-quality EVs from cultured CTX0E03 cells to study their effect in stroke.

Specifically, ReNeuron employs a combination of two isolation techniques, namely tangential flow filtration (TFF) and size exclusion chromatography (SEC), which in combination may produce exosomes of relatively high purity. TFF, or crossflow filtration, allows the removal of particles larger than the desired particle size. In TFF, the sample flows parallel to the filter surface and generates shear stress to scour the filters, so that no blockage is formed (Figure 3, A). Pressure is applied on the flow to force fluid and particles of the pore size or smaller into the filtrate stream (Figure 3, B). The retentate can be discarded to remove accumulated large particles or returned to a vessel. Product recovery per pass is typically lower than 20% and therefore recirculation of the retentate is needed for the complete product recovery. A new sample or diluent is added to the feed when required to keep the flow volume constant (Musumeci *et al.*, 2018; Schwartz and Seeley, 2022).

EV recovery and specificity	Isolation technique	Principle of technique and its limitations	Altered EV morph-y	Conta-minants		
				ApoB	MVs	Protein
Both high	None	N/A	o	o	o	o
High recovery, low specificity	Precipitation	EVs are captured based on their size in “polymer nets” using centrifugation. Polymer is not completely removed.	o	x	x	o
	Ultracentrifugation without lower speed steps	EVs are captured based on the sedimentation rate of particles, which depends on their density, size, and shape.	x	x	x	o
Both intermediate	Ultracentrifugation with lower speed steps	As above. Lower speeds remove particles larger than EVs.	x	x	x	o
	Differential ultracentrifugation	Several steps of increasing centrifugation speed to remove particles smaller and larger than EVs.	x	x	x	o
	Tangential flow filtration	EVs are filtered from larger particles.	o	x	x	x
Low recovery, high specificity	Combination of techniques separating EVs by their size	For example, size exclusion chromatography and tangential flow filtration	o	x	x	o

	Density gradient centrifugation	The sample is added on preconstructed density gradient. Particles form discrete solute zones during ultracentrifugation.	x	x	x	o
	Immunoaffinity chromatography	EV subtype is captured by antibodies against a specific membrane marker. Unbound particles are removed.	o	o	x	o

Table 2. Isolation techniques for purifying extracellular vesicles and disadvantages of these methods.

None of the commonly used isolation techniques can currently yield pure (high specificity) and abundant (high recovery) extracellular vesicles for functional studies. Therefore, the study objective should dictate what level of the EV purity is required for a study. Each method of EV isolation can have all three contaminants, namely lipoprotein (ApoB), MVs, and proteins. However, the frequent and abundant contaminants are shown as red “x”, and those contaminants which are rarely observed with a technique are shown as green “o”.

Unlike TFF, SEC removes particles smaller than the particle of interest. SEC is an isolation technique based on the elution of particles running through a column filled with porous beads. The beads constitute the stationary phase of the column. A mixture of particles, e.g. blood plasma or cell culture medium, is poured on the top of the column (Figure 4, A). Importantly, the column holds a certain volume of liquid inside the stationary phase. The mixture passes through a matrix of beads down the column. When a sample of known volume is added to the column, e.g., 0.5ml, then the same volume of the liquid from the stationary phase is collected as Fraction 0.0-0.5ml (Figure 4, B). Then, 0.5ml of PBS can be added to the column to collect Fraction 0.5-1.0ml. At some point, particles elute in some fractions. Exosomes are unable to enter the pores and pass around the beads down the column. Therefore, they elute first. Free proteins and lipids are collected later because they pass through pores inside the beads. SEC separated particles into two groups: one group which has particles larger than bead pore size elute first, and another group which has particles small enough to pass through the beads.

As mentioned above, CTX0E03 cells are of clinical grade, produced on a large scale, have the potential to mitigate I/R injury, and were safe in clinical trials. Additionally, ReNeuron produces large volumes of exosome-rich samples from differentiating and proliferating CTX0E03 cells. Therefore, the quality of CTX0E03 exosome stocks ought to be reproducible. A previous PhD student in the Hatter Cardiovascular Institute, Dr Kaloyan Takov, used exosomes from CTX0E03 exosomes in a pilot experiment. He observed endothelial tubule formation in an *in vitro* assay with HUVEC endothelial cells which was accompanied by activation of the reperfusion injury salvage kinase (RISK) pathway (unpublished data). Since the RISK pathway is well established as being a central mechanism of reducing myocardial infarction size, this suggested that CTX0E03 exosomes could be a promising cardioprotective reagent, at a stage ready for clinical trials (Derek J. Hausenloy and Yellon, 2007).

Currently, it is not known if exosomes from differentiating or proliferating stem cells would have a higher cardioprotective potential in the models of myocardial infarction. CTX0E03 cells are grown in different conditions depending on if they need to be differentiated or proliferated. Different growth conditions and different cell state affect the composition and function of secreted EVs. For example, serum starvation, hypoxia, oxidative stress, cell age, and cell differentiation change EVs (Lucchetti *et al.*, 2017; Haraszti *et al.*, 2019; Mao and Xu, 2020; Chiaradia *et al.*, 2021; Jiang *et al.*, 2022). Since ReNeuron company has cultures of both proliferating and differentiating stem cells, we requested exosomes from each of them, ExoDiff and ExoPr0, respectively. My intention was to characterize both EV preparations and compare them. Following this, the intention was to investigate differences in their composition and functionality in cell and animal models of myocardial infarction. If there is uniformity between batches of EVs, they confer cardioprotection better than any positive control, and their optimal dose for treatment of myocardial infarction is found, then it is possible that ReNeuron may consider starting clinical trials using their EVs.

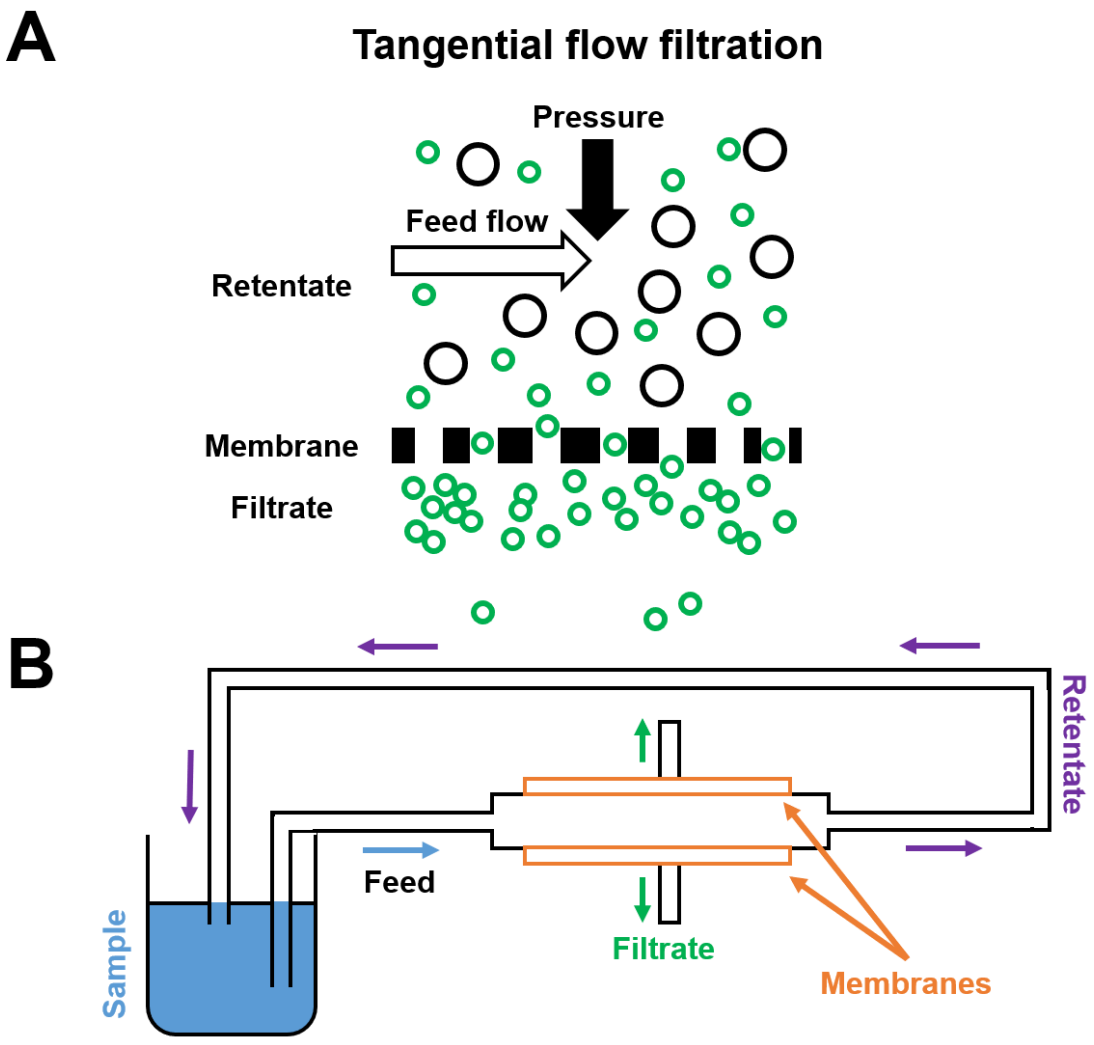

Figure 3. Principle of tangential flow filtration and schematic setup.

(**A**) Tangential flow filtration (TFF) is a sample filtration and concentration technique. The sample flows parallel to the filter while the pressure is applied. This allows the separation of particles based on their size. (**B**) This is a schematic setup to perform TFF. A sample containing particles of different sizes is pumped through the system. Pressure is applied on the feed to force particles of interest through the filter membrane pores. Concentrated particles are collected as filtrate. The retentate can be discarded or recirculated to increase the product recovery.

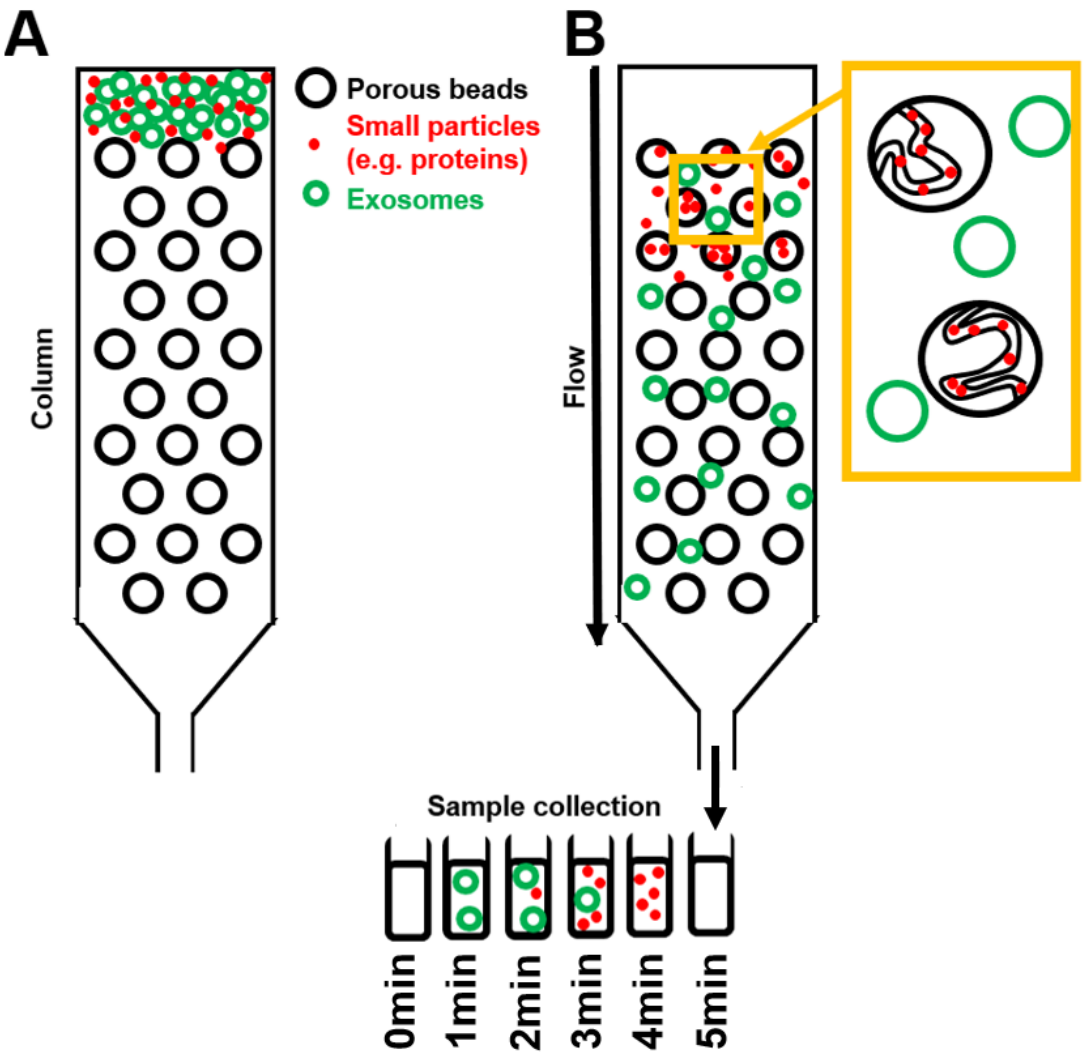

Figure 4. Principle of size exclusion chromatography.

(**A**) Size exclusion chromatography is performed to separate particles based on their size. The mixture of particles is added to the top of the column. The column is formed by porous beads. (**B**) Small particles such as protein pass through the pores and require a longer time to elute from the column. Larger particles, such as exosomes, pass around the beads down the column, faster than proteins. The sample fractions are collected at different time points.

Characterisation of CTX0E03 exosomes for myocardial ischaemia/reperfusion injury studies

Before ExoDiff and ExoPr0 being used for functional studies, their purity should be evaluated. For this, exosome characterization by several complimentary methods is required. In 2018, the International Society for Extracellular Vesicles (ISEV) published Minimal Information for Studies of Extracellular Vesicles (MISEV2018) (Théry *et al.*, 2019). MISEV2018 provides recommendations of which data should be reported about EV samples to ensure reproducibility and reliability of the data. According to the ISEV, compulsory information about EVs should include their quantity. Currently, exosome concentration is often measured indirectly. Protein assays are a common method to quantify exosomes. Since CTX0E03 exosomes were obtained with size exclusion chromatography, most protein, which is generally smaller than exosomes, is expected to have been removed. Protein concentration in the exosome-enriched sample can be quickly determined by measuring protein absorbance. For this, ultraviolet light is passed through the sample. The light at this wavelength (280nm) is readily absorbed by aromatic amino acid side chains, namely tyrosine and tryptophan. The absorbance values are then converted to protein concentration using the protein standard curve.

However, quantification of EVs with two independent methods is recommended by MISEV2018 guidelines. Therefore, nanoparticle tracking analysis (NTA) can be used for real-time direct visualisation and analysis of the size and quantity of particles. In NTA, the EV-containing sample flows through a sample chamber at a fixed speed, where it becomes a thin layer of fluid (Figure 5). Each particle is carried by the flow across the chamber. The rate of particle random movement is inversely proportional to particle size. The sample flows through the chamber where it is illuminated by a laser. Particles hit by the laser scatter the light in various directions. The scattered light travels through the microscope objective and is captured by a camera, e.g., a charge-coupled device (CCD). This detected light helps to track the Brownian motion of particles and to estimate their size and number.

Protein to particle ratio may be used as an additional indicator of exosome purity (Webber and Clayton, 2013). However, EV size can vary as well as their content. Also, particle quantification does not reveal the nature of particles. Therefore, close-up images of samples should be obtained. Due to the exosome size, high-resolution microscope techniques such as transmission electron microscopy (TEM) are used. TEM utilises electrons instead of light to image the ultrathin (<100nm) specimens. An electron gun shoots electrons into a vacuum space of the microscope column (Figure 6). Since electrons have a wavelength 100,000-fold shorter than the wavelength of visible light, they allow the magnification of the image by up to 500,000-fold. A magnetic condenser lens focuses electrons into a thin beam. The beam hits the specimen, that is placed on a grid (<100μm thickness), and electrons pass through it depending on the thickness of the sample or are diffracted. The transmitted electrons and slightly scattered electrons are focused by a magnetic objective lens. However, the high angle diffracted electrons are eliminated by the objective to ensure a high contrast image. Transmitted electrons then pass through a wide aperture opening and diffracted electrons are eliminated. Consequently, electrons pass through a magnetic projector lens, which enlarges the resultant specimen image. The electrons fall on a fluorescent screen, or a CCD and the signals are converted into the image of the specimen. The dark areas on the TEM image are created by particles that scatter electrons. Therefore, exosomes appear as dark cup-shaped structures. To provide contrast to visualize exosomes and other particles better, an electron dense stain like uranyl acetate can be used. The uranyl ions attach well to biological matter, e.g., lipids, proteins, and nucleic acids, and scatter electrons strongly.

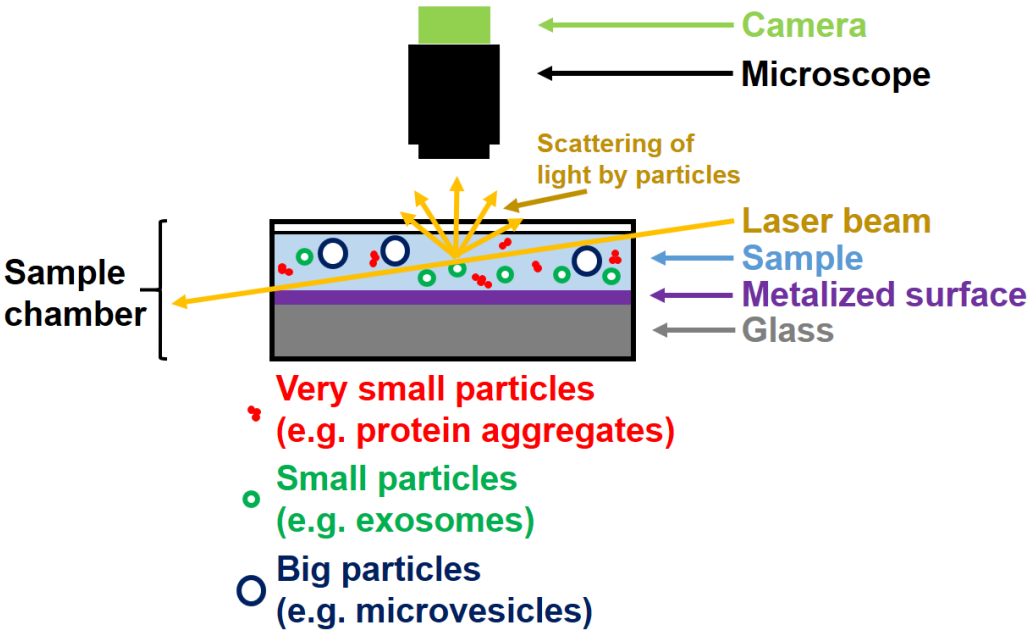

Figure 5. Principle of nanoparticle tracking analysis.

A sample containing particles such as extracellular vesicles is diluted and pushed through the sample chamber. The sample forms a thin layer on the metalized surface of glass inserted in the chamber. The particles are hit by the laser and the light is scattered in various directions. The scattered light travels through the microscope objective and is captured by a camera.

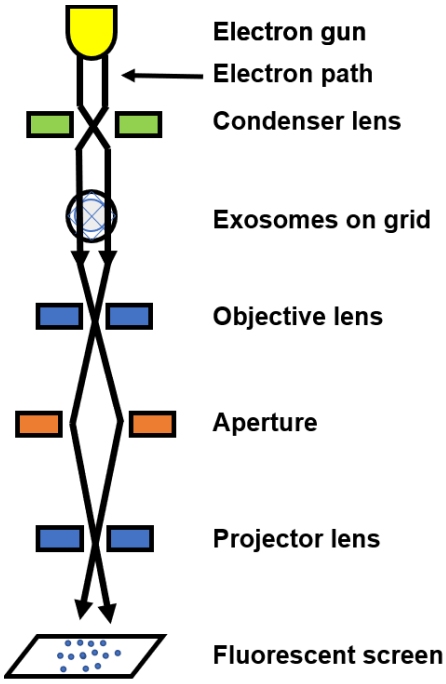

Figure 6. Principle of transmission electron microscopy.

An electron gun shoots electrons into the microscope column. Magnetic condenser focuses electrons into a beam, which hits the grid with the sample (here: exosomes). Electrons pass through the sample and are focused by an objective lens. Then, the electrons pass through an aperture and projector lens. Finally, electrons fall on a fluorescent screen and the signal is converted into an image.

Another requirement for reporting exosome studies is to confirm the presence of exosome-associated markers in the sample. ISEV does not propose specific surface markers to detect since even a single cell can produce different subtypes of exosomes with unique membrane compositions. However, tetraspanins CD9, CD63, and CD81 are frequently used as exosome markers because they are enriched in exosome membranes (7-124-fold more than in the parent cell) (Andreu and Yáñez-Mó, 2014). Tetraspanins form tetraspanin-enriched microdomains that may affect exosome cargo loading and exosome biogenesis (Andreu and Yáñez-Mó, 2014). For the studies on cardioprotection, one may be interested in the presence of markers that may activate pro-survival kinases. For example, heat shock protein HSP70 on exosomes was shown to activate toll-like receptor TLR4 on the recipient cell membrane (Vicencio *et al.*, 2015). This leads to the activation of extracellular signal-regulated kinases ERK1/2 that are a part of a universally cardioprotective RISK pathway. Additionally, expected contaminants can be identified. Size exclusion chromatography and tangential flow filtration are unlikely to remove all lipoproteins of exosome size, namely chylomicrons, very low and intermediate-density lipoproteins. Therefore, the presence of apolipoprotein B, a constituent of these lipoproteins, should be determined. Exosome and lipoprotein markers can be detected by dissociation-enhanced lanthanide fluorescence immunoassay (DELFIA), which is essentially an ELISA with an altered detection step (Aydin, 2015). In DELFIA, sample particles are bound to the plate and then incubated with primary antibodies against a specific marker, e.g., CD9. A secondary antibody with streptavidin-Europium conjugate binds the primary antibody. The conjugate has a strong signal allowing detection of even 10^{-15} of the markers. Therefore, this method only requires a small sample volume. If the signal for a specific marker is stronger than in the control, it indicates the marker presence.

However, DELFIA does not determine the number of exosomes positive for a specific marker. The authors of the MISEV guidelines suggest that the presence of one type of tetraspanin on an exosome-sized vesicle does not prove that the vesicle is a true exosome (Tkach, Kowal and Théry, 2018). For example, a small EV positive for CD81 but negative for CD63 may be not enriched in proteins derived from multivesicular bodies. To address these problems, Single Particle Interferometric Reflectance Imaging (SP-IRIS) method has been recently developed. SP-IRIS allows digital quantification and multiplexed phenotyping of different EV populations captured on a microassay-based sensor chip. It is based on interferometry. Interferometry is a technique that extracts information from the interference of superimposed waves. In SP-IRIS, capture antibodies against of marker of interest are printed on a chip. EVs in the sample can bind them, and marker-negative particles are washed away. Then, fluorescently tagged secondary antibodies against other markers bind captured EVs, allowing them to be distinguishable. Then, monochromatic LED light (light-emitting diode) illuminates a microarray sensor chip, and the reflection of the chip surface is captured on CCD (charge-coupled device) or CMOS (complementary metal-oxide-semiconductor) camera (Figure 7, A). The key to the visibility of EVs on the SP-IRIS system is the detection of interference of light reflected from the Si and SiO_2 interface (reference interface) of the chip with that from the surface of EVs (Figure 7, B). The reflectivity curves are obtained at different wavelengths from the reference interface and EV surface by the camera. The software calculates a phase shift between these two wavelengths (Figure 7, C). The phase shift enhances the contrast of EVs on the camera. EVs appear as diffraction-limited dots on the camera and their contrast is correlated to the EV size (Figure 7, B, and D). The detection of EV shape allows discrimination of the noise from other particles such as aggregates or dust. To determine the EV subtype (e.g., the presence of several tetraspanins), the software analyses the fluorescence colour emitted by every EV.

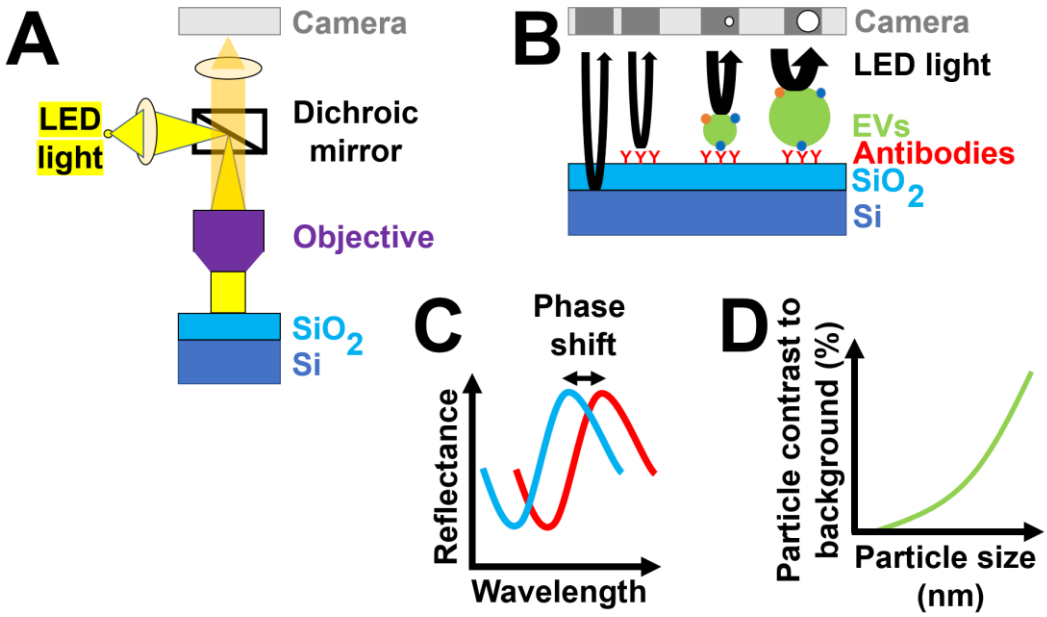

Figure 7. Principle of single-particle interferometric reflectance imaging.

(**A**) In single-particle interferometric reflectance imaging (SP-IRIS), the light shines onto a microarray chip which surface is made of SiO_2 and Si. The light is reflected to the camera. (**B**) The chips for analysis of extracellular vesicles (EVs) have capture antibodies against EV markers on their surface. The light reflected by EVs is compared to the light reflected from antibodies to determine the size of EVs. (**C**) Wavelengths reflected from the antibody-coated surface and EVs are compared, and the phase shift is determined. The size of the phase shift is used to calculate the size of EVs. (**D**) There is a correlation between the particle size and contrast of EVs relative to the background.

Aims and hypothesis

Hypothesis

Since the CTXE03 EVs are purified by both TFF and SEC, I hypothesised that CTX0E03 EVs are exosome-enriched samples with cardioprotective potential in models of myocardial infarction. I expected the batches of CTX0E03 EVs to be of consistent quality as they are produced industrially. .

Aims

1. Characterise the chosen exosomes, ExoDiff and ExoPr0, according to the latest recommendations of the International Society for Extracellular Vesicles (ISEV)
    a. Determine protein concentration by measuring protein absorbance values
    b. Confirm the presence of cup-shaped EVs with electron microscopy
    c. Quantify and measure the size of particles by using nanoparticle tracking analysis
    d. Confirm the presence of exosome-associated markers and the absence of common contaminants such as apolipoprotein by using dissociation-enhanced lanthanide fluorescence immunoassay (DELFIA)
    e. Phenotype EVs by using single-particle interferometric reflectance imaging sensor (SP-IRIS)
2. Analyse another batch of exosomes to confirm that exosome baches are of consistent quality

Methods

Materials and reagents

The list of solutions, chemicals, kits, instruments, and software is given in Supplementary table 1.

Purification of exosomes using tangential flow filtration and size exclusion chromatography

Exosomes from differentiating (ExoDiff) and proliferating (ExoPr0) CTX0E03 human neuronal stem cells were gifted by ReNeuron who established large-scale production of GMP-compatible (good manufacturing practice) stem cells. Exosome samples were produced by ReNeuron company using tangential flow filtration and size exclusion chromatography as described previously. For that, cells were grown in CELLine bioreactors or flasks coated with laminin (20µg/ml) for ExoDiff and ExoPr0 exosome collection, respectively. Media of the cells grown in the bioreactors was Dulbecco's Modified Eagle Medium/Nutrient Mixture F-12 (DMEM/F-12) supplemented with 0.03% human albumin, 2mmol/l glutamine, 10ng/ml basic fibroblast growth factor, 20ng/ml epidermal growth factor, 40ng/ml sodium selenite, 60ng/ml progesterone, 100nM 4-hydroxy-tamoxifen (4-OHT), 5µg/ml human insulin, 5µg/ml human transferrin, and 16.2µg/ml putrescine dihydrochloride (ExoPr0 media). Cell differentiation was induced by the removal of 4-OHT and growth factors from the cell media. To ensure differentiation, cells were deprived of these drugs for 6-15 weeks. ReNeuron did not provide information on how they confirmed the differentiating status of CTX0E03 cells. Conditioned media was collected from cells at 80-90% confluency, and then filtered through a 0.22µm Stericup filter to remove cells and their debris. Conditioned media was then subjected to tangential flow filtration using phosphate-buffered saline (PBS). Spectrum hollow fibre filter had a 100kDa molecular weight cut-off membrane. This procedure was followed by size exclusion chromatography using an iZon qEV column. The order number and manufacturer of all chemicals and equipment used by ReNeuron is published (Katsur *et al.*, 2021).

Protein quantification using spectrophotometry

The total protein content of exosome preparations was directly quantified using a low-volume microplate, the LVis absorbance microplate, in a FLUOstar OMEGA plate reader. Specifically, dilutions of bovine serum albumin (BSA) standard and exosomes were loaded onto the plate and protein absorbance was read at 280nm, the wavelength which is readily absorbed by an aromatic amino acid side chain. OMEGA Mars and Data Analysis software was used to record the absorbance of samples. Absorbance values of standard dilutions were plotted against their concentrations. The equation of the standard curve was used to calculate the concentration of exosome dilutions:

$$Sample\ concentration = Dilution\ factor * \frac{y - B}{a}$$

where

y = absorbance of the sample

x = slope of BSA standard curve

B = y-axis intercept of the BSA standard curve

Imaging of EVs using transmission electron microscopy

Imaging of EVs was performed according to the previously published methods (Théry *et al.*, 2006). For gold immunolabelling, formvar-carbon coated grids were placed on 2µl drops of EV-containing sample. After overnight incubation, the grids were placed on 100µl phosphate-buffered saline (PBS) drops three times for 3min to wash off all unbound particles. The excess fluid was removed by filter paper after each step of incubation. Then, the grids were blocked with 1%BSA/PBS for 10min to prevent the non-specific binding of antibodies. Afterwards, the grids were transferred to 10µl drops of the anti-CD81 primary antibody diluted in PBS (1:500) for 90min. The unbound antibody was washed off on PBS drops for 3min six times. After washes, the grids were incubated on 10µl drops of goat anti-mouse secondary antibody conjugated to 5nm gold nanoparticles. After 90min, the grids were washed with PBS for 2min eight times. To fix antibodies on EVs, the grids were transferred on 50µl drops 1% glutaraldehyde/PBS. After 5min, the grids were washed on PBS for 2min eight times. To contrast exosomes, grids were transferred to 50µl of uranyl-oxalate solution for 30sec. After blotting the excess of the liquid, the grids were airdried for 5-10min. EVs were visualised at Joel 1010 microscope at 80kV, as shown in Figure 6.

For EV imaging without immunogold staining, the grids were incubated on EV-containing sample for 10min or overnight, washed once on PBS, contrasted with uranyl-oxalate, and then imaged. Some grids were stained with uranyl-oxalate by Mark Turmaine. He and Elizabeth Slavik-Smith performed the start-up of the microscope and transferred grids into it.

Particle size measurement and quantification using nanoparticle tracking analysis

EV-containing samples were analysed by the NanoSight LM10 NTA instrument. Nanoparticle tracking analysis (NTA) allows the analysis of particles in a range between 10-2000nm. EV-containing sample was diluted in distilled water and pushed through the sample chamber by NanoSight syringe pump at a fixed speed (speed: 20). The sample in the chamber was illuminated with a 488nm laser by NanoSight laser unit (Figure 5). The scattered light was captured by a NanoSight CMOS camera. Three videos of 90sec or five 60sec-long videos per sample were captured. The camera level was set at 15 and the detection level was 5. The NanoSight software tracked the Brownian motion of particles and estimated their size by using the Stokes-Einstein equation:

$$D = \frac{\mathrm{kB} * \mathrm{T}}{6 * \pi * \eta * \mathrm{r}^3}$$

where

D = diffusion constant, the average distance moved by each particle

kB = Boltzmann's constant

T = sample temperature

π = pi value

μ = the ratio of the velocity of a particle to the applied force

η = the viscosity of the diluent

r = the radius of the particle

The concentration of sample dilutions used for calculations of original sample concentration was in the range of $2 * 10^8 - 8 * 10^8$particles/ml. Only this range allows the most precise particle number estimation, according to the manufacturer.

Detection of exosome markers with fluorescence immunoassay

The presence of exosome markers in EV-containing samples was detected with a dissociation-enhanced lanthanide fluorescence immunoassay (DELFIA). Several dilutions of the samples were prepared by using PBS. Then, 5µl of sample or diluent was loaded on protein high-binding Costar strip well plates. Each well was topped with 95µl PBS and left at 4°C. The next day, the plates were blocked with 1%BSA in PBS for 1h at room temperature. Then, the primary antibodies against exosome markers, namely CD9, CD63, CD81, and HSP70, and apolipoprotein marker ApoB were added to wells without mixing several antibodies in one well. After 2h incubation, plates were washed with DELFIA wash buffer. Then, samples were incubated with appropriate biotin-conjugated secondary antibodies for 1h. After another washing step, Europium-labelled streptavidin in DELFIA assay buffer (1:1,000) was added to wells for 1h. Finally, DELFIA enhancement solution was added, and the plates were shaken for 10min at 300rpm to induce an enhanced lanthanide fluorescence. Time-resolved fluorimetry was performed using a PHERAstar plate reader at the following settings: excitation and detection wavelengths were 337nm and 620nm, respectively. Also, integration time was 200µs and lag time was 60µs. The fluorescence value of each control, namely PBS with antibody against one of the markers bound by a secondary antibody, was subtracted from fluorescence values of an appropriate sample.

Single-particle interferometric reflectance imaging

ExoView Tetraspanin SP-IRIS kits containing chips and antibodies were provided by NanoView Diagnostics. The following procedure was performed by a representative of the company in the Hatter Cardiovascular Institute (Figure 8). Capture antibodies diluted in PBS, namely anti-CD9, CD63, and CD81 antibodies, were printed in triplicates on the chip. Additionally, mouse lgG was used as a negative control. The volume and concentration of the antibodies in spots are unknown. ReNeuron exosomes were diluted in 0.05%Tween20/PBS. Exosome dilutions (35µl) were added onto the chips placed inside a 24-well plate. Samples were incubated on the chip at room temperature to allow EV capture. After 16h, the unbound particles were washed away with PBS three times. CD9/Alexa488, CD63/Alexa647 and CD81/Alexa555 secondary antibodies were mixed and diluted 1:5,000 in 0.05%Tween20/2%BSA/PBS. After three washes as before, the chips were incubated with 250µl/chip the secondary antibody mix for 2h. The unbound fluorescent antibodies were washed once with 0.05%Tween20/PBS, three times with PBS, once with distilled water. Then, the chips were dried. Interferometric images of the chip were acquired with an ExoView reader using the ExoScan software. EVs bound to the antibodies appeared as bright spots. The light was quantified with ExoViewer software with a sizing threshold set to 50-200nm diameter. The mean light intensity of spot triplicates was found. EV size and number were determined by ExoViewer software. The vesicle binding to the capture antibodies was calculated by subtracting the signal measured after sample incubation from the one obtained before the incubation. To determine the EV subtype, ExoView captured fluorescence of secondary antibodies against CD9, CD63, and CD81 antibodies on EVs.

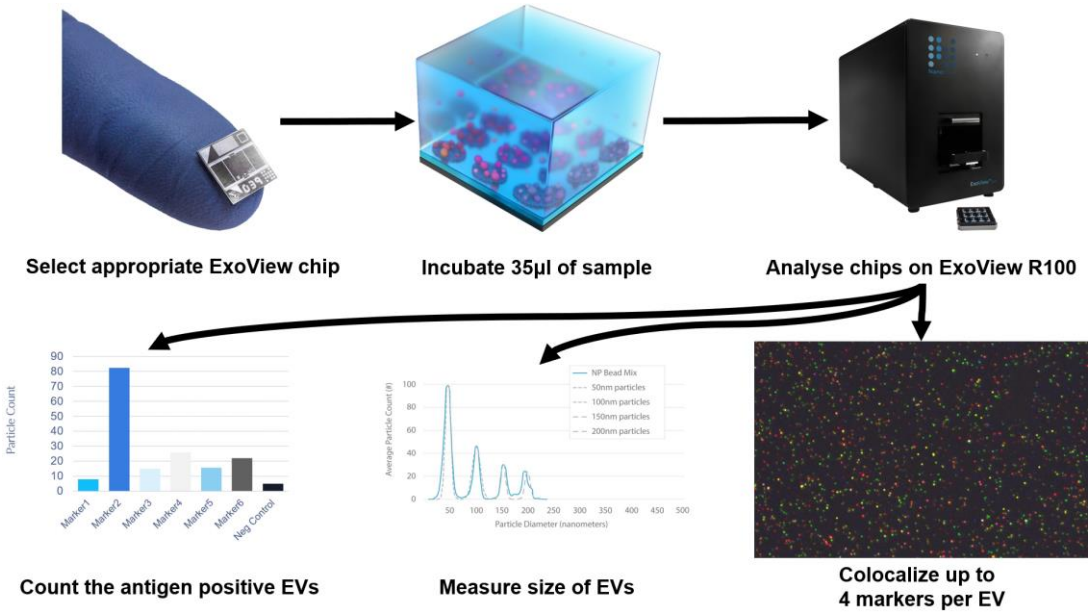

Figure 8. Single-particle interferometric reflectance imaging with ExoView Tetrasparin kit.

ExoView Tetrasparin Kit includes single-use microarray sensor ExoView chips with capture antibodies printed on its surface. Extracellular vesicles (EVs) are incubated on the chip and are bound by antibodies against EV markers. After incubating chips with appropriate secondary antibodies, ExoView R100 determines the number of EVs bound to specific antibodies, their relative size. The data is presented as the particle number expressing the EV marker. Moreover, the number and size of EVs can be plotted and images of colocalized markers can be obtained.

Results

ExoDiff and ExoPr0 exosome characterisation

ExoDiff and ExoPr0 EV-enriched samples were obtained from ReNeuron and characterised. First, the protein content was evaluated, which showed that ExoDiff and ExoPr0 contained 37.3mg/ml and 1.4mg/ml of protein, respectively (26.6-fold difference). This indicates that the ExoDiff sample had higher protein concentration and possibly higher concentration of EVs.

The presence of EVs in ExoDiff and ExoPr0 samples was confirmed by TEM of negatively stained samples (Figure 6). The negative staining makes EVs appear as cup-shaped structures, and such structures were observed in both samples (Figure 9). In addition to EVs, aggregates were observed, which may be a collection of vesicles and/or proteins (Figure 9; ExoDiff). Some vesicles were surrounded by web-like structures, that may be contaminating protein or staining artefacts (Figure 9, ExoDiff). ExoDiff had more particles than ExoPr0. A few vesicles were ≥150nm diameter and some vesicles appeared almost completely white (not shown). Therefore, the acquired images suggest both samples have exosomes, aggregates, and some contaminants.

Total particle size and quantity in EV-containing samples were determined by nanoparticle tracking analysis (NTA) using the NanoSight instrument (Figure 5). Modal and mean sizes of particles in ExoDiff and ExoPr0 samples were of the size of intraluminal vesicles (=exosomes) or slightly larger (<132nm) (Table 3). ExoDiff and ExoPr0 samples had most of the particles below or above 100nm, respectively (Figure 10). As expected, distilled filtered water, which was a diluent for exosome samples, and was used as a negative control, did not contain enough particles to be detected (data not shown). Particle concentration of ExoDiff and ExoPr0 samples was $30.4 * 10^{12}$particles/ml and $1.1 * 10^{12}$particles/ml, respectively (27.6-fold difference; Table 3). Therefore, the particle/protein ratio was $8.15 * 10^{11}$ and $7.86 * 10^{11}$particles/mg of protein for ExoDiff and ExoPr0 samples, respectively. Both ExoDiff and ExoPr0 samples had >150nm particles, with ExoPr0 having the most of them (Figure 10). To sum up, ExoDiff and ExoPr0 samples had different particle size distribution profiles and therefore different compositions.

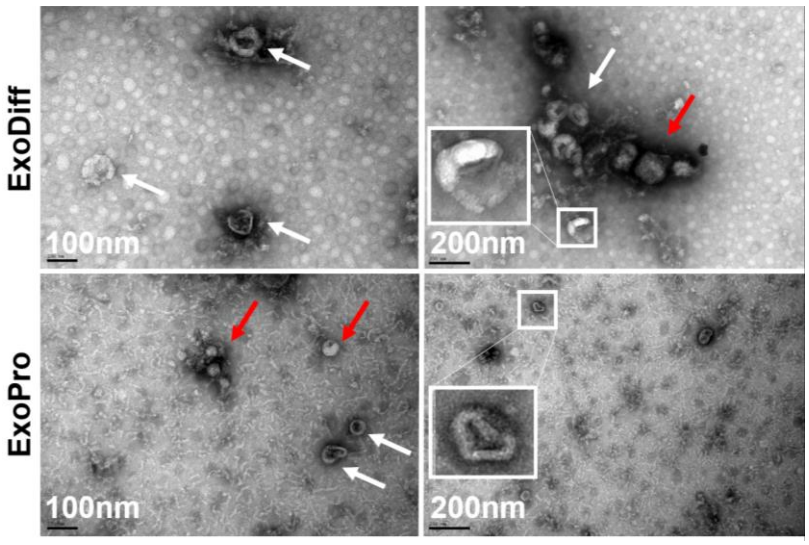

Figure 9. Presence of EVs in ExoDiff and ExoPr0 samples.

ExoDiff and ExoPr0 particles were negatively stained with uranyl acetate and imaged by a Joel 1010 transmission electron microscope. Two cup-shaped particles of exosome size are magnified in insets. Other exosome-like particles are shown with white arrows, and particles lacking a cup-shaped appearance are shown with red arrows. Size bars are as indicated.

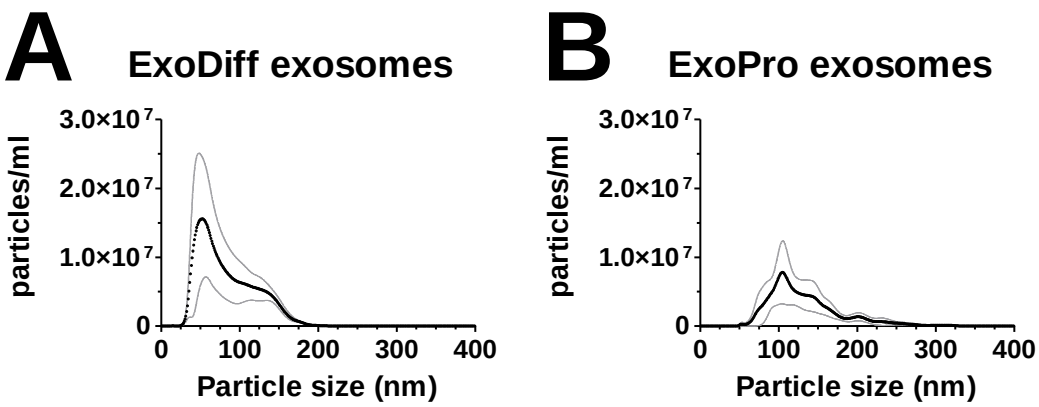

Figure 10. Particle size and distribution in ExoDiff and ExoPr0 samples.

The particle size of ExoDiff and ExoPr0 samples (assayed as dilutions) and their relative abundance were determined using nanoparticle tracking analysis (NanoSight). The black line is the mean of three sample analyses. The grey lines show the standard error (n=1, N=3).

Samples	Mean (nm)	Mode (nm)	Concentration ($x10^{12}$ particles/ml)
ExoDiff	88.9	50.9	30.4
ExoPr0	131.2	110.7	1.1

Table 3. Mean and modal particle size and concentration in ExoDiff and ExoPr0 samples.

The particle size of ExoDiff and ExoPr0 samples and their relative abundance were determined using nanoparticle tracking analysis (NanoSight; n=1, N=3).

The contents of exosome marker proteins were assessed by DELFIA. The data suggest the presence of all four markers, namely CD9, CD63, CD81, and HSP70, in ReNeuron samples (Figure 11). The concentration curves obtained when analysing ExoDiff and ExoPr0 overlap considerably. Interestingly, the ExoDiff curve forms an inverted U-shape, with the signal decreasing at higher and lower concentrations (Figure 11). Unlike ExoDiff curves, ExoPr0 curves were not U-shaped, probably because ExoDiff had more particles.

In addition to exosome-associated markers, the presence of ApoB, a marker of chylomicrons (ultralow density lipoprotein; 100-1,000nm), and very low (30-80nm), low (18-28nm), and intermediate (25-50nm) density lipoprotein was evaluated in the same assay. ApoB was not detected in the ExoPro sample, but, surprisingly, it was found in ExoDiff (Figure 11). ApoB curves of ExoDiff and ExoPr0 samples did not overlap. However, ExoPr0 had fewer particles than ExoDiff so fewer dilutions were tested in DELFIA. Overall, DELFIA results show that ExoDiff and ExoPr0 have exosome markers, and possibly there are similar subtypes of exosomes in both samples. However, ExoDiff may contain more contaminating lipoprotein.

To confirm DELFIA results and determine whether there are different exosome subtypes in ExoDiff and ExoPr0, single-particle interferometric reflectance imaging (SP-IRIS) was used (Figure 8). As expected, EVs of exosome size (50-150nm) expressed the CD9, CD63, and CD81 tetraspanins in both ExoDiff and ExoPr0 (Figure 12, A and B). CD9, CD63, and CD81 were mostly found in vesicles of 50-100nm size. Since the mode size of ExoDiff was in that range, SP-IRIS and NTA data may suggest that the ExoDiff sample may have more tetraspanin-positive vesicles than the ExoPr0 sample (Table 3; Figure 10, A and B). It is unknown if vesicles larger than 200nm or smaller than 50nm expressed the tetraspanins because of the sizing threshold on the ExoView software.

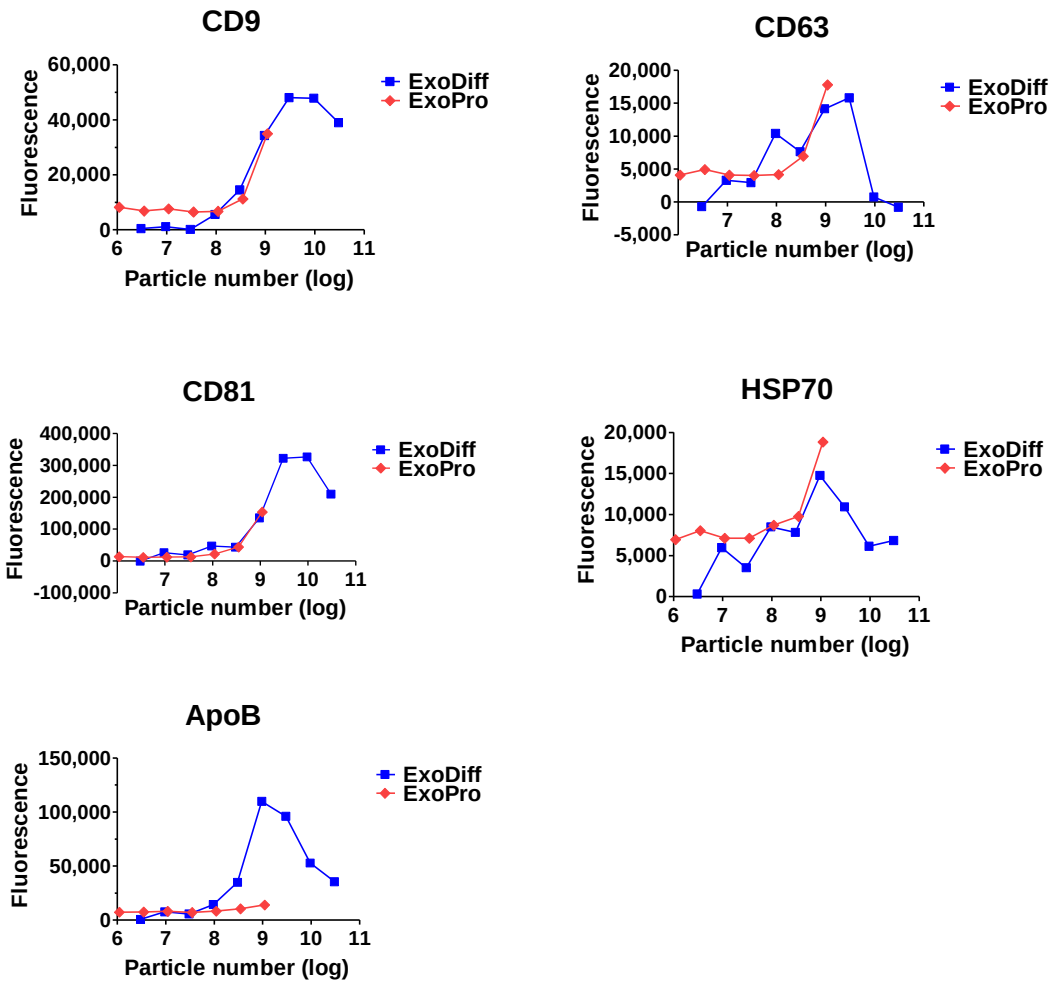

Figure 11. Relationship of ExoDiff and ExoPr0 particle number and fluorescent signal of antibodies against exosome and lipoprotein markers.

Dilutions of ExoDiff and ExoPr0 exosomes were analysed by DELFIA for the presence of exosome-specific (CD9, CD63, CD81, and HSP70) and apolipoprotein ApoB markers. Europium-labelled conjugate on the secondary antibodies was excited at 337nm and the resultant fluorescent signal was detected at 620nm (ExoPr0: n=1, N=2, and ExoDiff: n=2, N=2).

To determine the relative abundance of EVs expressing different tetraspanins, EVs bound to different tetraspanin antibody spots were quantified by ExoView software. The results suggest that most ExoDiff EVs were captured by CD9 whereas CD81-positive EVs constituted the majority of EVs in the ExoPr0 sample (Figure 12, A and B). CD63-positive EVs were least abundant among three EV subtypes in both ReNeuron samples, which supports the DELFIA results (Figure 11; Figure 12, A and B). Unsurprisingly, the ExoDiff sample had more tetraspanin-positive exosomes per volume of the sample.

To determine the co-localization of tetraspanins, the fluorescent signal from the secondary antibodies was analysed (Figure 13). Also, the software can recognise the position of specific capture antibodies on the chip. In both ReNeuron samples, CD81+/CD81+ exosome number (i.e., exosomes captured by anti-CD81 antibody and then labelled with anti-CD81 antibody) is the highest among all exosome subtypes, followed by CD81+/CD63+ vesicles (capture/detection antibodies; Figure 12, C and D). It is unknown how many vesicles were positive for all three tetraspanins. Nonetheless, these results suggest that CD81 was a more abundant marker than CD63 and CD9 on EVs in ReNeuron samples, which supports the DELFIA data (Figure 11). To sum up, ExoDiff and ExoPr0 samples had CD9, CD63, and CD81, which are commonly associated with exosomes.

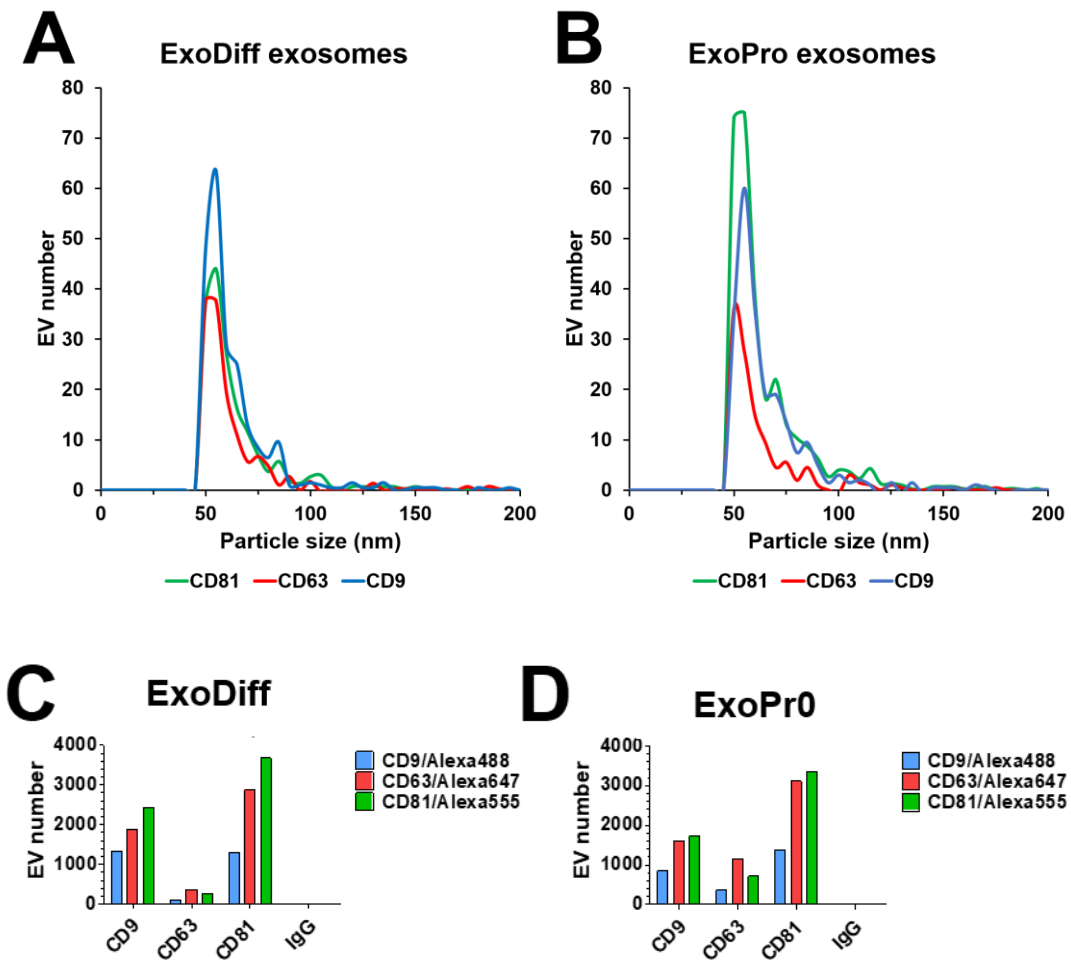

Figure 12. CD9, CD63, and CD81-positive EVs in ExoDiff and ExoPr0 samples.

ExoDiff and ExoPr0 samples were analysed by SP-IRIS revealing the number of EVs expressing CD9, CD63 and/or CD81. (**A-D**) Size and quantity of EVs expressing CD9, CD63, or CD81. (**C-D**) Fluorescent imaging was used to determine the co-localisation of the markers on individual EVs (n=1, N=1).

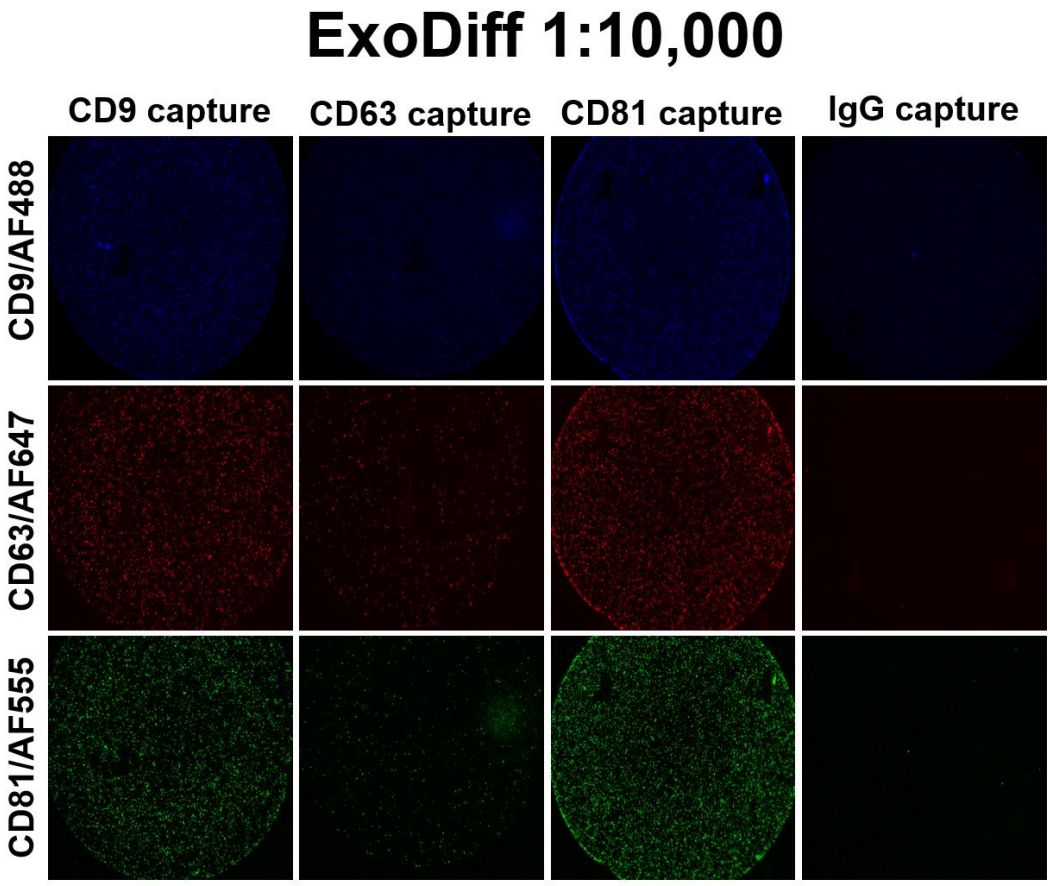
ExoDiff 1:10,000
CD9 capture
CD63 capture
CD81 capture
IgG capture
CD9/AF488
CD63/AF647
CD81/AF555

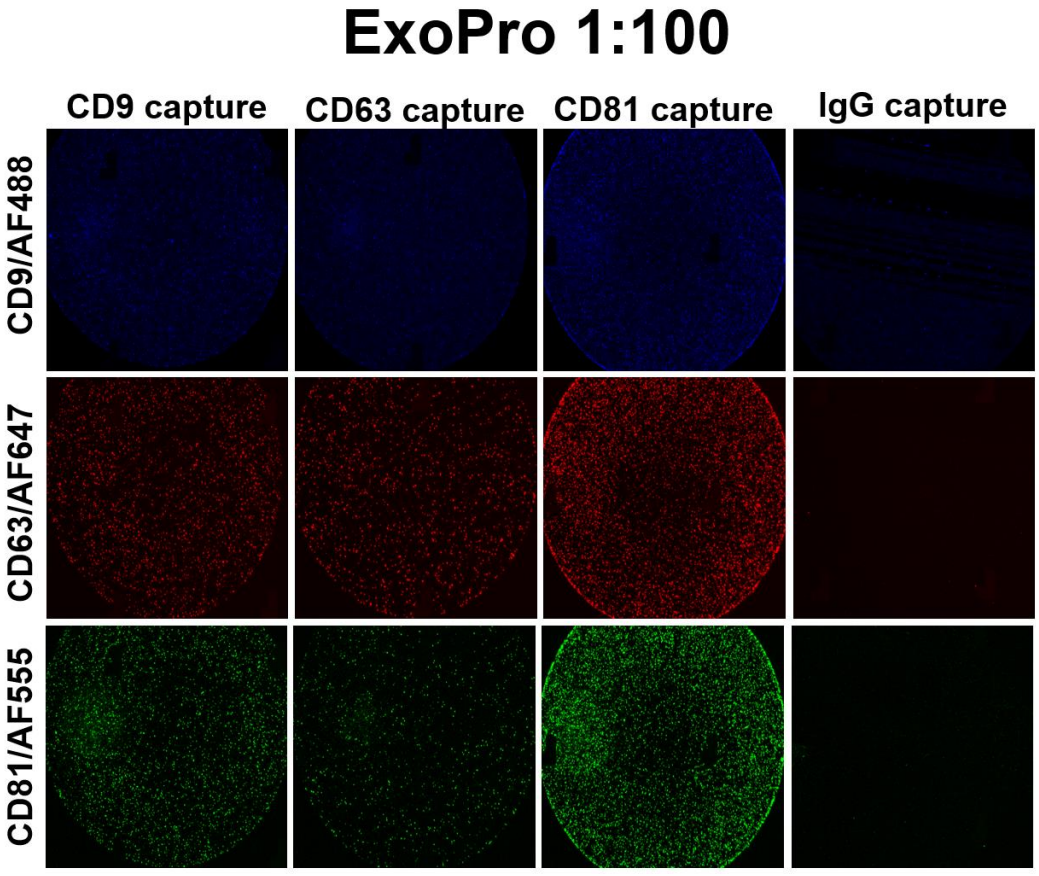
ExoPro 1:100
CD9 capture
CD63 capture
CD81 capture
IgG capture
CD9/AF488
CD63/AF647
CD81/AF555

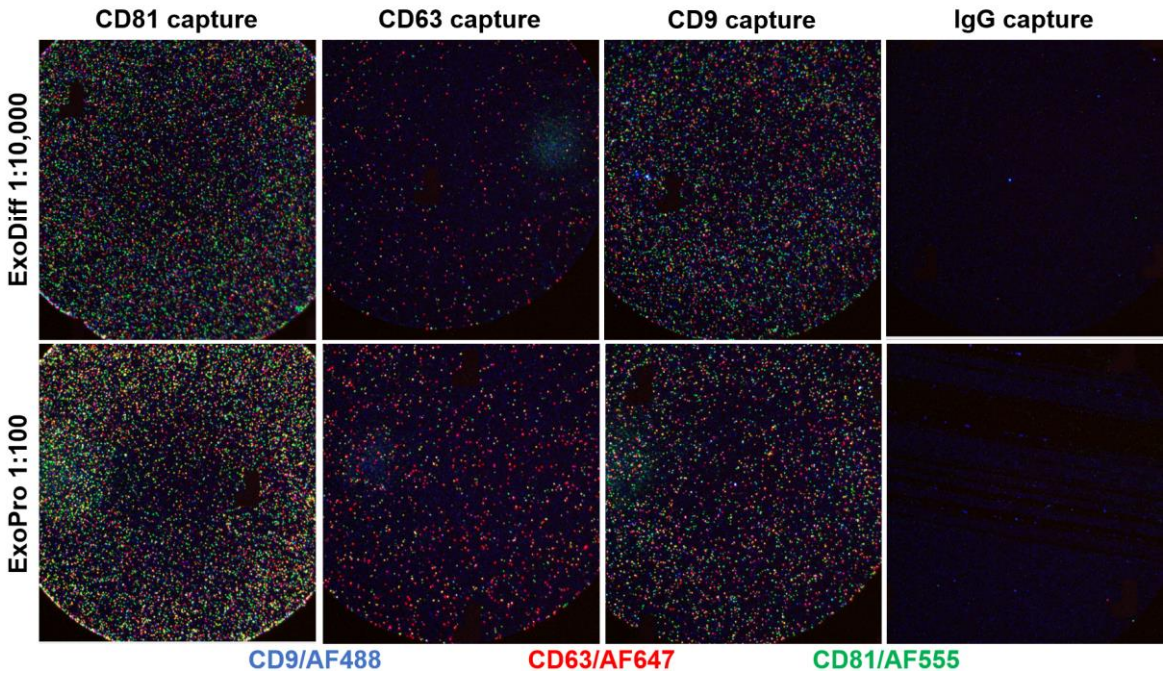

Figure 13. SR-IRIS immunophenotypic analysis of ExoDiff and ExoPr0 exosomes.

Dilutions of ExoDiff and ExoPr0 extracellular vesicles (EVs) were incubated on ExoView Tetraspanin chips with three different spots per capture antibody: anti-CD9, CD63, CD81, and mouse IgG antibodies. Later, the chips were incubated with a mix of fluorescent antibodies against CD9, CD63, and CD81. Then, single-particle interferometric reflectance imaging (SP-IRIS) was performed. Fluorescent light was used to determine the co-localisation of the markers. Here, fluorescent signal, alone or combined, is shown on different capture antibodies.

Unexpectedly, a large, flocculated precipitate was observed to form in the ExoDiff sample if the latter was left stationary for several days. Contaminating proteins and/or lipids from the serum were suspected to be the cause. Therefore, samples were centrifugated at 15,000rpm for 5min to remove the precipitate. Then, the ExoDiff sample was re-analysed to check if the number of contaminants was decreased, and the exosome level was largely unchanged. The protein concentration of the ExoDiff sample fell by 10.7% (33.3mg/ml). However, the number of particles decreased by 92.4%, bringing ExoDiff particle concentration close to ExoPr0 particle concentration (Table 3, Table 4). The number of 50nm ExoDiff particles fell by around 6 times, together with 50-100nm exosome-sized particles (Figure 14 and Figure 10). This may indicate a large portion of exosomes was lost during the pellet removal. Also, particles larger than 125nm were removed with the precipitate. Overall, NTA data suggests that most particles were lost with the precipitate removal and that the lost particles were mostly made of lipid.

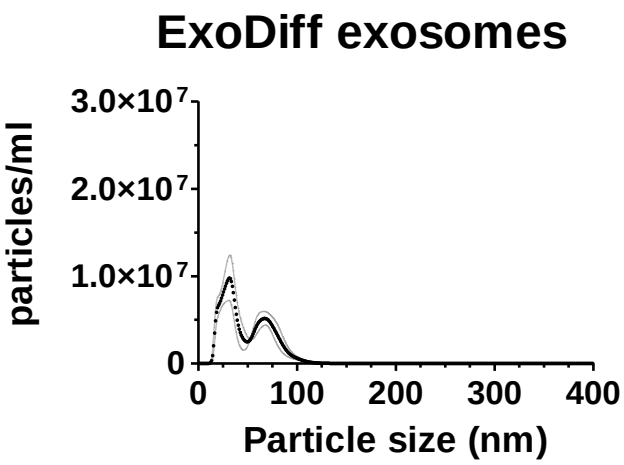

Figure 14. Particle size and distribution of ExoDiff sample without pellet.

The particle size of the ExoDiff sample (diluted) and their relative abundance were determined using nanoparticle tracking analysis (NanoSight). The black line is the mean of three sample analyses. The grey lines show the standard error (n=1, N=3).

Mean (nm)	Mode (nm)	Concentration (x10^{12} particles/ml)
48.1	25.7	2.3

Table 4. Mean and modal particle size and concentration in ExoDiff sample without pellet.

The particle size of the ExoDiff sample and their relative abundance was determined using nanoparticle tracking analysis (NanoSight; n=1, N=3).

To determine if the number of exosomes decreased with the precipitate removal, the presence of CD81 marker was evaluated in the ExoDiff sample using DELFIA. The CD81 signal was reduced by at least 20-fold after pellet removal (Figure 15 and Figure 11). In contrast, the ExoPr0 sample had a similar CD81 signal as before indicating that the pellet removal caused exosome loss (Figure 15 and Figure 11).

In addition to CD81, the presence of lipoprotein marker ApoB was measured with DELFIA. The ApoB signal in the ExoDiff sample was unchanged (Figure 15 and Figure 11). Although In ExoPr0 sample, that was used as a control, there was no difference in the ApoB signal. Overall, lipoprotein was probably not removed with the pellet.

To confirm that ExoDiff sample still contrained EV-shaped particles, I performed TEM of ExoDiff exosomes immunolabelled with anti-CD81 antibody conjugated to gold beads. There were exosome-like particles (Figure 16). TEM analysis of the ExoDiff sample suggests that the pellet removal resulted in the major loss of EVs, as less EV-shaped particles were observed compared to the original sample at the same dilution. Therefore, the ExoDiff sample was not suitable for analysis in ischaemia/reperfusion assays.

Another batch of ExoDiff and ExoPr0 samples was analysed as well. As described in another chapter about models of ischaemia/reperfusion, these samples were used by Dr He for an *in vivo* ischaemia/reperfusion experiment (Figure 44). The NTA data of this batch shows ExoPr0 samples had very similar particle distribution profiles and concentrations as in another batch (Figure 17 and Table 5). However, the particle mode size in ExoDiff of this batch was 81.5% larger than in the previous batch (Table 3 and Table 5). Additionally, this batch of ExoDiff had 7.4 times fewer particles. This means that the batches differed in their purity and, potentially, exosome content. It appears that the method of ExoPr0 sample may be more standardised and reproducible that ExoDiff.

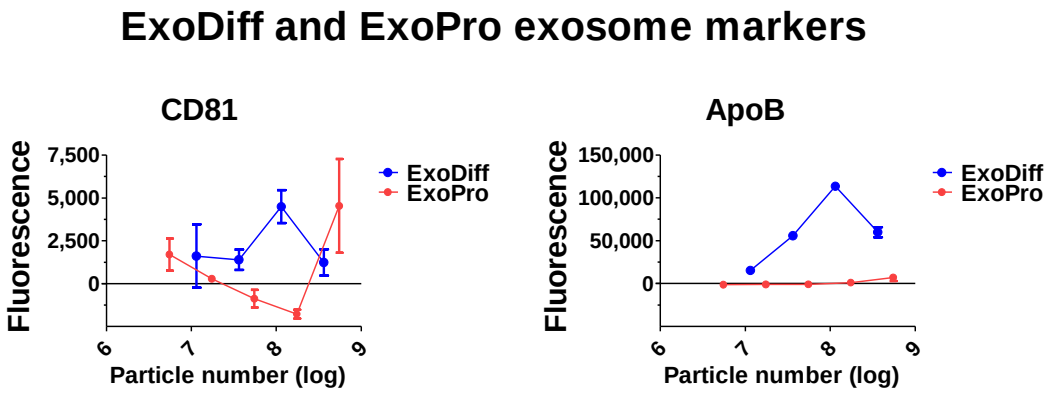

Figure 15. Relationship of particles in ExoDiff sample without pellet and fluorescent signal of antibodies against exosome and lipoprotein markers.

Dilutions of ExoDiff exosomes were analysed by DELFIA for the presence of exosome-specific marker CD81 and lipoprotein marker ApoB. Europium-labelled conjugate on the secondary antibodies was excited at 337nm and the resultant fluorescent signal was detected at 620nm (n=1, N=2).

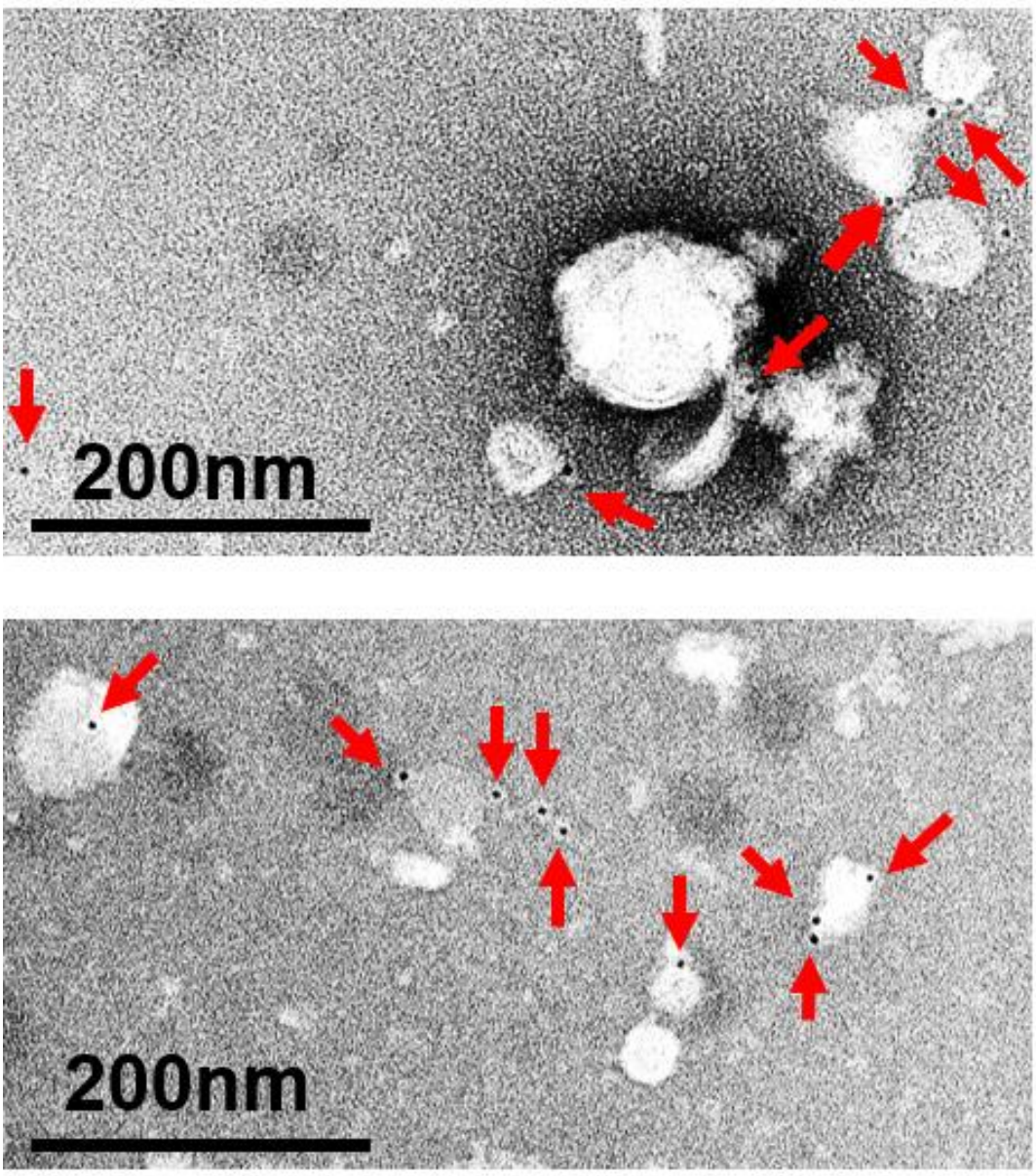

Figure 16. Presence of EVs in ExoDiff sample without pellet.

ExoDiff exosomes were labelled with an antibody against exosome-specific CD81 marker. This primary antibody was bound by a secondary antibody conjugated to 5nm gold particles (black dots indicated by red arrows). Afterward, ExoDiff particles were negatively stained with uranyl acetate and imaged by a Joel 1010 transmission electron microscope. Scale bars are as indicated.

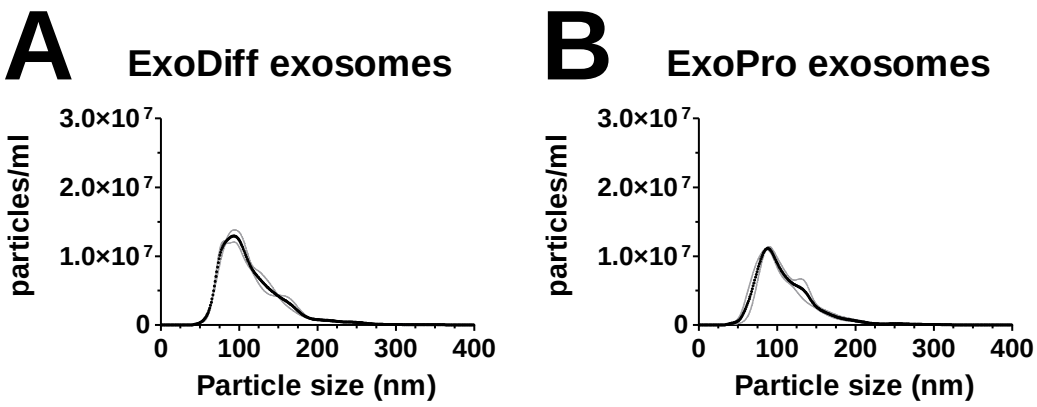

Figure 17. Particle size and distribution of the first batch of ExoDiff and ExoPr0 samples.

The particle size of ExoDiff (1:4,500) and ExoPr0 (1:1,500) samples and their relative abundance was determined using nanoparticle tracking analysis (NanoSight). The black line is the mean of three sample analyses. The grey lines show the standard error (n=1, N=3).

Samples	Mean (nm)	Mode (nm)	Actual concentration (x10^{12} particles/ml)
ExoDiff	116.7	92.4	4.1
ExoPr0	110.9	91.0	1.1

Table 5. Mean and modal particle size and concentration in the first batch of ExoDiff and ExoPr0 samples.

The particle size of ExoDiff and ExoPr0 samples and their relative abundance were determined using nanoparticle tracking analysis (NanoSight; n=1, N=3).

Discussion

Summary of the results

Exosomes from various stem cells have been reported to be cardioprotective in *in vivo* models of AMI. Before developing assays for comparing the cardioprotective potential of exosomes from different sources, I obtained and characterised exosome-enriched samples, ExoDiff and ExoPr0, from differentiating and proliferating stem cells. My results characterizing these EVs indicate that ExoDiff and ExoPr0 are enriched in exosomes, but their purity and exosome subtypes may be different. However, differences were noted in ExoDiff exosomes between their two batches.

ExoDiff and ExoPr0 exosome purity

I analysed ExoDiff and ExoPr0 according to MISEV2018 recommendations (Théry *et al.*, 2019). Exosomes were quantified indirectly by two methods: protein quantification by using spectrophotometry and particle number estimation by NTA. These two methods were chosen over other alternatives, such as total lipid, RNA, or specific molecule quantification because they are quick and require a small amount of sample. Both methods suggested the same difference in exosome concentration between the samples. The particle/protein ratio, which has been proposed as an additional measure of exosome purity, was $8.15 * 10^{11}$ and $7.86 * 10^{11}$particles/mg. This is sufficient for both samples to be considered pure according to this paper (Webber and Clayton, 2013). However, this method relies on the assumption that all particles are EVs of the same size and similar protein content. Therefore, ExoDiff and ExoPr0 are exosome-enriched samples, yet their purity is unknown, as it is currently impossible to obtain 100% pure exosomes and verify that reliably.

Exosome identity was confirmed with TEM which revealed EV cup-shaped vesicles of predominantly <150nm size. To increase confidence that the samples have exosomes, TEM with immunogold labelling against exosome markers such as tetraspanins CD9, CD63, and CD81 could be used (Tkach, Kowal and Théry, 2018). However, the presence of one marker enriched in exosomes does not prove that the vesicle is an exosome (Tkach, Kowal and Théry, 2018). Without an exosome-exclusive marker, no one can identify exosomes beyond reasonable doubt. What MISEV2018 suggests instead is to use a non-image-based method to analyse EVs, one of which is NTA. Data shown in this chapter indicates that both ExoDiff and ExoPr0 were mostly of exosome size, which supports my predictions that the combination of two isolation methods, SEC and TFF, can remove most of the particles larger and smaller than exosomes. Moreover, the DELFIA assay results suggested the presence of tetraspanins CD9, CD63 and CD81 in both samples. SP-IRIS assay confirmed this data and revealed that CD81 marker was most abundant. Since the majority of tetraspanin-enriched EVs were of size 50-75nm (size of intralumenal vesicles in endosomes), the samples were suspected to be enriched in exosomes.

In the ExoDiff sample, white spherical vesicles were observed with TEM which are likely to be lipoprotein particles (Chuang, Shon and Narayanaswami, 2017). The DELFIA data suggested the presence of ApoB in the ExoDiff sample as well, so lipoprotein is certainly a contaminant in the ExoDiff sample. However, ApoB was not detected in ExoPr0. Lipoprotein (very low, low density, and intermediate-density lipoprotein) and EV sizes overlap, and therefore SEC and TFF cannot remove them completely.Therefore, if ExoPr0 was as concentrated as ExoDiff, it is possible that ApoB would have been detected in it. ReNeuron claimed that they did not use sera for stem cell growth. As lipoprotein is produced by the liver and released into the blood, it is unclear why it was a contaminant in ExoDiff. Apart from lipoprotein, the samples could have contained microvesicles. The presence of markers enriched in microvesicles, such as ACTN4, LAMP2, MIC60, or GP96, could be investigated (Tkach, Kowal and Théry, 2018).

Differences between ExoDiff and ExoPr0 exosomes

ExoDiff and ExoPr0 were obtained from the same CTX0E03 cell line, but these cells were in different states: differentiating or proliferating. CTX0E03 cells in non-proliferating and/or differentiated states were protective in various *in vitro* and *in vivo* I/R injury models, namely stroke and hindlimb ischaemia (Katare *et al.*, 2014; Sinden *et al.*, 2017). It is known that the source cell state and their growth conditions affect the content and number of exosomes, therefore ExoDiff and ExoPr0 may have different effects in myocardial I/R models (Genneback *et al.*, 2013; Lopatina *et al.*, 2014).

Indeed, the ExoDiff and ExoPr0 samples differed in their concentration of exosomes. Yet, it is unknown if the cell number and medium volume were different for the respective cell culture during exosome collection. ReNeuron did not share information on the volume of the cell media used for isolating exosomes, the number of cells that produced exosomes, their doubling time, and the frequency of exosome collection.

ExoDiff and ExoPr0 samples were more enriched in <100nm and >100nm particles, respectively. Considering that SP-IRIS showed that tetraspanin-positive EVs were mostly of 50-75nm, it may be possible that ExoDiff had more exosomes if to adjust the samples to the same concentration. Alternatively, it is possible that ExoDiff and ExoPr0 had different subsets of exosomes. For example, one laboratory reported the existence of two populations of exosomes in melanoma cells, small exosomes (60-80nm) and large exosomes (90-120nm) (Zhang *et al.*, 2018). Small exosomes are more “canonical exosomes” since they are enriched in proteins associated with multivesicular bodies and endosomes. Large exosomes, in turn, are rich in flotillin, which is found in all EV subtypes (Tkach, Kowal and Théry, 2018).

Interestingly, CD9, CD63, CD81, and HSP70 curves in DELFIA overlapped between ExoDiff and ExoPr0 as if both samples were similarly enriched in these markers. Strangely, DELFIA curves formed a U-shape meaning that the signal decreased with increased exosome concentration. Theoretically, the higher number of exosomes allows more antibodies to bind, which increases the fluorescent signal. Yet, when exosomes are highly concentratedsome exosomes may not attach to the well because the well is completely coated with exosomes or contaminating protein. Moreover, the contaminating protein could have prevented exosomes from attaching to the plastic. Alternatively, contaminating protein could have created “exosome corona”, as it does in blood plasma (Tóth *et al.*, 2021). The corona could give exosome a charge which may lead to increased exosome aggregation. Resultant aggregates could have been washed away, resulting in the decrease of fluorescent signal.

The observed decrease in exosome markers with a higher exosome concentration highlights the importance of using several dilutions of an EV-containing sample to determine exosome marker presence in DELFIA. Interestingly, DELFIA data contradicts the data obtained with SP-IRIS which showed that ExoDiff and ExoPr0 were enriched in CD9 and CD81, respectively. It is important to remember that due to limited sample quantity and equipment access, it was not possible to perform DELFIA and SP-IRIS several times to allow statistical analysis. Therefore, it is hard to compare respective results.

The lipoprotein content of ExoPr0 was not detected with anti-apoB antibodies. However, ExoDiff did contain lipoprotein as suggested by the ApoB signal in DELFIA. It is unknown precisely how many lipoprotein particles were in the sample because the ApoB signal cannot be converted directly into the lipoprotein concentration. Considering that many ExoDiff particles were of 25-50nm, ExoDiff may be contaminated in VLDL, LDL, and IDL, which may have come from the serum of CTX0E03 cell media. It is unknown whether cell media for differentiating and proliferating CTX0E03 cells was different in lipid content. Alternatively, ExoDiff might contain exomeres that are around 35nm in diameter. Exomeres are non-membranous nanoparticles enriched in metabolic enzymes (Zhang *et al.*, 2018). They were shown not to contain any components of ESCRT complexes and HSP70. The role of exomeres in the organism needs to be elucidated, therefore it is unknown how they may potentially affect I/R assays. Their presence may be checked in both samples, yet it would be not possible to remove them effectively without losing some exosomes.

Another potential contaminant of the samples is protein. CTX0E03 media contains angiogenic factors such as EGF, VEGFA, TGFβ1, and HIF-1, although TFF and SEC can reduce the bulk of protein content (Hicks *et al.*, 2013). However, there is no effective way to remove all extra-exosome protein without damaging exosomes.Proteomics could have been performed to determine protein identity in the samples. Perhaps, a protocol can be established to lyse proteins outside exosomes.

One of the limitations of this study is that CTX0E03 cells were grown, and their exosomes harvested in ReNeuron company. As mentioned previously, it was not known what the cell number and medium volume were to obtain ExoDiff and ExoPro. The company did not provide a report on how they determined proliferating and differentiating potential of CTX0E03, or step by step protocol of exosome isolation which was done for batches I analysed. Moreover, when I informed them that I found their batches of exosomes to be different, they told me that their methods were consistent. Therefore, it was hard to elucidate why two batches of ExoDiff exosomes were different.

Conclusion

Here, ExoDiff and ExoPr0 were determined to be relatively enriched in exosomes although they also contained contaminating protein and/or lipids. These two samples have different compositions even though there are some similarities between them. Nevertheless, the quality of these samples is inconsistent. Moreover, I later observed in my *in vitro* (Chapter 4, Results) and *in vivo* (Chapter3, Introduction) studies that only ExoDiff, and not ExoPr0, was cardioprotective. In view of the inconsistency and concerns about the purity of the EVs, I decided not to use exosomes from CTX0E03 cells anymore. Instead, I would like to develop a method to improve purity of exosome isolation.

Chapter 3

Introduction

The overarching aim of this PhD is to use exosomes of high purity in a cell model of ischaemia/reperfusion. It was hoped that ExoDiff and ExoPr0, obtained with both SEC and TFF, would be of high purity and quantity. However, the data presented in Chapter 2 showed that their quality was inconsistent. Therefore, it was decided that my next project would be about designing a method of purification of highly pure exosomes.

In this chapter, various methods of exosome isolation are presented to justify why affinity purification is superior to SEC and TFF in obtaining highly pure exosomes. Currently available affinity purification method is not used to obtain high quantity of exosomes, that are also functional. Therefore, ALFA tag which can overcome this problem is described in the introduction. Next, the introduction describes transfection of cells, namely, how to design a sequence encoding ALFA tag and how to introduce it into stem cells. Finally, a new method of exosome quantification is presented. This method would complement other methods presented in Chapter 2 for characterization of ALFA tagged exosomes.

Methods of exosome isolation

Exosomes are extracellular vesicles of ~50-150nm. The isolation of pure quantities of such small particles is currently challenging. Several methods are available for exosome isolation, each with its advantages and disadvantages. Careful consideration of method choice should be taken before commencing exosome study. Fluid from which exosomes need to be isolated and its volume, the desired purity of exosomes, the purpose of exosome isolation (e.g., functional study), and many other factors may help to narrow the choice of methods to isolate exosomes. For example, exosomes should be separated from contaminants such as proteins, lipoproteins, and nucleic acids, so that biological effects observed *in vivo* can be attributed to exosome cargo and bioactive molecules on their membranes. However, no method is currently available that yields 100% pure exosomes. Instead, only some proportion of contaminants can be removed from exosome-containing samples. The resultant sample becomes enriched in exosomes. The population of isolated extracellular vesicles depends on the isolation method (Doyle and Wang, 2019; Veerman *et al.*, 2021). Exosome-containing samples can be purified further by combining several methods. Yet, the yield of exosomes is decreased by further purification. Therefore, studies that involve small sample volumes, such as cell culture media or the blood of a patient, typically cannot afford a combination of two exosome isolation methods.

Most of the techniques exploit biochemical or biophysical properties of exosomes, such as exosome density, size, or presence of specific markers on their membrane (Gurunathan *et al.*, 2019). Many of these methods belong to these categories: ultracentrifugation, immunoaffinity, ultrafiltration, and precipitation. There are newer methods as well which include nanomaterial innovations and microfluidics. However, ultracentrifugation is the most common technique for exosome separation since it requires minimal technical knowledge and sample preparation (Théry *et al.*, 2006; Gardiner *et al.*, 2016). This method involves the use of high centrifugal force to the sample. This results in a separation of particles based on their size and density. First, cells and cell debris are removed at 300-2000g. Then, large extracellular vesicles such as apoptotic bodies and large microvesicles are removed at 10,000g. Finally, exosomes are pelleted at 100,000g. The major limitations of ultracentrifugation are potential damage to exosomes, low exosome yield, and co-isolated contaminants of exosome size. Additionally, a large volume of starting sample and long centrifugation steps are required. Finally, ultracentrifugation does not produce reproducible yield and quality of exosomes (Momen-Heravi *et al.*, 2012; Cvjetkovic, Lötvall and Lässer, 2014).

To overcome most of these limitations, size exclusion chromatography (SEC) can be used (Figure 4). Importantly, SEC-purified exosomes are not damaged and therefore can be used for *in vitro* and *in vivo* studies. It was shown that SEC columns with Sepharose 2B can be successfully used to isolate biologically active, intact, and non-aggregated small extracellular vesicles of 50-200nm (Gámez-Valero *et al.*, 2016; Hong *et al.*, 2016). SEC requires little sample volume (up to 5% of volume inside the stationary phase). In this Chapter, SEC was used to separate exosomes from free lipids and proteins before purifying them further.

Purification of exosome subsets

Ultracentrifugation, SEC, ultrafiltration, precipitation, and many other exosome isolation methods do not remove exosome-sized contaminants, such as microvesicles, protein aggregates, and lipoproteins. Those contaminants make experiments with exosomes difficult to interpret. For example, many proteins co-isolated with mesenchymal stromal cell exosomes by SEC are involved in angiogenesis and cardiovascular development (Takov *et al.*, 2020). To avoid misattribution of bioactivity from contaminants, exosomes can be purified using antibodies against exosome biomarkers. For example, tetraspanins CD9, CD63, and CD81 are most used as exosome markers (Kowal *et al.*, 2016). The antibodies are usually attached to a solid surface such as magnetic beads, multi-well plate, resin, or surface of a microfluidics device (Doyle and Wang, 2019). Once exosomes are captured, all contaminants can be washed away. The attached exosomes can be used for analysis.

If exosomes need to be eluted, biotinylated antibodies can be attached to magnetic beads coated in streptavidin. Streptavidin has a high affinity for biotin, and their binding is exceptionally strong, so the antibody binds a bead quickly and firmly (Stayton *et al.*, 1999). Then, the sample is incubated with antibody-coated beads, and exosomes are captured. Importantly, beads have a larger surface area than a flat surface in multi-well plates. Moreover, exosome yield can be increased with a higher number of beads without making exosome isolation longer. It was also reported that the yield of exosomes captured with antibody-coated beads is 10-15 times higher than exosomes obtained with centrifugation (Zarovni *et al.*, 2015). After exosomes are attached to antibody-coated beads, the beads can be captured by a magnet and all unbound particles are washed away. This method is simple, fast, and does not damage exosomes as it does not require any harsh chemical treatment or centrifugation forces. It is possible to detach antibodies from the beads using solutions such as tris buffered saline. However, eluted exosomes would have large antibodies attached to them, and this would impact exosome bioactivity (Hong *et al.*, 2014).

ALFA tag and nanobody for the capture of exosome subset

Harsh chemicals can be used to detach exosomes from attached antibodies, but this will cause denaturation of most exosome proteins and potentially their collapse (Sheng and Kong, 2012). Milder chemicals can be potentially used if exosomes are captured by low-affinity monoclonal antibodies, antibody Fab fragments, and mini antibodies, as it was done for proteins (Engström, Andersson and Ohlson, 2005; Kellogg and Alberts, 2017). However, I hypothesized that there would be a way to avoid the use of any chemicals for exosome elution from antibodies by employing an epitope tag, the ALFA tag. Epitopes, i.e. molecule which is bound by antibody, can be designed and incorporated into a protein of interest (e.g. CD63) as a tag (Brizzard, 2018). Epitope tags are widely used for the purification of recombinant proteins and tracking the biogenesis and movement of specific proteins inside the cell (Nooh and Bahouth, 2017; Brizzard, 2018). Many tags have been developed for certain applications, e.g. myc-tag for immunostaining and His-tag for protein purification (Evan *et al.*, 1985; Hochuli, Döbeli and Schacher, 1987).

Recently, tags that are bound by single domain antibodies, nanobodies, have been developed, e.g. EPEA-tag (De Genst *et al.*, 2010). Nanobodies are produced by camelids such as alpacas, llamas, and camels, and are only 15kDa. Nanobodies have only one domain, whereas IgG1 has 12 domains, and IgG2 with IgG3 have 6 each. IgG1 recognises antigen with the paired variable domains, VH and VL, but IgG2 and IgG3 do that using the functional equivalent of that, VHH. A nanobody, however, consists of only an antigen-binding VHH domain (Muyldermans, 2013).

Most antibodies that bind small tags like EPEA-tag do so with a low affinity. Moreover, small tags adopt various conformations with unpredictable effects, can be cut with proteases, make protein they are attached to likely to be degraded, affect protein function and localization in cells, have strong charge, resemble proteins in the cells, and/or are unsuitable for chemical treatment e.g. for super-resolution microscopy (Schembri *et al.*, 2007; Tompa, 2012). Therefore, ALFA-tag was created to address all of those issues (Götzke *et al.*, 2019). ALFA-tag is a 15 amino acid-long sequence and is easy to produce for cells. ALFA-tag has no net charge, is unique, and resistant to protease and many chemicals including chemical fixators. Overall, it is expected to have little to no effect on the function or localization of protein it is attached to, be suitable for *in vivo* tracking of a specific protein, super-resolution microscopy, and other applications. A nanobody named NbALFA^{PE} has been developed which has a lower affinity to the ALFA-tag (Kd ~11nM), which is useful as it facilitates subsequent elution (Götzke *et al.*, 2019). Importantly, ALFA-tagged proteins can be eluted from NbALFA^{PE} nanobody by free ALFA peptides. Therefore, it may be possible to make cells incorporate ALFA-tag into exosome markers, capture them from cell media with NbALFA^{PE}-coated magnetic beads, wash unbound particles away and elute exosomes from the nanobody using ALFA peptide. The ALFA peptide may be removed by SEC or filtration. In this Chapter, it is shown how ALFA-tagged exosomes can be captured with anti-ALFA nanobody and that their purity is superior to SEC-purified exosomes.

Exosome marker CD63 and nanoluciferase

To make cells to express ALFA-tag, the target protein to “attach” the tag should be chosen first. CD63, an exosome marker, is a suitable candidate for it. CD63 is a tetraspanin (i.e., has four transmembrane domains). Considering that CD63 concentration is highly expressed on exosomes, CD63 is commonly used as an exosome marker. Since CD63 is not tissue-specific, it is used as a marker of any type of exosomes (Théry *et al.*, 2019). Therefore, CD63 is used for ALFA-tagging in this study.

To trace *in vitro* production and cellular uptake of exosomes, the luminescent molecule NanoLuc could be inserted between CD63 and ALFA-tag. NanoLuc design is based on a small subunit of luciferase found in sea shrimp *Oplophorus gracilirostris* (Hall *et al.*, 2012). When furimazine is added to cells or exosome mixture, NanoLuc converts oxygen to carbon dioxide to facilitate the formation of furimamide. This reaction yields luminescence. Unlike other luciferases and their substrates, NanoLuc is a nanosized particle (19kDa) and produces sustained luminescence (half-life >2h) which is ~150-fold stronger than the luminescence of commonly used firefly luciferase. A previous study suggested that NanoLuc does not affect the trafficking and function of the protein it is attached to (Stoddart *et al.*, 2015). Therefore, NanoLuc is expected to allow highly sensitive quantification of exosomes without interfering with CD63 transport to exosomes. Kojima and others supported this hypothesis by successfully tagging CD63 with NanoLuc using transfection and then monitoring exosome fate *in vivo* (Kojima *et al.*, 2018). Therefore, cells are transfected to co-express NanoLuc with ALFA-tag in this study.

Transfection of cells with ALFA-tag sequence

Transfection is a technique of introducing a gene into the host cell (Fus-Kujawa *et al.*, 2021). The choice of transfection method depends on cell type, its source, the aim of the study, and the type of nucleic acid which needs to be introduced. Transient transfection does not result in gene integration into the host genome. Therefore, cells express the transgene for up to several days and then lose the transgene through cell division. Typically, the gene is introduced into the cell in the form of a plasmid. Cells can be transfected using chemicals, such as cationic polymers. Cationic polymers, such as polyethyleneimine (PEI), form polyplexes with negatively charged DNA based on electrostatic interaction. This prevents DNA from degradation by nucleases. Polyplexes enter the cells by endocytosis (Vermeulen *et al.*, 2018). Endosomes with polyplexes rupture releasing nucleic acid into the cytoplasm. Now, polyplexes can travel to the nucleus where the transgene is transcribed to RNA, and RNA, in turn, is translated to the protein. Kojima used PEI to transfect kidney HEK-293 cells with pDB30 plasmid encoding CD63 with NanoLuc (Figure) (Kojima *et al.*, 2018). I also adopted the same method of transfecting HEK-293 kidney cells, which are easy to transfect with PEI, to make ALFA-tagged exosomes. This way, the method of purification of ALFA-tagged exosomes could be optimised.

However, MSCs are not easy to transfect with PEI. Therefore, stable transfection with viruses (transduction) or electroporation can be used to integrate the transgene into the MSC genome permanently (Chong, Yeap and Ho, 2021). This means that the transgene would be retained in cells after replication. Electroporation is a safer, cheaper, and faster way to transfect MSCs compared to transduction. In principle, electroporation is used to create pores in the cell membrane by applying a potential difference across it in a form of high voltage electric shock (Prasanna and Panda, 1997). The cell membrane is an electrical insulator that maintains electrical potential (~0.07V) due to the difference between ion concentration in the extracellular fluid and the cytosol. When the potential difference across the cell membrane reaches a certain threshold (~1V), the external electric field outperforms the membrane capacitance, and it starts to break down. This is because lipids re-orient themselves to form hydrophilic openings in the membrane, which is normally hydrophobic. These breaks in the membrane can be reversible if an electric pulse duration and intensity are chosen carefully. For electroporation, cells of interest are suspended with DNA of interest in a conducting buffer between two electrodes. Typically, the extent of permeabilized cell membrane area depends on pulse strength and the pore size is related to the pulse duration (Gehl, 2003). The pulse strength, distance, and duration should be chosen for each cell type individually to select the most optimal transfection efficiency with minimal cell death (Piñero *et al.*, 1997). When pores are formed in the membranes, external DNA can translocate into the cell. DNA delivery occurs by simple diffusion, endocytosis, or is dependent on electrophoretic forces applied during the pulse (Gehl, 2003; Escoffre *et al.*, 2009; Wu and Yuan, 2011; Venslauskas and Šatkauskas, 2015). DNA size affects the success of electroporation as well. The larger DNA reduces the likelihood of transfection efficiency (Hornstein *et al.*, 2016). To compensate for that, a longer duration of the pulse and/or higher DNA concentration can be used (Yao *et al.*, 2009; Chopra *et al.*, 2020). It is also important to design an appropriate DNA for cell electroporation. If the antibiotic resistance gene is co-expressed with the transgene, it can help to select and maintain successfully transfected cells in culture with the relevant antibiotic. Therefore, once a protocol for isolation of ALFA-tagged exosomes from HEK-293 cells is established, MSCs can be

transduced with the ALFA-tag sequence which also encodes for antibiotic resistance.

Conditionally immortalized mesenchymal stromal cells

As described in Chapter 1, stem cell therapy is a promising method to repair the heart after myocardial infarction. However, many researchers use the term “mesenchymal stem cell” interchangeably with “mesenchymal stromal cell” because there is no consensus on the guidelines for characterizing and distinguishing these cell types. According to the Mesenchymal Stromal Cell committee position statement, mesenchymal stem cells are stem cells with confirmed progenitor functionalities: proliferation and differentiation (Viswanathan *et al.*, 2019). Unlike them, mesenchymal stromal cells contain progenitor, stem, and differentiated cells (Wright, Arthaud-Day and Weiss, 2021). Currently, there is no known cell surface marker that can distinguish these two cell types. Instead, single-cell sequencing, proteomics, epigenomics, transcriptomics, and rigorous *in vitro* and *in vivo* evidence should be used to determine if cells are homogenous stem cells or heterogenous stromal cells. Therefore, the Mesenchymal Stromal Cell committee suggested that cells isolated from the mesenchyme are called mesenchymal stromal cells (hereafter MSCs) if no extensive characterization of cells is performed (Viswanathan *et al.*, 2019).

Currently, minimal criteria for MSC characterization include (1) capability of *in vitro* differentiation into osteoblast, adipocytes, and chondrocytes, (2) adherence to plastic, (3) presence of CD73, CD90, and CD105 cell membrane markers, and (4) absence of endothelial and hematopoietic markers, namely CD14, CD19, CD34, CD45, CD79a, and HLA-DR (Dominici *et al.*, 2006). Also, the origin of MSCs should be described because MSCs from various sources have different functions, phenotypes, secretome, and therefore functionality (Melief *et al.*, 2013; Phinney and Seneb́e, 2013). It is also recommended to provide a characterization of factors, e.g., exosomes, that MSCs produce and how their secretome modulates various biological functions, such as immune responses and angiogenesis (Viswanathan *et al.*, 2019).

Nonetheless, abundant evidence suggests that bone marrow-derived MSCs may be cardioprotective (Lai *et al.*, 2010; Mayourian *et al.*, 2017). Bone marrow (BM) MSCs were the first MSCs described in the literature (Dexter, Allen and Lajtha, 1977). They are easy to harvest and expand *in vitro*. This is likely why most preclinical research and clinical trials involve BM-MSCs and not MSCs from other sources (Miao *et al.*, 2017). It has been suggested that transplanted BM-MSCs reduce myocardial infarction in various models of myocardial infarction by e.g., immunomodulation, promotion of angiogenesis, and reduction of fibrosis (Miao *et al.*, 2017). As described in Chapter 1, stem cells exert their cardioprotective properties mostly via their secretome, and exosomes have been proposed to play a crucial role. Therefore, I was interested to explore if MSCs exosomes purified by the ALFA tag are cardioprotective.

However, MSCs have limited capability for *in vitro* expansion. For example, mouse BM-MSCs proliferate for three days before differentiation (Anastassiadis *et al.*, 2010). Of course, the conditions could be manipulated to ensure longer expansion of MSCs. However, nly a low percentage of bone marrow cells are MSCs, and therefore it may be challenging to expand MSCs enough before collecting exosomes for comprehensive *in vitro* and *in vivo* studies. It is possible to purchase large quantities of MSCs from companies such as Lonza or ThermoFisher Scientific. This can be expensive though.

Conditional immortalization can be used to grow cells in large quantities instead of performing isolation of MSCs from multiple donors. Simian virus 40 (SV40) large T antigen has been widely used to bypass cellular senescence (Ahuja, Sáenz-Robles and Pipas, 2005). Large T antigen makes infected cells repeatedly enter the S phase. For this, large T antigen binds to tumour suppressor p53 and retinoblastoma (Rb) tumour suppressors. Cell proliferation provides the SV40 virus with materials for its replication. Many cell types can be transformed if they express large T antigen. Transformed cells are immortal, grow in media with low or no serum, have no contact inhibition (i.e., can proliferate after reaching confluency), can grow on untransformed cells, and, finally, are viable in suspension (Ahuja, Sáenz-Robles and Pipas, 2005).

However, there is a way to control the expression of this gene using the Tet-On system (Gossen *et al.*, 1995). This transcriptional regulation system is based on Tet operator (TetO or TetOp) and Tet repressor protein (TetR) in *E.coli* bacteria. Tetracyclines are antibiotics that inhibit protein synthesis and therefore bacterial replication. Some bacteria have tetracycline resistance mediated by efflux of tetracycline by TetA protein (Chopra and Roberts, 2001; Bertram and Hillen, 2008). TetA expression is normally suppressed by tetracycline-responsive protein TetR binding to TetOp. This is because TetA is unnecessary for bacteria in the absence of tetracycline. However, tetracyclines trigger conformational changes in TetR. This allows TetA to be expressed and initiate tetracycline efflux. In the Tet-On system, the TetR variant, namely reverse tetracycline-controlled transcriptional activator rtTA, binds the tetOp only in the presence of tetracycline (Das, Tenenbaum and Berkhout, 2016). The TetOp, in turn, induces a gene of interest, e.g., large T antigen.

TET-ON has been used to conditionally immortalize various primary cells (May, Hauser and Wirth, 2004). Indeed, a similar technique was used to generate proliferating CTX3E03 cells and isolate ExoPr0 and ExoDiff. The disadvantage of this system is that the transgene can be occasionally induced by irtTA (modified rtTA) binding to TetOp in the absence of tetracycline (Bendiksen *et al.*, 2004). Anastassiadis *et al*. developed an improved TET-ON system using MSCs (Anastassiadis *et al.*, 2010). For example, they fused mutated glucocorticoid-binding domain (GBD) to the irtTA. This means that transcriptional activation of the transgene would require both tetracycline and a synthetic steroid (Anastassiadis *et al.*, 2002). Without these two drugs, irtTA-GBD fusion is associated with heat shock protein 90 (hsp90). This group used this improved TET-ON system in MSCs (Figure 18). They showed that mouse BM-MSCs can be conditionally immortalized if both tetracycline doxycycline and synthetic steroid dexamethasone are present in MSC media (Anastassiadis *et al.*, 2010). The authors confirmed that MSCs can be differentiated into adipocytes, osteocytes, and chondrocytes after the removal of doxycycline and dexamethasone. Therefore, I obtained these MSCs to transfect them with CD63, NanoLuc, and ALFA-tag sequences, proliferate them and obtain highly pure MSC exosomes in large quantities. Also, it would be interesting to compare exosomes from proliferating and differentiating MSCs.

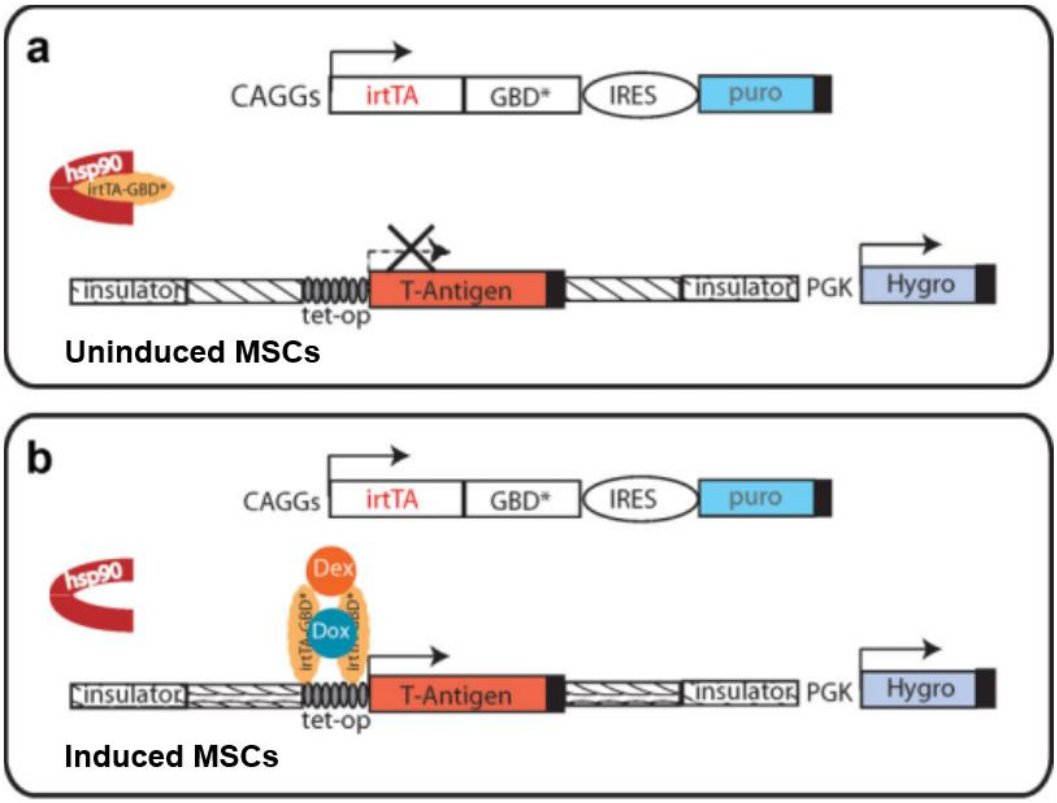

Figure 18. **An improved model of TET-ON transcriptional regulation system.**

Mesenchymal stromal cells (MSCs) have been genetically modified to express the tetracycline operator, TetOp, that induces large T antigen. These sequences are protected by insulator elements from the beta-globin gene. Downstream of TetOp, large T antigen, and insulator sequences is phosphoglycerate kinase promoter (PGK) that induces transcription of hygromycin resistance gene (Hygro). MSCs also have received reverse tetracycline-controlled transcriptional activator (irtTA) transgene that is co-transcribed with mutated glucocorticoid-binding domain (GBD). EMCV internal ribosome entry site (IRES) and puromycin resistance gene (puro) genes are downstream of irtTA and GBD genes. (**A**) In uninduced MSCs, irtTA-GBD fusion is bound by heat shock protein 90 (hsp90). Therefore, the large T antigen is not expressed. (**B**) When MSCs are treated with a synthetic steroid dexamethasone, irtTA-GBD is released by hsp90. In the presence of both dexamethasone and tetracycline, doxycycline, irtTA-GBD binds to TetOp. This initiated expression of the large T antigen. The picture is adopted (Anastassiadis *et al.*, 2010).

Lipid assay for quantifying and evaluating exosome purity

Before cells can be genetically altered to generate ALFA-tagged exosomes, methods of detecting exosomes and evaluating their purity should be considered. As described in the previous chapters, nanoparticle tracking analysis (NTA), protein quantification, sample imaging by electron microscope, and detection of exosome marker by DELFIA can be used. However, each of these methods does not differentiate between exosomes and other particles namely protein aggregates, microvesicles, and lipoprotein. For example, a protein assay will detect total exosome protein in addition to contaminating protein.

In the MISEV2018 guidance on exosome work, sulfo-phospho-vanillin assay is advised for lipid quantification in an exosome-enriched sample. When MISEV2018 was published, this method required a large amount of samples and specialized equipment (Osteikoetxea *et al.*, 2015). However, these limitations were later eliminated and assay accuracy was improved (Visnovitz *et al.*, 2019). The sulfo-phospho-vanillin reaction consists of two steps. First, lipids react with concentrated sulfuric acid at high temperatures to generate carbonium ion chromogens (alkenyl cations). Then, these chromogens react with vanillin in presence of phosphoric acid to form a pink chromophore. Initially, the sulfo-phospho-vanillin assay was thought to quantify all lipids (Chabrol and Charonnat, 1937). Later, the chemical basis of the assay was reassessed, and the sulfo-phospho-vanillin reaction was suspected to require either free hydroxyl groups or CH=CH olefinic group in lipid (Knight, Anderson and Rawle, 1972; Johnson, Ellis and Toothill, 1977). However, it was re-investigated again and now the sulfo-phospho-vanillin assay is recommended for the estimation of total lipids in samples that are predominantly composed of unsaturated triacylglycerol, unsaturated and saturated wax esters, and cholesteryl esters (McMahon, Lu and Butovich, 2013).

Since exosomes are rich in cholesterol (hydroxyl group), sphingomyelin (hydroxyl group and double bond), phosphatidylcholine (hydroxyl group, double bond, and ester), phosphatidylserine (ester), they are expected to be detected in the sulfo-phospho-vanillin assay (McMahon, Lu and Butovich, 2013; Skotland *et al.*, 2019). If, however, only unsaturated lipids can be quantified by the assay as previously reported, lipids in exosome samples are likely to be still quantified reliably. If the level of unsaturation in exosomes, microvesicles, and cell membranes is expressed in mmol unsaturated carbon bonds per gram of lipid, there is no variability between these lipid membranes (Visnovitz *et al.*, 2019). Therefore, there is not much difference between lipid quantity in the membranes of these entities. To find the purity of exosomes, protein to lipid may be used (Osteikoetxea *et al.*, 2015; Visnovitz *et al.*, 2019). This research group suggests that the protein/lipid ratio decreases as vesicle size decreases. For example, apoptotic bodies have a higher protein/lipid ratio than microvesicles, and exosomes have a smaller protein/lipid ratio than both. Therefore, lipid assay was added to exosome characterization methods in this Chapter.

Aims and hypothesis

Hypothesis

I hypothesised that exosomes obtained by affinity purification using ALFA tag would be purer than SEC-purified exosomes and that it is possible to transfect conditionally immortalized MSCs with ALFA tag sequence.

Aims

1. Design ALFA tag sequence for HEK293 cells.
2. Transfect HEK293 cells and obtain exosomes by affinity purification.
3. Characterize exosomes with methods presented in Chapter 2 and quantify lipid content using sulfo-phospho-vanillin assay.
4. Optimize various steps of exosome affinity purification using HEK293 exosomes.
5. Compare affinity-purified exosome purity with SEC-purified exosome purity.
6. Characterise conditionally immortalised MSCs.
7. Design ALFA tag sequence for MSCs.
8. Transfect MSCs with ALFA tag sequence.
9. Characterize MSC exosomes.

Methods

Materials and reagents

The list of solutions, chemicals, kits, instruments, and software is given in Supplementary table 1.

Cell culture

Human epithelial kidney cells, HEK-293 (ATCC), were grown in Dulbecco's Modified Eagle Medium (DMEM) with glucose with 10% foetal bovine serum (FBS) and 1% penicillin/streptomycin (Graham *et al.*, 1977). Bone marrow mesenchymal stromal (MSC) cells were gifted by Prof Anastassiadis (Rostovskaya and Anastassiadis, 2012). They were grown in DMEM with 10% FBS, 1% penicillin/streptomycin, 10^{-7}M dexamethasone, and 1µg/ml doxycycline. All cells were cultured in a humidified atmosphere of 95% air and 5% CO_2 at 37°C.

For subculturing or plating cells for experiments, cell media was removed, and the traces of serum were washed away with phosphate buffer saline (PBS). Cells were detached with TrypLE™ Express Enzyme at 37°C and pelleted for 5min at 300g. Cells were allowed to recover overnight before experiments.

CMV-CD63-Nluc-ALFA plasmid design for HEK-293 cells

Plasmid with ALFA-tag sequence was designed by Dr Golforoush. Plasmid pDB30 was donated by Kojima and colleagues (Figure 20) (Kojima *et al.*, 2018). It encodes for CD63 and nano-luciferase. To incorporate an additional ALFA-tag sequence, the plasmid was first cut with KflI and XbaI restriction enzymes, thus removing part of the nano-luciferase sequence. The plasmid was run on low melting point agarose gel (1.2%; w/v) with GelRed nucleic acid stain to ensure that its length in base pairs is as expected after being cut (Gel electrophoresis). The band of interest was cut using UV light and the plasmid was extracted using a GeneJET gel extraction kit.

To replace the lost part of nano-luciferase and insert ALFA-tag sequences, DNA encoding for them was produced by Integrated DNA Technologies. The sequence of the insert is:

ttcgacggcaaaaagatcactgtaacagggaccctgtggaacggcaacaaaattatcgacgagcgcctgat caaccccgacggctccctgctgttccgagtaaccatcaacggagtgaccggctggcggctgtgcgaacgcat tctggcgggaggaggaggaggcccatcacgtttggaagaggaactgagacgccgcttaactgaataaagc ggccgcgactctagatcataatcagccat. Before incorporation of this DNA to the plasmid, Quick CIP phosphatase was used to prevent the plasmid self-ligation by removing 5'- and 3'- phosphates from each end of the plasmid. Then, T4 DNA ligase was used to connect the insert with the plasmid, also according to the protocol of the manufacturer (Kojima *et al.*, 2018).

CMV-CD63-Nluc-ALFA and PGK-CD63-Nluc-ALFA plasmids were used for bacterial transformation (PGK-CD63-Nluc-ALFA Plasmid design for MSCs

To swap promoter in CMV-CD63-Nluc-ALFA plasmid, mouse PGK promoter was copied from W531 plasmid using PCR (Figure 22). For that, 10µl GoTaq DNA polymerase, <250ng W531 plasmid which has hPGK promoter, 1µl 10µM forward primer which adds MluI restriction enzyme site (CAGATATACGCGTTAGTGATCTAATTCTAC), 1µl 10uM reverse primer which adds NheI restriction enzyme site (GAGCTAGCATTGGCTGCAGGTCGAAAG), and nuclease-free water were mixed in a total volume of 20µl. Then, PCR was run as follows: 1min at +95°C, 15 cycles of 1min at +95°C, 1min at +53°C and 1min at +72°C. As a control, PCR run for 30 cycles. Then, Gel electrophoresis was performed using GelRed nucleic acid stain to isolate the correct PCR product.

To remove CMV promoter and enhancer, CMV-CD63-Nluc-ALFA plasmid was incubated with MluI and NheI restriction enzymes according to the recommendations of the manufacturer. Specifically, 2µl of the plasmid (≥1µg), 1µl of NheI restriction enzyme, 2µl of 10x FastDigest Green buffer and 15µl of nuclease-free water were mixed and incubated at 37°C for 15min. In the 5min, the sample was additionally incubated with 1µl of NheI restriction enzyme. PGK promoter was digested in the same way. Then, Gel electrophoresis was performed using GelRed nucleic acid stain to isolate the correct PCR product and plasmid without CMV promoter and enhancer.

Next, the plasmid ends were dephosphorylated with calf intestinal alkaline phosphatase Quick CIP to prevent self-ligation. This procedure was followed by ligation of the PCR product and the plasmid using T4 DNA ligase. For this, 100ng linearized plasmid was mixed with PGK promoter (1:5 molar ratio), and then 1U T4 DNA ligase, 2µl of T4 DNA ligase buffer, and nuclease-free water were added (20µl total volume). After the mixture was incubated at +22°C for 10min, 5µl of it was used for bacterial transformation as described below.

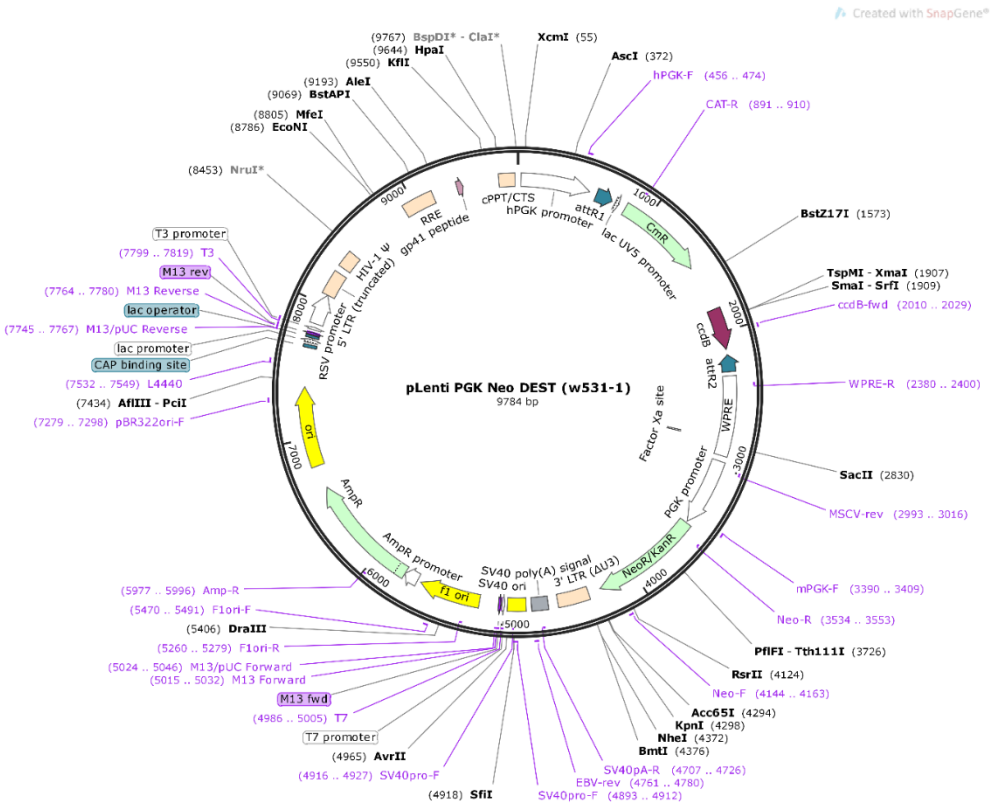

Figure 19. W531 plasmid and its unique cutters.

W531 plasmid (pLenti PGK Neo DEST) has the following sequences (clockwise): **f1 ori**, bacteriophage origin of replication; **AmpR**, sequence encoding for beta-lactamase, which confers resistance to ampicillin, carbenicillin, and related to them antibiotics; **ori**, high copy number origin of replication; **RSV promoter**, Rous sarcoma virus enhancer/promoter; **LTR (truncated)**, truncated 5' long terminal repeat from human immunodeficiency virus HIV-1; **HIV-1 Ψ**, packaging signal of HIV-1; **RRE**, Rev response element of HIV-1 which allows for Rev-dependent mRNA export from the nucleus to the cytoplasm for translation and virion packaging; **gp41 peptide**, sequence encoding for the peptide which is part of HIV-1 envelope; **cPPT/CTS**, central polypurine tract and central termination sequence of HIV-1 for nuclear importation of viral genetic information; **lac UV5 promoter**, E.coli lac promoter with an "up" mutation; **CmR**, sequence encoding for chloramphenicol acetyltransferase, which confers resistance to chloramphenicol; **ccdB**, sequence encoding for bacterial toxin that interferes with DNA gyrase; **WPRE**, woodchuck hepatitis virus posttranslational regulatory element; **hPGK promoter**, human phosphoglycerate kinase 1 promoter; **NeoR/KanR**, sequence encoding for aminoglycoside phosphotransferase from Tn5, which confers resistance to neomycin, kanamycin and G418 geneticin; **3' LTR (ΔU3)**, self-inactivating 3' long terminal repeat from HIV-1; **SV40 poly(A) signal**, simian virus SV40 polyadenylation signal; **SV40 ori**, SV40 origin of replication. Unique restriction enzymes are shown outside the plasmid circle with their position in the plasmid.

JM109 bacterial transformation, selection, and cloning). Transformed bacteria recovered in Lysogeny broth for 1h at 37°C shaker before being plated on agar plates with ampicillin (0.1mg/ml). The next day, five colonies were grown in Lysogeny broth with ampicillin overnight and DNA from them was separately extracted using QIAGEN Plasmid Mini Kit. DNA was digested by KflI and XbaI restriction enzymes and then cut plasmid length was confirmed on agarose gel as before. Undigested DNA was sent for sequencing to Source BioScience company to check if the plasmid was designed correctly, i.e., the ALFA-tag sequence is incorporated and in the right direction in the plasmid. Two primers were used for sequencing of the designed plasmid: forward primer 5'-cgccgaacatgatcgactat-3' and reserve primer 5'-gctggcaactagaaggcaca-3' (temperature for annealing: 55°C and 58°C, respectively). The concentration of the correctly designed plasmid was found by using an LVis absorbance microplate (DNA quantification; Figure 21).

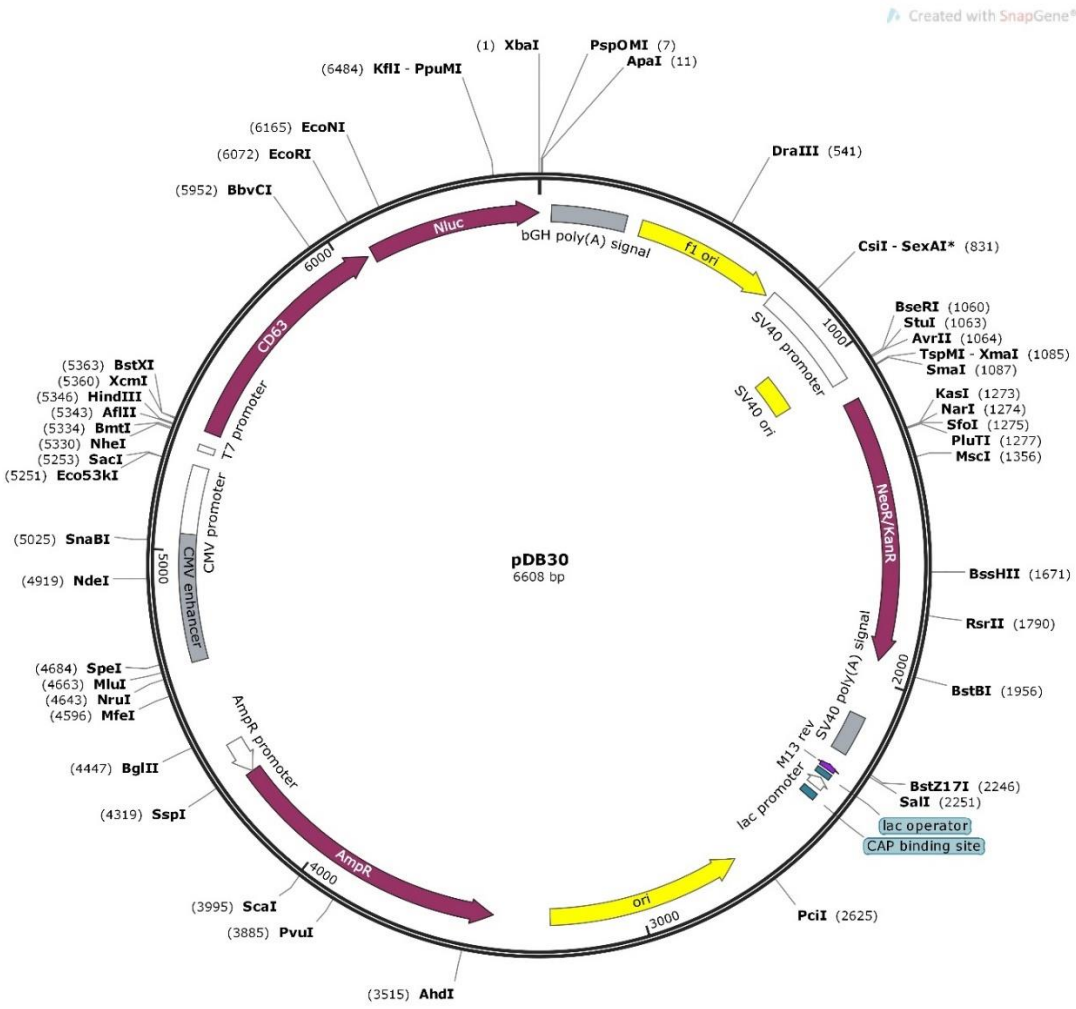

Figure 20. pDB30 plasmid map with unique cutters.

pDB30 plasmid has the following sequences (clockwise): **f1 ori**, bacteriophage origin of replication; **SV40 promoter**, simian virus SV40 enhancer, and early promoter; **NeoR/KanR**, sequence encoding for aminoglycoside phosphotransferase from Tn5, which confers resistance to neomycin, kanamycin, and G418 geneticin; **SV40 poly(A) signal**, simian virus SV40 polyadenylation signal; **lac operator**; sequence which lac repressor can bind to inhibit transcription in E.coli; **CAP binding site**, catabolite activator protein binding site; **lac promoter**, promoter of E.coli lac operon; **ori**, high copy number origin of replication; **AmpR**, sequence encoding for beta-lactamase, which confers resistance to ampicillin, carbenicillin, and antibiotics related to them; **CMV enhancer**, human cytomegalovirus immediate-early enhancer; **T7 promoter**, promoter for bacteriophage T7 RNA polymerase; **bGH poly(A) signal**, bovine growth hormone polyadenylation signal. Unique restriction enzymes are shown outside the plasmid circle with their positions in base pairs relative to the XbaI cutting site.

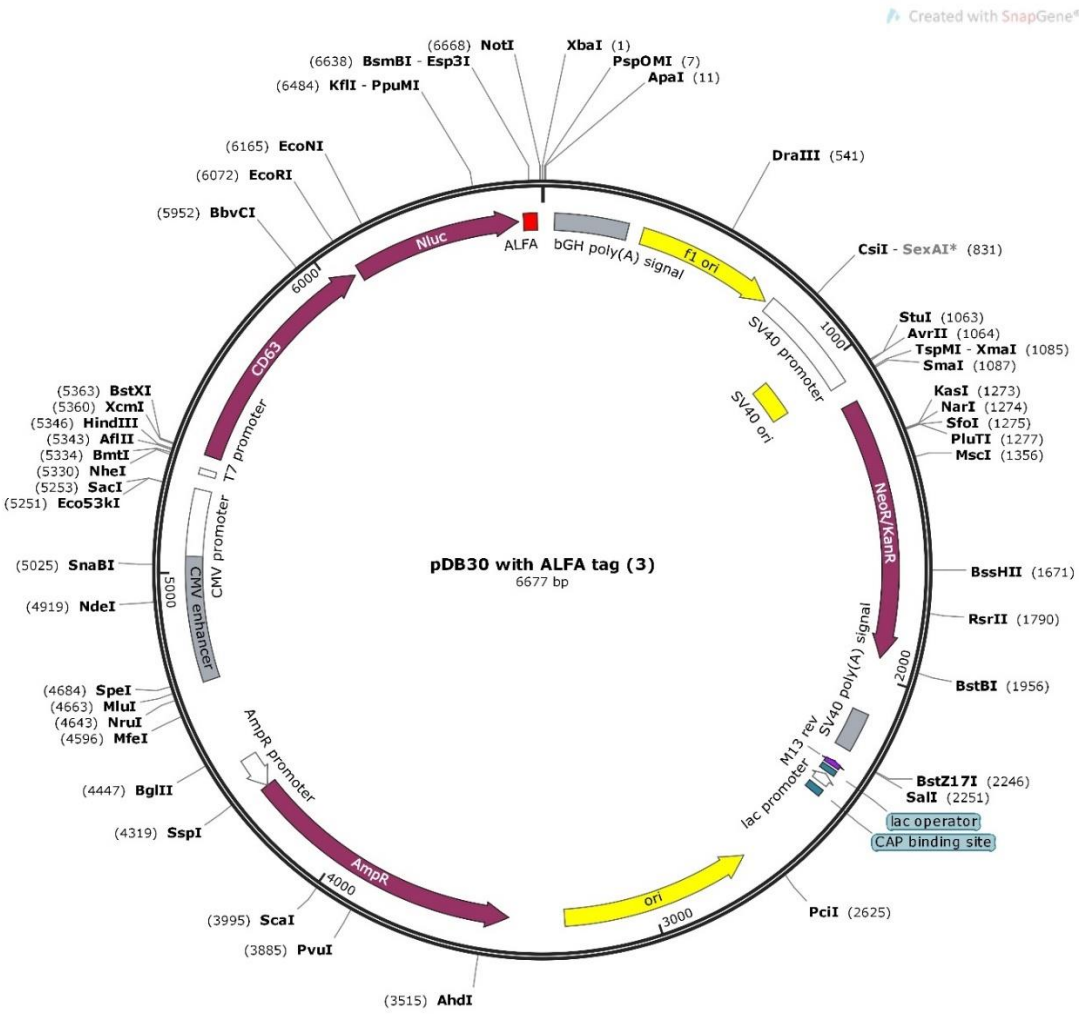

Figure 21. CMV-CD63-Nluc-ALFA plasmid and its unique cutters for HEK-293 cells.

Unlike pDB30, this plasmid has a small ALFA-tag sequence inserted between nano-luciferase and bGH poly(A) signal sequences. Also, it has two additional unique cutters, namely BSMBI-Esp3I and NotI. Unique restriction enzymes are shown outside the plasmid circle with their positions in base pairs relative to the XbaI cutting site.

PGK-CD63-Nluc-ALFA Plasmid design for MSCs

To swap promoter in CMV-CD63-Nluc-ALFA plasmid, mouse PGK promoter was copied from W531 plasmid using PCR (Figure 22). For that, 10µl GoTaq DNA polymerase, <250ng W531 plasmid which has hPGK promoter, 1µl 10µM forward primer which adds MluI restriction enzyme site (CAGATATACGCGTTAGTGATCTAATTCTAC), 1µl 10uM reverse primer which adds NheI restriction enzyme site (GAGCTAGCATTGGCTGCAGGTCGAAAG), and nuclease-free water were mixed in a total volume of 20µl. Then, PCR was run as follows: 1min at +95°C, 15 cycles of 1min at +95°C, 1min at +53°C and 1min at +72°C. As a control, PCR run for 30 cycles. Then, Gel electrophoresis was performed using GelRed nucleic acid stain to isolate the correct PCR product.

To remove CMV promoter and enhancer, CMV-CD63-Nluc-ALFA plasmid was incubated with MluI and NheI restriction enzymes according to the recommendations of the manufacturer. Specifically, 2µl of the plasmid (≥1µg), 1µl of NheI restriction enzyme, 2µl of 10x FastDigest Green buffer and 15µl of nuclease-free water were mixed and incubated at 37°C for 15min. In the 5min, the sample was additionally incubated with 1µl of NheI restriction enzyme. PGK promoter was digested in the same way. Then, Gel electrophoresis was performed using GelRed nucleic acid stain to isolate the correct PCR product and plasmid without CMV promoter and enhancer.

Next, the plasmid ends were dephosphorylated with calf intestinal alkaline phosphatase Quick CIP to prevent self-ligation. This procedure was followed by ligation of the PCR product and the plasmid using T4 DNA ligase. For this, 100ng linearized plasmid was mixed with PGK promoter (1:5 molar ratio), and then 1U T4 DNA ligase, 2µl of T4 DNA ligase buffer, and nuclease-free water were added (20µl total volume). After the mixture was incubated at +22°C for 10min, 5µl of it was used for bacterial transformation as described below.

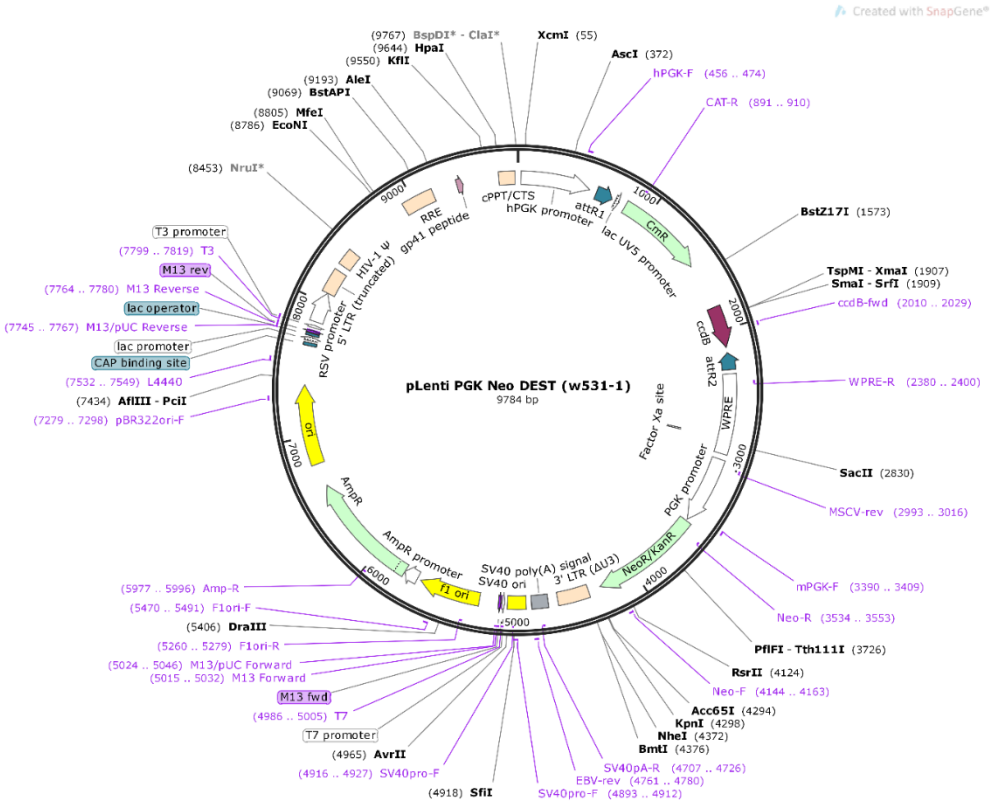

Figure 22. W531 plasmid and its unique cutters.

W531 plasmid (pLenti PGK Neo DEST) has the following sequences (clockwise): **f1 ori**, bacteriophage origin of replication; **AmpR**, sequence encoding for beta-lactamase, which confers resistance to ampicillin, carbenicillin, and related to them antibiotics; **ori**, high copy number origin of replication; **RSV promoter**, Rous sarcoma virus enhancer/promoter; **LTR (truncated)**, truncated 5' long terminal repeat from human immunodeficiency virus HIV-1; **HIV-1 Ψ**, packaging signal of HIV-1; **RRE**, Rev response element of HIV-1 which allows for Rev-dependent mRNA export from the nucleus to the cytoplasm for translation and virion packaging; **gp41 peptide**, sequence encoding for the peptide which is part of HIV-1 envelope; **cPPT/CTS**, central polypurine tract and central termination sequence of HIV-1 for nuclear importation of viral genetic information; **lac UV5 promoter**, E.coli lac promoter with an "up" mutation; **CmR**, sequence encoding for chloramphenicol acetyltransferase, which confers resistance to chloramphenicol; **ccdB**, sequence encoding for bacterial toxin that interferes with DNA gyrase; **WPRE**, woodchuck hepatitis virus posttranslational regulatory element; **hPGK promoter**, human phosphoglycerate kinase 1 promoter; **NeoR/KanR**, sequence encoding for aminoglycoside phosphotransferase from Tn5, which confers resistance to neomycin, kanamycin and G418 geneticin; **3' LTR (ΔU3)**, self-inactivating 3' long terminal repeat from HIV-1; **SV40 poly(A) signal**, simian virus SV40 polyadenylation signal; **SV40 ori**, SV40 origin of replication. Unique restriction enzymes are shown outside the plasmid circle with their position in the plasmid.

JM109 bacterial transformation, selection, and cloning

Plasmids with ALFA-tag sequence (2µl) were added separately to competent JM109 bacteria (50µl; L200B, Promega). Alternatively, phosphate-buffered saline (PBS) was added to JM109 bacteria to create a negative control. The bacteria were placed on ice for 30min. Then, bacteria were heat-shocked by being placed to +42°C for 45sec to ensure the plasmid uptake by them. Afterward, the bacteria were put on ice for a minimum 2min to recover. Before stressing weakened bacteria with ampicillin, 250µl of Lysogeny broth was added to bacteria and the tubes were put on a shaker at +37°C for 1h. Transformed and control bacteria were streaked onto agar plate with or without ampicillin (0.1mg/ml) and left at +37°C. The next day, the absence of the untreated bacteria on agar plates with ampicillin was confirmed. One colony from the plate with transformed bacteria was re-streaked on another plate with ampicillin to ensure that it is a single clone of bacteria. After incubation overnight as before, a single colony of transformed bacteria was inoculated into 10ml of Lysogeny broth containing ampicillin (0.1mg/ml). Importantly, the lid on a flask with bacteria allowed air exchange. The solution with bacteria was left on a shaker (300rpm) at +37°C. When bacteria were in the logarithmic growth phase (after 6-8h, bacteria were inoculated into at least x4 greater volume of Lysogeny broth at 1:500-1:1,000 dilution. Again, the broth contained ampicillin. The bacteria were grown to saturation (12-16h). Plasmids with ALFA-tag sequence were extracted from bacteria using QIAGEN Plasmid Maxi Kit.

Sequencing of plasmids

Sanger sequencing was performed by Source Bioscience to confirm that the plasmids were designed correctly. For this, plasmids and primers were diluted to 100ng/µl and 3.2pMol/µl, respectively (5µl/reaction). Source Bioscience provided the following primers for sequencing: M13R for NeoR/KanR gene (CAGGAAACAGCTATGACC), T7 forward primer for CD63 gene (TAATACGACTCACTATAGGG), and CMVF_pCDNA3 primer for CMV promoter and CD63 gene (CAACGGGACTTTCCAAAATG). Two primers were custom designed by Sigma: IZ401Seq for CMV enhancer and promoter (GACATTGATTATTGACTAGTTATT) and W531Seq for CD63 gene (TTAAGCTTGCCACCATGGCG). Additional primers were designed by Source Bioscience: IZ401_60C to sequence NanoLuc, ALFA-tag, and the respective bGH Poly(A) sequences (CCATGGTCTTCACACTCG), mPGK forward primer and reverse primers to sequence mPGK promoter,

CAGATATACGCGTTAGTGATCTAATTCTACCGGG

and GAGCTAGCATTGGCTGCAGGTCGAAAG, respectively.

All primers are written as 5'-x-3'. The sequencing data were analysed using the Basic Local Alignment Search Tool (U.S. National Library of Medicine, 2022). Global Align function was chosen to compare the obtained sequence to the plasmid entire span using the Needleman-Wunsch algorithm, which aligns nucleotide sequences between two of them and provides a score for each matched nucleotide. Instead of using the score, the plasmid was chosen for further experiment if it is perfectly aligned with the expected sequence.

Gel electrophoresis

Tris-acetate-EDTA (TAE) buffer was mixed with low melting point agarose and heated to allow agarose to melt. Then, GelRed nucleic acid stain or Syto60 was added to melted agarose to allow gel purification or imaging with a scanner later, respectively. Agarose gel was poured into a gel tray with a comb in it to create wells. While gel was solidifying at 4°C (~45min), PRC product or plasmid was mixed with 10x BlueJuice gel loading buffer. If DNA was cut with restriction enzymes, it was mixed with 10x FastDigest Green Buffer instead. Additionally, the DNA ladder (1Kb Plus) was diluted with BlueJuice and nuclease-free water (1:1:8 ratio). After briefly vortexing and spinning all samples, they were loaded into wells of the gel (18-20µl/well) and run at 100V using Electrophoresis Power Supply. To purify desired DNA, gel with GelRed nucleic acid stain was imaged with a UV lamp briefly. The image was taken with a smartphone and the UV lamp was promptly turned off to avoid DNA damage. The ladder helped to determine the position of desired bands. This PCR product of 30 cycles was used as a guide to find the band of interest in the PCR product of 15 cycles, which contained insufficient DNA to be visualised with GelRed nucleic acid stain. If a plasmid was cut with two restriction enzymes, three controls were used: undigested plasmid, and two plasmids digested with either restriction enzyme. Then, DNA from the cut-out gel band was extracted using the GeneJET gel extraction kit according to its instructions. Alternatively, gel with Syto60 was visualised with Odyssey scanner using ‘700’ channel.

DNA quantification

DNA was quantified by using 2µl of DNA or diluent, Tris-EDTA (TE) buffer, on LVis absorbance microplate with a FLUOstar OMEGA plate reader. The background signal from the diluent was subtracted from the DNA signal at 230nm, 260nm, 280nm, and 340nm wavelength. Plasmid purity at 230nm, 260nm, and 280nm was found by subtracting the blank-corrected signal at 340nm from these three wavelengths. The results were used to find two ratios, 260nm/280nm, and 260nm/230nm. The primary indicator of DNA purity, 260nm/280nm, and the secondary one, 260nm/230nm, should be 1.8≥. DNA concentration was found by the following formula:

$$DNA\ conc. = (absorbance\ at\ 260nm - absorbance\ at\ 340nm) * (dilution\ factor) * \frac{50\mu g}{ml}$$

HEK-293 cell transfection and exosome collection

To transfect HEK-293 cells with the plasmid encoding for ALFA-tag, an appropriate concentration of polyethyleneimine (PEI), which is used for cell transfection with the plasmid, was determined. For that, 100mg of cationic polymer PEI was dissolved in 90ml distilled water and brought to pH=<2 with HCl. PEI was left to stir for 3h until dissolved completely. NaOH was added to the solution to make pH=7 and extra water was added to reach 100ml. The PEI was filter sterilised.

Then, HEK-293 cells were plated 40,000cells/well in 96 well plates. The next day, 1µg plasmid with ALFA sequence was added to PEI at different dilutions (1:1-1:6) and topped up with the cell media. After vortexing, the plasmid solution was added to cells dropwise. The next day, the cell media was removed and processed for luciferase assay (Luciferase assay). The most effective dilution of plasmid with PEI was chosen (1:4) so that it allowed minimal use of PEI.

For exosome collection, six T225 flasks of HEK-293 cells at 70-90% density were treated with 100µg plasmid and 400µl of PEI per flask. After overnight incubation, cell media was substituted to serum-free cell media for 24h collection of exosomes.

Electroporation of MSCs, selection of positive clone, and exosome collection

Before MSCs were transfected with the plasmid encoding for ALFA-tag, the appropriate concentration of selective antibiotic was selected. For that, MSCs were plated at 60% confluency in 24 well plates. The next day, 50-1000µg/ml G418 antibiotic was added to cells. The antibiotic solution was refreshed every two days for one week. Untreated cells were used as a control. Cell imaging was performed daily to determine what the lowest antibiotic dose should be used to cause 100% cell death after one week.

Appropriate settings for electroporation were chosen. As recommended in the manual for Neon™ Transfection System, various combinations of pulse voltages (850-1700V), pulse width (10-40ms), and pulse number (1-3) were tested on MSCs. For this, MSCs were grown to 70-90% confluency. Then, they were detached and centrifuged at 300g for 5min. After, cells were washed with PBS and centrifuged again. The cell pellet was mixed with Resuspension Buffer R at a final density of 10^7cells/ml. Within less than 30min, 9µl of cell suspension was mixed with 1µg plasmid which encodes for CD63 and enhanced GFP under the same promoter (gift from Dr Kaloyan). Next, cells were aspirated by Neon™ Transfection System Pipette and electroporated in the Neon™ Transfection System Pipette Station. The next day, cells were imaged, and their viability and transfection efficiency (i.e., GFP+ cells relative to the total number of cells) was rated on a scale of ten.

Once the appropriate settings for MSCs transfection were chosen, namely 1,300V, 40ms, and 1 pulse number, MSCs were transfected with the plasmid encoding for ALFA-tag as six replicates. The plasmid was linearized with ScaI restriction enzyme to allow plasmid incorporation into the MSC genome. Non-electroporated MSCs were used as a control. MSCs were allowed to recover for a day before being treated with 300µg/ml G418 for a week to select the positive clone.

After the selection of the positive clones was finished, MSCs were plated in 96 well plates. The next day lysed transfected and non-transfected MSCs, respective cell media, and PBS were tested for luminescence. When luminescence was confirmed in both transfected cells and their media, transfected cells were grown to 70-100% confluency in six T225 flasks. Then, cell media was changed to FBS-free media, and exosomes were collected for 24h before size exclusion chromatography.

Cell imaging

Brightfield and fluorescent imaging were performed using x20 objective on GXM-XDS401 inverted fluorescence biological microscope.

Flow cytometry

MSCs were detached with 200µl TrypLE™ Express Enzyme and mixed with 300µl of respective media. Cells were stained with 0.5µg/ml propidium iodide (PI), dead cell dye, to determine the number of live cells only. Importantly, PI was added to each sample right before analysis. Flow cytometry was performed by using a 585/40nm FL2 filter in an Accuri flow cytometer. The samples were run at a fast flow rate with a limit set to a minimum of 10,000 cells. The percentage of the dead cells was determined using FlowJo. First, the “Cells” gate was drawn on a side scatter versus a forward scatter graph of the water sample to exclude >99% events. This gate was applied to all samples with cells (Figure 23; FSC-A vs SSC-A). Cell aggregates were removed by drawing a gate diagonally starting at zero on forward scatter height versus area (Figure 23; FSC-A vs FSC-H). Finally, to determine the percentage of dead cells, single cells were plotted on a graph with their number against PI fluorescence (FL2-H-positive cells). The sample without PI staining was used to draw a gate to exclude a peak representing the natural fluorescence of cells. This gate was applied to stained samples, so that the fluorescent peak represented PI-positive cells (Figure 23; count vs FL2-H). “Cells”, “Single Cells” and FL2-H-negative gates were the same for all analysed samples. The number of live PI-negative cells was then recorded.

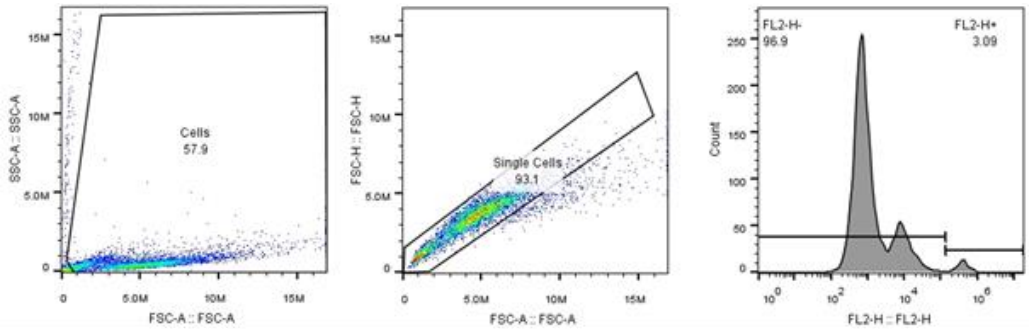

Figure 23. Flow cytometry gating strategy for identification of dead cells.

Dead cell number was determined using BD Accuri C6 flow cytometer. The data were processed using FlowJo software. (**Left**) Water was used to draw a cell gate which excludes >99% of events. Here, this gate was applied to the cell-containing sample. The gate shows that 57.9% of detected particles ("events") are gated as cells. (**Middle**) The diagonal gate was drawn using an untreated cell-containing control sample. Only 93.1% were single cells, and the rest was assumed to be cell aggregates. (**Right**) Finally, an unstained control sample was used to identify a peak of unstained cells (FL2-H-) and draw an FL2-H+ gate as wide as possible with 0 cells. Here, this gate was applied to a stained cell-containing sample. This sample contains 3.09% of stained dead cells (FL2-H+) and the rest are unstained live cells (FL2-H-).

Cell lysis and Western blot

T antigen expression in MSC cells was evaluated using Western blot. Specifically, MSC cells (clone 6472) were plated at 175,000 cells per 10cm^2 dish. Next day (day 0), cell media was changed to DMEM with 10% FBS, 1% penicillin/streptomycin with (treatment) or without (control) 10^{-7}M dexamethasone and 1µg/ml doxycycline. The media was refreshed every day for four days. Each day, cells were washed with ice-cold PBS twice. Then, they were scrapped into ice-cold PBS and pelleted at 600rpm at 4°C for 5min. The pellet was lysed in the minimum amount of lysis buffer, i.e., sufficient to dissolve cells and push them effortlessly through an insulin syringe. The samples were sonicated five times for 5sec with 5sec intervals at 4°C using Vibra-Cell Ultrasonic Liquid Processor. Cell debris was pelleted at 10,000rpm at 4°C for 10min.

Next, protein quantity in samples was quantified BCA assay (Protein assay). Protein in samples was denatured by mixing samples with 10% 2-mercaptoethanol in NuPAGE LDS sample buffer (4:1). Samples were then heated at 80°C for 10min, cooled, and stored at -80°C.

The next day, 20µg of samples were loaded into a 4-20% Novex mini gel. Additionally, Precision Plus Protein™ Dual Xtra protein standard was loaded on the gel to estimate the molecular weight of sample proteins. The gels were placed in chambers with Running Buffer. Sample proteins were separated by electrophoresis at 160V for 1h 15min using high current power supply. The proteins were transferred from the gel to the nitrocellulose membrane at 100V for 1h 20min by the same device. After blocking membranes with 5% BSA in 0.1% Tween in Tris-buffered saline (TBS) to prevent unspecific binding, the membranes were incubated with monoclonal primary mouse antibodies, namely anti-T antigen (Anti-SV40 T Ag; 1:200) and anti-actin (1:500) at 25oscillations/min at 4°C. The next day, blots were washed with 0.1%Tween/TBS three times for 5min. The membranes were incubated with anti-mouse IRDye 800CW secondary antibody (1:15,000) in Odyssey blocking buffer, which was diluted 1:2 with 0.1%Tween/TBS. After 1h of membrane incubation at 25oscillations/min at room temperature, the membranes were washed. Immunolabelled bands were visualised with an Odyssey infrared imager. Protein expression was quantified using Odyssey software. The background signal was subtracted from the data.

Size exclusion chromatography of cell media

Pooled cell media from HEK-293 cells or MSCs was centrifuged at 4,500g for 10min at +4°C to remove cells. The supernatant was transferred to Vivaspin 15R concentrator tubes to reduce water content and remove most of the particles smaller than 30,000Da. The tubes were spun at 3,000g at +4°C. When cell media was concentrated sufficiently, it was transferred to Vivaspin 2 tubes to concentrate it to 0.5ml at 4,000g. The concentrate was reverse spun at 3,000g for 2min in the same tubes to collect it. Finally, qEVoriginal column (35nm) was used for size exclusion chromatography (SEC). For that, 0.5ml of concentrated media was added to the column and, simultaneously, Fraction 0 (i.e., the first 0.5ml) was collected. Then, 0.5ml PBS was degassed to reduce the likelihood of SEC column blockage and it was added to the column and Fraction 0.5 (i.e., the second 0.5ml) was collected. PBS (0.5ml) was added to collect consequent fractions until Fraction 11.0-11.5ml (F11) was obtained. Samples were stored at -80°C.

Nanoparticle tracking analysis

Nanoparticle tracking analysis (NTA) is described in Chapter 2. The mean concentration and particle size were found. However, fractions that were diluted 1:10 to 1:250 were analysed only once. Those fractions whose concentration was not detected at 1:10 were assigned zero particles/ml.

Protein assay

Protein quantification of exosome-rich samples was done using a BCA protein assay kit for low concentrations. Each sample was diluted at 1:75 or 1:150 in water and pipetted in duplicates. The absorbance of samples was read at 562nm on a FLUOstar OMEGA plate reader. The blank absorbance (distilled water) was subtracted from standard dilutions and samples. Protein concentration in samples was found using a standard curve as described in Chapter 2.

Protein content in cells was measured after cell lysis (see

Cell lysis and Western blot). Pierce™ BSA Standard Pre-Diluted Set was used to build a standard curve (1.25-20µg/well). Lysed cells and standard dilutions were used as triplicates. Samples and standards absorbance values were normalised to lysis buffer and standard diluent, respectively. The absorbance was read at 562nm as before.

DELFIA

DELFIA is described in Chapter 2. Each sample was pipetted in a single well, 1µl/well topped to 100µl/well with PBS. However, controls, i.e., PBS with primary and secondary antibodies or PBS alone, were used as triplicates. Anti-CD9, anti-CD63, and anti-CD81 antibodies were used as primary antibodies. Fluorescence values of controls were excluded from analysis if they were twice higher than PBS alone.

Transmission electron microscopy

Transmission electron microscopy (TEM) was performed as described in Chapter 2 with some modifications. This time, TEM was performed by the author of this thesis. Samples (2µl) were put on a grid and allowed to dry for a few minutes. The attached particles were stained by placing the grid of 20µl uranyl-oxalate drop for 30sec. The grid was washed on three 20µl drops of distilled waters sequentially for 1min on each. The images were obtained with a JEM-1400 transmission electron microscope and software. Circular particles larger than 30nm were measured manually using ImageJ analogue, Fiji software (Schindelin *et al.*, 2012). The length of the scale bar was used to determine the pixel to nm ratio. I tried to draw the longest line within each vesicle to determine its diameter.

Luciferase assay

Luminescence in samples was determined by using Nano-Glo Dual-Luciferase Reporter Assay System. See sample dilution and information on how luminescence signal was normalised under relevant figures. Water was used as a diluent. The data was obtained with a FLUOstar OMEGA plate reader using a lens as an emission filter and gain 2,200a.u. The efficacy of exosome elution was evaluated using the following formula:

$$\frac{Luminescence(Eluted\ Exosomes)}{Luminescence\ sum\ of\ (Unbound, Washed\ away, Eluted\ and\ Bound\ exosomes)} * 100\%$$

Lipid assay

Lipid content in samples was determined by a lipid quantification assay developed by Visnovitz and others (Visnovitz *et al.*, 2019). For that, a lipid standard was prepared using DOPC (1,2-Dioleoyl-sn-glycero-3-phosphocholine) liposomes. DOPC was dissolved in chloroform (1mg/ml) and then kept at +60°C to allow chloroform to evaporate. The dried DOPC cake was vortexed with 1ml PBS and sonicated with 35kHz at +45°C for 10min with Clifton Ultrasonic Bath. After vortexing it for 2min at maximum speed, a lipid standard was prepared (6.25-400ng/ml). Both standard dilutions in triplicates, samples, or sample diluent (water) in duplicates were prepared as 40µl samples in acid-resistant Eppendorf polypropylene tubes. Then, 200µl of 96% sulphuric acid was added to each tube and vortexed. The tubes were incubated at +90°C in a fume hood for 20min. Meanwhile, the phospho-vanillin reagent was prepared by dissolving 50mg of vanillin in 50ml of 17% phosphoric acid. After cooling tubes down at +4°C for a minimum 5min, 120µl of phospho-vanillin reagent was added to standard dilutions, samples, and their diluent. After vortexing, contents of the tubes were pipetted into 96 well plates, 280µl/well and colour reaction developed at +37°C for 1h. Absorbance was found at 540nm with a FLUOstar OMEGA plate reader. The blank absorbance (distilled water) was subtracted from standard dilutions and samples. Lipid concentration in samples was found using a standard curve using the same formula as for protein.

Exosome elution

The most particle-rich fraction was used for exosome elution with an anti-ALFA-tag antibody. For this, 20mM ALFA peptide stock was prepared in distilled water and incubated at +37°C for 30min. Also, Dynabeads M280 Streptavidin magnetic beads were diluted in PBS (see dilution under relevant figures). Anti-ALFA tag antibody was mixed with beads and incubated for 15min (300pMol; 9.3µl of antibody per 100µl of beads). The tubes were placed on a DynaMag-2 magnetic stand and antibody solution was removed. After removing tubes from the stand, beads were washed in 0.5ml PBS twice, and each time PBS was removed when tubes were on the stand. Then, exosomes were added to the tubes with antibody-labelled beads (see dilution under relevant figures). After 1h rotation at +4°C with head-over-tail rotation, tubes were placed on the magnetic stand and non-bound particles were collected. Next, beads were washed twice with 0.5ml PBS as before, and this PBS was collected as a “wash” sample. Finally, 1mM ALFA elution peptide was incubated with exosomes bound to the beads for 10min at room temperature (167µl per 100µl beads). The eluted exosomes, or affinity-purified exosomes, were collected, and beads were diluted in PBS.

Results

CMV-CD63-Nluc-ALFA plasmid for transfection of HEK-293 cells

The aim of the experiments described in this chapter was to develop an immunoaffinity-based isolation method by incorporating the ALFA-tag on exosomes. Thus, with the assistance of Dr Golforoush, I used a pDB30 plasmid that encodes CD63 and NanoLuc and incorporated the ALFA-tag sequence. I confirmed the plasmid size using electrophoresis with GelRed nucleic acid stain and Dr Golforoush assisted with sequencing it. When CMV-CD63-Nluc-ALFA plasmid is cut with one restriction enzyme, the plasmid becomes linear and is visualised as a band of predicted plasmid length. The length of the plasmid linearized by the KflI restriction enzyme was as expected (Figure 24). Additionally, the plasmid was cut using an additional restriction enzyme, XbaI. The resulting bands, the plasmid and the DNA fragment containing ALFA-tag sequence were of the predicted lengths. The uncut CMV-CD63-Nluc-ALFA plasmid showed the expected presence of supercoiled and nicked plasmid DNA. The gel containing supercoiled DNA was cut and the DNA was purified using a GeneJET gel extraction kit. JM109 *E.Coli* bacteria was transformed with the correctly designed plasmid. Since CMV-CD63-Nluc-ALFA plasmid encodes for ampicillin resistance, transformed bacteria were selected using this antibiotic. The plasmid was isolated from bacteria using QIAGEN Plasmid Maxi Kit and its purity and concentration were determined.

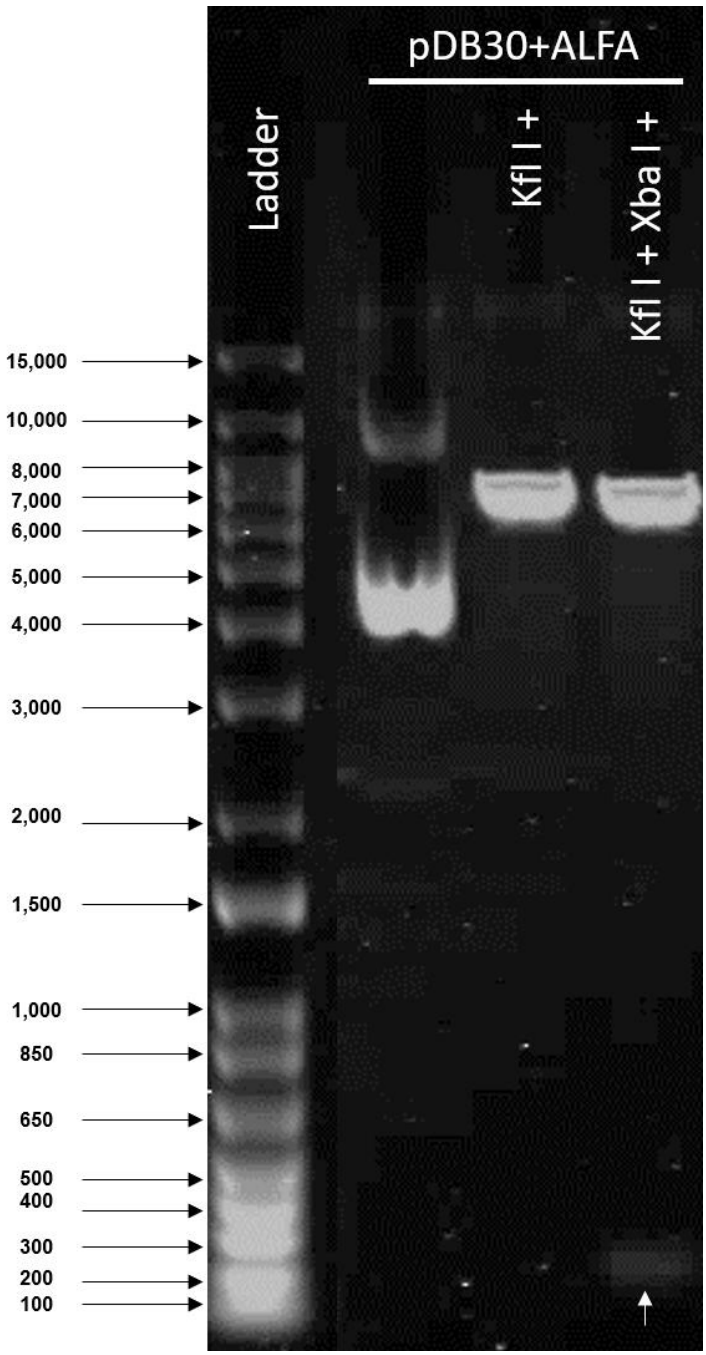

Figure 24. Agarose gel electrophoresis of three plasmids.

CMV-CD63-Nluc-ALFA plasmid was digested with KflI or both KflI and XbaI restriction enzymes for 5min at 37°C. Digested and undigested plasmids were run on 0.8% agarose gel with Syto60 dye for 100min. Predicted sizes of the plasmid linearized with restriction enzymes: CMV-CD63-Nluc-ALFA plasmid without ALFA tag sequence – 6,677bp and ALFA tag sequence - 193bp. The samples were run on 0.8% agarose gel at 100V for 1h 40min.

Analysis of SEC fractions from transfected HEK-293 cells

Kidney HEK-293 cells were transfected with the CMV-CD63-Nluc-ALFA plasmid using PEI. HEK-293 cell exosomes were collected in serum-free media for 24h and subjected to size exclusion chromatography (SEC). The SEC fractions were first analysed using nanoparticle tracking analysis (NTA; Figure 25, A). The particle concentration was highest in fractions 3-4, with the fraction 3.5 being the most particle-rich. All three fractions had a mean particle size just below 100nm, which is the predicted size of exosomes. The presence of CD9, CD63, and CD81 tetraspanins, which are associated with exosomes, was checked using DELFIA (Figure 25, B). Fraction 3.5 had the highest concentration of these three markers, which indicates that this fraction is the most exosome-rich. The most particle rich fractions are called SEC-purified exosomes hereafter. CD63 signal was the strongest in it because HEK-293 cells overexpress CD63 after the transfection. Finally, the luminescence signal was recorded (Figure 25, C). SEC-purified exosomes had the strongest luminescence, indicating that at least some exosomes got ALFA-tag sequence with NanoLuc successfully incorporated into them.

All samples were analysed with protein and lipid assays (Figure 25, D, and E). SEC-purified exosomes had an increased concentration of protein and lipid relative to earlier fractions. Protein and lipid concentration drops in the next fractions but then raises. It indicates that SEC-purified exosomes were collected, and small protein and lipids passed the column in later fractions. The peak protein and lipid concentration is reached in fractions 7.5 and 9.5, respectively. Importantly, protein and lipid concentration in these fractions are higher than in the SEC-purified exosomes. Since the later fractions have particles of smaller size than exosomes (i.e., it was below limit of NTA detection, which is 10nm), this data suggests that most of free protein and lipid were successfully separated from SEC-purified exosomes. However, protein and lipid of exosome size could be co-isolated with exosomes. This was confirmed with electron microscope imaging (Figure 29, A). The images show particles of all shapes, and they are aggregated instead of only cup-shaped exosomes.

HEK-293 exosomes were isolated several times (i.e., several biological replicates). The mean particle, protein, and lipid concentrations as well as ratios of various parameters were found for SEC-purified exosome samples (Table 6). Mode particle size is slightly above 100nm. There is no consensus what the diameter of exosomes. However, intraluminal vesicles in mature endosomes, which later become exosomes, are ~50-100nm. Therefore, mode particle size indicates potential contaminants such as microvesicles. Particle, protein, lipid concentration, and the ratio between them vary hugely across the experiments. This may be due to various cell densities because HEK-293 cells detach easily at higher confluency. The particle/protein ratio was $9.3 * 10^9$/µg. This ratio indicates low exosome purity ($> 3 * 10^{10}$/µg is high purity and $< 10^8$/µg is impure exosome sample) (Webber and Clayton, 2013). The sample protein/lipid ratio was 3.4, which indicates that the SEC-purified exosomes have more protein than lipid. However, exosomes have a higher lipid ratio to protein because of their bilayer membrane. Osteikoetxea and colleagues, who obtained exosomes by methods based on density and size separation, suggested that the protein/lipid ratio of exosomes should be ~0.25 (Osteikoetxea *et al.*, 2015). Therefore, SEC-purified exosomes are likely to have protein contaminants. Other ratios, such as lipid/particle, CD63 fluorescence/particle, and CD63 fluorescence/lipid were found so that exosomes eluted from SEC-purified exosome sample by ALFA tag (affinity-purified exosomes hereafter) can be compared to this fraction. All this data shows that SEC-purified exosomes are highly likely to be an exosome-rich fraction, but it has contaminating particles.

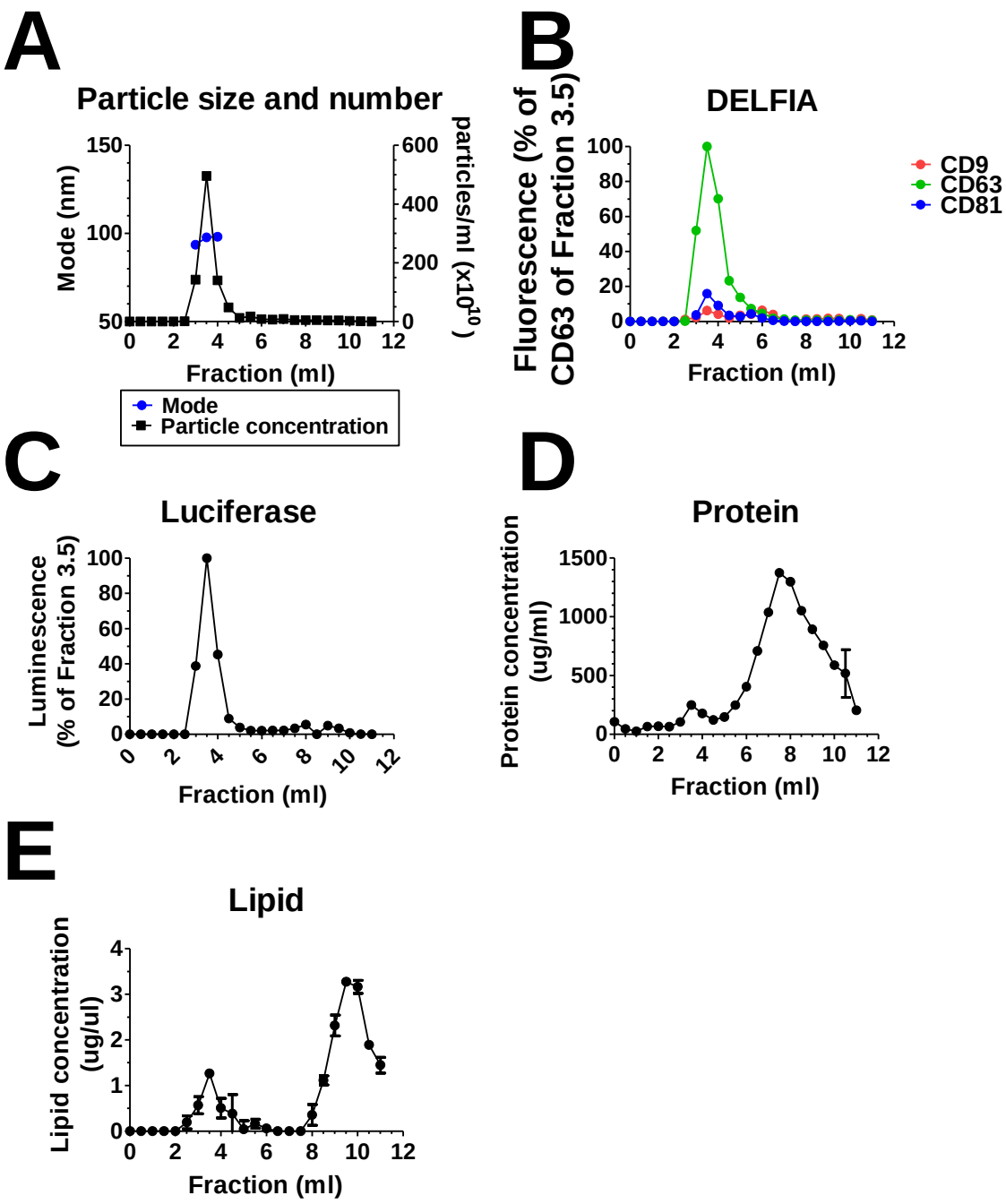
A
Particle size and number
Mode (nm)
particles/ml (x10^10)
Fraction (ml)
Mode
Particle concentration
B
DELFIA
Fluorescence (% of CD63 of Fraction 3.5)
CD9
CD63
CD81
Fraction (ml)
C
Luciferase
Luminescence (% of Fraction 3.5)
Fraction (ml)
D
Protein
Protein concentration (ug/ml)
Fraction (ml)
E
Lipid
Lipid concentration (ug/ul)
Fraction (ml)

Figure 25. Representative analysis of HEK-293 cell media fractions collected by SEC.

(**A**) The particle size of SEC fractions and their relative abundance was determined using nanoparticle tracking analysis (NanoSight). The black line is the mean of three sample analyses. The grey lines show the standard error. (**B**) Protein quantity was measured in the fractions using a BCA assay. Mean±SD of duplicates is plotted. (**C**) Luciferase signal in the fractions was normalised to the Fraction 3.5. All fractions were diluted at 1:8,000 in water. (**D**) The presence of CD9, CD63, and CD81 exosome-associated markers was checked in the fraction using DELFIA. Each sample was used in a single well. (**E**) Lipid quantity was determined using a lipid assay. Mean±SD of duplicates was plotted. (**A-E**) The data represent n=1.

Characteristics of the SEC-purified exosomes	Mean	SD
Particle mode diameter (nm); n=5	104.1	±16.3
Particle concentration (10^{10}/ml); n=4	330.6	±200.6
Protein concentration (µg/ml); n=4	312.3	±79.1
Lipid concentration (µg/µl); n=4	0.096	±0.043
Particle to protein ratio (10^9/ µg); n=8	9.3	±4.8
Protein to lipid ratio (µg/µg); n=4	3.4	±1.8
Lipid to particle number ratio (µg/10^9); n=4	0.041	±0.017
CD63 fluorescence to particle ratio (a.u./ 10^7); n=5	4.0	±3.1
CD63 fluorescence to lipid ratio; n=4	1.328	±0.651

Table 6. Analysis of the most particle-rich SEC fraction.

SEC-purified exosomes from HEK-293 cell media were analysed by NTA, lipid assay, BCA protein assay and DELFIA to determine exosome purity.

Optimization of the luminescence assay protocol

Before eluting exosomes from SEC-purified exosome samples, it was necessary to confirm that SEC-purified exosomes had the strongest luminescence signal. However, SEC-purified exosomes had almost zero luminescence signal (Figure 26, A), which was unexpected considering that most CD63+ particles were in SEC-purified exosomes (Figure 25, B). One possible explanation was that assay reagents were consumed rapidly in wells with SEC-purified exosomes, and this results in apparent signal loss. To investigate this, dilutions of SEC-purified exosomes were analysed in luminescence assay. The results showed that measured luminescence decreased as the particle number increased (Figure 26, B). Furthermore, the luminescence was observed to decay rapidly, and that speed depends on particle number (Figure 26, B). Therefore, it was decided to analyse samples immediately using one replicate per sample to minimize the analysis duration.

To confirm that, three most particle-rich fractions were diluted to 10^4-10^8 particles/well and their luminescence was read immediately. No difference in luminescence was observed at these concentrations (Figure 26, C). Therefore, it was decided to find an appropriate sample dilution for the most exosome-rich SEC fraction (SEC-purified exosomes hereafter) and apply the same dilution for other SEC samples and affinity-purified exosomes.

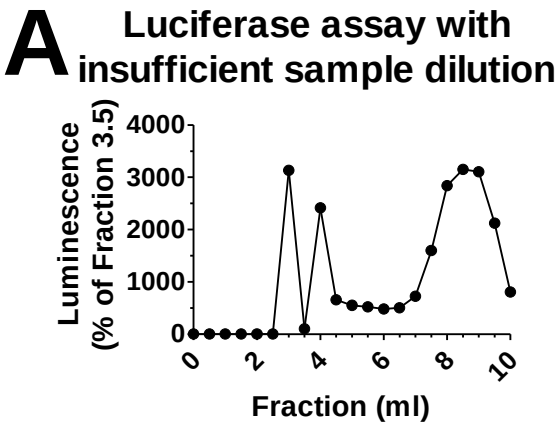
A
Luciferase assay with insufficient sample dilution
Luminescence (% of Fraction 3.5)
4000
3000
2000
1000
0
0
2
4
6
8
10
Fraction (ml)

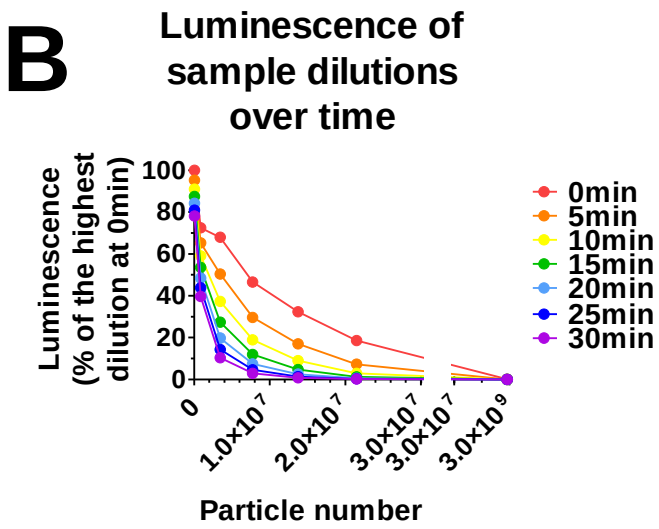
B
Luminescence of sample dilutions over time
Luminescence (% of the highest dilution at 0min)
100
80
60
40
20
0
0
1.0×10^7
2.0×10^7
3.0×10^7
3.0×10^7
3.0×10^9
Particle number
0min
5min
10min
15min
20min
25min
30min

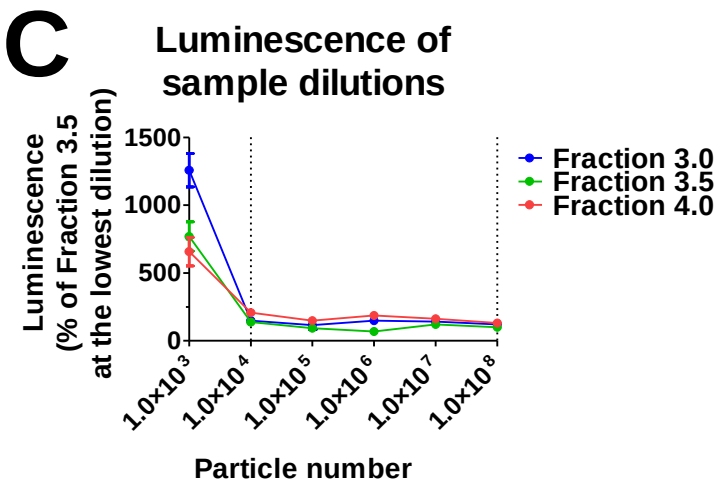
C
Luminescence of sample dilutions
Luminescence (% of Fraction 3.5 at the lowest dilution)
1500
1000
500
0
1.0×10^3
1.0×10^4
1.0×10^5
1.0×10^6
1.0×10^7
1.0×10^8
Particle number
Fraction 3.0
Fraction 3.5
Fraction 4.0

Figure 26. Time and sample dilution effect on luminescence.

(**A**) Luminescence signal of SEC-purified exosomes was normalised to the most particle-rich fraction, Fraction 3.5. Samples were not diluted for luminescence assay. n=1, N=1. (**B**) Luminescence of SEC-purified exosome dilutions was read every 5min. n=1, N=1. (**C**) Luminescence of the most and the second most particle-rich samples, i.e., Fraction 3.5 or Fraction 3.0 and Fraction 4.0, was measured immediately (time=0min). The data is shown as mean±SEM. n=5, N=1.

Development of the protocol for elution of exosomes by ALFA-tag

An excess quantity of free ALFA peptide was added to the bead-bound exosomes to release the free exosomes. The approximate ratio of beads to nanobody and beads to particle number was estimated based on binding affinity to biotin, bead, and exosome size. Using this protocol, several pilot experiments were performed to determine if it needs adjustments. First, SEC-purified exosomes were incubated with nanobodies. After unbound particles were washed away, 50µl of ALFA peptide was added. Every 10min, 10µl of this solution was collected to evaluate if prolonged elution would increase the yield of exosomes. After no liquid was left to collect, 50µl of fresh ALFA peptide was added to see if second elution of exosomes may be necessary. The data showed that most of the luminescent exosomes were released from the beads after the first 10min incubation step (Figure 27, A).

In another experiment, exosomes were eluted for 10min, and then the second time with fresh ALFA peptide for an extra 10min. The results indicate that the second portion of ALFA peptide eluted ~20% exosomes compared to the first elution (Figure 27, B). Even though the quantity of affinity-purified exosomes increases with time and repeated elution, it was not sufficiently high for us to justify prolonged protocol with extra steps.

Additionally, the concentration of ALFA peptides used for exosome elution was optimized. Exosome elution efficiency increased by ~71% when ALFA peptide concentration was increased from 12pMol to 120pMol (Figure 27, C). A further increase did not seem to enhance exosome elution further. Therefore, it was decided to use 200pMol of ALFA peptide.

Finally, various concentrations of beads were tested for exosome elution by myself and an MSc student, Elias Sulaiman, whom I supervised. Previously, a ratio of 6,000 particles/bead was used. However, altering the particle/bead ratio to 3,000 and 20,000 did not improve exosome yield significantly (Figure 27, D).

Affinity-purification if HEK-293 exosomes increase their purity

ALFA-tagged exosomes from HEK-293 cell media were first enriched by SEC. To capture these ALFA-tagged exosomes, anti-ALFA-tag nanobodies were used. After unbound particles were washed away, exosomes were eluted from the nanobodies using free ALFA peptide. Affinity-purified exosomes were compared to the SEC-purified exosomes to determine if the former is purer. First, mode particle diameter, concentration, and particle distribution were found using NTA. SEC-purified exosomes had particles in a range of 50-275nm, whereas affinity-purified exosome samples had 50-200nm particles (Figure 28). Particle mode diameter was reduced by 20nm in affinity-purified exosome sample relative to SEC-purified exosomes (Table 7). The yield of particles was reduced to ~12% and luminescence was reduced to ~15% (Table 7), indicating that most of tagged EVs were not captured.

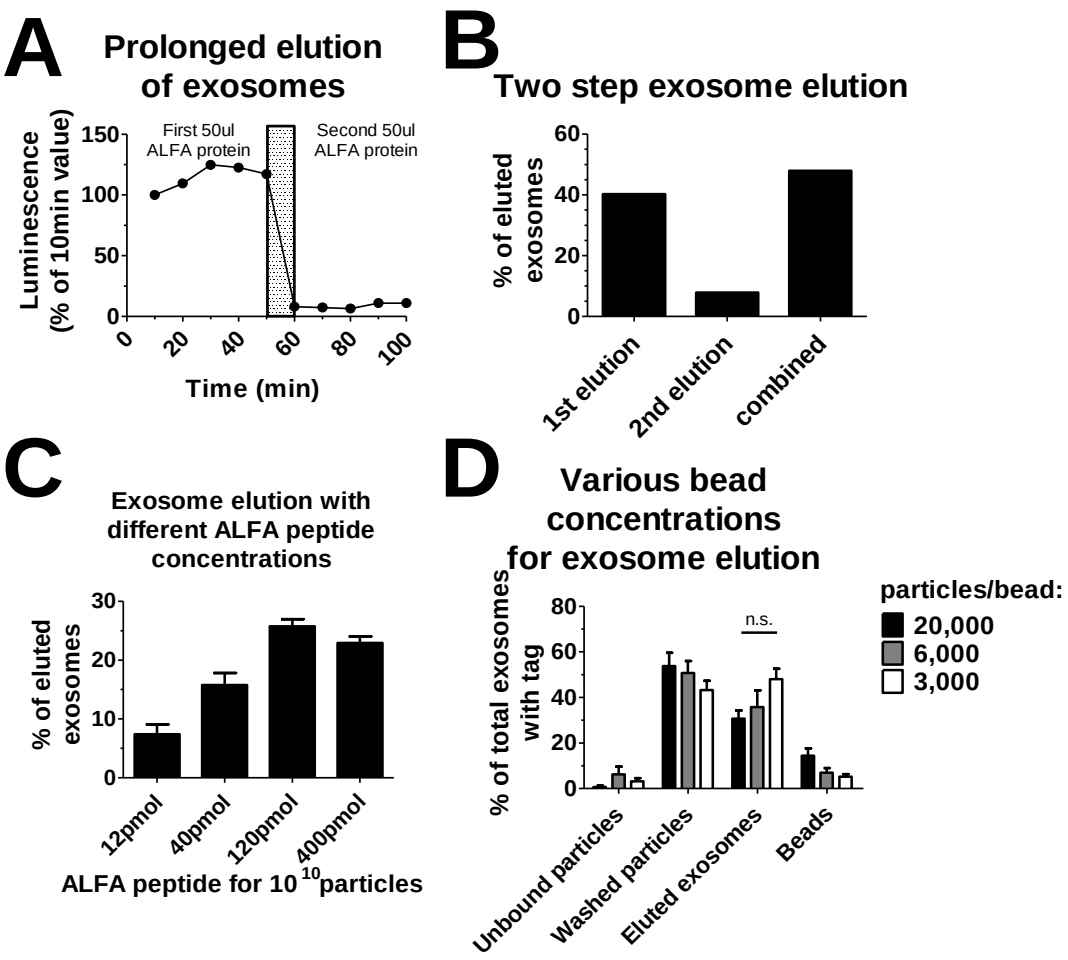

Figure 27. Refinement of protocol for elution of HEK-293 exosomes by ALFA-tag.

SEC-purified exosomes were used for elution (**A-C**: 100µl, D: 4x10^10). (**A**) Exosomes bound to the antibody were incubated with 50µl of 2mM ALFA peptide for 10min. ALFA peptide solution was collected, 10µl per 10min. Then, a fresh ALFA peptide was added, and the procedure was repeated. Only affinity-purified exosomes were checked for luminescence undiluted. (**B**) Exosomes were eluted with 50µl 2mM ALFA peptide for 10min, and then with an extra 50µl ALFA peptide for a further 10min. (**C**) Exosomes were eluted with 50µl of ALFA peptide of different concentrations for 10min only. (**D**) Various bead dilutions for exosome elution were tested. Exosomes were eluted with 50µl 1mM ALFA peptide for 10min. (**B-D**) Affinity-purified exosomes, as well as exosomes that were non-bound, washed away, or still attached to anti-ALFA-tag peptide antibody were analysed with luminescence assay undiluted. The percentage of affinity-purified exosomes relative to all these four samples was plotted. (**A-D**) All experiments are n=1, N=1, except for D, which is n=4.

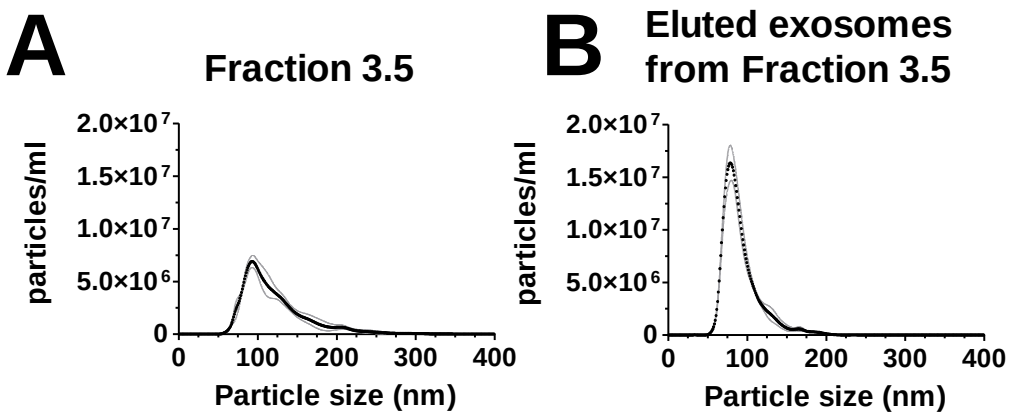

Figure 28. Representative analysis of HEK-293 affinity-purified exosomes relative to SEC-purified exosomes using NTA.

(**A-C**) The particle size of diluted samples and their relative abundance was determined using nanoparticle tracking analysis (NanoSight). (**A**) SEC-purified exosomes and (**B**) unbound particles were analysed with NTA three times each. The data is shown as mean (black line) ±SEM (grey lines). (**A-B**) The data represent n=1. The black line is the mean of three sample analyses. The grey lines show the standard error.

Sample	Particle mode diameter (nm)	Particle concentration (10^10/ml)	% of SEC-purified exosomes
SEC-purified exosomes	98	496	100
Affinity-purified exosomes	78	60	12

Table 7. Mode diameter, particle concentration, and efficacy of HEK-293 exosome elution from SEC-purified exosomes.

The data represent n=1 and are obtained from the plots in Figure 2. Particle mode size and concentration in the samples were measured with NTA.

Transmission electron microscopy images were obtained of both affinity-purified exosomes and the SEC-purified exosome sample (Figure 29, A). The SEC-purified exosomes had aggregated particles, proteins, and extracellular vesicles, all different sizes. However, affinity-purified exosome samples had mostly circular particles which are likely to be exosomes (Figure 29, A, white arrows). No classical “cup-shaped” exosomes were observed in these samples. Instead, round particles looked either intact or had one or more wedges. Nonetheless, affinity-purified exosomes had much fewer contaminants. The small dots on images of affinity-purified exosomes are likely to be ALFA peptides (Figure 29, A, blue arrow; Figure 30). No PEI was observed in these samples (Figure 29, A, and Figure 30). The diameter of round particles was manually determined using ImageJ. Particles of <50nm were excluded because intraluminal vesicles (later exosomes) are ≥50nm in diameter and exomeres are 30-50nm. This analysis supports NTA data. The particle size distribution in both samples was surprisingly similar except that the SEC-purified exosomes had >200nm particles unlike affinity-purified exosome sample (Figure 29, B).

Exosome elution was performed 24 times using SEC-purified exosomes from HEK-293 cells transfected with ALFA-tag sequence on four separate occasions. On average, 21.2% of exosomes were eluted according to luminescence data (±1.6% SEM). However, the particle concentration was too low in affinity-purified exosome samples to reliably quantify them with NTA. However, affinity-purified exosomes were imaged with electron microscopy to validate their morphology and purity. It was consistently observed that the exosome elution produces purer exosomes relative to the SEC-purified exosomes, and the size of round particles is smaller than particles in affinity-purified exosome samples (Figure 29, A). Data from DELFIA analysis showed that the CD63/CD81 ratio was ~28 times higher in affinity-purified exosome sample relative to the SEC-purified exosomes (Figure 31). At the same time, the total amount of CD63 in affinity-purified exosomes was 3.4 times smaller than in SEC-purified exosomes. CD9 was not detected in affinity-purified exosomes even when the sample volume was increased 10-fold for DELFIA.

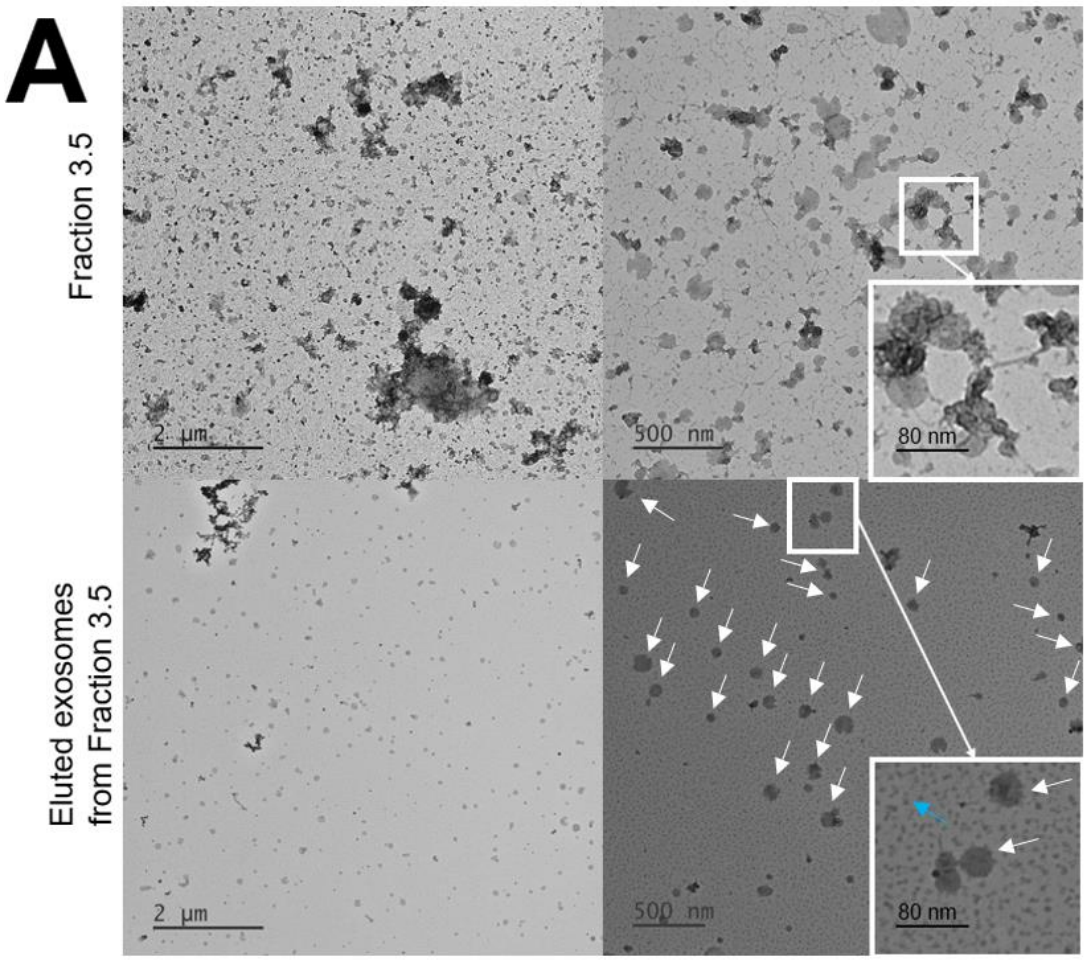
A
Fraction 3.5
Eluted exosomes from Fraction 3.5
2 µm
500 nm
80 nm
2 µm
500 nm
80 nm

B

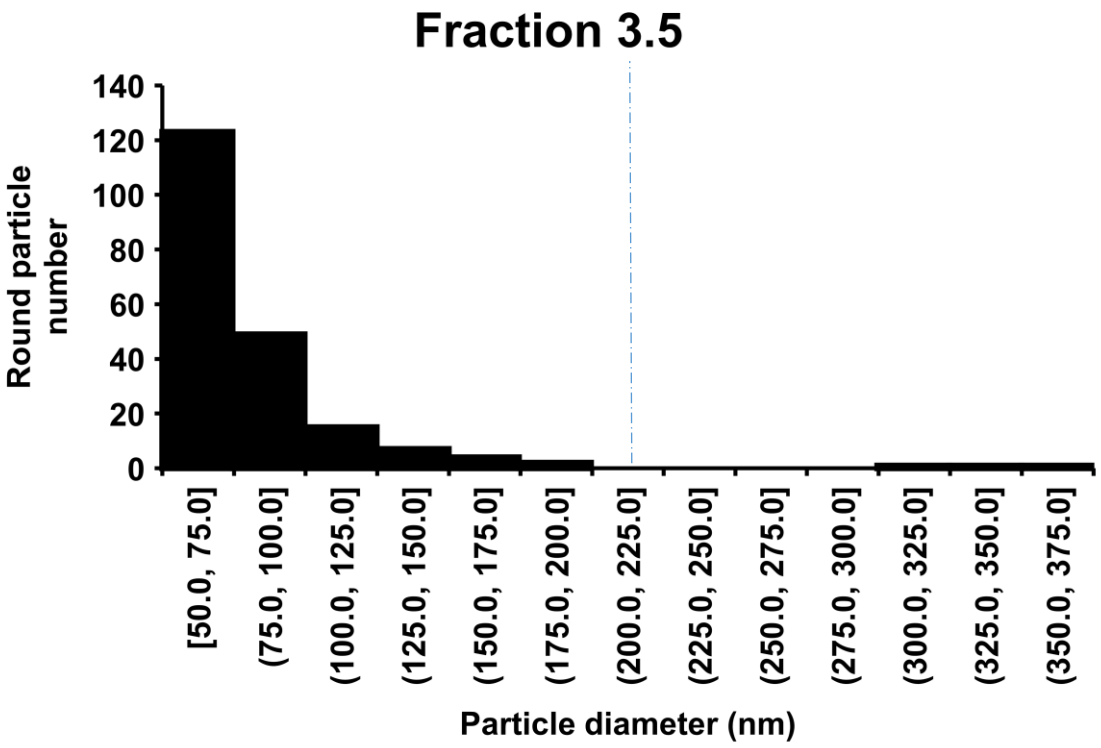
Fraction 3.5
Round particle number
140
120
100
80
60
40
20
0
[50.0, 75.0]
(75.0, 100.0]
(100.0, 125.0]
(125.0, 150.0]
(150.0, 175.0]
(175.0, 200.0]
(200.0, 225.0]
(225.0, 250.0]
(250.0, 275.0]
(275.0, 300.0]
(300.0, 325.0]
(325.0, 350.0]
(350.0, 375.0]
Particle diameter (nm)

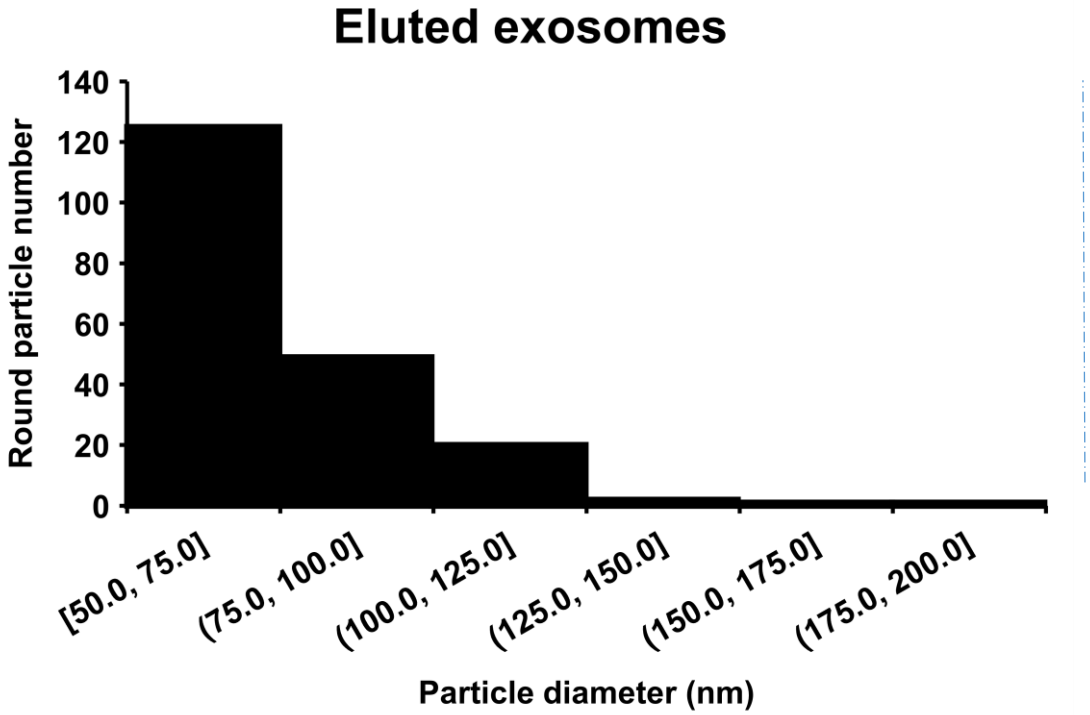
Eluted exosomes
Round particle number
140
120
100
80
60
40
20
0
[50.0, 75.0]
(75.0, 100.0]
(100.0, 125.0]
(125.0, 150.0]
(150.0, 175.0]
(175.0, 200.0]
Particle diameter (nm)

Figure 29. Representative TEM images of HEK-293 SEC-purified exosomes and affinity-purified exosomes and diameter of extracellular vesicles.

(**A**) Particles in SEC-purified exosomes and affinity-purified exosomes were negatively stained with uranyl acetate and imaged by transmission electron microscopy. White arrows indicate possible exosomes and blue arrows show ALFA peptide. Size bars as indicated. (**B**) The diameter of extracellular vesicles (>50nm only) was determined manually using Fiji software. The combined number of vesicles counted from n=4 is N=203 for SEC-purified exosomes, N=198 for affinity-purified exosomes. The dashed line helps comparison of two graphs.

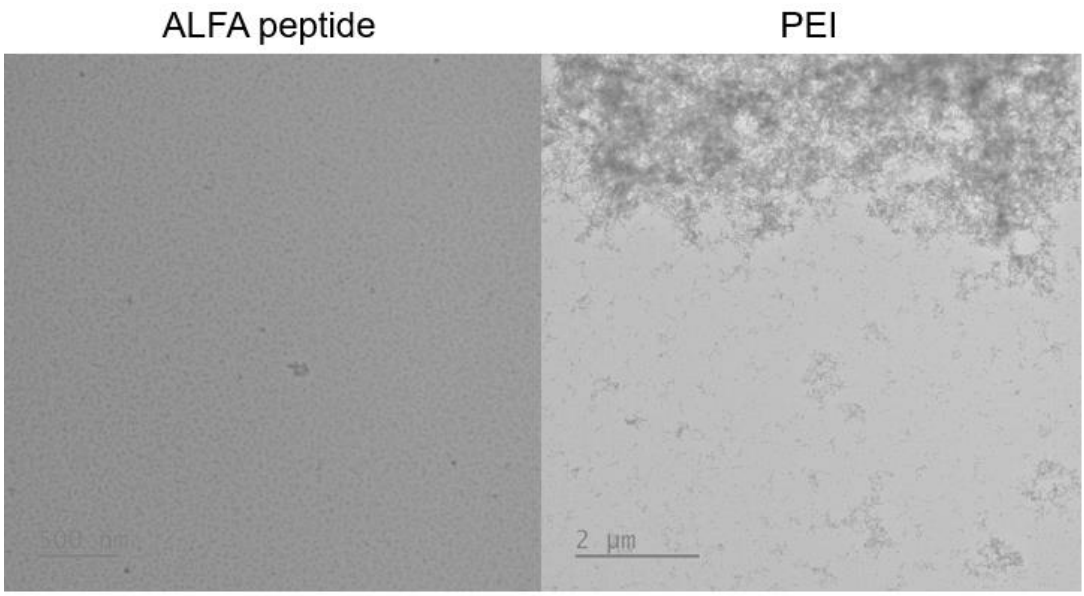

Figure 30. TEM images of ALFA peptide and PEI.

ALFA peptide (1mM) and PEI (1mg/ml) were negatively stained with uranyl acetate and imaged by transmission electron microscopy. Size bars as indicated.

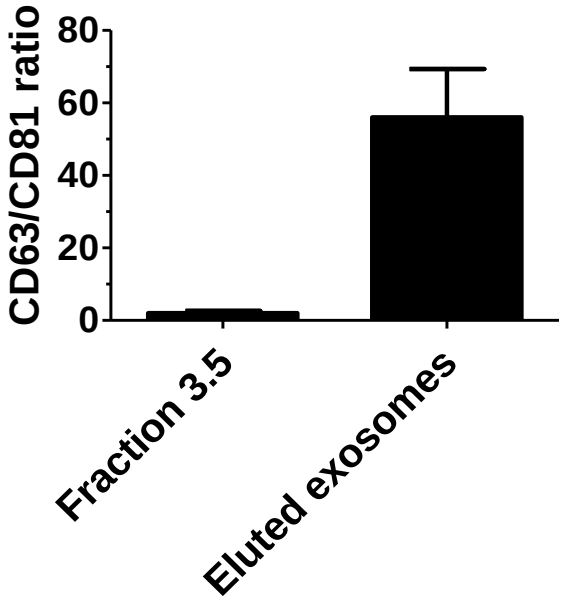

Figure 31. The ratio of exosome markers in HEK-293 affinity-purified exosome and relevant SEC-purified exosome samples.

SEC-purified exosomes from HEK-293 cell media and relevant affinity-purified exosomes was analysed by DELFIA. The fluorescence of the CD63 marker was divided by CD81 fluorescence. The data represent the mean of n=4 (affinity-purified exosomes) or n=6 (SEC-purified exosomes) with SD.

To remove contaminating ALFA peptide, affinity purified samples were concentrated using Vivaspin 2 columns. After that, it was not possible to detect any protein in these samples. Also, NTA analysis suggested that almost all particles were lost because there was no significant difference between water and filtered exosome samples (data not shown). Therefore, it was suspected that exosomes were lost during concentration.

Only one affinity-purified exosome sample was analysed by lipid assay. The sample and a respective SEC-purified exosome sample have 0.024µg/µl and 0.127µg/µl. Lipid/particle ratio for these samples were 0.039µg/10^9 particles and 0.026µg/10^9 particles.

Exosome elution from serum-rich media

Serum deprivation is known to affect cell health and therefore exosome quality and quantity. HEK-293 starts dying without serum within days. If cells express ALFA-tag constitutively, they could provide a continuous supply of exosomes in serum-rich media. Therefore, I wanted to investigate if ALFA-tagged exosomes could be obtained from cells in standard media with 10% serum. For that, HEK-293 cells were transiently transfected with ALFA-tag sequence as before and their SEC-purified exosomes were obtained. Then, SEC-purified exosomes were mixed with serum (1% or 10% final concentration). The exosome capturing, elution, and calculations were done using the same protocol as described above. However, the yield of exosomes was less than 1% (data not shown). When exosomes were incubated with anti-ALFA-tag antibodies for 24h instead of 1h, exosome recovery increased to >20% (Figure 32). Importantly, there was no significant difference between yield of exosomes obtained from serum-free media or media with 1% or 10% serum. Therefore, when MSCs are transfected to express ALFA-tag constitutively, MSC exosomes could be potentially obtained from cells grown in 10% FBS.

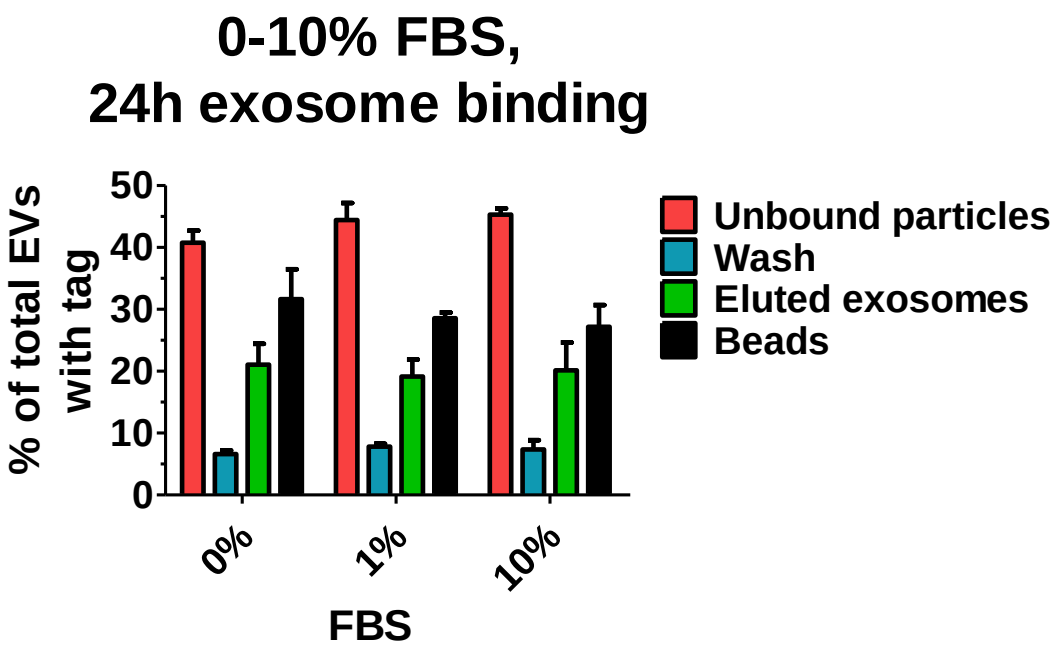

Figure 32. Prolonged elution of ALFA-tagged HEK-293 exosomes from cell media with FBS.

HEK-293 media with 0% FBS was used to prepare SEC-purified exosomes. Exosomes from HEK-293 cell media (2.8x10^10 particles) were mixed with FBS and/or PBS to get 0%, 1%, or 10% FBS in the sample. The samples were incubated with beads (6,000 particles of the SEC-purified exosome sample per bead) for 24h and eluted with 1mM ALFA peptide. All samples were diluted at 1:200 for luciferase assay. n=4, N=1.

Characterization of conditionally immortalized MSCs

After testing the protocol for exosome capture on HEK-293 cells, I wanted to transfect conditionally immortalised mesenchymal stem cells (MSCs) with ALFA-tag sequence (Anastassiadis *et al.*, 2010). These cells can divide continuously in the presence of dexamethasone and doxycycline (Dox/Dex) and differentiate after withdrawal of these two drugs. To confirm that, MSCs were seeded at around 1% density and allowed to grow for 10 days. One group of cells was grown with Dox/Dex present every day. The control group was not treated with these drugs until day 6. Microscope images confirmed that the Dox/Dex group had proliferated resulting in more cells (Figure 33, A). On day 9, the experiment had to be stopped since Dox/Dex cells reached 100+% confluency in the treatment group (Figure 33, A). Cells in both groups were counted with a flow cytometer (Figure 33, B). In the group with constant Dox/Dex treatment, cells proliferated most between days 4 and 9. Cells in the control group never increased in number since the day they were plated, possibly because they differentiated. These results show that MSCs proliferate continuously only in the presence of Dox/Dex.

Once the required quantity of MSCs is reached, Dox/Dex can be removed to stop their proliferation and cause their differentiation. To determine the earliest time when cells stop expressing large T antigen following Dox/Dex removal, proliferating MSCs that has been grown in Dox/Dex medium were plated with cell media containing Dox/Dex (day 0) and grown either in the presence or absence of Dox/Dex. T antigen was detectable by Western blot all days in the control group. Without Dox/Dex treatment, T antigen protein expression was lost by day 1 (Figure 34).

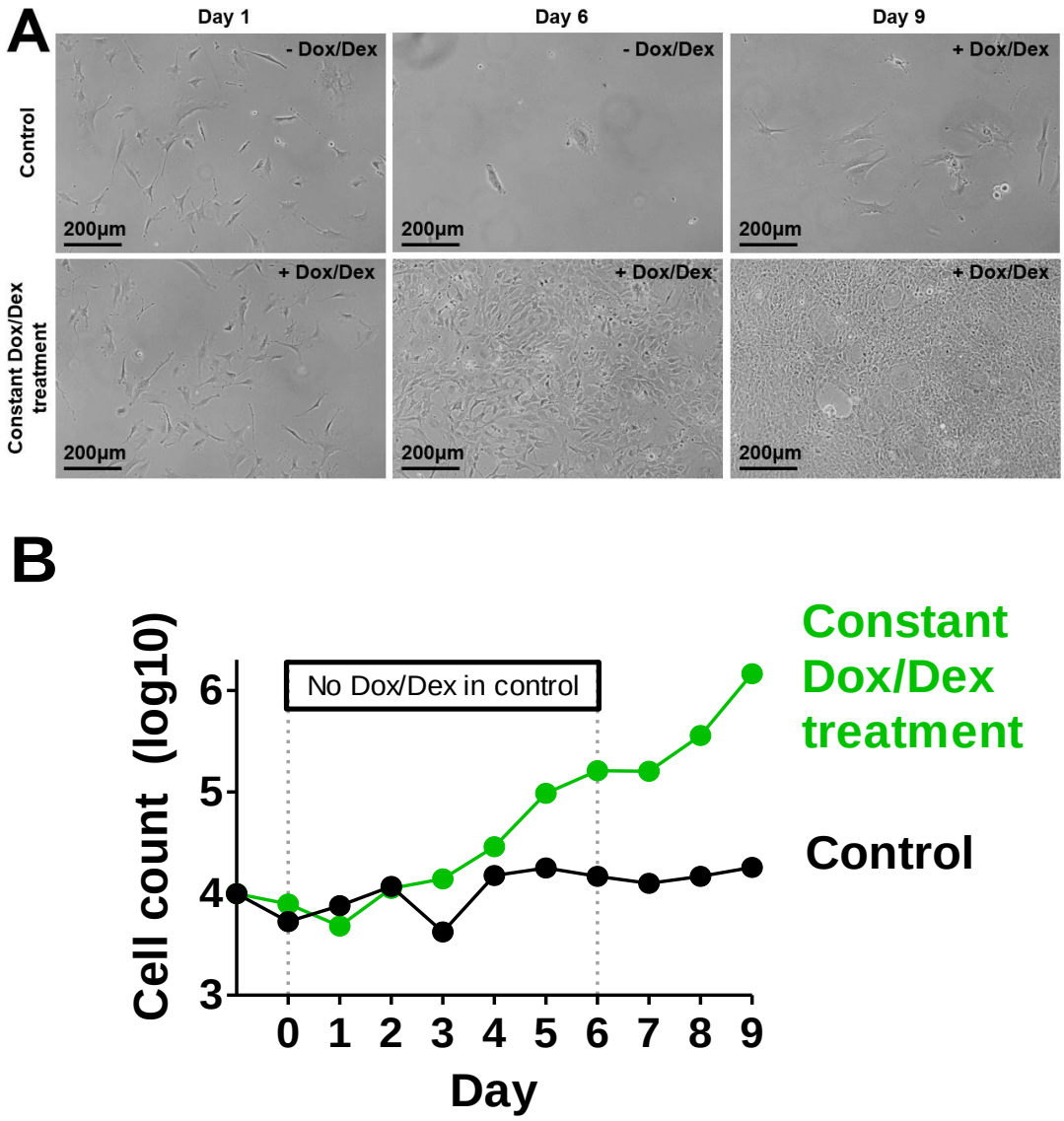

Figure 33. Growth of conditionally immortalised MSCs.

(**Day -1**) Conditionally immortalised mesenchymal stem cells were plated at a density of 10,000 cells per plate dish, which is 10cm2 in diameter. (**Day 0**) The next day, DMEM with FBS, dexamethasone (Dex), doxycycline (Dox), and penicillin/streptomycin were changed to the fresh one. Alternatively, the media of control cells was changed to DMEM with FBS and penicillin/streptomycin. Cell media was changed to the respective media on days 2 and 4. Starting from day 6, cell media was changed to DMEM with FBS, dexamethasone (Dex), doxycycline (Dox), and penicillin/streptomycin every day in both control and treatment groups. (**A**) Each day, cells were imaged with a brightfield microscope. (**B**) Live cell number was quantified with flow cytometry using propidium iodide for staining dead cells (n=1).

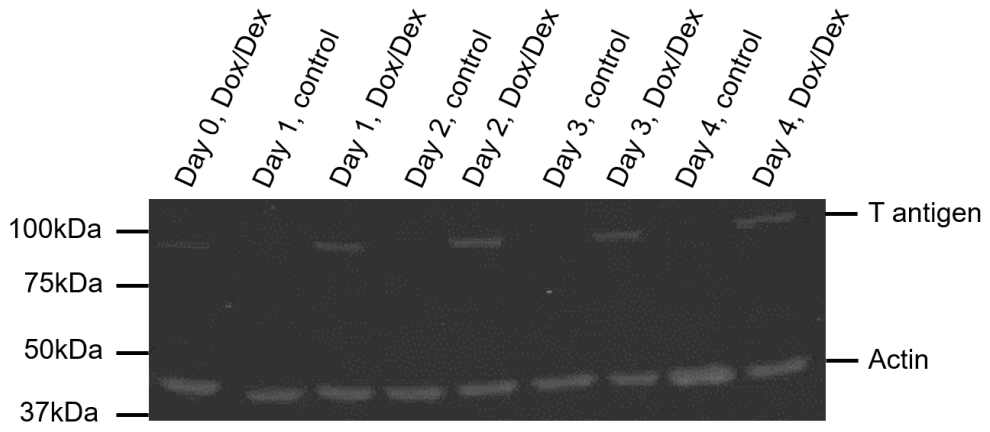

Figure 34. T antigen expression in conditionally immortalised MSCs in the presence of dexamethasone and doxycycline.

MSCs were plated with DMEM, 10% FBS, 1% penicillin/streptomycin with 10^{-7}M dexamethasone and 1µg/ml doxycycline. The next day (Day 0), cell media was refreshed with the same media (Dox/Dex group) or changed to the media without dexamethasone and doxycycline (control group). The media was changed daily for 4 days. Each day, cells were lysed and the presence of T antigen and actin was detected in these samples using Western blot. The blot was visualised with Odyssey software. n=1, N=1.

PGK-CD63-Nluc-ALFA plasmid for transfection of conditionally immortalized MSCs

CMV promoter in CMV-CD63-Nluc-ALFA plasmid drives the highest transgene expression in HEK-293 cells (Wen *et al.*, 2014). However, the PGK promoter performs better than the CMV promoter in MSCs (McGinley *et al.*, 2011). Therefore, the CMV promoter, CMV enhancer and T7 promoter were removed with restriction enzymes and replaced with the complimentary PGK promoter to generate PGK-CD63-Nluc-ALFA plasmid.

The protocol for electroporation of conditionally immortalized MSCs was optimised using a plasmid expressing a green fluorescent protein, enhanced GFP (Supplementary table 2). The electroporation of conditionally immortalized MSCs using 1 pulse of 1,300V and 40ms pulse width was the most optimal. Additionally, an appropriate concentration of G418 antibiotic selection reagent was selected for conditionally immortalized MSC (Supplementary Figure 7). It was determined that 300µg/ml G418 was the most suitable concentration, as it was for the research group who gifted us these cells (Anastassiadis *et al.*, 2010).

To stably transfect conditionally immortalized MSCs, they were electroporated with linearized PGK-CD63-Nluc-ALFA plasmid to generate ALFA-MSCs. G418 killed most of the cells by the end of the first week, but cells were growing successfully in their presence (data not shown). To confirm that the transfected ALFA-MSCs produce luminescent exosomes, luminescence assay was performed. PBS, non-transfected cells, and their media had similar luminescence (~300a.u.). ALFA-MSCs and their media had luminescence of 63,903a.u. and 13,090a.u., respectively. Therefore, MSCs were successfully transfected with the plasmid and the transgene was expressed.

Analysis of SEC fractions from transfected MSCs

To confirm that exosomes produced by the ALFA-MSCs were expressing luciferase, exosomes were purified from conditioned media using SEC. Particle numbers were found to peak within F3.0-4.0 range, although in one experiment the peak was quite broad (F2.5-4.0; Figure 35, A). The particle size, 82.9-113.8nm, was close to what was expected for exosomes, 50-100nm. The most particle-rich fraction from ALFA-MSCs had ~6 times fewer particles than the most particle-rich fraction from HEK-293 cells. Some SEC purified exosomes were further analysed to determine their particle size distribution. Most of the particles were ≥100nm (Figure 36).

The protein content was below the level of detection in the particle-rich fractions (Figure 35, B). However, the bulk protein could be easily detected elution from the SEC column in F5 onwards.

Fractions F3.0-4.0 had luminescence which was indicative of exosomes (Figure 35, C). Yet, exosome luminescence was almost five times lower than in protein-rich fractions.

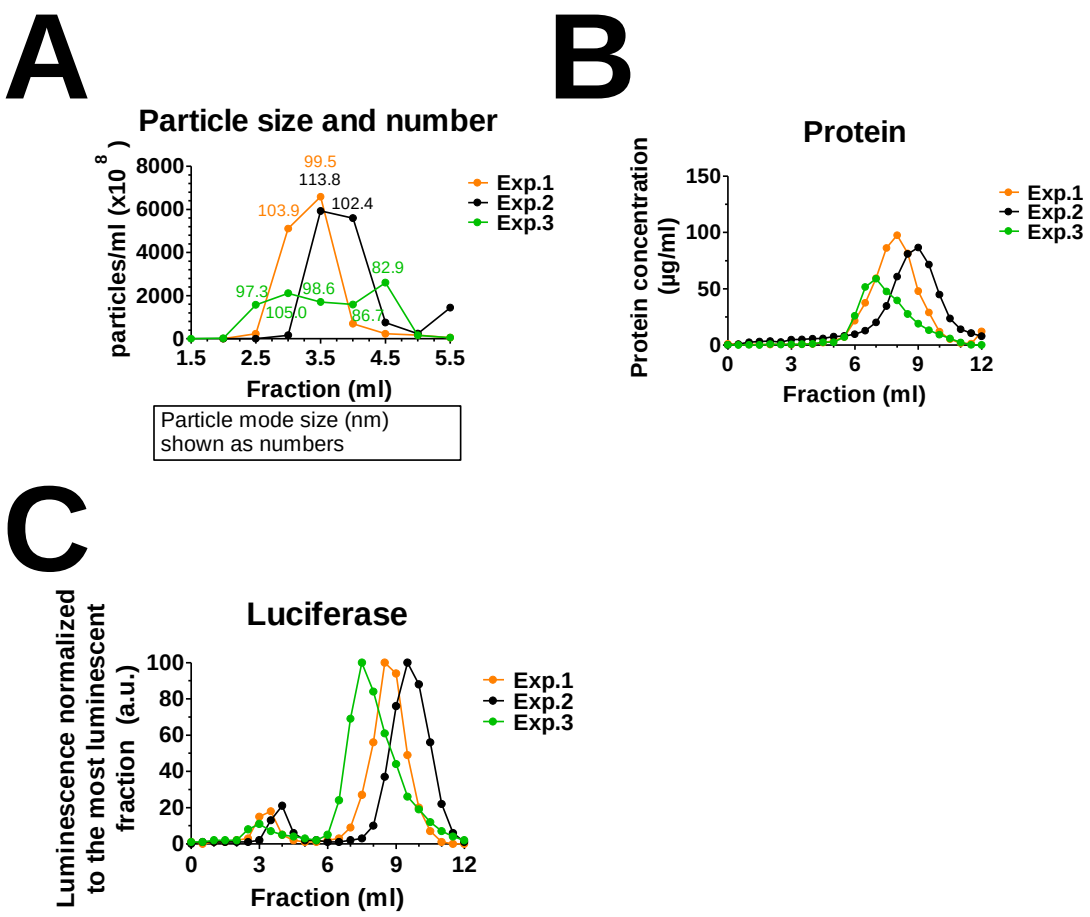

Figure 35. Analysis of ALFA-MSCs cell media fractions collected by SEC.

(**A, B, E**) SEC fractions from three independent SEC experiments were analysed. (**A**) The particle size of SEC fractions and their relative abundance was determined using nanoparticle tracking analysis (NanoSight). Particle mode size is written as a number near the respective data point. (**B**) Protein quantity was measured in the fractions (singlets) using a BCA assay. (**C**) Luciferase signal in the fractions was normalised to the most luminescent fraction within the experiment. All fractions were used undiluted.

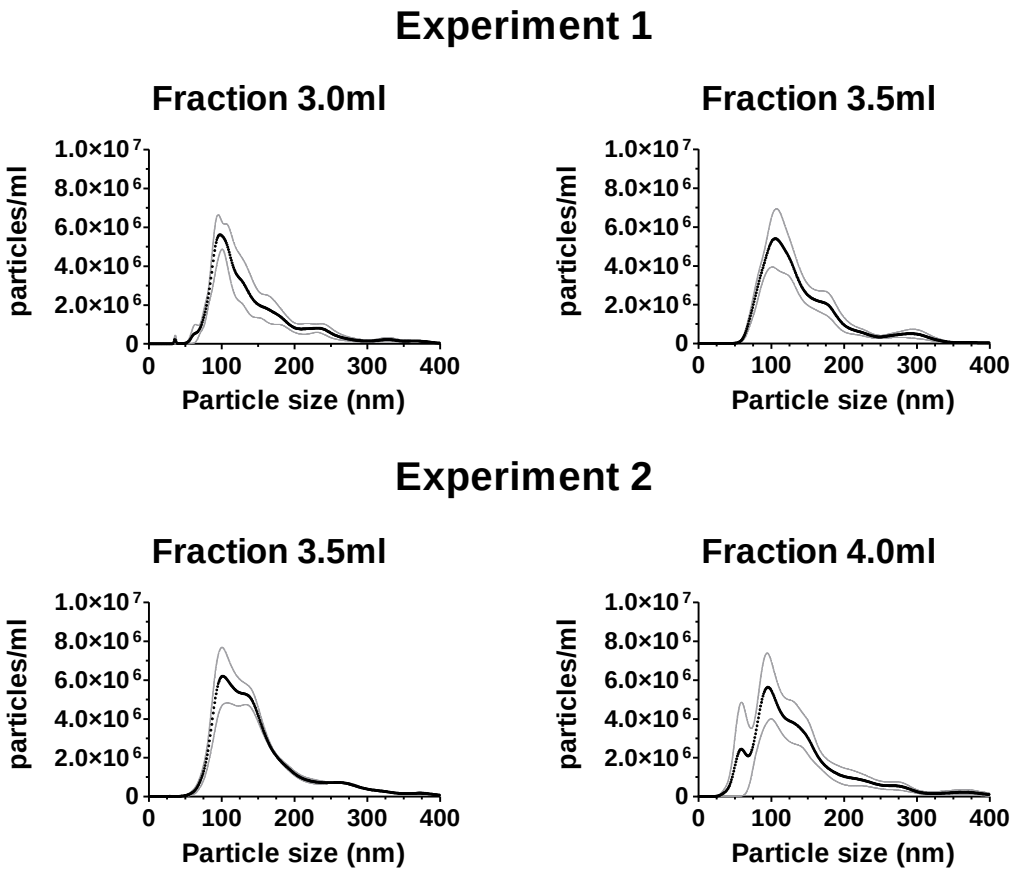

Figure 36. Particle size distribution of MSC SEC purified exosomes analysed using NTA.

The particle size of diluted samples and their relative abundance was determined using nanoparticle tracking analysis (NanoSight). SEC-purified exosomes were analysed with NTA four times each. The data is shown as Mean (black line) ±SEM (grey lines).

To determine the nature of particles, SEC purified exosomes were imaged using TEM. Exosome-sized and exosome-shaped particles were found (Figure 37). Yet, their quantity was low. Exosome-like particles seemed to have protein corona, which is surprising considering that exosomes were collected from serum-free MSC conditioned media. Protein was abundant in the samples (irregularly shaped particles). Large aggregates seen at 1µm could be PBS salts.

The presence of exosome and lipoprotein markers was checked in some SEC purified exosomes using DELFIA. All of them had CD63 present (Figure 38). CD63 was the most prevalent in SEC purified samples from Experiment 3 and was the second most prevalent marker in the other two experiments. CD9 and CD81 were detected in some fractions. ApoB signal was lower than signal from exosome-specific markers.

To compare ALFA-MSC SEC purified exosomes to HEK-293 SEC purified exosomes, a ratio between three exosome markers was found for these samples. CD63 and CD81 levels were similar and CD9 content was the lowest in ALFA-MSC SEC purified exosomes (Figure 39, B). CD63 fluorescence to particle ratio for ALFA-MSC SEC purified exosomes was 0.1-0.4a.u./10^7 particles, which is 10-40 times less than the same value for HEK-293 SEC purified exosomes.

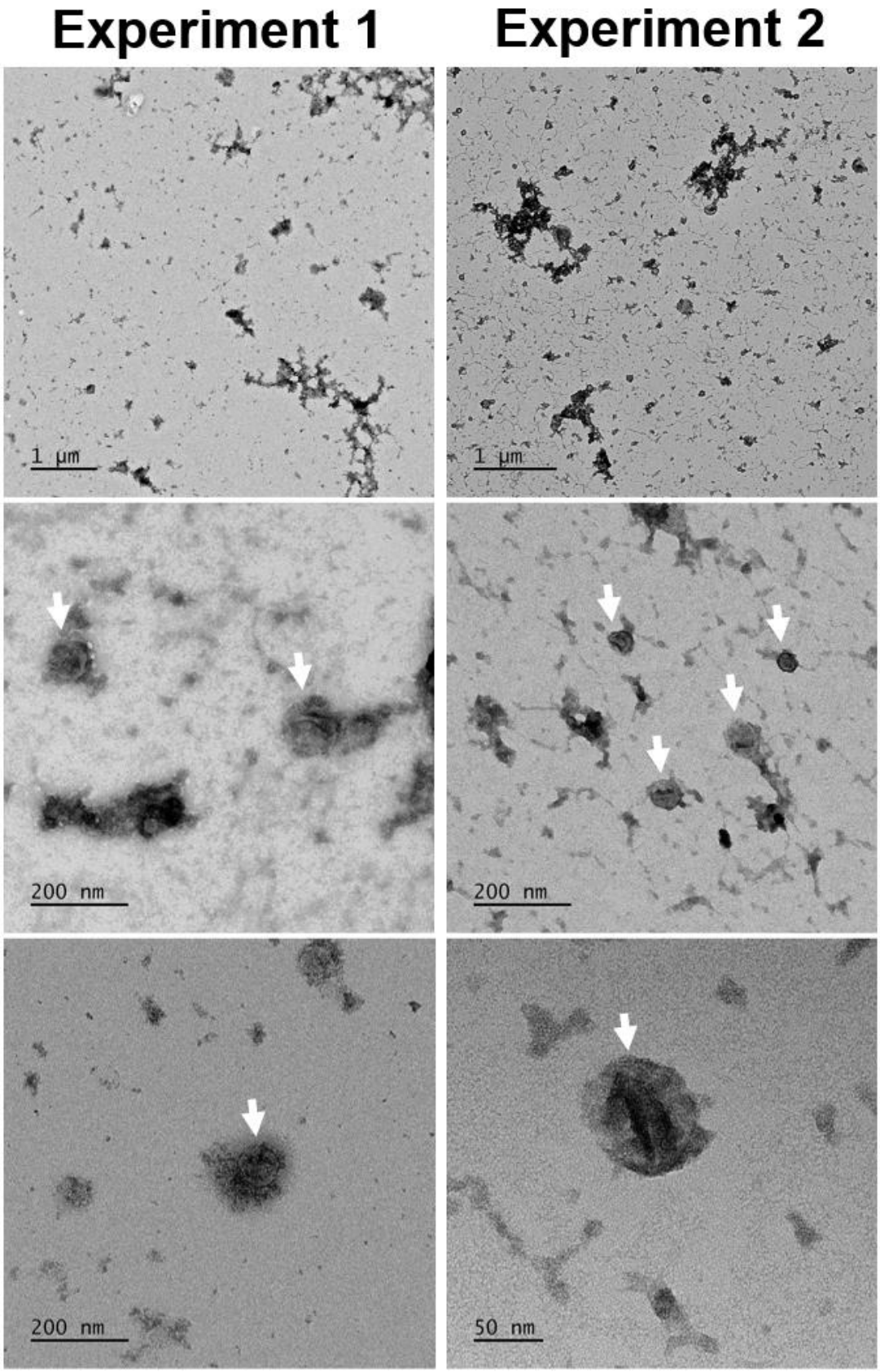
Experiment 1
Experiment 2
1 µm
1 µm
200 nm
200 nm
200 nm
50 nm

Figure 37. Representative TEM images of ALFA-MSC SEC-purified exosomes.

Particles in SEC-purified exosomes were negatively stained with uranyl acetate and imaged by transmission electron microscopy. Particles resembling exosomes are shown with arrows. Size bars as indicated.

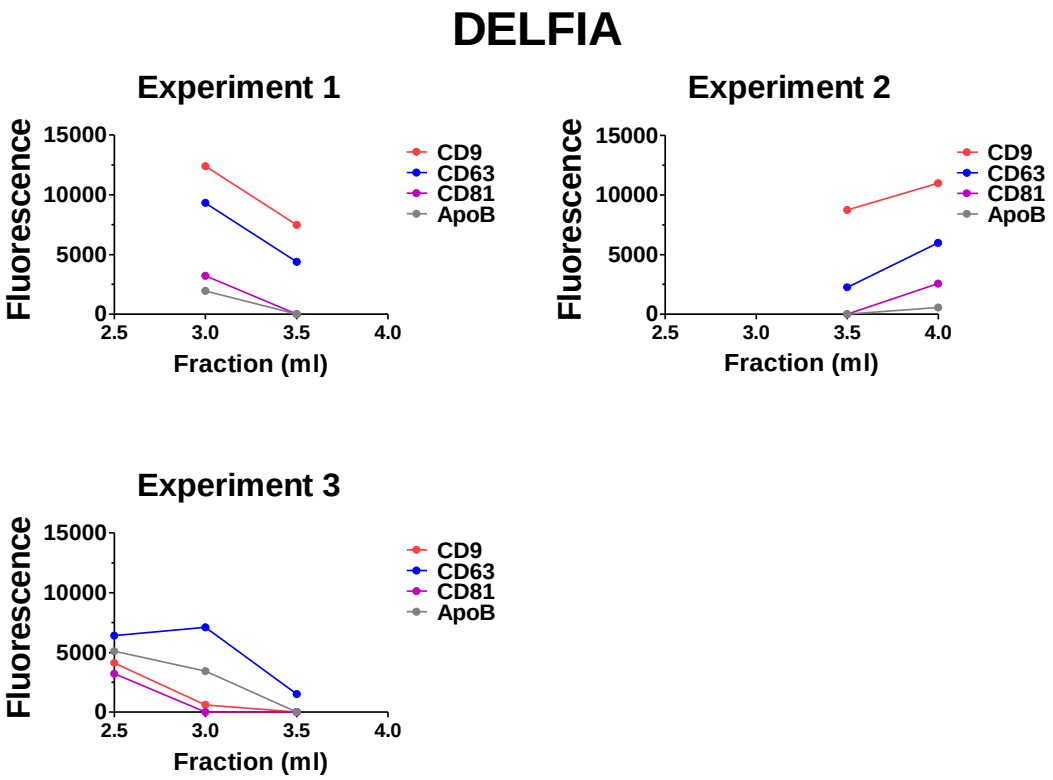

Figure 38. Exosome markers in ALFA-MSC SEC purified exosomes.

The presence of CD9, CD63, and CD81 exosome-associated markers was checked in SEC purified exosomes using DELFIA. Each sample was used in a single well. Negative values were changed to zero.

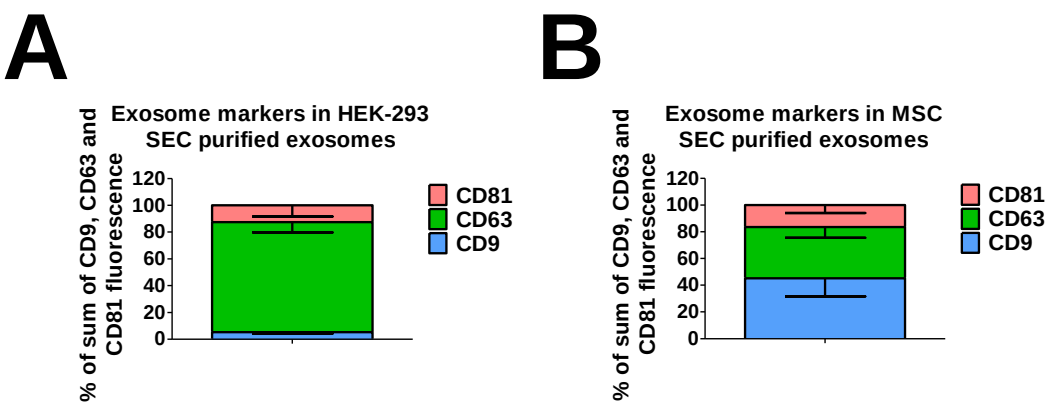

Figure 39. Exosome markers in SEC-purified exosomes.

SEC purified exosomes from (**A**) HEK-293 and (**B**) **ALFA-**MSC cell media was analysed by DELFIA. Fluorescence from each marker was divided by the sum of fluorescence from all three markers, CD9, CD63, and CD81. The data represent the mean of (**A**) n=6 and (**B**) n=3 with SD.

Discussion

Summary of the results

In this chapter, a novel method of affinity exosome purification has been developed. For this, HEK-293 cells were transiently transfected with a CMV-CD63-Nluc-ALFA plasmid encoding for CD63, NanoLuc, and ALFA tag. SEC purified exosomes were obtained and characterized. These exosomes were used to obtain affinity-purified exosomes. The latter were purer than the SEC purified exosomes. Also, conditionally immortalized MSCs were transfected with PGK-CD63-Nluc-ALFA plasmid. SEC purified exosomes were characterized by all methods except for lipid assay.

Affinity purification of exosomes

Bioactive molecules co-isolated with exosomes make interpretation of data in exosome studies challenging. Affinity purification of exosomes can produce pure exosomes, albeit unsuitable for *in vitro* and *in vivo* studies and in small quantities. Therefore, we designed a protocol of exosome affinity purification which would circumvent those issues. The protocol presented in this chapter allows exosome capture by ALFA tag. This necessitates introduction of the relevant transgene in the target cell. The conditioned media needs to be concentrated to allow efficient mixing of exosomes with beads covered in nanobodies. Since cell and beads number can be increased, the quantity of affinity purified exosomes could be scaled up.

What makes our method unique is that exosomes can be eluted from the capture nanobodies. Other methods require the use of harsh chemicals. For example, exosome subset purification can be purified with a novel ExoDIF device. This device has two layers, each with different patterns (Kang *et al.*, 2017). These layers form bridges and curved walls, which expand and shrink. This design promotes fluidic whirling and binding of extracellular vesicles by an anti-CD63 antibody. The antibody is immobilised in ExoDIF device with 3,3'-dithiobis (sulfosuccinimidyl propionate), or DTSSP. Once exosomes are bound and the contaminants are washed away, the disulphide bond in DTSSP can be cleaved by a reducing agent dithiothreitol (DTT). However, DTT can damage exosomes.

New methods of exosome affinity purification, such as EV-CATCHER assay, allow their collection with chemicals which do not damage exosomes. This assay requires streptavidin-coated 96 well plates (Mitchell *et al.*, 2021). Uracilated DNA linker with biotin is added to wells where it binds to streptavidin. DNA linker has azide on another end which binds dibenzocyclooctyne-N-hydroxysuccinimidyl ester attached to an antibody of choice. After exosomes in conditioned media bind to the antibody, all other particles can be washed away. The linker can be then degraded by uracil-glycosylate. However, the antibody will remain attached to the extracellular vesicle, as it does when exosomes are eluted from ExoDIF device. Due to the large size of the antibody (~150kDa) relative to the vesicle, it may impact exosome function in *in vitro* and *in vivo* studies. ALFA-tagged exosomes have a smaller tag attached to them (34kDa), so the effect on exosome function would be minimized. The developers of the ALFA tag did not observe that the tag affected protein function in their pilot studies, but this must be confirmed in the future studies.

It is currently not feasible to determine if the ALFA tag affects exosome function. However, it is still possible to evaluate the effect of ALFA tagged exosomes in the models of myocardial infarction to answer the question if they possess cardioprotective properties. Additionally, it is possible to investigate if the introduction of the ALFA tag sequence into the cell genome affects exosome production. For example, exosome quantities from transfected and non-transfected cells can be compared. GW4869, a potent neutral sphingomyelinases inhibitor, can be used as a control, because it inhibits the production of ILVs and, therefore, exosomes. These studies would help to understand if our method can yield functional exosomes, unlike other affinity purification methods.

HEK-293 SEC-purified exosomes

ALFA tag purification of exosomes is hoped to be suitable for isolation of functional exosomes. Therefore, it has been compared to exosome purification by SEC. SEC allows the collection of functional exosomes purified from most of the free protein and lipid, as it was confirmed by my data. There are many advantages that SEC offers. For example, it allows separation of molecules larger and smaller than a pore size (i.e., in two groups) with a minimal volume of eluate, so that exosomes can be concentrated. Moreover, SEC preserves the biological activity of particles as it is a gentler way of particle separation compared to methods which involve centrifugal force or chemical treatment. There is a minimal sample loss as solutes do not interact with the stationary phase.

Yet, unlike affinity purification, SEC purification of exosomes produced exosomes of low purity in my study. This was confirmed by the fact that my SEC-purified exosome samples had 3.4 protein/lipid ratio. Exosomes have lipid membrane, and it is expected that their lipid content is higher than protein amount. Osteikoetxea and colleagues, who obtained exosomes by methods based on density and size separation, suggested that the protein/lipid ratio of exosomes should be ~0.25 (Osteikoetxea *et al.*, 2015). Another indicator of contaminating protein in SEC purified exosomes is particle/protein ratio (Webber and Clayton, 2013). HEK-293 SEC purified exosomes cells had a low ratio, i.e., were of low purity, and therefore had protein contaminants.

Apart from protein, SEC purified exosomes could be contaminated with lipoprotein. Since I did not detect lipoprotein using an anti-ApoB antibody, it may be possible that lipoprotein contamination was low. Lipoprotein is abundant in serum whereas HEK-293 cells were grown in serum-free conditions prior exosome collection. Previous studies indicated that SEC does not remove lipoprotein from serum-containing conditioned cell media (Takov, Yellon and Davidson, 2019). Therefore, lipoprotein traces could be found in SEC purified exosomes if e.g., larger sample quantity was tested.

Fortunately, SEC purified exosomes had high enough number of particles to analyse them by several methods, so that they could be compared to affinity purified exosomes. Interestingly, SEC purified exosomes had the highest CD63 content compared to other markers. HEK-293 cells could naturally produce a high level of CD63 exosomes, which could be easily determined using untransfected HEK-293 media in DELFIA. Alternatively, HEK-293 were overexpressing CD63 because of the transfection. After all, HEK-293 cells naturally encode CD63 and then they got transfected with CD63-containing construct. Could it be that ALFA-tagged exosomes have higher CD63 content? Exosomes are naturally enriched in tetraspanins and associated proteins (~45% of exosome proteome) (Perez-Hernandez *et al.*, 2013). Changes in tetraspanin composition and concentration can affect the composition of tetraspanin-associated proteins and, consequently, exosome function. It would be interesting to compare CD63 level of SEC purified exosomes from transfected and non-transfected HEK-293 cells.

In summary, HEK-293 SEC purified exosomes had high quantity of contaminants present, i.e., protein. These samples were enriched in exosome marker, CD63.

Protocol for affinity purification of exosomes

ALFA tag elution protocol was originally developed to elute proteins (Götzke *et al.*, 2019). We, however, optimized this protocol for exosome elution using conditioned media from HEK-293 cells. ALFA peptide concentration was increased ten-fold, compared to the concentration used by Götzke *et al*., to achieve >3-fold increase in yield of eluted exosomes. Moreover, exosome elution time was decreased from 20mins to 10mins. This could make possible exosome elution quicker.

Additionally, I investigated what bead concentration would be suitable for exosome elution. The percentage of affinity-purified exosomes increased with a higher particle quantity number. However, this relationship was not linear, e.g., extra ~25% affinity-purified exosomes could be obtained if the number of SEC-purified exosomes was increased by 70%. This means that a higher proportion of exosomes would be captured if SEC-purified exosomes are diluted. Therefore, it was not obvious which particle/bead ratio was best. If to assume that the surface area of an average exosome is ~4000nm^2, one bead (Dynabeads) could bind 6,000 exosomes. This ratio was therefore chosen for exosome affinity purification.

Importantly, our affinity purification can allow purification of exosomes from serum rich conditioned media if conditioned media is incubated with nanobody-covered beads for longer. A longer elution than 1h for 10% FBS concentrated media was probably required because serum contains many particles, such as lipoprotein and protein, which preclude ALFA-tagged exosomes binding anti-ALFA nanobody. Only 1h and 24h elution was tested, so potentially the duration of elution could be reduced. Nonetheless, affinity purification of exosomes from serum-rich media is possible. Since our method relies on capture of ALFA tag, it is expected that serum EVs are not eluted with tagged exosomes. However, serum EVs is expected to be in wash and unbound fractions as SEC, a step before elution, does not separate exosomes based on their origin.

The reason why I tested if exosome affinity purification is possible from serum rich media is because we wanted to obtain MSC exosomes. MSCs are typically grown in serum-rich media. However, a question remains though if serum is necessary for exosome collection. Without serum, the quality and quantity of exosomes may be negatively affected. On the other side, serum from different batches, i.e., collected from different calves and at different times, may have a different effect on cells. These effects can be observed as changes in cell growth rate, morphology, viability, and responses to physiological stimuli (Pirkmajer and Chibalin, 2011; Barosova *et al.*, 2021). An alternative to serum, defined media, could be used. For example, MSCs can be grown in serum free media which has nutritional and hormonal formulations. Yet, it is not clear what the role of media components, serum included, is on maintaining MSCs regenerative and immunomodulatory properties (i.e., crucial MSC characteristics). Therefore, various media batches would have to be compared. Also, it is not known in what media MSCs have the physiologically relevant phenotype. Therefore, it may be premature to exclude serum from MSC culture (Sharma *et al.*, 2014).

Irrespective of whether conditioned media contains serum or not, the yield of exosomes is the same. The final protocol allowed the collection of 21.2±1.6% (SEM) affinity eluted exosomes, according to luminescence data. However, there is a potential to increase exosome yield by increasing duration and the number of elution steps. Additionally, the protocol could be improved by introduction of an additional step. Specifically, affinity purified exosomes should be removed from ALFA peptide to ensure correct characterization of these vesicles. For this, Sepharose CL-2B could be used to make a 0.5ml SEC column. In summary, the affinity purification protocol has been established for exosome elution using conditioned cell media from HEK-293 cells. The protocol allows exosome purification from media with and without serum. The yield of exosomes was improved by modifying steps of the protocol.

HEK-293 affinity-purified exosomes

HEK-293 affinity-purified exosomes were found to be purer than SEC-purified exosomes by various methods. Particle size distribution detected with NTA was narrower and 90+% particles were of 50-100nm size. There is no consensus on what size exosomes are. Various papers claim that the minimum and maximum sizes of exosomes are between 30-50nm and 100-150nm, respectively. It is known that extracellular vesicles cannot be physically smaller than 30nm (Huang *et al.*, 2017). However, exomeres, which are small extracellular vesicles, have a size <50nm. Therefore, particles of <50nm size were not considered to be exosomes in my study. Intraluminal vesicles in mature endosomes, which later become exosomes, are ~50-100nm. Therefore, I had higher confidence in that 50-100nm particles were exosomes. Particles of ≥100nm size in affinity eluted exosome samples could be microvesicles that had CD63.

TEM imaging also confirmed that HEK-293 affinity-purified exosome samples were purer. Their size distribution supported NTA findings that affinity purified exosomes are of smaller size. Yet, exosomes could be ruptured or shrunk by negative staining due to dehydration and this alters their size (Dragovic et al., 2011). Also, only a small number of particles can be measured compared to NTA, and this measurement is subjective. After all, it is challenging to distinguish extracellular vesicles from the same-sized particles such as lipoprotein in a negative stain of TEM (Veerman *et al.*, 2021). Extracellular vesicles usually appear cup-shaped due to the dehydration process of sample preparation for TEM, but not always (Jung and Mun, 2018; Malenica *et al.*, 2021). Therefore, if extracellular vesicles should be distinguished from lipoprotein, it is better to use cryo-TEM, which allows identification of double membrane of extracellular vesicles and single membrane of lipoproteins. Alternatively, exosomes can be imaged on TEM after being incubated with immunogold-labelled antibodies against CD63.

DELFIA results revealed that affinity purified exosomes were enriched in CD63, as expected. Even though CD63 can be found on microvesicles as well, NTA data suggest that ~90% affinity-purified particles are <100nm, which are smaller than microvesicles. Therefore, affinity purified exosomes are at least 90% pure.

Because affinity purified exosomes had low particle number, only one sample of affinity purified exosomes was successfully analysed with the lipid assay. The lipid content of affinity-purified exosomes decreased 5.3 folds relative to SEC-purified exosomes. Lipoproteins, microvesicles, and other lipid-containing particles were potentially lost due to exosome affinity purification. Lipid/particle ratio, however, was increased in affinity-purified exosomes by 1.5 times. This suggests that the percentage of lipid-containing particles relative to total particle number was increased. Since nanobodies captured CD63, it means that lipid assay data indicates that affinity-purified exosome samples had purer exosomes than the respective SEC-purified exosome sample. Yet, this data should be confirmed.

In summary, affinity purification of exosomes allows collection of exosome subset. These exosomes are purer than exosomes obtained with SEC.

Conditionally immortalized MSCs

In this study, conditionally immortalized BM MSCs were used for exosome purification (Anastassiadis *et al.*, 2010). I confirmed that these MSCs require dexamethasone and doxycycline for proliferation because they activate T antigen. It was also determined than T antigen protein expression is abolished within 24h after withdrawal of these drugs. Therefore, MSCs could stop proliferation within 1-2 days and then start to differentiate. It would be beneficial to determine how long does it takes for these MSCs to differentiate using dyes for osteoblast, adipocytes, and chondrocytes, the three cell types MSCs differentiate into. Moreover, it is worth to investigate if the introduction of TET-ON transcriptional regulation system alters biology of MSCs and their EVs. The creators of this MSC line introduced TET-ON system to embryonic stem cells and then induced T antigen expression (Anastassiadis *et al.*, 2010). They reported that 32 and 92 genes were upregulated and downregulated >1.5 fold compared to the original embryonic cell line. However, all altered genes returned toward the normal level after T antigen expression was stopped. The authors did not report similar findings about their MSC cell line. If the authors do not have original MSCs, then it is not possible to compare them to the conditionally immortalized MSCs. Therefore, it may be necessary to repeat transfection of other BM MSCs, determine changes in gene expression and compare exosome functionality in an assay of myocardial infarction, such as mPTP or hypoxia/reoxygenation assays, and endothelial tube formation.

I did not analyse conditionally immortalized MSCs with flow cytometry. However, the creators of this cell line did that (Anastassiadis *et al.*, 2010). Interestingly, they did not confirm the presence of MSC-specific markers, CD73, CD90, and CD105 according to the minimal criteria of the International Society for Cellular Therapy (Dominici *et al.*, 2006). Without publishing justification, the authors claimed that their BM MSCs express CD9, CD44, CD49e, CD140b, and Sca-1. Moreover, Anastassiadis *et al*. confirmed the absence of only two markers, CD34 and CD45, among six markers that Dominici *et al.* suggested that MSCs should not have. It is unclear why the authors chose alternative markers to check. However, it is important to note that the minimal criteria for MSC characterisation are based upon human BM MSCs (Dominici *et al.*, 2006). The assumption that MSCs from all species and tissues share the same phenotype is unlikely. Numerous papers report that MSCs derived from different tissues, various culture mediums, donors, or species, have differences in their marker expression. For example, mouse BM MSCs have different cell marker expressions compared to human BM MSCs, frequently missing two of the three “MSC markers” (Wright, Arthaud-Day and Weiss, 2021). Also, the minimal criteria propose that 95% of MSCs should be positive for CD73, CD90, and CD105. Again, MSCs derived from various donors, species, using various methods, are unlikely to be positive for the entire marker panel. This percentage has not been justified by the International Society for Cellular Therapy. Finally, there are no standardized methods for MSC isolation and culture, which precludes the improvement of MSC characterization guidelines. This all adds another layer of complexity and uncertainty to already challenging attempt to isolate, characterize and determine functions of MSC exosomes.

In summary, conditionally immortalized MSCs we obtained behaved in the cell culture as previously reported (Anastassiadis *et al.*, 2010). However, the MSC markers were not analysed.

Affinity purified exosomes from conditionally immortalized ALFA-MSCs

PGK-CD63-Nluc-ALFA plasmid for conditionally immortalized MSC transfection was created successfully, as confirmed with sequencing. Exosomes from transfected ALFA-MSCs were luminescent, indicating successful transfection. Due to the time constraints, SEC purification of ALFA-MSC exosomes was done three times. The particle concentration of SEC purified exosomes was low enough to analyse them more thoroughly or characterize affinity eluted exosomes. The confluency of HEK-293 and ALFA-MSCs before exosome collection was comparable. Could it be that HEK-293 secrete more exosomes than ALFA-MSCs? To investigate that, the exosome quantity from the same number of HEK-293 and ALFA-MSCs cells could be compared.

I found that luminescence of ALFA-MSC SEC purified exosomes was five times smaller than in protein SEC fractions. This is the opposite of what was observed with HEK-293 SEC purified exosomes. It may be possible that ALFA tag is not incorporated into exosomes efficiently. This could have occurred if the transgene is silenced. To investigate that, cells can be treated with DNA methyltransferase and histone deacetylase inhibitors such as 5-aza-c and Trichostatin A (TSA), respectively. If luminescence would increase in the presence of inhibitors, then silencing was an issue. In rat MSCs, however, PGK promoter was reported to be not subjected to DNA methyltransferase and histone deacetylase (McGinley *et al.*, 2011). If the same is the case with our mouse ALFA-MSCs, maybe the promoter or the transgene got mutated. In this case, the ALFA-MSC genome can be sequenced. If the promoter and transgene have the correct sequence, maybe PGK is a weak promoter for mouse ALFA-MSCs. However, it would be still expected that exosomes should have higher tag concentration than protein-rich SEC fractions. It might be possible that CD63 is not incorporated into exosomes efficiently and/or instead is targeted for degradation. Finally, ALFA-MSC exosomes may be enriched in other markers that are more abundant than CD63. If so, those markers can be tagged.

In summary, conditionally immortalized MSCs were transfected to produce ALFA-tagged luminescent exosomes. Further studies should be performed to understand how to improve tag incorporation into ALFA-MSC exosomes.

Luminescence assay

Luminescence assay was essential for confirming the success of cell transfection and exosome affinity purification. Here, I showed that luminescence assay is very time-sensitive and depends on sample dilution. It is important to analyse luminescent samples as soon as possible. Additionally, luminescent signal increases with concentration, then decreases and disappears. This suboptimal luminescent signal can be caused by insufficient concentration of Furimazine, NanoLuc substrate. Additionally, luminescence quenching, i.e., reduction of luminescence intensity, could have occurred. Quenching occurs if the total absorbance of the solution is greater than 0.1a.u. (inner filter effect) (Omary and Patterson, 2017). Ideally, the absorbance of the sample should be ≤0.05a.u. to achieve deviations from linearity of ≤6% (Zwinkels, DeRose and Leland, 2014). I recommend that the most particle rich SEC fraction should be diluted so that its optimal luminescence is as high as possible. Then, all other SEC fractions and relevant affinity-purified exosomes are diluted to the same extent.

Limitations and further studies

I developed a method which purifies exosomes better than SEC and found MSCs which could be used to collect potentially high quantities of tagged exosomes. However, several challenges should be overcome in the future. In particular, the yield of affinity-eluted ALFA-MSC exosomes should be increased. One way to achieve that is to increase cell number. For example, Vertical-Wheel™ bioreactors can be used for growing MSCs. The manufacturer, PBS Biotech, has developed an improved method of axial and radial fluid flow using Vertical-Wheel™ impeller. This method minimizes shear stress while creating homogenous environment for MSCs (Croughan *et al.*, 2016). Since I showed that exosomes can be purified from serum-rich fraction, exosomes could be collected daily from ALFA-MSCs grown in serum-supplemented media. Potentially, tangential flow filtration (TFF) can be used to concentrate the media. This method could be performed with little input from the user. In my study, the media (6xT225 flasks) filtration process would take ~5h before SEC could be performed. If I wanted to process more media, I would require additional centrifuges, more non-reusable filters and SEC columns, which is expensive and likely to require an assistant. If I used TFF instead, it would be cheaper because this method requires pumps and reusable filters.

Once the yield of affinity-purified exosomes from ALFA-MSCs is improved, affinity purified exosomes could be used in various models of myocardial infarction to determine if they have cardioprotective effect. Since assays which mimic myocardial infarction were not successful in my study, it may be necessary to develop an alternative method, or to assess them *in vivo*. However, there is a possibility that affinity purified exosomes may be not cardioprotective. It can be due to their tag or removal of many cardioprotective proteins. The creators of the ALFA tag did preliminary studies and observed no effect of the tag on protein function (Götzke *et al.*, 2019). This is not possible to evaluate in exosomes currently since it would require untagged exosomes of the same purity as affinity purified exosomes. Therefore, if affinity purified exosomes are found not to be cardioprotective, it would be challenging to find an explanation.

Nonetheless, our method of exosome purification can improve methods of exosome characterization. For example, lipid/protein and protein/particle ratios of affinity-purified exosomes could be used as an improved standard of highly pure exosomes. Moreover, the protein and RNA content of affinity-purified exosomes can be studied with proteomics and transcriptomics, respectively. SEC purified exosomes from untransfected and transfected cells could compare to determine if transfection affects the protein and RNA content of exosomes. If there is no significant difference, our affinity purification method could be used to study protein and RNA content of exosomes positive for various markers and, possibly, allow elucidation of the exosome role *in vivo*.

One of limitations of tagging exosomes with luminescent molecule is that this method does not offer high sensitivity or absolute quantification of the luminescence. Luminescent imaging has high signal-to-noise ratio compared to fluorescent imaging, and luminescent imaging does not require expensive equipment, specialized training and policies in place as imaging with radionuclides. However, luminescent signal can be reduced or lost when it is in deep internal organs of the animal (Ahn, 2014). Also, luciferase substrates need to be injected to produce luminescence and they can cause toxicity to the animal. It is important to track EVs *in vivo* to determine their biodistribution, removal, their effective dose and potential side effects. Therefore, an additional “tag” may be necessary for ALFA-tagged exosomes if quantifiable and sensitive imaging of EVs is needed. For example, parent cells can be loaded with 5nm magnetic nanoparticles which could be packaged into exosome, or exosomes could be electroporated with them. Then, MRI imaging could be performed. Alternatively, radionuclide labelling could be used for positron emission tomography (PET). For example, cells can be genetically modified to produce exosome protein conjugated with streptavidin and then those exosomes can be collected and treated with biotin conjugated with a radioisotope Iodine-125 (Morishita *et al.*, 2015). These two and other methods may modify exosomes further affecting their functionality and distribution. A method which allows exosome tracking without affecting their functionality is yet to be determined.

In the future studies, it would be important to consider another way of MSCs transfection with ALFA tag. Here, electroporation was used to introduce ALFA tag sequence which could have disrupted MSCs genes. This, in turn, could have affected exosome quality. Moreover, our method involved overexpression of CD63 by MSCs. As discussed above in “Discussion” (HEK-293 SEC-purified exosomes), exosome function could be altered as a result.

Additionally, an appropriate storage of affinity purified exosomes should be determined. ISEV recommends storage of isolated EVs in PBS at −80°C (Witwer *et al.*, 2013). There is insufficient data to support this recommendation as many studies comparing storage conditions had inconsistent results. For example, HEK-293 exosomes were found to be most stable at +4°C, -20°C or -70-80°C, depending on a study (Sokolova *et al.*, 2011; Lee *et al.*, 2016; Cheng *et al.*, 2019). Some recent studies focus on lyophilization of exosomes as this method provides long-term stability for lipid nanoparticles (Muramatsu *et al.*, 2022; Trenkenschuh *et al.*, 2022). When the protocol of affinity purification is improved to ensure neglectable batch-to-batch variability (EV physiochemical and functional characteristics), storage conditions, namely acceptable storage temperature, the number of freezing and thawing cycles, and storage duration should be determined.

In this study, HEK-293 were transfected with ALFA tag sequence. Transient transfection of cells, as in the case with HEK-293, is expected to last 3-4 days. To determine the exact duration of ALFA tag expression, cells could be seeded in multi-well plate or dishes, transfected as usual, and then subjected to luminescence assay to determine how luminescence signal increase and decrease over time. In this study, I collected cells as soon as the transfection was over as HEK-293 start dying without serum within a couple of days.

Finally, it would be important to investigate if ALFA tag causes activation of cell-mediated immunity. As it was mentioned before, ALFA tag sequence is unique, i.e., different compared to endogenous proteins. Therefore, cells may react to ALFA tag as if it is an antigen. Therefore, before these exosomes are tested *in vivo,* they should be tested in macrophage, dendritic cell, or T cell culture to determine if they cause activation of these cells.

Conclusion

In this chapter, CMV-CD63-Nluc-ALFA and PGK-CD63-Nluc-ALFA plasmids were constructed and used to transfect HEK-293 cells and conditionally immortalized MSCs, respectively. The protocol for affinity purification of exosomes was developed and optimized. The affinity purified exosomes were found to be purer than SEC purified exosomes. Further studies should be done to increase the quantity of affinity purified exosomes from ALFA-MSCs and to determine their cardioprotective potential.

Chapter 4

Introduction

Ischaemia/reperfusion injury in cardiomyocytes

During acute myocardial infarction, the blood supply to the heart is reduced or completely restricted. This rapidly causes a multitude of changes inside the affected cardiomyocytes Figure 40, A vs B). Without oxygen supply, oxidative phosphorylation in the mitochondria ceases (Padilla *et al.*, 2003). ATP levels rapidly decrease due to the high energy demand of the cardiomyocytes. To meet the energy demand, the cell employs anaerobic glycolysis until glucose and oxygen levels are depleted. Mitochondrial F1Fo ATPase, which normally produces ATP during oxidative phosphorylation, utilises leftover ATP to maintain mitochondrial membrane potential (Δψm). When ATP levels are depleted, Δψm is lost (Halestrap, 2009). Meanwhile, anaerobic respiration generates lactate as a by-product. Lactate drives acidification of the cytosol which, in turn, stimulates extrusion of protons from the cell via the sodium/hydrogen antiporters (Figure 40, B). The Na+/Ca2+ exchanger extrudes the sodium pumped in by sodium/hydrogen antiporter in exchange for calcium. The sarcoplasmic reticulum (SR) is unable to take up calcium uptake without ATP. Mitochondria can take some cytosolic calcium and therefore contribute to the regulations of cytosolic calcium levels (Figure 41, Normal vs Ischaemia). Additionally, mitochondria generate an excessive amount of reactive oxygen species (ROS). ROS damage mitochondrial components and reduce the pool of coenzyme Q needed for the forward electron transport chain to produce ATP. Intracellular acidosis, ion disbalance, and ATP depletion lead to rigour contracture and termination of cardiomyocyte contraction (Carmeliet, 1999).

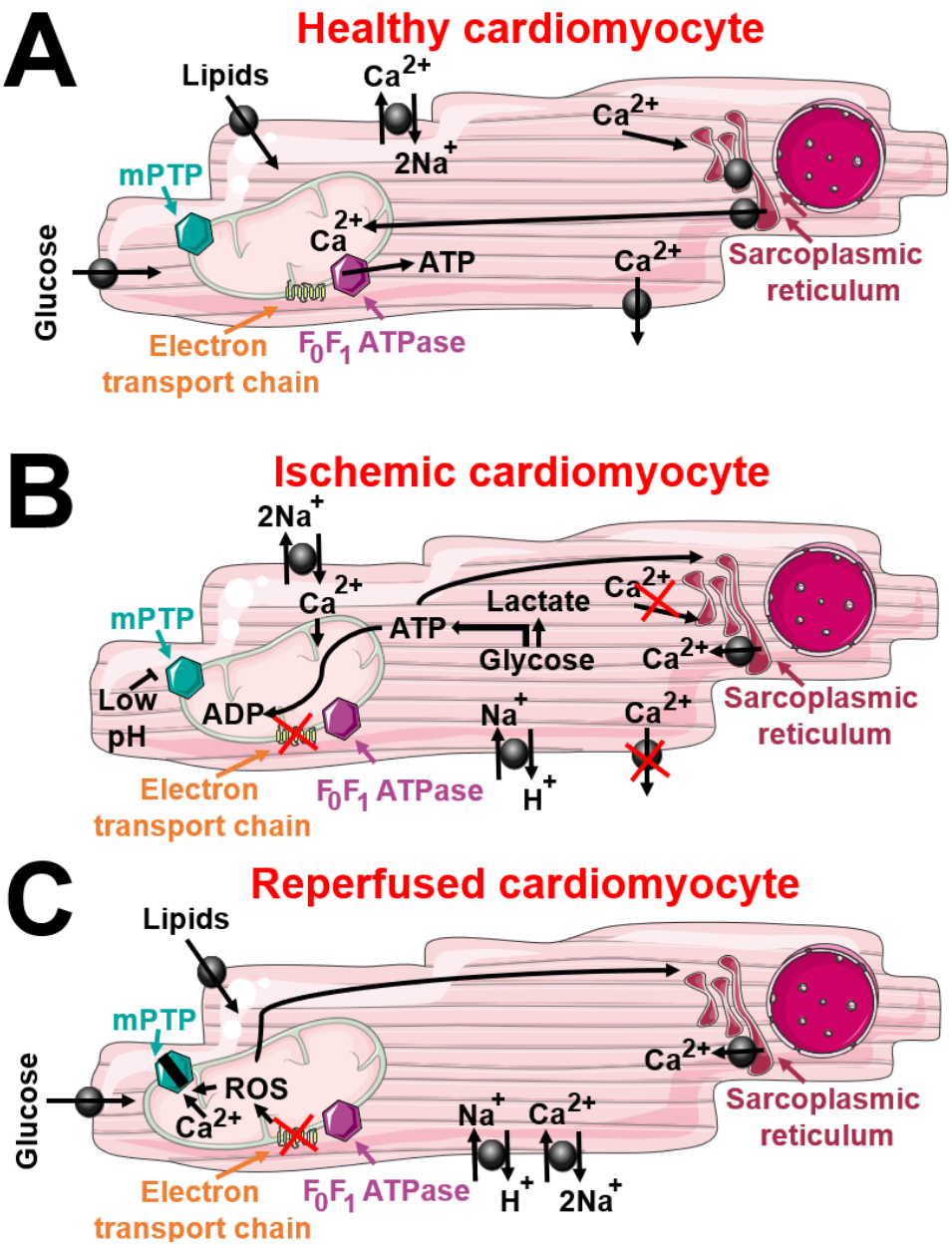

Figure 40. Ischaemia/reperfusion injury in cardiomyocytes.

(**A**) In healthy cardiomyocytes, mitochondria utilise derivatives of lipids and glucose to synthesise ATP by oxidative phosphorylation. The sarcoplasmic reticulum, ATP-fuelled sodium/calcium exchanger, and calcium ATPase maintain calcium homeostasis. Mitochondria can accept calcium, which is usually supplied by the sarcoplasmic reticulum. (**B**) During ischaemia, oxidative phosphorylation stops due to the depletion of substrates and oxygen. Cardiomyocytes switch to anaerobic metabolism. At the same time, cytosolic calcium levels increase. Resultant cytoplasmic acidification inhibits mitochondrial permeability transition pores (mPTP). (**C**) In reperfusion, damaged mitochondria produce a limited amount of ATP by oxidative phosphorylation. Restored cytoplasmic pH, the excess of mitochondrial ROS, and calcium drive mPTP opening. ROS and ever-increasing calcium levels in the cytoplasm contribute to dysfunction of the sarcoplasmic reticulum.

Although reperfusion is necessary to salvage the ischaemic heart tissue, it causes ~50% infarct compared to the injury caused by ischaemia alone (Yellon and Hausenloy, 2007; Kalogeris *et al.*, 2016). As a double-edged sword, reperfusion rapidly restores intracellular pH and increases energy levels, but it also promotes cardiomyocyte death via different mechanisms (Figure 40, C) (Inserte *et al.*, 2011; Garcia-Dorado *et al.*, 2012; Fernandez-Sanz *et al.*, 2015). Upon reperfusion, the reduced coenzyme Q pool causes the reversal in the flow of electrons through the electron transport chain making mitochondria pump electrons inside its matrix (Figure 41, Reperfusion). This results into a decrease in $\Delta\psi_m$ and ROS generation. High level of mitochondrial superoxide are produced in the first minutes of reperfusion (Chouchani *et al.*, 2016).

The sodium/calcium exchanger removes the excess of sodium and increases cytosolic calcium levels (Marber *et al.*, 1993; Ruiz-Meana *et al.*, 1999). The increase in ATP levels enables the sarcoplasmic reticulum to uptake calcium ions. However, cytosolic calcium levels exceed the capacity of the SR to store it. In a healthy heart, the SR transiently releases calcium to stimulate cardiomyocyte contraction. However, excess or uncoordinated SR calcium release may cause life-threatening arrhythmias (Ruiz-Meana *et al.*, 2009). Re-established mitochondrial potential facilitates further uptake of calcium inside the mitochondria (Garcia-Dorado *et al.*, 2012; Chouchani *et al.*, 2014).

Eventually, increased levels of mitochondrial calcium may trigger transient mPTP opening, which stops the electron flow in the respiratory complex (Altschuld *et al.*, 1992). High level of calcium causes short bursts of ROS production. This, in turn, promotes the transient opening of mPTP in other mitochondria in the cell and ROS production there (ROS-induced ROS release) (Zorov, Juhaszova and Sollott, 2006). If a certain threshold is reached, mitochondrial ROS and calcium enter a vicious cycle in which one increases levels of another, ultimately causing prolonged mPTP opening (Peng and Jou, 2010). Opening of the mPTP results in proton flow into the mitochondrial matrix, leakage of mitochondrial calcium and ROS to the cytosol, and mitochondrial depolarisation (i.e., the collapse of proton motive force), which halts oxidative phosphorylation. ROS produced outside mitochondria contribute to the secondary injury of cardiomyocytes (Abramov, Scorziello and Duchen, 2007; Murphy, 2009). Hypercontracture, oxidative stress, and mPTP opening lead to cardiomyocyte cell death during reperfusion.

Mitochondria play a central role in cardiomyocyte cell death in cardiac I/R injury. For example, mPTP opening in the inner mitochondrial membrane initiates mitochondria-mediated necrosis. Water, ions >1.5kDa, and other solutes freely enter mitochondria upon mPTP opening. The resultant osmotic pressure draws water inside the mitochondria causing its swelling and rupture. Without ATP, the cardiomyocyte cannot function nor orchestrate apoptosis. Consequently, the cell swells, the plasma membrane loses its integrity, and ruptures (Davidson *et al.*, 2020). Therefore, prevention of mitochondrial injury is paramount to preserve functional cardiomyocytes.

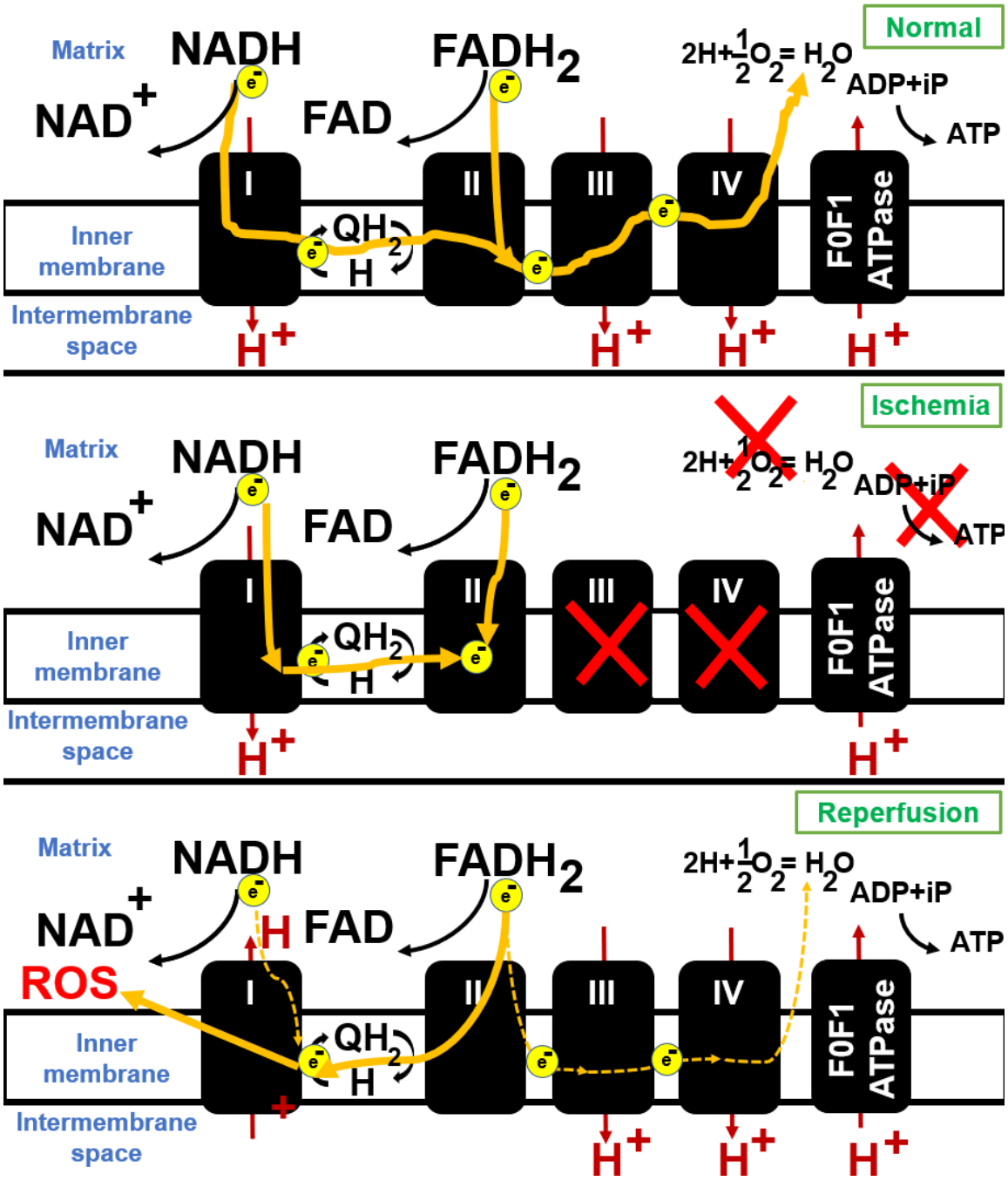
Normal
Matrix
NADH
NAD+
FADH2
FAD
2H+½O2= H2O
ADP+iP
ATP
I
II
III
IV
F0F1 ATPase
Inner membrane
Intermembrane space
QH2
H
H+
Ischemia
Reperfusion
ROS

Figure 41. Electron transport chain in physiological conditions, and during ischaemia or reperfusion.

(**Normal**) Aerobic metabolism produces NADH and FADH, which are substrates for the electron transport chain (ETC). The ETC consists of Complexes I-IV and coenzyme Q. Together, the complexes harness the energy of substrates and contribute to the proton gradient in the intermembrane space. Those protons flow back inside the mitochondria through F1Fo ATPase so that ATP can be generated.

(**Ischaemia**) During ischaemia, the ETC function is terminated since there is no oxygen available to accept electrons from it. Electron donors and carries, e.g., NADH and Coenzyme Q, become maximally reduced.

(**Reperfusion**) With reperfusion, oxygen levels rise to allow the ETC to function. Yet, electron donors and carries get so rapidly oxidised that most electrons flow backward (the reverse electron transport). Free electrons in mitochondria contribute to the generation of reactive oxygen species (ROS).

Experimental models for the assessment of mPTP opening

Since mitochondrial damage and mPTP opening is central to cardiac I/R injury, it would be desirable to have an experimental *in vitro* cellular model for the assessment of mPTP opening. The effects of the I/R injury can be studied on mitochondria, either isolated mitochondria or in live cells. The identity of the mPTP is under investigation (Ong *et al.*, 2015). One of the leading theories suggests that mitochondrial ATP synthase and adenine nucleotide translocator (ANT) are important constituents of mPTP (Elustondo *et al.*, 2016; Karch *et al.*, 2019). One approach to inducing mPTP opening in cells, would be to increase ROS levels inside the mitochondria. This is possible to achieve with a photosensitive fluorescent dye such as ethyl ester of tetramethyl rhodamine (TMRM). TMRM is a voltage-sensitive cationic lipophilic dye. Its partitioning and accumulation in the mitochondria follow the principles of the Nernst equation. The following equation describes the relationship between concentrations of a charged particle in two compartments separated by a membrane which is selective for this particle and the membrane potential:

$$\Psi = -59 * log\left(\frac{Fin}{Fout}\right)$$

where Ψ is the electrical potential, F_{in} and F_{out} are the fluorophore concentration within and outside mitochondria, respectively.

It was reported that TMRM concentrates 10-fold in the cytoplasm and 400-600-fold in the mitochondria compared to the extracellular space (Davidson, Yellon and Duchen, 2007). At high concentration (>100nM) in the cell medium, this fluorophore stacks and forms “J-aggregates” in mitochondria, which cause dye quenching and red-shift in absorbance (lower energy and frequency wavelength). Quenching results in a submaximal fluorescent signal. Upon light illumination such as with the laser, TMRM generates high levels of mitochondrial singlet oxygen molecules ($^1O_2$) in mitochondria. As a result, the mitochondrial membrane potential is lost, the electron transport is inhibited, and mPTP is permanently open. However, even a slight disruption of the mitochondrial membrane potential would result in TMRM leakage to the cytoplasm and easily detectable dequenching. Dequenching is observed as a sudden increase in fluorescence as TMRM diffuses from depolarized mitochondria. Then, the fluorescence increases to the expected intensity as the dye is redistributed throughout the cytoplasm. To determine how TMRM escaped mitochondria, cyclosporin A (CsA), an inhibitor of mPTP, may be used. If the dye leaked through mPTP, CsA addition would slow down the time of its dequenching (Broekemeier, Dempsey and Pfeiffer, 1989). Although the above model has been successfully used as an assay of mPTP opening, some potential criticisms could be raised (Davidson *et al.*, 2006). For example, mitochondrial superoxide (and not singlet oxygen molecules produced by TMRM) are the physiological ROS that are elevated in cardiac I/R injury (Murphy, 2009).

An alternative cell-based model for the assessment of mPTP opening might employ a recently developed chemical called MitoParaquat (MitoPQ), which is capable of continuous production of superoxide inside the mitochondrion (Antonucci *et al.*, 2019). It is composed of a mitochondria-targeting triphenyl phosphonium cation and a redox cycling moiety joined by a hydrophobic carbon chain. A negative charge of the cytoplasmic side of the cell membrane drives MitoPQ inside the cell. Then, mitochondrial membrane potential drives MitoPQ from the cytoplasm inside the mitochondria. Within the mitochondria, MitoPQ is reduced to a radical cation by an electron at the flavin site of Complex I (Figure 42). This radical reacts with oxygen to generate superoxide and return to its original state. Then, the reaction repeats until ROS levels are high enough to disturb mitochondrial membrane potential and open mPTP permanently. To track changes in mitochondria caused by MitoPQ, cells can be treated with a TMRM and imaged only briefly at the lowest laser power. This will hopefully prevent ROS generation by TMRM. If low TMRM concentration is used, the leakage of TMRM out of mitochondria is observed as a decrease in fluorescent signal, i.e., no TMRM dequenching will occur.

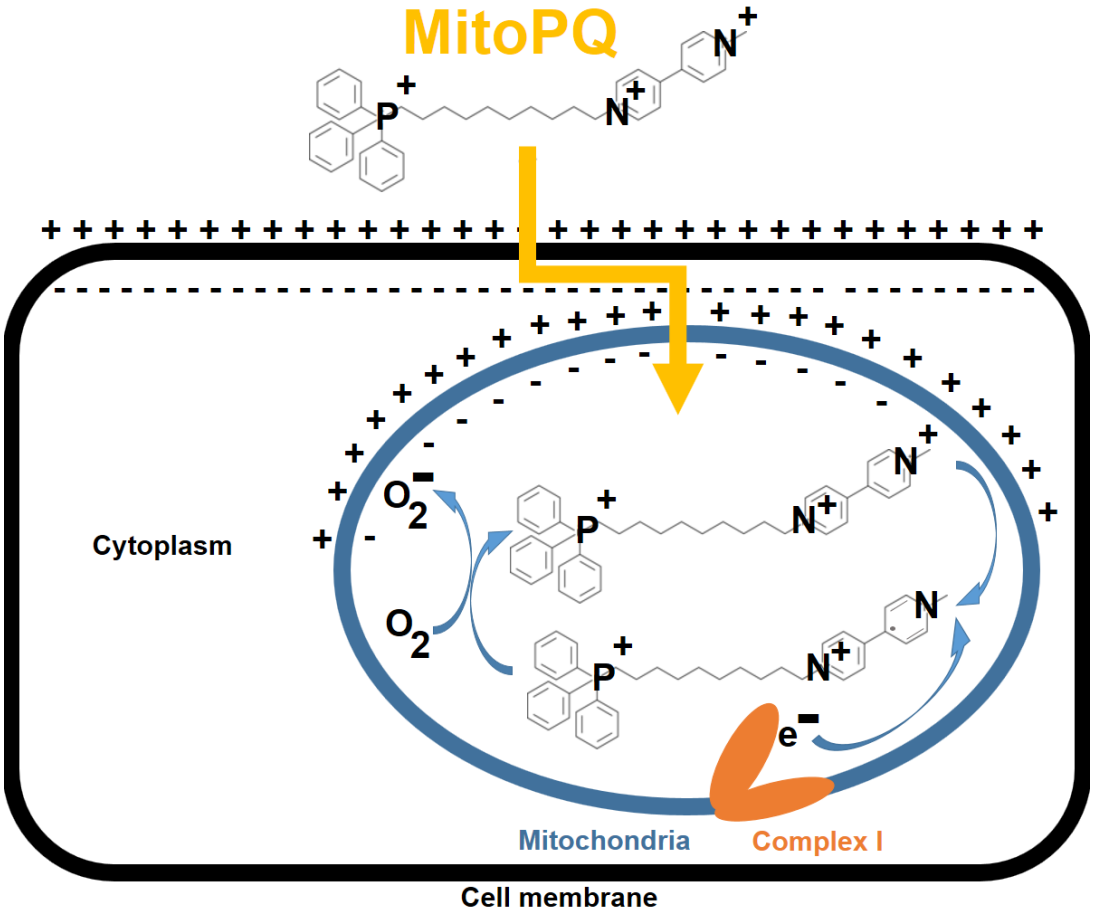

Figure 42. Generation of mitochondrial superoxide by MitoParaquat.

MitoParaquat (MitoPQ) is a cationic lipophilic dye that goes inside the mitochondria. There, it continuously generates superoxide.

Another way that might theoretically be used to achieve mPTP opening is to increase mitochondrial calcium levels (Altschuld *et al.*, 1992). A calcium ionophore A23187 is an ion carrier that transports divalent cations (mostly Mn^{2+}, Ca^{2+}, and Mg^{2+}) across subcellular membranes, including mitochondrial membranes, in exchange for two hydrogen ions. However, A23187 was shown not to trigger mPTP opening in cardiomyocytes. This is likely because a combination of ROS and calcium is required for mPTP opening (Javadov, 2015). This suggests that A23187 should be used together with a ROS-producing drug (Panel, Ghaleh and Morin, 2017).

An alternative method of detecting mPTP opening is by monitoring calcein leakage from mitochondria (Petronilli *et al.*, 1999). For this, acetoxymethyl ester (AM) of calcein is typically used. It is a non-fluorescent hydrophobic compound that easily permeates all subcellular compartments. The AM group obscures the part of calcein which chelates calcium, magnesium, zinc, and some other ions. When calcein AM is hydrolysed by cellular esterases, it can bind the mentioned ions what causes it to fluoresce green. Since dead cells do not have active esterases, they do not fluoresce. Therefore, this dye is suitable and commonly used for cell viability assays. Importantly, calcein fluorescence can be strongly quenched (i.e., diminished) by some divalent cations e.g., cobalt. Cobalt enters the cell, but the intact inner mitochondrial membrane is not permeable to cobalt. Calcein in the cytosol get quenched by cobalt. This means that only mitochondria will fluoresce. If mPTP opens, cobalt would enter the mitochondria and they would not fluoresce anymore. In previous studies, it was shown that a combination of A23187 and MitoPQ can rapidly decrease calcein fluorescence within a few minutes (Antonucci *et al.*, 2019).

Measuring mPTP opening with confocal microscopy and plate reader

The opening of mPTP can be studied in individual cells by using fluorescence microscopy. A confocal microscope can obtain thin plane images to reveal fine details of the cells, e.g., mitochondria. This is achieved by removing out-of-focus light using a pinhole in the light path. The light passes through the pinhole and then through a filter cube (Figure 43, A). The filter cube is an optical block that consists of excitation and emission filters, and a dichromatic mirror. Light of the specific wavelength passes through an excitation filter and is reflected by the dichromatic mirror. It passes through an objective that focuses the light onto the subject, in this case cells labelled with fluorescent dye(s). Light is emitted from the fluorophores back through the objective lens and then through the emission filter. The latter blocks light of different wavelengths except one chosen by the operator. If several fluorophores are used, the range of emission for each fluorophore is defined to avoid overlapping of emission spectra. (Figure 43, A). Finally, the emitted light passes back through the pinhole and hits a detector which multiplies the fluorescent signal and transduces it to the computer. The operator can perform imaging of fixed samples or, using an inverted microscope, live cells in a buffer, and detect the changes in the fluorescence.

Mitochondria in cells can be stained with TMRM within 15mins. When TMRM leaks out from depolarized mitochondria (following mPTP opening for example), the fluorescence in the cytosol rapidly increases, due to dye dequenching. The half-time to the peak TMRM fluorescence value can be measured as an index of mPTP sensitivity to opening. However, if TMRM is used at low concentration, its fluorescence decreases without dequenching as it leaves the mitochondria and then the cell. Low levels of TMRM, i.e. low enough not to cause mPTP opening, are commonly used to track changes in mitochondrial membrane potential (Scaduto and Grotyohann, 1999; Davidson, Yellon and Duchen, 2007). For the calcein assay, however, cells should be first imaged to confirm that the dye is sequestered in mitochondria, i.e., mitochondria are green, and the cytosol is dark. As the mPTP open, cobalt redistributes into mitochondria. Calcein fluorescence, in turn, rapidly decreases due to dye quenching, until it is distinguished. The time needed for the fluorescence to disappear after the drug is added gives an estimation of how rapidly mPTP opens.

Fluorescence plate readers are useful because they can monitor fluorescence changes in cells plated in a multi-well plate. A typical plate reader records total fluorescence in a well rather than being restricted to the fluorescence within a cell. This makes it more difficult to detect redistribution of fluorescent signal, e.g., from mitochondria to cytosol. Since fluorescence changes are recorded in all cells altogether, no decrease in TMRM fluorescence would be observed since TMRM concentration does not change in the well. However, if cells are loaded with TMRM of high concentration, its leakage from mitochondria can be observed as the dye dequenches. CsA can be used to confirm that the increase in fluorescence relates to mPTP opening. To determine what proportion of mitochondria had mPTP opened, carbonyl cyanide m-chlorophenyl hydrazone (CCCP) can be used. It rapidly inhibits oxidative phosphorylation which results in the loss of mitochondrial membrane potential without mPTP opening (Heytler, 1963). The low concentration of TMRM can be used for measuring mitochondrial membrane potential on the plate reader though. Specifically, cells that opened mPTP have less to no mitochondrial membrane potential and therefore TMRM accumulation is less than in the untreated cells.

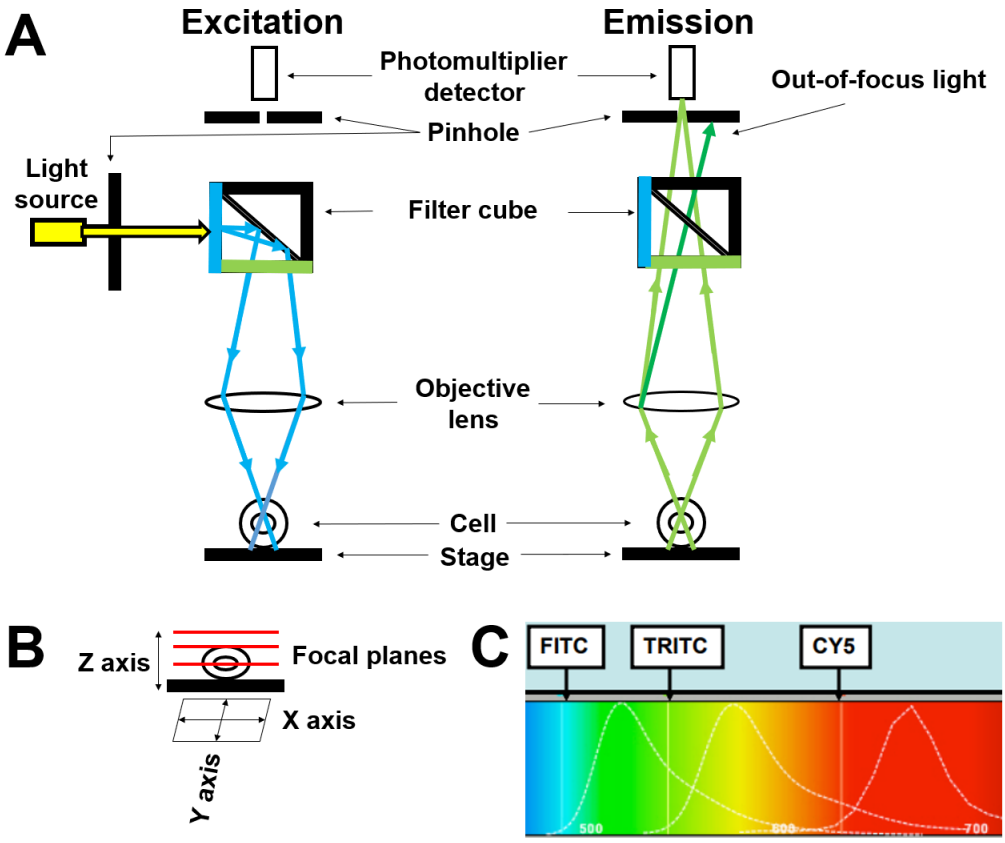

Figure 43. Principle of confocal microscopy.

(**A**) Pinholes remove out-of-focus light emitted by the fluorescent cell upon excitation with a laser. This reveals fine details of the cell such as organelles. (**B**) The specimen can be moved along the X and Y axes and focused along the Z axis. (**C**) Light sources, e.g., FITC, TRITC, and CY5, excite fluorophores in cells at a specific wavelength. The emitted light by a fluorophore is typically longer than its excitation wavelength. If several fluorophores are used, their emission spectra may overlap.

Once an mPTP assay is established, a cardioprotective effect of exosomes from various stem cells can be evaluated. Previously, ExoDiff and ExoPr0 exosomes were extensively characterised. ExoDiff and ExoPr0 were tested by Dr David He (the Hatter Cardiovascular Institute) in a mouse model of myocardial infarction (Figure 44). Dr He injected these exosomes via a jugular vein of male mice 5min prior to heart ischaemia. Myocardial I/R injury was caused by ligation of the left anterior descending artery for 40min followed by 2h reperfusion. Then, hearts were excised and stained with Evan's blue (EB) dye and triphenyl tetrazolium chloride (TTC) (Katsur *et al.*, 2021). EB-negative heart tissue was the "area at risk" and EB and TTC-negative heart tissue was the infarct. The infarct size was found relative to the "area at risk". In this pilot experiment, only a few of exosomes were tested. The doses were decided based on the previous experiments with plasma exosomes (Vicencio *et al.*, 2015). ExoDiff exosomes (dose: $0.7x10^{10}$ particles) significantly decreased the infarct size by one third. Interestingly, ExoPr0 increased the infarct size when used at the same dose and a twice higher dose of ExoDiff exosomes had no effect on the infarct size relative to the control group. To understand the mechanism of ExoDiff and ExoPr0 action on cardiomyocytes, these samples could be tested in an mPTP assay.

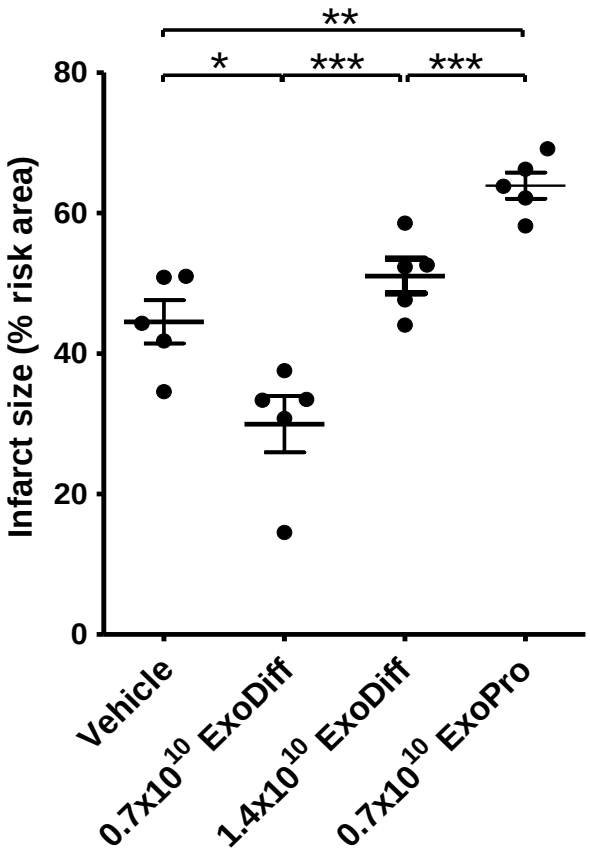

Figure 44. Cardioprotective effect of ExoDiff exosomes from neuronal stem cells in mice prior heart ischaemia.

Wild-type C57B1/6 mice were anaesthetised and operated on as described previously (Davidson *et al.*, 2017). Exosomes from differentiating (ExoDiff) or proliferating (ExoPr0) CTX0E03 cells were injected via a jugular vein 5min prior heart ischaemia was induced. Heart ischaemia was caused by the occlusion of the left anterior descending coronary artery for 40min followed by 2h reperfusion. The infarct size was measured as a percentage of "area at risk" using tetrazolium staining and Evan's blue dye. Hearts with the risk area of <30% were excluded from the analysis. The experiment was performed by Dr David He in the Hatter Cardiovascular Institute.

Aims and hypothesis

Hypothesis

I hypothesised that ExoDiff exosomes from CTX0E03 cells may inhibit mPTP opening in an *in vitro* cardiomyocyte model of simulated I/R injury, thus preventing cell death. If this is shown to be the case, the plan is then to compare the cardioprotective potential of exosomes from various types of stem cells.

Aims

1. Develop an *in vitro* mPTP opening assay using cardiomyocytes.
2. Find positive controls and test exosomes in mPTP opening assay.

Methods

Materials and reagents

The list of solutions, chemicals, kits, instruments, and software is given in Supplementary table 1.

in vivo ischaemia/reperfusion injury

This study was performed by Dr David He. Male wild-type C57BI mice of 12-15 weeks old were anaesthetized with an intraperitoneal injection of 80mg/kg pentobarbital. Mice were placed in supine position on a heating pad (~37°C). Tracheostomy was performed to establish artificial ventilation using a 19G cannula. The animals were connected to a MiniVent type 845 animal ventilator (Harvard Apparatus). The air flow rate was 1L/min with stroke volume of 200µL at 130strokes/min. An expiratory tube was immersed into water to apply 2cmH_2O positive end-expiratory pressure. Electrocardiogram was initiated using one lead and PowerLab/4SP system. The electrocardiogram was continuously plotted in LabChart 7 software (ADInstruments).

Animals were randomized and the investigator, Dr David He, was blinded to the treatments. An incision was made at the fourth intercostal space. Equal volume of saline containing ExoDiff or ExoPr0 were injected into a jugular vein five minutes prior to heart ischaemia. PBS was used as a negative control. Myocardial ischaemia/reperfusion injury was induced by ligation of the left anterior artery with a silk suture. The ischaemia was confirmed by blanching of myocardial tissue distal to the suture and by changes in electrocardiogram. The 40min of ischaemia was followed by 2h of reperfusion. Then, animals were sacrificed.

The excised hearts were cannulated, and blood was washed out with saline. The left anterior artery was ligated with the suture and the heart was perfused with 1% Evan's blue dye in saline (w/v) to determine the area at risk. Hearts were frozen, sectioned and stained with 1% triphenyl tetrazolium chloride in phosphate buffer (w/v; pH7.4) at 37°C for 15mins. Heart sections were fixed with 4% formaldehyde in water (v/v) overnight and then scanned with CanoScan LiDE 220 scanner (Cannon). The area at risk (Evan's Blue-negative) and the infarct size (non-stained with both dyes) were determined using ImageJ (National Institutes of Health). The infarct size was measured as a percentage of the area at risk. Hearts with <30% were excluded from the analysis (Katsur *et al.*, 2021).

Cell cultures

Immortalised rat heart tissue-derived H9c2 cardiac myoblasts were routinely grown in supplemented Dulbecco's Modified Eagle Medium (DMEM) with glucose (Kimes and Brandt, 1976). The HL-1 cardiac muscle cell line, which was originally established from the AT-1 mouse atrial tumour, was grown in flasks coated with 0.005% fibronectin and 0.02% gelatine (Claycomb *et al.*, 1998). HL-1 cells were maintained in supplemented Claycomb medium which was changed five days per week. HL-1 and H9c2 cells were split after or before reaching confluence, respectively, for re-plating and experiments. All cells were cultured in a humidified atmosphere of 95% air and 5% CO_2 at 37°C. H9c2 and HL-1 cells were plated 100,000cells per dish with the glass bottom for imaging on a confocal microscope or 40,000cells/well in 96 well plates for imaging on a plate reader. On the next day, cells were used for various experiments.

Clonetics™ rat cardiac myocytes (neonatal cardiomyocytes hereafter) were purchased from Lonza (R-CM-561; USA) and grown according to the instructions provided by the manufacturer. Specifically, rat cardiac myocyte growth media (RCGM) was prepared by combining rat cardiomyocyte basal medium with horse serum, foetal bovine serum, and gentamicin/amphotericin-B. Also, 96 well plate was precoated with 0.005% fibronectin and 0.02% gelatine. Then, a vial of 4,000,000 cells in 1ml cell suspension was diluted dropwise with 4.3ml RCGM. The resultant cell suspension was transferred 200µl/well into 96 well plates. Then, cells were incubated in a humidified atmosphere of 95% air and 5% CO_2 at 37°C. After 4h, 80% of RCGM was removed from each well and replaced with 200µM bromodeoxyuridine (BrdU) in RCGM to inhibit fibroblast growth. On day 3 of incubation, 50% of RCGM was removed from each well and replaced with the fresh 200µM BrdU in RCGM. On the same day, cells were used for various experiments.

Experiment	Confocal microscope	Plate reader
All experiments	Leica TCS SP5, LAS AF software, x20 objective, Leica TRITC emission settings, DD 488/543 excitation filter Minimum three cell culture dishes were analysed. If possible, multiple spots in the dish were photographed. All drugs/exosomes were diluted in a recording buffer.	FLUOstar OMEGA plate reader, xenon flash lamp. Fluorescence values recorded by the plate reader were normalized to the mean absorbance of the negative control group at time zero of the baseline recording.
1. Oxidative stress assay	Helium-Neon laser at 543nm	N/A
2. mPTP assay using MitoPQ and A23187	TMRM: same as in **1** Calcein: Argon laser at 10% power	TMRM: ex/em 544/590nm Calcein: ex/em 485±12/520nm
3. MitoSOX assay	Agron laser at 10% power	Same as in **2** for TMRM
4. Cal-520 assay	N/A	Same as in **2** for calcein
5. Mitochondrial membrane potential assays	Helium-Neon laser at 543nm	Both assays: same as in **2** for TMRM

Table 8. Settings on confocal microscope and plate reader.

mPTP opening assay using TMRM to generate ROS

To evaluate the potential of exosomes to protect cardiomyocytes from oxidative stress, mitochondrial permeability transition pore (mPTP) opening rate in the presence or absence of exosomes was assessed by using an oxidative stress model (Hausenloy, 2004). Specifically, cells were incubated with tetramethyl rhodamine methyl ester (TMRM; 3µM) for 15min. During TMRM incubation, cells were co-incubated with the mPTP inhibitor cyclosporine A (CsA; 0.2µM), DMSO (TMRM vehicle), ExoPr0 or ExoDiff exosomes (10^{10}particles/ml). This dose was selected based on previous experiments with endothelial tube assays (unpublished data by another PhD student). After TMRM was washed off, CsA, DMSO, or exosomes were added to cells for the whole duration of the recording. Time lapse images of cells were obtained using a Leica TCS SP5 confocal microscope (see settings in Table 8). Then, half-time needed for TMRM to dequench (i.e., to reach the maximum fluorescence value) was found for each individual field, containing several cells.

mPTP opening assays using MitoPQ and A23187 to raise ROS and calcium levels

To continuously monitor mPTP opening by both high ROS and calcium levels, H9c2, HL-1 cells, and neonatal cardiac cells were treated with 20µM TMRM for 10min at 37°C and then washed. Alternatively, cells were incubated with 1µM calcein in 1M cobalt (II) chloride, $CoCl_2$, for 15min, washed, and then calcein de-esterification was allowed for a further 20min. Importantly, neonatal cardiac cells were pre-treated with 1µM DMSO or CsA before calcein treatment. Then, cells were analysed on a FLUOstar OMEGA plate reader (see settings in Table 8). After reading baseline, 10µM MitoParaquat (MitoPQ) and/or 10µM A23187 were added to wells and recording continued. DMSO was used as a negative control. At the end of the recording, the drug solution was changed to 1µM CCCP in cells treated with TMRM to depolarize all mitochondria, and then recording continued further. These assays are based on previously published experiments (Antonucci *et al.*, 2020).

For detecting mPTP opening and changes in mitochondrial morphology with a Leica confocal microscope, H9c2 or HL-1 cells were treated with 20µM TMRM or 1µM calcein as described in the previous paragraph. To minimise the possibility of TMRM contributing to mPTP opening, only three pictures of cells were taken instead of continuous video. Alternatively, cells were treated with 100nM TMRM for 30min. Images were obtained using the confocal microscope immediately before the treatment with 10µM MitoPQ and/or 10µM A23187, 1µM CCCP (2-[2-(3-chlorophenyl)-hydrazinylidene] propanedinitrile) or DMSO (see settings in **Error! Reference source not found.**). Images were obtained immediately b efore the treatment at 0min, 15min and 60min after the treatment was added to the dish. Between the first and the second imaging, the dish with cells was at room temperature at a fixed position on the microscope platform. Then, the dish was placed in the incubator between the second and third imaging, which resulted in a change of imaging field.

Detection of ROS and calcium changes with MitoSOX and Cal-520

To monitor changes in ROS continuously, H9c2, HL-1, and neonatal cardiac cells were incubated with 1µM mitochondrial ROS tracker MitoSOX for 30min. Then, cells were washed. After reading the baseline with a FLUOstar OMEGA plate reader, cells were incubated with 10µM MitoPQ (see settings in Table 8). DMSO and 1M H_2O_2 were negative and positive controls, respectively. For detecting ROS changes on the Leica confocal microscope, H9c2 or HL-1 cells were treated with 1µM MitoSOX as before. Then, cells were imaged before and after treatment with 10µM MitoPQ, 1M H_2O_2, and DMSO (see settings in Table 8).

For monitoring calcium changes continuously, H9c2 and HL-1 cells were treated with 2µM Cal-520 for 30min and then washed. After reading the baseline on the FLUOstar OMEGA plate reader, cells were treated with 10µM A23187 or DMSO and the reading continued (see settings in Table 8).

Detection of changes in mitochondrial membrane potential

To monitor changes in mitochondrial membrane potential, H9c2, HL-1, and neonatal cardiac cells were treated with MitoPQ or DMSO for 2h. In the last 30min of incubation, 100nM TMRM was added into each well or dish. Then, cells were washed and analyzed using the FLUOstar OMEGA plate reader or LEICA confocal microscope (see settings inTable 8). This experiment is based on previously published experiments (Antonucci *et al.*, 2019).

Additionally, neonatal cardiomyocytes were used in an alternative assay to measure their mitochondrial membrane potential. Specifically, cells were treated with 100nM TMRM in combination with 1.6µM cyclosporine H (CsH) with or without 1µM CsA for 30min. After wash, baseline reading was obtained with the FLUOstar OMEGA plate reader (see settings in Table 8. Then, 10µM MitoPQ or DMSO was added and reading continued. Cells pre-treated with CsH and then subjected to DMSO treatment were the negative control. This experiment is based on previously published experiments (Antonucci *et al.*, 2020).

Statistics

Statistical analysis was conducted using GraphPad Prism 6 software (GraphPad Software, Inc., La Jolla, USA). Statistical significance was shown only if P-value was ≤0.05.

Results

ExoDiff exosomes delay mPTP opening caused by singlet oxygen species

As mentioned before, Dr David He showed that ExoDiff, but not ExoPr0, reduced the infarct size in an *in vivo* model of ischaemia/reperfusion (Figure 44) (Katsur *et al.*, 2021). Therefore, it was hypothesised that ExoDiff may delay mPTP opening. A method developed by Duchen and colleagues was selected to investigate this hypothesis (Duchen, 2000). Specifically, HL-1 cells were incubated for 15min with a high concentration (3μM) of tetramethyl rhodamine methyl ester (TMRM), a red fluorescent dye. TMRM accumulates selectively inside the mitochondria according to the mitochondrial membrane potential. Upon illumination with the 543nm helium/neon laser, TMRM generates ROS (singlet oxygen species) within the mitochondria that induce mPTP opening. As TMRM leaves mitochondria, its dequenching is observed as a temporal increase in fluorescence. Changes in fluorescence were recorded using time-lapse imaging on a confocal microscope. Before illumination, cells were treated with an mPTP inhibitor 0.2μM cyclosporine A, 10^{10}particles/ml ExoDiff or ExoPr0 exosomes. This dose of ExoDiff enhanced tubule formation in endothelial cell culture (unpublished data by another PhD student).The duration of laser-stimulated ROS production required to cause mPTP opening was estimated by calculating the half-time until maximal TMRM dequenching. The experiment was performed in collaboration with Dr Vladimir Vinokur.

Delayed dequenching of TMRM with CsA was observed, as expected, which was outperformed by ExoDiff exosomes (by ~50% and ~70%, respectively; Figure 45, A). ExoPr0 exosomes were ineffective in delaying mPTP opening. This suggests that ExoDiff exosomes may delay mPTP pore opening in the setting of high oxidative stress. Dr Vinokur continued this project alone to determine the cardioprotective mechanism of ExoDiff exosomes (Katsur *et al.*, 2021). Unfortunately, however, in subsequent work, I was unable to replicate this experiment, i.e. I observed no difference between DMSO, CsA, ExoDiff, and ExoPr0 groups (Figure 45, B). I was unable to pinpoint the issue which made this experiment unreproducible. I used various cell passages and shared cells with Dr Vinokur. Also, we shared the dyes and other solutions, the same protocols, and the same microscope settings. This is why I did not test other exosome concentrations.

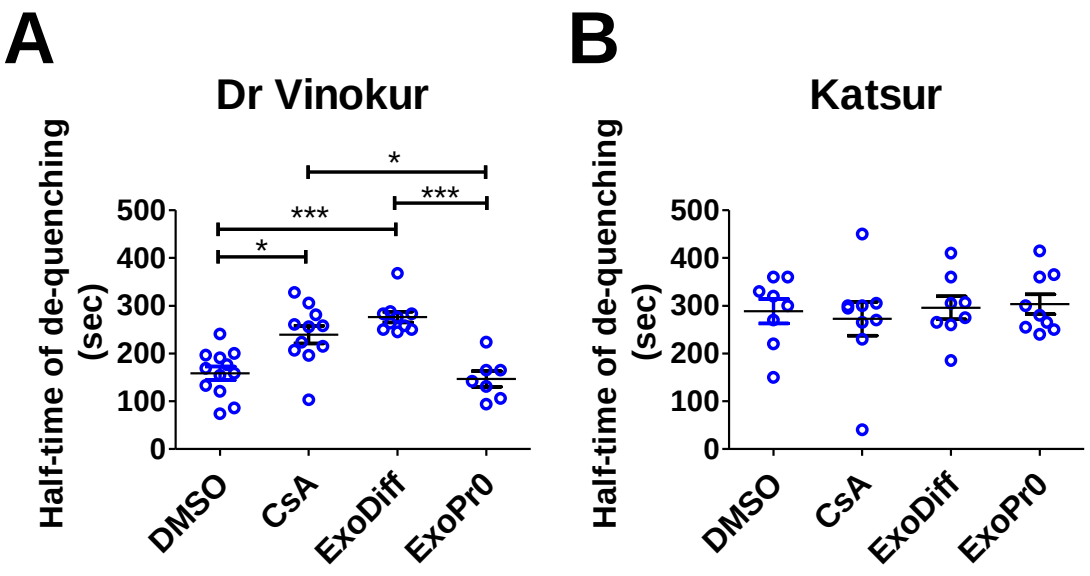

Figure 45. ExoDiff exosomes and cyclosporin A delay mPTP opening.

HL-1 cardiomyocytes were treated 3μM TMRM for 15min. During cell incubation with fluorescent dye TMRM, cells were loaded with 10^{10}particles/ml ExoDiff or ExoPr0 exosomes, 0.2μM mPTP inhibitor CsA, or the CsA vehicle DMSO. Then, TMRM was washed, and recording buffer with exosomes, CsA, or DMSO was added. Immediately after that, lapse video of cells was obtained using a 543nm laser. Illumination of cells caused TMRM to produce reactive oxygen species inside the mitochondria, which led to mPTP opening and the dye leak. The half-time to the maximal increase in dye intensity was recorded. The data is recorded as means of a minimum of (**A**) seven or (**B**) eight experiments with standard deviation. (**B**) Statistical analysis was performed by using non-parametric Kruskal-Wallis test, since normality test, D'Agostino & Pearson test, was not passed. P-value: * is <0.05, ** is ≤0.01 and *** is ≤0.001.

MitoPQ and A23187 do not open mPTP in H9c2 cells

The aim of this experiment was to evaluate the cardioprotective potential of exosomes in a different assay that is more reproducible and effective at simulating the ischaemia/reperfusion injury in cardiac cells. The mitochondria-targeted redox cycler MitoParaquat (MitoPQ) and calcium ionophore A23187 were chosen to stimulate mPTP opening by raising physiological ROS (superoxide) and calcium levels, based on a previous publication. Antonucci *et al*. previously used a low concentration of TMRM to track mitochondrial membrane potential changes caused by MitoPQ and A23187 in neonatal cardiomyocytes (Antonucci *et al.*, 2020). Here, H9c2 cells were treated with TMRM of concentration low enough not to cause the loss of mitochondrial potential within 1h (data not shown). H9c2 cell images were taken before or after treatment with 10μM MitoPQ and/or 10μM A23187, CCCP, or DMSO. As expected, CCCP disrupted mitochondrial potential, which was observed as the decrease in TMRM fluorescence and mitochondrial fragmentation at 15min and 60min (Supplementary Figure 1). A23187 caused a slower decrease in TMRM fluorescence which is seen as mitochondrial fragmentation in some cells at 15min and all cells at 60min. Combined MitoPQ and A23187 caused similar changes as A2317 alone. MitoPQ or DMSO caused minimal TMRM dequenching and no mitochondrial fragmentation. These results suggest that A23187 is more effective in disrupting mitochondrial membrane potential than MitoPQ on their own.

I hypothesized that MitoPQ treatment might have been too short. In addition to using a short treatment (<15min) with MitoPQ, Antonucci and colleagues treated neonatal cardiomyocytes with 0.1-0.5μM MitoPQ for 2h and then observed a decrease in TMRM fluorescence (Antonucci *et al.*, 2019). Therefore, H9c2 cells were subjected to different concentrations of MitoPQ or DMSO for 2h. Cells were treated with 100nM TMRM in the last 30min of incubation with MitoPQ. There was no difference in mitochondrial potential between MitoPQ and the control groups (Figure 46, A, and B). This experiment was repeated using cell imaging and the results were unchanged (Supplementary Figure 1). Therefore, 10μM MitoPQ is unlikely to disrupt mitochondrial membrane potential even after 2h treatment.

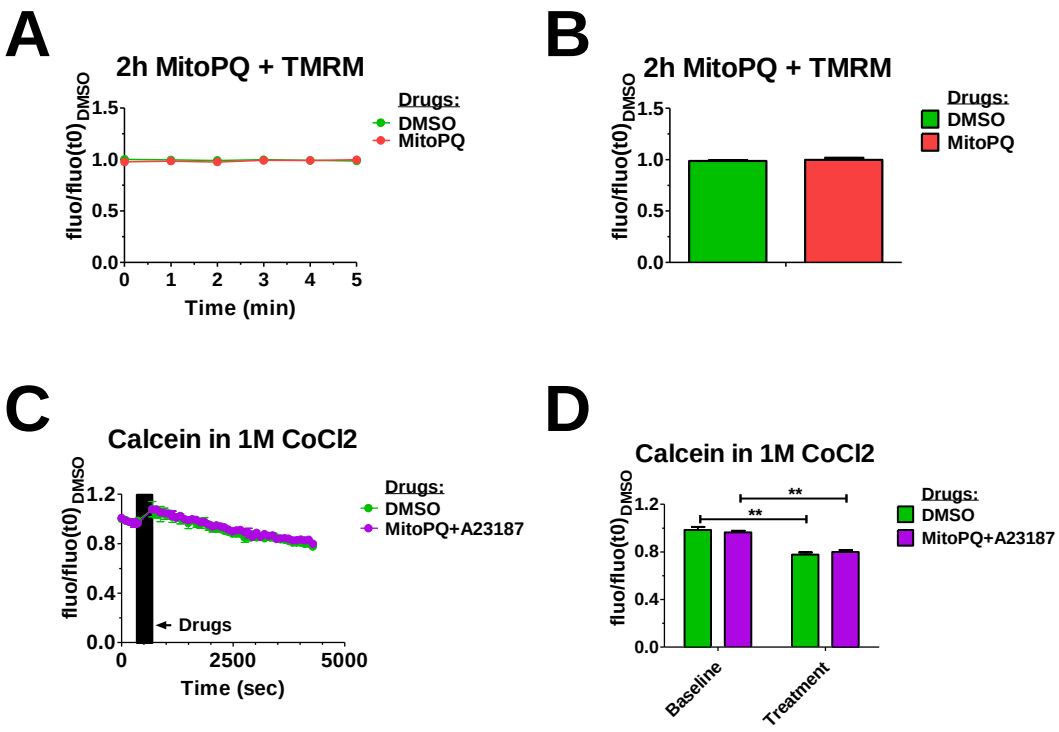

Figure 46. Effect of MitoPQ and A23187 on mitochondrial potential and mPTP opening in H9c2 cells monitored with a plate reader.

H9c2 cardiac myoblasts were treated with (**A, B**) 10µM MitoPQ or DMSO for 2h, and then 100nM TMRM was added to the cells in the last 30min of 2h incubation. (**C, D**) Alternatively, cells were treated with 1µM calcein in 1M $CoCl_2$ for 15min. Then, de-esterification of calcein was allowed for a further 20min. (**A-D)** The baseline was read by a plate reader. Afterward, 10µM MitoPQ and/or 10µM A23187 was added. DMSO was used as a negative control. The black rectangle indicates the drug loading time. All raw values were divided by the mean of DMSO values at 0min to find the fluorescence ratio to the control, $fluo/fluo(t0)_{DMSO}$. The data are presented as mean with SEM of n=5 with 3-5 replicates. Statistical analysis was performed by using a t-test. For this, the last recorded values in baseline and treatment were used. P-value: ** is ≤0.01.

The combination of both MitoPQ and A23187 was suggested to cause rapid mPTP opening (<7min) in neonatal cardiomyocytes (Antonucci *et al.*, 2020). To test these drugs, H9c2 cells were incubated with 20µM TMRM for 10min. Then, cells were imaged on a plate reader and fluorescence was normalized to the fluorescence at 0min with DMSO. TMRM fluorescence was expected to produce a stable signal during baseline recording because the intermittent illumination by the plate reader was thought to be insufficient to photoactivate TMRM to produce ROS and cause mPTP opening. However, the baseline fluorescence increased by almost 16% in 5min (Figure 47, A). When 10µM MitoPQ and/or 10µM A23187 or DMSO were added to the wells, TMRM fluorescence also rose (, A). After 1h incubation with drugs, TMRM fluorescence was significantly increased in all four groups relative to the baseline (Figure 47, A and B). A23187 alone or with MitoPQ significantly increased TMRM fluorescence by ~3.1 and ~2.8 times compared to the baseline values, respectively. However, there was no significant difference between any of the groups (Figure 47, B).

To cause rapid mitochondrial depolarisation in all present mitochondria, mitochondrial oxidative phosphorylation uncoupler CCCP was added to cells. This depolarized mitochondria and caused TMRM to diffuse out of mitochondria and dequench without opening mPTP (Figure 47, A and B). Surprisingly, the TMRM signal decreased in MitoPQ and A23187 and A23187 treated groups (Figure 47, A). This may indicate a washout of the dye. However, an increase in TMRM signal in MitoPQ or DMSO groups after CCCP treatment indicates that either no or minimal mPTP opening was achieved in these groups. Possibly, A23187 caused mitochondrial depolarisation only. These findings were confirmed by imaging cells on a confocal microscope (Supplementary Figure 1).

To determine if A23187 causes mPTP opening or just mitochondrial depolarisation, an alternative mPTP opening assay was used. H9c2 cells were treated with calcein, the compound which accumulates inside all subcellular compartments. Cobalt was added to the cell media to quench calcein outside the cells and in the cytoplasm. Since this ion does not penetrate mitochondria, mPTP opening would result in calcein diffusion into any mitochondria and decrease calcein fluorescence. The baseline fluorescence value recorded with the plate reader fell continuously (by around 1%/minute;Figure 46, C). All treatments first resulted in a slight increase in fluorescence (7% compared to the first baseline value), and then it continued decreasing. Even though calcein fluorescence dropped by >20% in both groups within 1h of treatment, there were no significant differences between the control and treatment groups (Figure 46, D). Taken together, these results suggest that A23187, but not MitoPQ, destabilises mitochondrial potential. However, since A23187 caused dequenching of TMRM but had no effect on calcein fluorescence, A23187 is unlikely to cause mPTP opening.

Since there was no significant difference between MitoPQ and DMSO-treated cells in any of the above experiments (Figure 47, A), I conducted experiments to confirm that MitoPQ increased mitochondrial ROS as expected. Therefore, H9c2 cells were incubated with fluorescent mitochondrial superoxide indicator MitoSOX. After the baseline measurement was taken, the cells were treated with 10µM MitoPQ, DMSO, or a positive control of hydrogen peroxide. As expected, hydrogen peroxide caused a rapid increase in MitoSOX fluorescence, reaching a 2.1-fold increase in fluorescence after 1h treatment (Figure 47, C and D). One-hour treatment with MitoPQ caused a 17% increase in ROS. Yet, this ROS increase with MitoPQ was not significantly different from the control. These findings were confirmed with the confocal microscope (Supplementary Figure 2). Therefore, the reason that 10µM MitoPQ did not cause mPTP opening appears to be that it failed to raise mitochondrial ROS levels sufficiently.

I wanted to confirm that A23187 elevated calcium levels in H9c2 cells (Figure 47, A). For this, cells were loaded with the calcium-sensitive dye Cal-520. The baseline was recorded and then 10µM A23187 or DMSO were added. As shown in Figure 47(E), A23187 caused a sudden ≈50% increase in calcium levels compared to the baseline as expected, which dropped over the next 4-5min and then started to continuously rise. Interestingly, 1h DMSO treatment also resulted in a significant increase in Cal-520 signal (1.3-fold after 1h;Figure 47, F). This is significantly less than a 2.4-fold increase in Cal-520 fluorescence caused with 1h A23187 treatment. Therefore, a rapid increase of calcium levels with 10µM A23187 in H9c2 cells was a probable reason for the loss of mitochondrial potential in H9c2 cells.

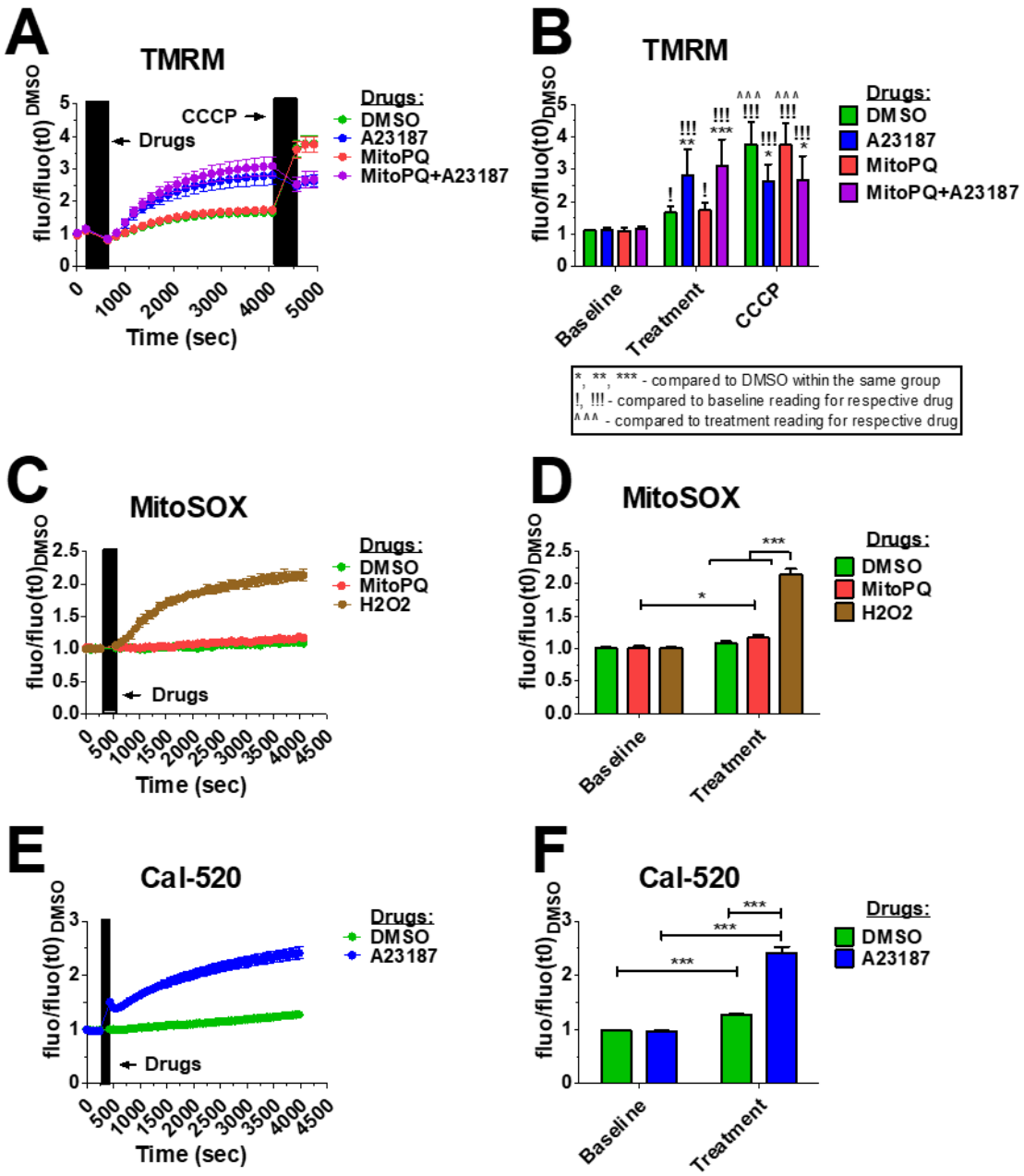
A
TMRM
fluo/fluo(t0)DMSO
CCCP
Drugs
Time (sec)
Drugs:
DMSO
A23187
MitoPQ
MitoPQ+A23187
B
TMRM
Baseline
Treatment
CCCP
Drugs:
DMSO
A23187
MitoPQ
MitoPQ+A23187
*, **, *** - compared to DMSO within the same group
!, !!! - compared to baseline reading for respective drug
^^^ - compared to treatment reading for respective drug
C
MitoSOX
Drugs
Time (sec)
Drugs:
DMSO
MitoPQ
H2O2
D
MitoSOX
Baseline
Treatment
Drugs:
DMSO
MitoPQ
H2O2
E
Cal-520
Drugs
Time (sec)
Drugs:
DMSO
A23187
F
Cal-520
Baseline
Treatment
Drugs:
DMSO
A23187

Figure 47. Effect of MitoPQ and A23187 on mPTP opening in H9c2 cells monitored with a plate reader.

H9c2 cardiac myoblasts were treated with (**A, B**) 20µM TMRM for 10min, (**C,D**) 1µM MitoSOX for 30min or (**E, F**) 2µM Cal-520 for 30min. (**A-F**) A baseline was read by a plate reader before the addition of 10µM MitoPQ and/or 10µM A23187 or 1M H_2O_2. DMSO was used as a negative control. The black rectangle indicates the drug loading time. (**A, B**) CCCP was added to each treatment group at the end of the experiment. (**A-F**) All raw values were divided by the mean of DMSO values at 0min to find the fluorescence ratio to the control, $fluo/fluo(t0)_{DMSO}$. The data are presented as mean with SEM of (**A, B, E, F**) n=8 or (**C, D**) n=3 with 5 or 4 replicates. Statistical analysis was performed by using one-way ANOVA with Tukey post-hoc test (**B and D,** within "baseline", "treatment" and "CCCP" groups; **B**, within each "drug") or t-test (**D, F** within each "drug"). For statistical analysis, the last recorded values in baseline, treatment, and CCCP were used. P-value: * and ! is ≤0.05, ** is ≤0.01 and ***, !!!, and ^^^ is ≤0.001.

MitoPQ and A23187 do not open mPTP in HL-1 cells

One explanation for the lack of response seen in H9c2 cells could be that they are resistant to the effects of MitoPQ. HL-1 cells were expected to have a better response to MitoPQ since mPTP opening was previously observed in them with high ROS levels (Figure 45**Error! Reference source not found.**). Therefore, the same experiments with HL-1 cardiomyocytes were performed. First, cells were incubated with 20μM TMRM. As shown in Figure 48**Error! Reference source not found.** (A), the baseline fluorescence was rapidly rising, similarly to what was observed with H9c2 cells (17-29% increase in 5min; Figure 47**Error! Reference source not found.**, A). MitoPQ and/or A23187 (10μM each) or DMSO were added to HL-1 cells. Again, the sudden drop in fluorescence (-23-30% compared to the first baseline value) was followed by a constant increase. However, 1h treatment with mentioned drugs did not significantly increase TMRM fluorescence (Figure 48**Error! Reference source not found.**, B). When drug solutions were changed to CCCP to depolarise all mitochondria, TMRM dropped to almost baseline level in all groups (**Error! Reference source not found.**, A). This may be due to the media change. Imaging of HL-1 cells on the confocal microscope confirmed these results (the top of Supplementary Figure 3). Overall, these results indicate that MitoPQ and A23187 did not cause mPTP opening in this assay.

The alternative mPTP opening assay with calcein in 1M $CoCl_2$ was used as before. As it was observed with H9c2 cells (**Error! Reference source not found.**, C), the baseline fluorescence values decreased continuously (Figure 49**Error! Reference source not found.**). However, treatments with DMSO or 10μM MitoPQ with or without 10μM A23187 did not cause a temporal increase in calcein fluorescence. MitoPQ and A23187 caused a sharper decrease in calcein fluorescence than DMSO for approximately 20min, and then the slope of all curves was similar for the next 40min. The calcein signal difference between these two groups in the last 40min was around 10%. A23187 was likely responsible for the decrease in fluorescence since MitoPQ and DMSO curves overlapped. The results were confirmed with the confocal microscope (Supplementary Figure 4). Even though it was a pilot experiment, it suggests that A23187, but not MitoPQ, can cause minimal mPTP opening in HL-1 cells.

MitoPQ and A23187 caused little to no mPTP opening in HL-1 cells. However, it was possible that they depolarized mitochondria. Therefore, cells were treated with 100nM TMRM and then subjected to 10µM MitoPQ and/or 10µM A23187 on the confocal microscope. DMSO and CCCP were negative and positive controls, respectively. As expected, no change in TMRM fluorescence was observed with DMSO but CCCP treatment minimised the TMRM signal by 15min (the bottom of Supplementary Figure 3). As it was observed with H9c2 cells (Supplementary Figure 1), A23187 alone or with MitoPQ reduced TMRM fluorescence by 1h post-treatment best (the bottom of Supplementary Figure 3). MitoPQ caused less fluorescence loss than A23187 but more than DMSO. This suggests that A23187 decreased mitochondrial membrane potential to some extent, but MitoPQ had little effect in HL-1 cells.

To understand why the mPTP assays did not work in HL-1 cells, mitochondrial ROS and calcium levels were measured with MitoSOX and Cal-520 as described previously. Unlike hydrogen peroxide, MitoPQ treatment for 1h did not produce detectable ROS when HL-1 cells were analysed with the plate reader (Figure 48**Error! Reference source not found.**, C and D). The same results were obtained using the confocal microscope (Supplementary Figure 2). On the other hand, 1h treatment with A23187 resulted in increased calcium levels (36%) compared to the relevant baseline (**Error! Reference source not found.**, E and F). However, this increase was not significantly higher than what was observed with 1h DMSO treatment. To sum up, MitoPQ and A23187 did not cause mPTP opening, and this could be because MitoPQ did not increase ROS levels.

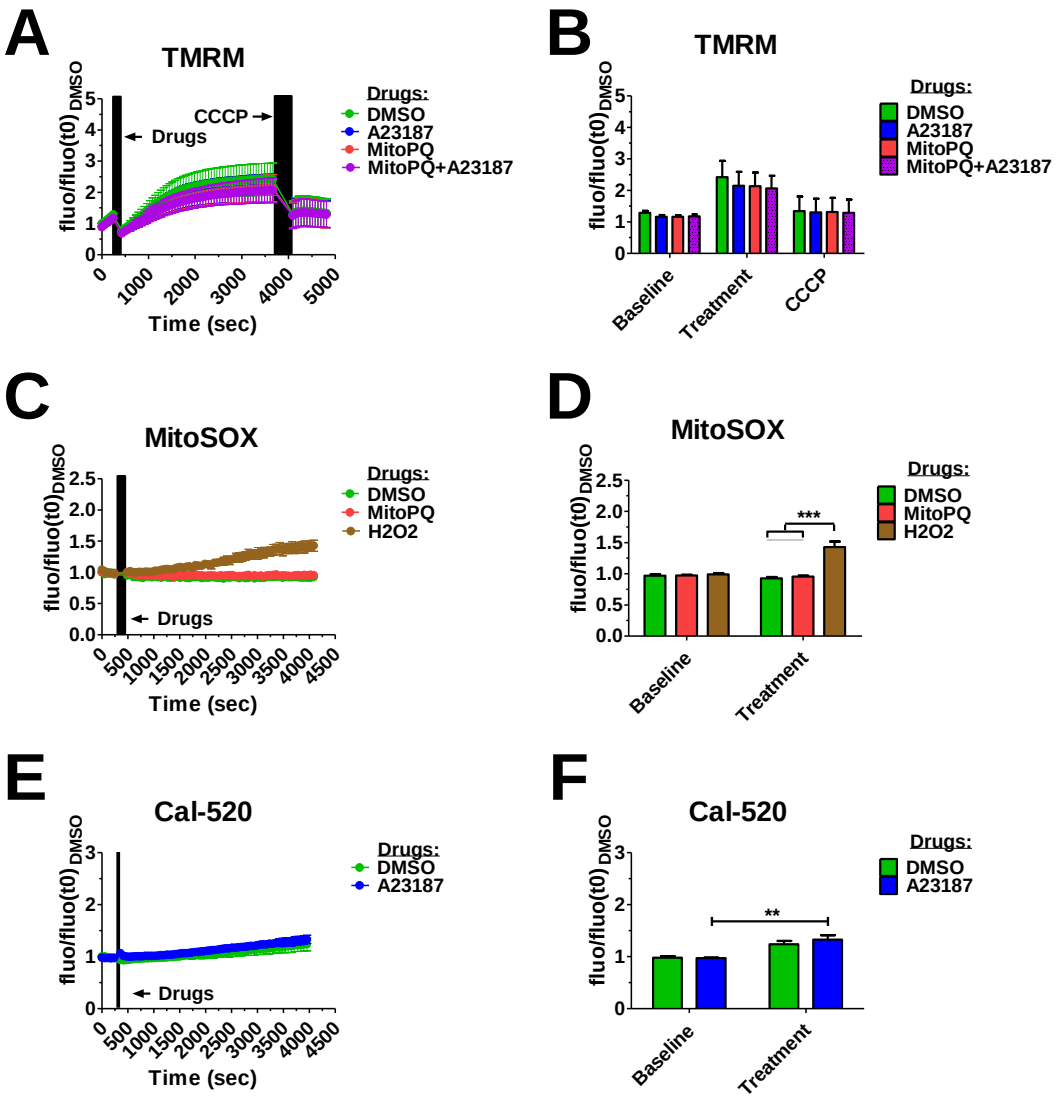

Figure 48. Effect of MitoPQ and A23187 on mPTP opening in HL-1 cells monitored with a plate reader.

HL-1 cardiac muscle cells were treated with (**A, B**) 20μM TMRM for 10min, (**C, D**) 1μM MitoSOX for 30min or (**E, F**) 2μM Cal-520 for 30min. (**A-F**) The baseline was read by a plate reader before the addition of 10μM MitoPQ and/or 10μM A23187, or 1M H_2O_2. DMSO was used as a negative control. The black rectangle indicates the drug loading time. (**A, B**) CCCP was added to each treatment group at the end of the experiment. (**A-F**) All raw values were divided by the mean of DMSO values at 0min to find the fluorescence ratio to the control, $fluo/fluo(t0)_{DMSO}$. The data are presented as mean with SD of (**A, B**) n=5 or (**C-F**) n=4 with 5 replicates. Statistical analysis was performed by using (**B**) one-way ANOVA with Tukey post-hoc test (**D, F**) or t-test. For statistical analysis, the last recorded values in baseline, treatment, and CCCP were used. P-value: ** is ≤0.01, and *** is ≤0.001.

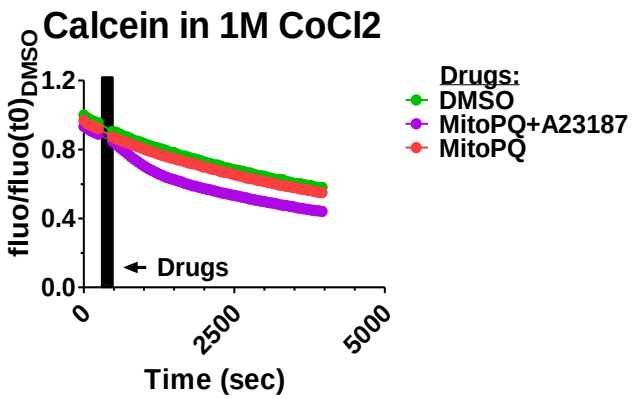

Figure 49. HL-1 cells in calcein assay monitored with a plate reader.

HL-1 cardiac muscle cells were treated with 1µM calcein in 1M $CoCl_2$ for 15min. De-esterification of calcein was allowed for a further 20min. The baseline was read by a plate reader. Afterward, 10µM MitoPQ with or without 10µM A23187 was added. DMSO was used as a negative control. The black rectangle indicates the drug loading time. All raw values were divided by the mean of DMSO values at 0min to find the fluorescence ratio to the control, $fluo/fluo(t0)_{DMSO}$. The data is presented as mean with SD of n=3 (DMSO or MitoPQ and A23187) or n=2 (MitoPQ) with 5 replicates.

MitoPQ does not open mPTP in neonatal cardiomyocytes

MitoPQ and A23187 did not cause mPTP opening in H9c2 and HL-1 cell lines. Therefore, it was decided to use primary rat cardiomyocytes which, as Antonucci *et al*. showed, rapidly respond to treatment with MitoPQ with or without A23187 in calcein and TMRM assays (<7min) (Antonucci *et al.*, 2019, 2020). A limited number of the primary cells were purchased from a company because of their high cost. Therefore, pilot experiments (n=1) were conducted. In the TMRM mPTP assay, the fluorescence baseline measurements decreased by 2%/min instead of increasing as had been observed with H9c2 and HL-1 cell lines (Figure 50, A vsFigure 47, A andFigure 48, A). The addition of either DMSO or 10µM MitoPQ and 10µM A23187 caused a rapid decrease (>40% drop) in TMRM fluorescence. This was followed by an increase in TMRM fluorescence until it reached a plateau. The final reading of TMRM fluorescence after 1h treatments was >20% less than the baseline, suggesting a possible loss of TMRM with cell media change. CCCP treatment, however, increased TMRM signal 2.3-2.4-fold in both treatment groups. At all stages, fluorescence signals in DMSO or MitoPQ and A23187 overlapped. Therefore, MitoPQ and A23187 did not cause mPTP opening in neonatal cells treated with TMRM.

Also, neonatal cardiomyocytes were used in a calcein mPTP assay exactly as described by Antonucci *et al*. (Antonucci *et al.*, 2020). Specifically, neonatal cardiomyocytes were pre-treated with cyclosporin A (CsA), an inhibitor of mPTP, or DMSO before the treatment with calcein. The recorded baseline decreased slightly over time (0.2-0.4%/min), and this decrease continued after cells were treated with either DMSO or 10µM MitoPQ (Figure 50, B). After 1h treatment, calcein fluorescence had dropped by 20%. There was no difference between the four treatment groups, yet it is important to remember that this is only one experiment. Nonetheless, MitoPQ was shown not to cause mPTP opening in the calcein mPTP assay.

The effect of MitoPQ on mitochondrial membrane potential in neonatal cardiomyocytes was evaluated. First, cells were treated the same way as in the previous studies (Antonucci *et al.*, 2020). Specifically, neonatal cardiomyocytes were incubated with 100nM TMRM and cyclosporin H (CsH) with or without an mPTP inhibitor CsA. Both CsA and CsH inhibit the multidrug resistance P-glycoprotein, which may alter TMRM distribution. However, CsH does not delay mPTP opening. After recording the baseline reading, DMSO or 10μM MitoPQ were added. There was a moderate decrease (around 10%) in TMRM fluorescence in all treatment groups by the end of 1h treatment compared to the baseline (Figure 50, D). Yet, the difference between treatments never exceeded 12%. Since the experiment was conducted once, it is impossible to draw any definite conclusions here. However, it is interesting that “CsH to MitoPQ” fluorescence is lower compared to other groups, and “CsH” baselines are lower than “CsA” baselines. Nonetheless, MitoPQ did not decrease mitochondrial membrane potential in neonatal cardiomyocytes.

Also, neonatal cells were treated with MitoPQ for 2h. As previously, cells were treated with 100nM TMRM in the last 30min of MitoPQ treatment. The membrane potential recorded with the plate reader was higher for cells treated with 10μM MitoPQ than DMSO by almost 40%. This contradicts the previous studies which showed >80% decrease in TMRM fluorescence with 2h treatment with 0.5μM MitoPQ (Antonucci *et al.*, 2019). Therefore, it is unclear what effect MitoPQ has on the mitochondrial membrane potential.

To understand why MitoPQ failed to open mPTP in neonatal cardiomyocytes, the changes in mitochondrial levels were tracked with MitoSOX, as described previously. There was no difference between the control and treatment groups (Figure 50, C). Hydrogen hydroxide was successful in raising ROS levels. This assay confirms that MitoPQ fails to increase mitochondrial ROS in neonatal cardiomyocytes.

To sum up, the experiments with three cell types, namely H9c2, HL-1, and neonatal cardiomyocytes, showed that MitoPQ does not increase mitochondrial ROS. Therefore, a physiologically relevant mPTP opening assay was not established to determine if exosomes may prevent mPTP opening in cardiomyocytes subjected to simulated ischaemia/reperfusion injury.

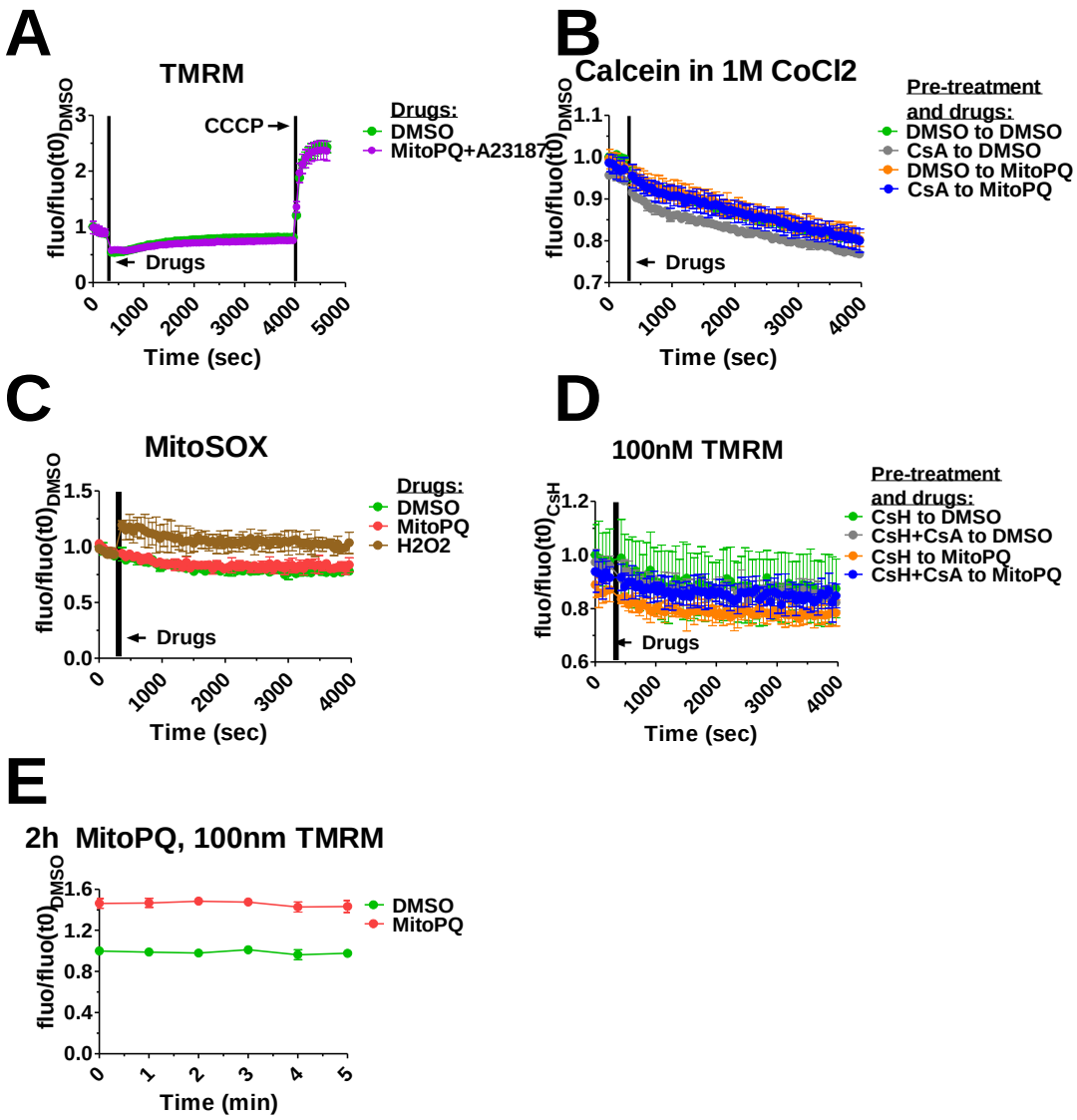

Figure 50. Various mPTP opening assays and mitochondrial potential in primary cardiomyocytes treated with MitoPQ.

Neonatal rat cardiomyocytes were treated with (A) 20μM TMRM for 10min, (B) 1μM CsA or DMSO for 30min, 1μM calcein in 1M $CoCl_2$ for 15min, and then cells were allowed to de-esterify calcein for extra 20min, (C) 1μM MitoSOX for 30min, (D) 100nM TMRM in combination with 1.6μM CsH with or without 1μM CsA for 30min, (E) or 10μM MitoPQ for 2h and with 100nM TMRM in the last 30min of incubation with MitoPQ. The baseline was read by a plate reader before the addition of drugs: 10μM MitoPQ with or without 10μM A23187, or 1M H_2O_2. (A, C, E) DMSO, (B) DMSO to DMSO, (D) CsH to DMSO were used as negative controls. The black rectangle indicates the drug loading time. (A) CCCP was added to each treatment group at the end of the experiment. (A-E) All raw values were divided by the mean of the respective negative control values at 0min to find the fluorescence ratio to the control, e.g. $fluo/fluo(t0)_{DMSO}$. The data are presented as the mean of replicates with SD (all figures N=3 except for D, which is N=4).

Discussion

ExoDiff and ExoPr0 exosomes in the *in vivo* I/R mouse model

Exosomes from various stem cells were previously shown to reduce the infarct size in different models of myocardial infarction (Lai *et al.*, 2010; Lucio Barile *et al.*, 2014; Vicencio *et al.*, 2015; Gallet, Dawkins, Valle, Simsolo, de Couto, *et al.*, 2017). Before comparing the potential of different exosomes to delay mPTP opening, the cardioprotective effect of ExoDiff exosomes was evaluated in an *in vivo* model of myocardial infarction by Dr David He from our laboratory. Depending on their concentration, ExoDiff exosomes had either cardioprotective or no effect on the infarct size after ischaemia/reperfusion injury. At the same time, ExoPr0 exosomes increased the infarct size. The difference between these two exosomes may be explained by the different states of the parent cells, i.e., they were differentiating or proliferating. Yet, further studies would be needed to understand the differences between these exosomes and whether the difference between exosomes from differentiating and proliferating cells can be generalized or is specific to these cells.

These *in vivo* results also supported the idea that exosome concentration is an important factor. According to previous studies, endothelial microparticles promoted angiogenesis at one concentration and inhibited neovascularisation at higher concentrations, whereas high concentrations of exosomes (400µg) caused rapid death by asphyxiation in mice (Lacroix *et al.*, 2007; Smyth *et al.*, 2015). Since ExoDiff exosomes caused decrease or no effect on the infarct size depending on their concentration, it could be possible that lower ExoPr0 concentration could be cardioprotective. It would be better if different doses of ExoDiff and ExoPr0 were tested in this animal study to build dose-response curve. This way, it would be possible to determine the safety and the maximum efficiency of the treatment with ExoDiff and ExoPro. However, as we found later, the ExoDiff, which reduced the infarct size, had inconsistent quality, and therefore improved animal testing of CTX0E03 is not justified at this moment.

Apart from exosome concentration, other factors might have affected the efficacy of exosomes in our AMI model (Figure 44). We used healthy young mice without any metabolic disorders (e.g., diabetes, hypertension, dyslipidaemia, obesity), without prolonged treatments for these disorders (e.g., beta-blockers, angiotensin, statins, metformin), comorbidities (such as left ventricular hypertrophy), and treatments administered to patients during and after surgery for a heart attack (e.g., opioids, P2Y12 antagonists, nitrates) (see Methods). Transient remote ischaemia, which dramatically reduces infarction size in various animal models if administered before, during, or after myocardial ischaemia, is rendered ineffective by these pathologies and treatments (Bosnjak and Ge, 2017). Therefore, these pathologies or treatments may affect the efficacy of exosome treatment.

This AMI model relied on external occlusion of a healthy artery whereas AMI patients have an inflammatory condition that results in rupture of an atherosclerotic plaque. The pathological environment of the infarcted heart in a typical patient may affect the therapeutic potential of exosomes. For example, emerging data suggest that extracellular vesicles from mesenchymal stem cells may have impaired proangiogenic potential in patients with obesity, which are at higher risk of myocardial infarction (Togliatto *et al.*, 2016). Also, the hearts of old mice are more resistant to anti-apoptotic therapies (Boyle *et al.*, 2013). However, there is currently no *in vivo* model which can mimic every aspect of a typical patient with AMI.

Importantly, only the infarction size was measured by Dr He in this *in vivo* study (Figure 44). It would be beneficial to evaluate other endpoints which are of utmost importance for cardiologists in cardiac patients, such as subsequent ventricular remodelling and heart failure. Additionally, exosome injection before the onset of myocardial infarction is unrealistic for most of the patients, in whom myocardial infarction cannot be predicted and therefore it would be important to see whether injection of ExoDiff exosomes during or after reperfusion is cardioprotective. Yet, short *in vivo* studies like ours are important in the development of a hypothesis and understanding the mechanism of cardioprotection.

Finally, ExoDiff and ExoPr0 were injected in the jugular vein of the animals. It means that exosomes passed through the pulmonary circulation and a considerable quantity of them could be lost there. Those exosomes that are not taken by the heart tissue could have ended up in the spleen. Previous research on exosomes showed that they are likely to be cleared from the circulation rapidly, i.e., within minutes, because they get sequestered in lungs and spleen (Takahashi *et al.*, 2013). However, intravenous injection is more attractive as a means of delivery than, e.g., intramyocardial injection, since it would be easier to apply clinically at the time of percutaneous intervention, without the need for guided endomyocardial injection strategies and identification of the infarct border zone.

mPTP opening assays

Cardiac ischaemia/reperfusion injury impairs ATP synthesis, causes mitochondrial calcium overload and excessive ROS levels (Ong *et al.*, 2015). This results in mPTP opening and subsequent cardiomyocyte death. In this study, the suitability of several mPTP opening assays for studying exosome cardioprotection was evaluated. ExoDiff delayed the time of mPTP opening by almost 70% in an assay where TMRM produces mitochondrial ROS upon laser illumination (Duchen, 2000). Importantly, ExoDiff conferred protection against ROS within 15min of cardiomyocyte pre-treatment. This suggests exosome membrane may contain bioactive molecules which activate a cardioprotective cascade by interacting with the cardiomyocyte membrane. For example, plasma exosomes contain HSP70 on their membrane which acts on toll-like receptor 4 on the cardiomyocyte cell wall (Vicencio *et al.*, 2015). As a result, ERK1/2 is phosphorylated within 5min and confers cardioprotection. Indeed, Dr Vinokur found that ExoDiff activated gp130 on cardiomyocytes (Katsur *et al.*, 2021). However, co-isolated cardioprotective proteins could also contribute to delayed mPTP opening. It was shown with proteomics that hundreds of such proteins are co-isolated with exosomes (Takov *et al.*, 2020).

Nonetheless, I found that the TMRM-based mPTP opening assay was not reproducible, i.e., there was no difference between any treatment groups compared to the control when I performed this experiment (data not shown). However, the cause of this discrepancy was not found. As mentioned before, I shared the same cells, protocols, buffers, EVs, and microscope settings with Dr Vinokur. It is unlikely that cell plating was responsible for differences we observed in this assay, as when I used cells seeded by Dr Vinokur, I saw no difference in mPTP opening between negative, positive, and treatment groups, and vice versa. When I finished with mPTP assay experiments, I found out that Dr Vinokur used 10 times higher concentration of exosomes. This, however, does not explain why CsA positive control did not work. I could have tried using another cell type. However, since TMRM produces singlet oxygen species that, unlike superoxide, do not accumulate in the mitochondria in the setting of the I/R injury (Murphy, 2009),it was decided to change both the cell type and mPTP assay.

The mitochondrial ROS generating compound, MitoPQ, was investigated as a possible alternative assay to study mPTP opening. However, 1h long 10μM MitoPQ treatment failed to open mPTP in H9c2 cells, HL-1 cells, and neonatal cardiomyocytes. This MitoPQ dose was believed to be high enough considering that Antonucci found that 0.5-1μM MitoPQ caused mitochondrial dysfunction and mPTP opening in neonatal ventricular myocytes within a few minutes (Antonucci *et al.*, 2019). The MitoPQ stock was prepared fresh every month to avoid auto-oxidation. On several occasions, MitoPQ stock was used for the experiments immediately after being made. Yet, this did not help to open mPTP. Lower concentrations of MitoPQ were also tested, but the results were the same (data not shown). It is unclear why it was not possible to repeat previously published results by Antonucci *et al*. when using the same method, cell line, and treatments (Antonucci *et al.*, 2020).

The effect of 2h long treatment with 10μM MitoPQ on mitochondrial potential using H9c2 cells, HL-1 cells, and neonatal cardiomyocytes was also investigated. It was initially expected that MitoPQ caused some disturbance in mitochondrial potential without causing mPTP opening. Yet, in contrast to Antonucci *et al*., MitoPQ did not disturb mitochondrial potential in these cell types. Specifically, 2h treatment with 0.01-0.5μM MitoPQ decreased mitochondrial potential significantly, with 0.5μM MitoPQ almost abolishing it (Antonucci *et al.*, 2019). This was attributed to the generation of mitochondrial ROS. However, MitoPQ did not raise mitochondrial ROS in the experiments. This suggests that the drug was maybe rendered ineffective for some reason. These results were confirmed with the calcein mPTP opening assay developed by the same research group (Antonucci *et al.*, 2019, 2020).

By contrast, A23187 was successful in causing a disturbance in the mitochondrial potential of H9c2 and HL-1 cells. This is not surprising considering that calcium overload in the mitochondria is known to increase ROS, mitochondrial depolarisation, and consequent mPTP opening, either transient or prolonged (Rasola and Bernardi, 2011). However, the effect of A23187 on mPTP opening was less clear in the experiments, as it caused TMRM dequenching but not calcein fluorescence loss in H9c2 cells. In HL-1 cells and neonatal cardiomyocytes, A23187 did not cause mPTP opening. Interestingly, previous research showed that A23187 does not trigger mPTP opening or disturb mitochondrial potential in murine cardiomyocytes (Panel, Ghaleh and Morin, 2017). The same paper suggests that A23187 can decrease calcein fluorescence by transporting cobalt inside the mitochondria, which quenches calcein fluorescence which contradicts my findings.

Interestingly, during baseline recording, TMRM fluorescence increased and calcein fluorescence decreased continuously when cells were monitored on the plate reader. Permeabilization of mitochondria with the diluent of the drugs, DMSO, was ruled out since its concentration (0.2%) was carefully selected in a pilot experiment (Supplementary Figure 5). Some TMRM probably leaked out after wash until it would reach a perfect ratio of its concentration in the mitochondria, cytoplasm, and outside the cell. However, it is unclear why calcein fluorescence was decreasing. It may be due to fluorescence decay.

Conclusion

The goal of this study was to establish an mPTP opening assay to compare cardioprotective exosomes from different cells in their ability to reduce the effects of the I/R injury. ExoDiff and ExoPr0 were chosen to be tested first in my study. ExoDiff, but not ExoPr0, reduced the infarction size in the mouse model of myocardial infarction. The mPTP opening assay, where TMRM was used to raise ROS, was not reproducible. Other mPTP opening assays were unsuccessful as well because MitoPQ failed to increase ROS levels. Therefore, this project was discontinued to allow me to focus on a more promising one.

Final summary and conclusions

The aim of my PhD was to develop a method of studying exosomes in a cell model of myocardial infarction. This required functional exosomes of high purity and a cell model that mimics ischaemia/reperfusion injury. In Chapter 2, stem cell exosome-enriched samples ExoDiff and ExoPr0, which are of clinical grade and produced on a large scale, were characterized. They were determined to be not of high purity and their quality was inconsistent. Therefore, it was decided that these exosomes were not suitable for achieving my PhD goal.

In Chapter 3, a breakthrough in my PhD is described. The affinity purification of exosomes was developed and optimized. This required transfection of HEK293 and MSCs with CD63-Nluc-ALFA plasmids. The data presented here shows that it is possible to obtain highly pure exosomes which quality is superior to exosomes obtained with SEC. Future work should focus on how to grow cells in quantity high enough to produce exosomes for complete characterization and functional studies. At the same time, the cell number should be manageable for work in a standard academic laboratory. Once this goal is achieved, exosomes obtained by our method could be used to establish the characteristics of highly pure exosomes, including protein/lipid ratio. Additionally, further studies should be done to determine if exosomes can be used as a treatment for various diseases, such as myocardial infarction, neurodegeneration, and cancer. Finally, protein and RNA cargo of exosomes subsets from various cells could be studied to elucidate their role in healthy and diseased conditions.

While characterizing different batches of ExoDiff and ExoPro, various cell-based mPTP opening assays were tested as models of ischaemia/reperfusion in Chapter 4. The first batch of ExoDiff, and not ExoPr0, was cardioprotective a cell models of myocardial infarction where TMRM was responsible for mitotoxicity. The same was observed in the mouse model of myocardial infarction. This indicates that the source of exosomes may matter for their cardioprotection. However, this cell assay was not reproducible. Moreover, the observed cardioprotective effect could be caused by contaminating protein in exosome samples. Other cell models were not successful. They were expected to mimic ischaemia/reperfusion better with high calcium and mitochondrial ROS. Yet, the chosen drug MitoPQ that ensures continuous production of superoxide did not raise ROS. Since that project was time consuming and not promising, it was decided to focus on exosome purification first.

References

Abramov, A. Y., Scorziello, A. and Duchen, M. R. (2007) 'Three distinct mechanisms generate oxygen free radicals in neurons and contribute to cell death during anoxia and reoxygenation.', *The Journal of Neuroscience : the official journal of the Society for Neuroscience*, 27(5), pp. 1129–38. doi: 10.1523/JNEUROSCI.4468-06.2007.

Adamiak, M. *et al.* (2018) 'Induced Pluripotent Stem Cell (iPSC)-derived extracellular vesicles are safer and more effective for cardiac repair than iPSCs', *Circulation Research*, 122(2), pp. 296–309. doi: 10.1161/CIRCRESAHA.117.311769.

Ahn, B. C. (2014) 'Requisites for successful theranostics with radionuclide-based reporter gene imaging', *Journal of Drug Targeting*, 22(4), pp. 295–303. doi: 10.3109/1061186X.2013.878940.

Ahuja, D., Sáenz-Robles, M. T. and Pipas, J. M. (2005) 'SV40 large T antigen targets multiple cellular pathways to elicit cellular transformation', *Oncogene 2005 24:52*, 24(52), pp. 7729–7745. doi: 10.1038/sj.onc.1209046.

Algranati, D., Kassab, G. S. and Lanir, Y. (2011) 'Why is the subendocardium more vulnerable to ischemia? A new paradigm', *American Journal of Physiology - Heart and Circulatory Physiology*, 300(3). doi: 10.1152/ajpheart.00473.2010.

Altschuld, R. A. *et al.* (1992) 'Cyclosporin inhibits mitochondrial calcium efflux in isolated adult rat ventricular cardiomyocytes', *American Journal of Physiology - Heart and Circulatory Physiology*, 262(6 31-6). doi: 10.1152/ajpheart.1992.262.6.h1699.

Anastassiadis *et al.* (2010) 'Precise conditional immortalization of mouse cells using tetracycline-regulated SV40 large T-antigen', *Genesis*, 48(4), pp. 220–232. doi: 10.1002/DVG.20605.

Anastassiadis, K. *et al.* (2002) 'A predictable ligand regulated expression strategy for stably integrated transgenes in mammalian cells in culture', *Gene*, 298(2), pp. 159–172. doi: 10.1016/S0378-1119(02)00979-4.

Anderson, J. L. and Morrow, D. A. (2017) ‘Acute myocardial infarction.’, *The New England Journal of Medicine*, 376(21), pp. 2053–2064. doi: 10.1056/NEJMra1606915.

Andreu, Z. and Yáñez-Mó, M. (2014) ‘Tetraspanins in extracellular vesicle formation and function’, *Frontiers in Immunology*, 5(SEP). doi: 10.3389/FIMMU.2014.00442.

Antonucci, S. *et al.* (2019) ‘Selective mitochondrial superoxide generation in vivo is cardioprotective through hormesis’, *Free Radical Biology and Medicine*, 134, pp. 678–687. doi: 10.1016/j.freeradbiomed.2019.01.034.

Antonucci, S. *et al.* (2020) ‘A novel class of cardioprotective small-molecule PTP inhibitors’, *Pharmacological Research*. doi: 10.1016/j.phrs.2019.104548.

Arslan, F. *et al.* (2013) ‘Mesenchymal stem cell-derived exosomes increase ATP levels, decrease oxidative stress and activate PI3K/Akt pathway to enhance myocardial viability and prevent adverse remodeling after myocardial ischemia/reperfusion injury’, *Stem Cell Research*. 2013/02/13, 10(3), pp. 301–312. doi: 10.1016/j.scr.2013.01.002.

Aydin, S. (2015) ‘A short history, principles, and types of ELISA, and our laboratory experience with peptide/protein analyses using ELISA’, *Peptides*. doi: 10.1016/j.peptides.2015.04.012.

Barile, L *et al.* (2014) ‘Extracellular vesicles from human cardiac progenitor cells inhibit cardiomyocyte apoptosis and improve cardiac function after myocardial infarction’, *Cardiovascular Research*, 103(4), pp. 530–541. doi: 10.1093/cvr/cvu167.

Barile, Lucio *et al.* (2014) ‘Extracellular vesicles fromhuman cardiac progenitor cells inhibit cardiomyocyte apoptosis and improve cardiac function aftermyocardial infarction’, *Cardiovascular Research*. doi: 10.1093/cvr/cvu167.

Barosova, H. *et al.* (2021) ‘Inter-laboratory variability of A549 epithelial cells grown under submerged and air-liquid interface conditions’, *Toxicology in Vitro*, 75, p. 105178. doi: 10.1016/J.TIV.2021.105178.

Bendiksen, S. *et al.* (2004) ‘Autoimmunity to DNA and nucleosomes in binary tetracycline-regulated polyomavirus T-Ag transgenic mice’, *Journal of Immunology*, 173(12), pp. 7630–7640. doi: 10.4049/JIMMUNOL.173.12.7630.

Bergmann, O. *et al.* (2009) ‘Evidence for cardiomyocyte renewal in humans’, *Science*, 324(5923), pp. 98–102. doi: 10.1126/science.1164680.

Bertram, R. and Hillen, W. (2008) ‘The application of Tet repressor in prokaryotic gene regulation and expression’, *Microbial Biotechnology*, 1(1), pp. 2–16. doi: 10.1111/J.1751-7915.2007.00001.X.

Bloom, D. E. *et al.* (2011) *The global economic burden of noncommunicable diseases*. Geneva: World Economic Forum. Available at: http://www3.weforum.org/docs/WEF_Harvard_HE_GlobalEconomicBurdenNonCommunicableDiseases_2011.pdf.

Bosnjak, Z. J. and Ge, Z. D. (2017) ‘The application of remote ischemic conditioning in cardiac surgery’, *F1000Research*. doi: 10.12688/f1000research.11018.1.

Bot, I. *et al.* (2007) ‘Perivascular mast cells promote atherogenesis and induce plaque destabilization in apolipoprotein E-deficient mice’, *Circulation*, 115(19), pp. 2516–2525. doi: 10.1161/CIRCULATIONAHA.106.660472.

Bowler, J. V. *et al.* (1998) ‘Natural history of the spontaneous reperfusion of human cerebral infarcts as assessed by 99mTc HMPAO SPECT’, *Journal of Neurology Neurosurgery and Psychiatry*. doi: 10.1136/jnnp.64.1.90.

Boyle, A. J. *et al.* (2013) ‘The effects of aging on apoptosis following myocardial infarction’, *Cardiovascular Therapeutics*, 31(6). doi: 10.1111/1755-5922.12043.

Brizzard, B. (2018) ‘Epitope tagging’, *BioTechniques*, 44(5), pp. 693–695. doi: 10.2144/000112841.

Broekemeier, K. M., Dempsey, M. E. and Pfeiffer, D. R. (1989) ‘Cyclosporin A is a potent inhibitor of the inner membrane permeability transition in liver mitochondria’, *Journal of Biological Chemistry*, 264(14), pp. 7826–7830.

Caplan, A. I. and Dennis, J. E. (2006) ‘Mesenchymal stem cells as trophic mediators.’, *Journal of Cellular Bochemistry*, 98(5), pp. 1076–84. doi: 10.1002/jcb.20886.

Carmeliet, E. (1999) ‘Cardiac ionic currents and acute ischemia: from channels to arrhythmias.’, *Physiological Reviews*, 79(3), pp. 917–1017. doi: 10.1152/physrev.1999.79.3.917.

Chabrol, E. and Charonnat, R. (1937) ‘Une nouvelle reaction pour l’études des lipides: l’oleidemie.’, *La Presse Medicale*, 45, pp. 1713–1714.

Chen, Y., Li, G. and Liu, M. L. (2018) ‘Microvesicles as emerging biomarkers and therapeutic targets in cardiometabolic diseases’, *Genomics, Proteomics and Bioinformatics*, pp. 50–62. doi: 10.1016/j.gpb.2017.03.006.

Cheng, Y. *et al.* (2019) ‘Effect of pH, temperature and freezing-thawing on quantity changes and cellular uptake of exosomes’, *Protein & cell*. Protein Cell, 10(4), pp. 295–299. doi: 10.1007/S13238-018-0529-4.

Chiaradia, E. *et al.* (2021) ‘Extracellular Vesicles under Oxidative Stress Conditions: Biological Properties and Physiological Roles’, *Cells*. Multidisciplinary Digital Publishing Institute (MDPI), 10(7), p. 1763. doi: 10.3390/CELLS10071763.

Chistiakov, D. A. *et al.* (2017) ‘Mechanisms of foam cell formation in atherosclerosis’, *Journal of Molecular Medicine*, 95(11), pp. 1153–1165. doi: 10.1007/s00109-017-1575-8.

Chong, Z. X., Yeap, S. K. and Ho, W. Y. (2021) ‘Transfection types, methods and strategies: a technical review’, *PeerJ*, 9, p. e11165. doi: 10.7717/PEERJ.11165.

Chopra, I. and Roberts, M. (2001) ‘Tetracycline antibiotics: mode of action, applications, molecular biology, and epidemiology of bacterial resistance’, *Microbiology and Molecular Biology Reviews*, 65(2), p. 232. doi: 10.1128/MMBR.65.2.232-260.2001.

Chopra, S. *et al.* (2020) ‘Investigation of plasmid DNA delivery and cell viability dynamics for optimal cell electrotransfection in vitro’, *Applied Sciences*, 10(17), p. 6070. doi: 10.3390/APP10176070.

Chouchani, E. T. *et al.* (2014) 'Ischaemic accumulation of succinate controls reperfusion injury through mitochondrial ROS', *Nature*, 515(7527), pp. 431–435. doi: 10.1038/nature13909.

Chouchani, E. T. *et al.* (2016) 'A unifying mechanism for mitochondrial superoxide production during ischemia-reperfusion injury', *Cell Metabolism*, 23(2), pp. 254–263. doi: 10.1016/j.cmet.2015.12.009.

Chuang, S. T., Shon, Y. S. and Narayanaswami, V. (2017) 'Apolipoprotein E3-mediated cellular uptake of reconstituted high-density lipoprotein bearing core 3, 10, or 17 nm hydrophobic gold nanoparticles', *International Journal of Nanomedicine*. doi: 10.2147/IJN.S145326.

Claycomb, W. C. *et al.* (1998) 'HL-1 cells: a cardiac muscle cell line that contracts and retains phenotypic characteristics of the adult cardiomyocyte', *Proceedings of the National Academy of Sciences*, 95(6), pp. 2979–2984. Available at: https://www.ncbi.nlm.nih.gov/pubmed/9501201.

Cocucci, E., Racchetti, G. and Meldolesi, J. (2009) 'Shedding microvesicles: artefacts no more.', *Trends in Cell Biology*, 19(2), pp. 43–51. doi: 10.1016/j.tcb.2008.11.003.

Croughan, M. S. *et al.* (2016) 'Novel single-use bioreactors for scale-up of anchorage-dependent cell manufacturing for cell therapies', *Stem Cell Manufacturing*, pp. 105–139. doi: 10.1016/B978-0-444-63265-4.00005-4.

Cvjetkovic, A., Lötvall, J. and Lässer, C. (2014) 'The influence of rotor type and centrifugation time on the yield and purity of extracellular vesicles', *Journal of Extracellular Vesicles*, 3(1). doi: 10.3402/JEV.V3.23111.

Das, A. T., Tenenbaum, L. and Berkhout, B. (2016) 'Tet-On Systems For Doxycycline-inducible Gene Expression', *Current Gene Therapy*, 16(3), p. 156. doi: 10.2174/1566523216666160524144041.

Davidson, S. M. *et al.* (2006) 'Signalling via the reperfusion injury signalling kinase (RISK) pathway links closure of the mitochondrial permeability transition pore to cardioprotection', *International Journal of Biochemistry and Cell Biology*. doi: 10.1016/j.biocel.2005.09.017.

Davidson, S. M. *et al.* (2020) ‘Mitochondrial and mitochondrial-independent pathways of myocardial cell death during ischaemia and reperfusion injury’, *Journal of Cellular and Molecular Medicine*, 24(7), pp. 3795–3806. doi: 10.1111/jcmm.15127.

Davidson, S. M. *et al.* (2022) ‘Methods for the identification and characterization of extracellular vesicles in cardiovascular studies - from exosomes to microvesicles’, *Cardiovascular research*. Cardiovasc Res. doi: 10.1093/CVR/CVAC031.

Davidson, S. M., Yellon, D. and Duchen, M. R. (2007) ‘Assessing mitochondrial potential, calcium, and redox state in isolated mammalian cells using confocal microscopy.’, *Methods in Molecular Biology*. doi: 10.1007/978-1-59745-365-3_30.

Davidson and Yellon (2018) ‘Exosomes and cardioprotection - a critical analysis’, *Molecular Aspects of Medicine*, 60, pp. 104–114. doi: 10.1016/j.mam.2017.11.004.

Dexter, T. M., Allen, T. D. and Lajtha, L. G. (1977) ‘Conditions controlling the proliferation of haemopoietic stem cells in vitro’, *Journal of Cellular Physiology*, 91(3), pp. 335–344. doi: 10.1002/JCP.1040910303.

Dominici, M. *et al.* (2006) ‘Minimal criteria for defining multipotent mesenchymal stromal cells. The International Society for Cellular Therapy position statement’, *Cytotherapy*, 8(4), pp. 315–317. doi: 10.1080/14653240600855905.

Doyle, L. M. and Wang, M. Z. (2019) ‘Overview of extracellular vesicles, their origin, composition, purpose, and methods for exosome isolation and analysis’, *Cells*, 8(7), p. 727. doi: 10.3390/CELLS8070727.

Drago, D. *et al.* (2013) ‘The stem cell secretome and its role in brain repair’, *Biochimie*. doi: 10.1016/j.biochi.2013.06.020.

Duchen, M. R. (2000) ‘Mitochondria and Ca2+ in cell physiology and pathophysiology’, *Cell Calcium*, pp. 339–348. doi: 10.1054/ceca.2000.0170.

Elustondo, P. A. *et al.* (2016) ‘Mitochondrial permeability transition pore induction is linked to formation of the complex of ATPase C-subunit, polyhydroxybutyrate and inorganic polyphosphate’, *Cell Death Discovery*, 2(1), pp. 1–9. doi: 10.1038/cddiscovery.2016.70.

Engström, H. A., Andersson, P. O. and Ohlson, S. (2005) ‘Analysis of the specificity and thermodynamics of the interaction between low affinity antibodies and carbohydrate antigens using fluorescence spectroscopy’, *Journal of Immunological Methods*, 297(1–2), pp. 203–211. doi: 10.1016/J.JIM.2004.12.010.

Escoffre, J. M. *et al.* (2009) ‘What is (still not) known of the mechanism by which electroporation mediates gene transfer and expression in cells and tissues’, *Molecular Botechnology*, 41(3), pp. 286–295. doi: 10.1007/S12033-008-9121-0.

Evan, G. *et al.* (1985) ‘Isolation of monoclonal antibodies specific for human c-myc proto-oncogene product’, *Molecular and Cellular Biology*, 5(12), pp. 3610–3616. doi: 10.1128/MCB.5.12.3610-3616.1985.

Eve, D. J. *et al.* (2009) ‘Methodological study investigating long term laser Doppler measured cerebral blood flow changes in a permanently occluded rat stroke model’, *Journal of Neuroscience Methods*. doi: 10.1016/j.jneumeth.2009.02.016.

Fernandez-Sanz, C. *et al.* (2015) ‘Altered FoF1 ATP synthase and susceptibility to mitochondrial permeability transition pore during ischaemia and reperfusion in aging cardiomyocytes.’, *Thrombosis and Haemostasis*, 113(3), pp. 441–51. doi: 10.1160/TH14-10-0901.

French, J. K. *et al.* (2010) ‘Mechanical complications after percutaneous coronary intervention in ST-elevation myocardial infarction (from APEX-AMI)’, *American Journal of Cardiology*, 105(1), pp. 59–63. doi: 10.1016/j.amjcard.2009.08.653.

Fus-Kujawa, A. *et al.* (2021) ‘An overview of methods and tools for transfection of eukaryotic cells in vitro’, *Frontiers in Bioengineering and Biotechnology*, p. 634. doi: 10.3389/FBIOE.2021.701031.

Gallet, R., Dawkins, J., Valle, J., Simsolo, E., De Couto, G., *et al.* (2017) ‘Exosomes secreted by cardiosphere-derived cells reduce scarring, attenuate adverse remodelling, and improve function in acute and chronic porcine myocardial infarction’, *European Heart Journal*, 38(3), pp. 201–211. doi: 10.1093/eurheartj/ehw240.

Gallet, R., Dawkins, J., Valle, J., Simsolo, E., de Couto, G., *et al.* (2017) ‘Exosomes secreted by cardiosphere-derived cells reduce scarring, attenuate adverse remodelling, and improve function in acute and chronic porcine myocardial infarction’, *European Heart Journal*, 38(3), pp. 201–211. doi: 10.1093/eurheartj/ehw240.

Gámez-Valero, A. *et al.* (2016) ‘Size-exclusion chromatography-based isolation minimally alters extracellular vesicles’ characteristics compared to precipitating agents’, *Scientific Reports*, 6. doi: 10.1038/SREP33641.

Garcia-Dorado, D. *et al.* (2012) ‘Calcium-mediated cell death during myocardial reperfusion.’, *Cardiovascular Research*, 94(2), pp. 168–80. doi: 10.1093/cvr/cvs116.

Gardiner, C. *et al.* (2016) ‘Techniques used for the isolation and characterization of extracellular vesicles: results of a worldwide survey’, *Journal of Extracellular Vesicles*, 5(1). doi: 10.3402/JEV.V5.32945.

Gehl, J. (2003) ‘Electroporation: theory and methods, perspectives for drug delivery, gene therapy and research’, *Acta Physiologica Scandinavica*, 177(4), pp. 437–447. doi: 10.1046/J.1365-201X.2003.01093.X.

Genneback, N. *et al.* (2013) ‘Growth factor stimulation of cardiomyocytes induces changes in the transcriptional contents of secreted exosomes’, *Journal of Extracellular Vesicles*, 2, p. 20167. doi: 10.3402/jev.v2i0.20167.

De Genst, E. J. *et al.* (2010) ‘Structure and properties of a complex of α-synuclein and a single-domain camelid antibody’, *Journal of Molecular Biology*, 402(2), pp. 326–343. doi: 10.1016/J.JMB.2010.07.001.

Gil-Pulido, J. and Zernecke, A. (2017) ‘Antigen-presenting dendritic cells in atherosclerosis’, *European Journal of Pharmacology*, 816, pp. 25–31. doi: 10.1016/j.ejphar.2017.08.016.

Gossen, M. *et al.* (1995) ‘Transcriptional activation by tetracyclines in mammalian cells’, *Science*, 268(5218), pp. 1766–1769. doi: 10.1126/SCIENCE.7792603.

Götzke, H. *et al.* (2019) ‘The ALFA-tag is a highly versatile tool for nanobody-based bioscience applications’, *Nature Communications*, 10(1), pp. 1–12. doi: 10.1038/s41467-019-12301-7.

Graham, F. L. *et al.* (1977) ‘Characteristics of a human cell line transformed by DNA from human adenovirus type 5’, *Journal of General Virology*, 36(1), pp. 59–72. doi: 10.1099/0022-1317-36-1-59.

Gurunathan, S. *et al.* (2019) ‘Review of the isolation, characterization, biological function, and multifarious therapeutic approaches of exosomes’, *Cells*, 8(4), p. 307. doi: 10.3390/CELLS8040307.

Haider, H. K. *et al.* (2008) ‘IGF-1-overexpressing mesenchymal stem cells accelerate bone marrow stem cell mobilization via paracrine activation of SDF-1alpha/CXCR4 signaling to promote myocardial repair’, *Circulation research*, 103(11), pp. 1300–8. doi: 10.1161/CIRCRESAHA.108.186742.

Halestrap, A. P. (2009) ‘What is the mitochondrial permeability transition pore?’, *Journal of Molecular and Cellular Cardiology*, pp. 821–831. doi: 10.1016/j.yjmcc.2009.02.021.

Hall, M. P. *et al.* (2012) ‘Engineered luciferase reporter from a deep sea shrimp utilizing a novel imidazopyrazinone substrate’, *ACS Chemical Biology*, 7(11), pp. 1848–1857. doi: 10.1021/CB3002478.

Haraszti, R. A. *et al.* (2019) ‘Serum Deprivation of Mesenchymal Stem Cells Improves Exosome Activity and Alters Lipid and Protein Composition’, *iScience*. Elsevier, 16, p. 230. doi: 10.1016/J.ISCI.2019.05.029.

Hassani, Z. *et al.* (2012) ‘Human neural progenitor cell engraftment increases neurogenesis and microglial recruitment in the brain of rats with stroke’, *PLoS One*, 7(11), p. e50444. doi: 10.1371/journal.pone.0050444.

Hausenloy, D. J. (2004) ‘Preconditioning protects by inhibiting the mitochondrial permeability transition’, *AJP: Heart and Circulatory Physiology*. doi: 10.1152/ajpheart.00678.2003.

Hausenloy, Derek J. and Yellon, D. M. (2007) ‘Reperfusion injury salvage kinase signalling: Taking a RISK for cardioprotection’, *Heart Failure Reviews*, 12(3–4), pp. 217–234. doi: 10.1007/s10741-007-9026-1.

Hausenloy, D J and Yellon, D. M. (2007) ‘The evolving story of “conditioning” to protect against acute myocardial ischaemia-reperfusion injury’, *Heart*, 93(6), pp. 649–651. doi: 10.1136/hrt.2007.118828.

Head, T., Daunert, S. and Goldschmidt-Clermont, P. J. (2017) ‘The aging risk and atherosclerosis: a fresh look at arterial homeostasis’, *Frontiers in Genetics*. doi: 10.3389/fgene.2017.00216.

Hessvik, N. P. and Llorente, A. (2018) ‘Current knowledge on exosome biogenesis and release’, *Cellular and Molecular Life Sciences*, pp. 193–208. doi: 10.1007/s00018-017-2595-9.

Heytler, P. G. (1963) ‘Uncoupling of oxidative phosphorylation by carbonyl cyanide phenylhydrazones. Some characteristics of m-Cl-CCP action on mitochondria and chloroplasts’, *Biochemistry*. doi: 10.1021/bi00902a031.

Hicks, C. *et al.* (2013) ‘In vivo and in vitro characterization of the angiogenic effect of CTX0E03 human neural stem cells’, *Cell Transplantation*. doi: 10.3727/096368912X657936.

Hirsch, A. *et al.* (2011) ‘Intracoronary infusion of mononuclear cells from bone marrow or peripheral blood compared with standard therapy in patients after acute myocardial infarction treated by primary percutaneous coronary intervention: results of the randomized controlled HEBE’, *European Heart Journal*, 32(14), pp. 1736–47. doi: 10.1093/eurheartj/ehq449.

Hochuli, E., Döbeli, H. and Schacher, A. (1987) ‘New metal chelate adsorbent selective for proteins and peptides containing neighbouring histidine residues’, *Journal of Chromatography*, 411, pp. 177–184. doi: 10.1016/S0021-9673(00)93969-4.

Hong, C. *et al.* (2016) ‘Isolation of biologically active and morphologically intact exosomes from plasma of patients with cancer’, *Journal of Extracellular Vesicles*, 5(1). doi: 10.3402/JEV.V5.29289.

Hong, C. S. *et al.* (2014) ‘Isolation and characterization of CD34+ blast-derived exosomes in acute myeloid leukemia’, *PLoS ONE*, 9(8), p. 103310. doi: 10.1371/JOURNAL.PONE.0103310.

Hornstein, B. D. *et al.* (2016) ‘Effects of circular DNA length on transfection efficiency by electroporation into HeLa cells’, *PloS ONE*, 11(12). doi: 10.1371/JOURNAL.PONE.0167537.

Hromada, C. *et al.* (2017) ‘Endothelial extracellular vesicles - promises and challenges’, *Frontiers in Physiology*. doi: 10.3389/fphys.2017.00275.

Huang, C. *et al.* (2017) ‘Formation and size distribution of self-assembled vesicles’, *Proceedings of the National Academy of Sciences*, 114(11), pp. 2910–2915. doi: 10.1073/PNAS.1702065114.

Inserte, J. *et al.* (2011) ‘Contribution of delayed intracellular pH recovery to ischemic postconditioning protection.’, *Antioxidants & Redox Signaling*, 14(5), pp. 923–39. doi: 10.1089/ars.2010.3312.

Javadov, S. (2015) ‘The calcium-ROS-pH triangle and mitochondrial permeability transition: Challenges to mimic cardiac ischemia-reperfusion’, *Frontiers in Physiology*, 6, p. 83. doi: 10.3389/FPHYS.2015.00083/BIBTEX.

Jennings, R. B. and Ganote, C. E. (1974) ‘Structural changes in myocardium during acute ischemia.’, *Circulation Research*, 35(3), pp. 156–72. Available at: https://www.ncbi.nlm.nih.gov/pubmed/4607107.

Jiang, H. *et al.* (2022) ‘Hypoxia Induced Changes of Exosome Cargo and Subsequent Biological Effects’, *Frontiers in Immunology*, 13(April). doi: 10.3389/fimmu.2022.824188.

Johnson, K., Ellis, G. and Toothill, C. (1977) ‘The sulfophosphovanillin reaction for serum lipids: a reappraisal’, *Clinical Chemistry*, 23(9), pp. 1669–1678. Available at: https://pubmed.ncbi.nlm.nih.gov/556319/ (Accessed: 25 August 2021).

Jung, M. and Mun, J. (2018) ‘Sample preparation and imaging of exosomes by transmission electron microscopy’, *Journal of Visualized Experiments (JoVE)*, 131. doi: 10.3791/56482.

Kalladka, D. *et al.* (2016) ‘Human neural stem cells in patients with chronic ischaemic stroke (PISCES): a phase 1, first-in-man study’, *Lancet*, 388(10046), pp. 787–796. doi: 10.1016/S0140-6736(16)30513-X.

Kalogeris, T. *et al.* (2016) ‘Ischemia/reperfusion’, *Comprehensive Physiology*, 7(1), pp. 113–170. doi: 10.1002/cphy.c160006.

Kang, Y. *et al.* (2017) ‘High-purity capture and release of circulating exosomes using an exosome-specific dual-patterned immunofiltration (ExoDIF) device’, *Nanoscale*, 9(36), pp. 13495–13505. doi: 10.1039/C7NR04557C.

Karch, J. *et al.* (2019) ‘Inhibition of mitochondrial permeability transition by deletion of the ANT family and CypD’, *Science Advances*, 5(8). doi: 10.1126/SCIADV.AAW4597/SUPPL_FILE/AAW4597_SM.PDF.

Katare, R. *et al.* (2014) ‘Clinical-grade human neural stem cells promote reparative neovascularization in mouse models of hindlimb ischemia’, *Arteriosclerosis, Thrombosis, and Vascular Biology*, 34(2), pp. 408–418. doi: 10.1161/ATVBAHA.113.302592.

Katsur, M. *et al.* (2021) ‘Exosomes from neuronal stem cells may protect the heart from ischaemia/reperfusion injury via JAK1/2 and gp130’, *Journal of Cellular and Molecular Medicine*, p. 16515. doi: 10.1111/jcmm.16515.

Kellogg, D. R. and Alberts, B. M. (2017) ‘Purification of a multiprotein complex containing centrosomal proteins from the Drosophila embryo by chromatography with low-affinity polyclonal antibodies.’, *Molecular Biology of the Cell*, 3(1), pp. 1–11. doi: 10.1091/MBC.3.1.1.

Kervadec, A. *et al.* (2016) ‘Cardiovascular progenitor-derived extracellular vesicles recapitulate the beneficial effects of their parent cells in the treatment of chronic heart failure’, *Journal of Heart and Lung Transplantation*, 35(6), pp. 795–807. doi: 10.1016/j.healun.2016.01.013.

Khan, M. *et al.* (2015) ‘Embryonic stem cell-derived exosomes promote endogenous repair mechanisms and enhance cardiac function following myocardial infarction’, *Circulation Research*, 117(1), pp. 52–64. doi: 10.1161/CIRCRESAHA.117.305990.

Khanabdali, R. *et al.* (2016) ‘Harnessing the secretome of cardiac stem cells as therapy for ischemic heart disease’, *Biochemical Pharmacology*, 113, pp. 1–11. doi: 10.1016/j.bcp.2016.02.012.

Kimes, B. W. and Brandt, B. L. (1976) ‘Properties of a clonal muscle cell line from rat heart’, *Experimental Cell Research*. doi: 10.1016/0014-4827(76)90447-X.

Knight, J., Anderson, S. and Rawle, J. (1972) ‘Chemical basis of the sulfo-phospho-vanillin reaction for estimating total serum lipids’, *Clinical Chemistry*, 18(3), pp. 199–202. Available at: https://pubmed.ncbi.nlm.nih.gov/5020813/ (Accessed: 25 August 2021).

Kojima, R. *et al.* (2018) ‘Designer exosomes produced by implanted cells intracerebrally deliver therapeutic cargo for Parkinson’s disease treatment’, *Nature Communications*, 9(1), pp. 1–10. doi: 10.1038/s41467-018-03733-8.

Konoshenko, M. Y. *et al.* (2018) ‘Isolation of extracellular vesicles: general methodologies and latest trends’, *BioMed Research International*. doi: 10.1155/2018/8545347.

Kowal, J. *et al.* (2016) ‘Proteomic comparison defines novel markers to characterize heterogeneous populations of extracellular vesicle subtypes’, *Proceedings of the National Academy of Sciences*, 113(8), pp. E968–E977. doi: 10.1073/pnas.1521230113.

Lacroix, R. *et al.* (2007) ‘Activation of plasminogen into plasmin at the surface of endothelial microparticles: a mechanism that modulates angiogenic properties of endothelial progenitor cells in vitro’, *Blood*, 110(7), pp. 2432–2439. doi: 10.1182/blood-2007-02-069997.

Lai, R. C. *et al.* (2010) ‘Exosome secreted by MSC reduces myocardial ischemia/reperfusion injury’, *Stem Cell Research*. doi: 10.1016/j.scr.2009.12.003.

Lee, M. *et al.* (2016) ‘Influence of storage condition on exosome recovery’, *Biotechnology and Bioprocess Engineering 2016 21:2*. Springer, 21(2), pp. 299–304. doi: 10.1007/S12257-015-0781-X.

Libby, P., Ridker, P. M. and Hansson, G. K. (2011) ‘Progress and challenges in translating the biology of atherosclerosis’, *Nature*, pp. 317–325. doi: 10.1038/nature10146.

Lin, L., Wang, X. and Yu, Z. (2016) ‘Ischemia-reperfusion injury in the brain: mechanisms and potential therapeutic strategies’, *Biochemistry & Pharmacology: Open Access*, 5(4). doi: 10.4172/2167-0501.1000213.

Littlewood, T. D. *et al.* (1995) ‘A modified oestrogen receptor ligand-binding domain as an improved switch for the regulation of heterologous proteins’, *Nucleic Acids Research*. doi: 10.1093/nar/23.10.1686.

Lopatina, T. *et al.* (2014) ‘Platelet-derived growth factor regulates the secretion of extracellular vesicles by adipose mesenchymal stem cells and enhances their angiogenic potential.’, *Cell Communication and Signaling*, 12, p. 26. doi: 10.1186/1478-811X-12-26.

Lucchetti, D. *et al.* (2017) ‘Differentiation Affects the Release of Exosomes from Colon Cancer Cells and Their Ability to Modulate the Behavior of Recipient Cells’, *The American Journal of Pathology*. Elsevier, 187(7), pp. 1633–1647. doi: 10.1016/J.AJPATH.2017.03.015.

Madonna, R. *et al.* (2016) ‘Position paper of the European Society of Cardiology Working Group Cellular Biology of the Heart: cell-based therapies for myocardial repair and regeneration in ischemic heart disease and heart failure’, *European Heart Journal*, 37(23), pp. 1789–1798. doi: 10.1093/eurheartj/ehw113.

Makkar, R. R. *et al.* (2012) ‘Intracoronary cardiosphere-derived cells for heart regeneration after myocardial infarction (CADUCEUS): a prospective, randomised phase 1 trial’, *The Lancet*, 379(9819), pp. 895–904. doi: 10.1016/S0140-6736(12)60195-0.

Malenica, M. *et al.* (2021) ‘Perspectives of microscopy methods for morphology characterisation of extracellular vesicles from human biofluids’, *Biomedicines*, 9(6), p. 603. doi: 10.3390/BIOMEDICINES9060603.

Malik, Z. A. *et al.* (2013) ‘Cardiac myocyte exosomes: stability, HSP60, and proteomics.’, *American Journal of Physiology: Heart and Circulatory Physiology*, 304(7), pp. H954-65. doi: 10.1152/ajpheart.00835.2012.

Mao, G. and Xu, X. (2020) ‘Exosomes Derived From Senescent Cells Promote Cellular Senescence’, *Innovation in Aging*. Oxford University Press, 4(Suppl 1), p. 132. doi: 10.1093/GERONI/IGAA057.435.

Marber, M. S. *et al.* (1993) ‘Cardiac stress protein elevation 24 hours after brief ischemia or heat stress is associated with resistance to myocardial infarction.’, *Circulation*, 88(3), pp. 1264–72. doi: 10.1161/01.cir.88.3.1264.

Marote, A. *et al.* (2016) ‘MSCs-derived exosomes: cell-secreted nanovesicles with regenerative potential’, *Frontiers in Pharmacology*, 7, p. 231. doi: 10.3389/fphar.2016.00231.

May, T., Hauser, H. and Wirth, D. (2004) ‘Transcriptional control of SV40 T-antigen expression allows a complete reversion of immortalization’, *Nucleic Acids Research*, 32(18), p. 5529. doi: 10.1093/NAR/GKH887.

Mayourian, J. *et al.* (2017) ‘Experimental and computational insight into human mesenchymal stem cell paracrine signaling and heterocellular coupling effects on cardiac contractility and arrhythmogenicity’, *Circulation Research*, 121(4), pp. 411–423. doi: 10.1161/CIRCRESAHA.117.310796.

McGinley, L. *et al.* (2011) ‘Lentiviral vector mediated modification of mesenchymal stem cells & enhanced survival in an in vitro model of ischaemia’, *Stem Cell Research & Therapy*, 2(2), p. 12. doi: 10.1186/SCRT53.

McMahon, A., Lu, H. and Butovich, I. (2013) ‘The spectrophotometric sulfo-phospho-vanillin assessment of total lipids in human meibomian gland secretions’, *Lipids*, 48(5), pp. 513–525. doi: 10.1007/S11745-013-3755-9.

Meldolesi, J. (2018) ‘Exosomes and ectosomes in intercellular communication’, *Current Biology*, pp. R435–R444. doi: 10.1016/j.cub.2018.01.059.

Melief, S. M. *et al.* (2013) ‘Adipose tissue-derived multipotent stromal cells have a higher immunomodulatory capacity than their bone marrow-derived counterparts’, *Stem Cells Translational Medicine*, 2(6), pp. 455–463. doi: 10.5966/SCTM.2012-0184.

Mendis, S. *et al.* (2011) *Global atlas on cardiovascular disease prevention and control*. Geneva : World Health Organization in collaboration with the World Heart Federation and the World Stroke Organization.

Miao, C. *et al.* (2017) ‘A brief review: the therapeutic potential of bone marrow mesenchymal stem cells in myocardial infarction’, *Stem Cell Research and Therapy*, 8(1), pp. 1–6. doi: 10.1186/S13287-017-0697-9/METRICS.

Mirotsou, M. *et al.* (2011) ‘Paracrine mechanisms of stem cell reparative and regenerative actions in the heart.’, *Journal of Molecular and Cellular Cardiology*, 50(2), pp. 280–9. doi: 10.1016/j.yjmcc.2010.08.005.

Mitchell, M. I. *et al.* (2021) ‘Extracellular Vesicle Capture by AnTibody of CHoice and Enzymatic Release (EV-CATCHER): a customizable purification assay designed for small-RNA biomarker identification and evaluation of circulating small-EVs’, *Journal of Extracellular Vesicles*, 10(8), p. e12110. doi: 10.1002/JEV2.12110.

Momen-Heravi, F. *et al.* (2012) ‘Impact of biofluid viscosity on size and sedimentation efficiency of the isolated microvesicles’, *Frontiers in Physiology*, 3. doi: 10.3389/FPHYS.2012.00162.

Monguió-Tortajada, M. *et al.* (2017) ‘Nanosized UCMSC-derived extracellular vesicles but not conditioned medium exclusively inhibit the inflammatory response of stimulated T cells: implications for nanomedicine’, *Theranostics*, 7(2), pp. 270–284. doi: 10.7150/thno.16154.

Moran, A. E. *et al.* (2014) ‘The global burden of ischemic heart disease in 1990 and 2010’, *Circulation*, pp. 1493–1501. doi: 10.1161/CIRCULATIONAHA.113.004046.

Morishita, M. *et al.* (2015) ‘Quantitative analysis of tissue distribution of the B16BL6-derived exosomes using a streptavidin-lactadherin fusion protein and Iodine-125-Labeled biotin derivative after intravenous injection in mice’, *Journal of Pharmaceutical Sciences*. Elsevier Masson SAS, 104(2), pp. 705–713. doi: 10.1002/jps.24251.

Mount, S. and Davis, D. R. (2016) ‘Electrical effects of stem cell transplantation for ischaemic cardiomyopathy: friend or foe?’, *Journal of Physiology*, 594(9), pp. 2511–2524. doi: 10.1113/JP270540.

Muir, K. W. *et al.* (2020) ‘Intracerebral implantation of human neural stem cells and motor recovery after stroke: multicentre prospective single-arm study (PISCES-2)’, *Journal of Neurology, Neurosurgery and Psychiatry*. doi: 10.1136/jnnp-2019-322515.

Muramatsu, H. *et al.* (2022) ‘Lyophilization provides long-term stability for a lipid nanoparticle-formulated, nucleoside-modified mRNA vaccine’, *Molecular therapy : the journal of the American Society of Gene Therapy*. Mol Ther, 30(5), pp. 1941–1951. doi: 10.1016/J.YMTHE.2022.02.001.

Murphy, M. P. (2009) ‘How mitochondria produce reactive oxygen species.’, *The Biochemical Journal*, 417(1), pp. 1–13. doi: 10.1042/BJ20081386.

Musumeci, T. *et al.* (2018) ‘Tangential flow filtration technique: an overview on nanomedicine applications’, *Pharmaceutical Nanotechnology*, 6(1), pp. 48–60. doi: 10.2174/2211738506666180306160921.

Muyldermans, S. (2013) ‘Nanobodies: natural single-domain antibodies’, *Annual Review of Biochemistry*, 82, pp. 775–797. doi: 10.1146/ANNUREV-BIOCHEM-063011-092449.

Naghavi, M. *et al.* (2017) ‘Global, regional, and national age-sex specifc mortality for 264 causes of death, 1980-2016: a systematic analysis for the Global Burden of Disease Study 2016’, *The Lancet*, 390(10100), pp. 1151–1210. doi: 10.1016/S0140-6736(17)32152-9.

Nigro, P. *et al.* (2018) ‘Cell therapy for heart disease after 15 years: unmet expectations.’, *Pharmacological Research*, 127, pp. 77–91. doi: 10.1016/j.phrs.2017.02.015.

Nooh, M. M. and Bahouth, S. W. (2017) ‘Visualization and quantification of GPCR trafficking in mammalian cells by confocal microscopy’, *Methods in Cell Biology*, 142, pp. 67–78. doi: 10.1016/BS.MCB.2017.07.010.

Oliveira, P. H., da Silva, C. L. and Cabral, J. M. S. (2014) ‘Concise review: Genomic instability in human stem cells: current status and future challenges’, *Stem Cells*, 32(11), pp. 2824–2832. doi: 10.1002/stem.1796.

Omary, M. A. and Patterson, H. H. (2017) ‘Luminescence, theory’, *Encyclopedia of Spectroscopy and Spectrometry*. Academic Press, pp. 636–653. doi: 10.1016/B978-0-12-803224-4.00193-X.

Ong, S. B. *et al.* (2015) ‘The mitochondrial permeability transition pore and its role in myocardial ischemia reperfusion injury’, *Journal of Molecular and Cellular Cardiology*, pp. 23–34. doi: 10.1016/j.yjmcc.2014.11.005.

Orlic, D. *et al.* (2001) ‘Bone marrow cells regenerate infarcted myocardium.’, *Nature*, 410(6829), pp. 701–5. doi: 10.1038/35070587.

Osteikoetxea, X. *et al.* (2015) ‘Improved characterization of EV preparations based on protein to lipid ratio and lipid properties’, *PLOS ONE*, 10(3), p. e0121184. doi: 10.1371/JOURNAL.PONE.0121184.

Otsuka, F. *et al.* (2014) ‘Has our understanding of calcification in human coronary atherosclerosis progressed?’, *Arteriosclerosis, Thrombosis, and Vascular Biology*, 34(4), pp. 724–736. doi: 10.1161/ATVBAHA.113.302642.

Padilla, F. *et al.* (2003) ‘Protection afforded by ischemic preconditioning is not mediated by effects on cell-to-cell electrical coupling during myocardial ischemia-reperfusion.’, *American Journal of Physiology. Heart and Circulatory Physiology*, 285(5), pp. H1909-16. doi: 10.1152/ajpheart.00438.2003.

Panel, M., Ghaleh, B. and Morin, Di. (2017) ‘Ca2+ ionophores are not suitable for inducing mPTP opening in murine isolated adult cardiac myocytes’, *Scientific Reports*, 7(1). doi: 10.1038/s41598-017-04618-4.

Peng, T. I. and Jou, M. J. (2010) ‘Oxidative stress caused by mitochondrial calcium overload’, in *Annals of the New York Academy of Sciences*. Blackwell Publishing Inc., pp. 183–188. doi: 10.1111/j.1749-6632.2010.05634.x.

Perez-Hernandez, D. *et al.* (2013) ‘The intracellular interactome of tetraspanin-enriched microdomains reveals their function as sorting machineries toward exosomes’, *The Journal of Biological Chemistry*, 288(17), pp. 11649–11661. doi: 10.1074/JBC.M112.445304.

Perrino, C. *et al.* (2017) ‘Epigenomic and transcriptomic approaches in the post-genomic era: path to novel targets for diagnosis and therapy of the ischaemic heart? Position Paper of the European Society of Cardiology Working Group on Cellular Biology of the Heart’, *Cardiovasc Res*, 113(7), pp. 725–736. doi: 10.1093/cvr/cvx070.

Petronilli, V. *et al.* (1999) ‘Transient and long-lasting openings of the mitochondrial permeability transition pore can be monitored directly in intact cells by changes in mitochondrial calcein fluorescence’, *Biophysical Journal*. doi: 10.1016/S0006-3495(99)77239-5.

Phelps, J. *et al.* (2018) ‘Bioprocessing of mesenchymal stem cells and their derivatives: eoward cell-free therapeutics’, *Stem Cells International*. doi: 10.1155/2018/9415367.

Phinney, D. G. and Senseḃe, L. (2013) ‘Mesenchymal stromal cells: misconceptions and evolving concepts’, *Cytotherapy*, 15(2), pp. 140–145. doi: 10.1016/J.JCYT.2012.11.005.

Piñero, J. *et al.* (1997) ‘Apoptotic and necrotic cell death are both induced by electroporation in HL60 human promyeloid leukaemia cells’, *Apoptosis*, 2(3), pp. 330–336. doi: 10.1023/A:1026497306006.

Pirkmajer, S. and Chibalin, A. V (2011) ‘Serum starvation: caveat emptor’, *American Journal of Physiology: Cell Physiology*, 301(2), pp. C272-C279. doi: 10.1152/ajpcell.00091.2011.

Pollock, K. *et al.* (2006) ‘A conditionally immortal clonal stem cell line from human cortical neuroepithelium for the treatment of ischemic stroke’, *Experimental Neurology*, 199(1), pp. 143–155. doi: 10.1016/j.expneurol.2005.12.011.

Prasanna, G. L. and Panda, T. (1997) ‘Electroporation: basic principles, practical considerations and applications in molecular biology’, *Bioprocess Engineering*, 16(5), pp. 261–264. doi: 10.1007/S004490050319.

Raposo, G. and Stoorvogel, W. (2013) ‘Extracellular vesicles: exosomes, microvesicles, and friends’, *Journal of Cell Biology*, pp. 373–383. doi: 10.1083/jcb.201211138.

Rasola, A. and Bernardi, P. (2011) ‘Mitochondrial permeability transition in Ca2+-dependent apoptosis and necrosis’, *Cell Calcium*, pp. 222–233. doi: 10.1016/j.ceca.2011.04.007.

Richardson, W. J. *et al.* (2015) ‘Physiological implications of myocardial scar structure’, *Comprehensive Physiology*, 5(4), pp. 1877–1909. doi: 10.1002/cphy.c140067.

Ripa, R. S. *et al.* (2007) ‘Short- and long-term changes in myocardial function, morphology, edema, and infarct mass after ST-segment elevation myocardial infarction evaluated by serial magnetic resonance imaging’, *American Heart Journal*. Mosby, 154(5), pp. 929–936. doi: 10.1016/J.AHJ.2007.06.038.

Roger, V. L. *et al.* (2010) ‘Trends in incidence, severity, and outcome of hospitalized myocardial infarction.’, *Circulation*, 121(7), pp. 863–9. doi: 10.1161/CIRCULATIONAHA.109.897249.

Rostovskaya, M. and Anastassiadis, K. (2012) ‘Differential expression of surface markers in mouse bone marrow mesenchymal stromal cell subpopulations with distinct lineage commitment’, *PloS ONE*, 7(12). doi: 10.1371/JOURNAL.PONE.0051221.

Ruiz-Meana, M. *et al.* (1999) ‘Propagation of cardiomyocyte hypercontracture by passage of Na+ through gap junctions’, *Circulation Research*, 85(3), pp. 280–287. doi: 10.1161/01.RES.85.3.280.

Ruiz-Meana, M. *et al.* (2009) ‘Role of sarcoplasmic reticulum in mitochondrial permeability transition and cardiomyocyte death during reperfusion.’, *American Journal of Physiology: Heart and Circulatory Physiology*, 297(4), pp. H1281-9. doi: 10.1152/ajpheart.00435.2009.

Sahoo, S. *et al.* (2011) ‘Exosomes from human CD34(+) stem cells mediate their proangiogenic paracrine activity’, *Circulation Research*, 109(7), pp. 724–728. doi: 10.1161/CIRCRESAHA.111.253286.

Scaduto, R. C. and Grotyohann, L. W. (1999) ‘Measurement of mitochondrial membrane potential using fluorescent rhodamine derivatives’, *Biophysical Journal*. doi: 10.1016/S0006-3495(99)77214-0.

Schembri, L. *et al.* (2007) ‘The HA tag is cleaved and loses immunoreactivity during apoptosis’, *Nature Methods*, 4(2), pp. 107–108. doi: 10.1038/nmeth0207-107.

Schindelin, J. *et al.* (2012) ‘Fiji: an open-source platform for biological-image analysis’, *Nature Methods*, 9(7), pp. 676–682. doi: 10.1038/NMETH.2019.

Schmidt, M. *et al.* (2012) ‘25 year trends in first time hospitalisation for acute myocardial infarction, subsequent short and long term mortality, and the prognostic impact of sex and comorbidity: a Danish nationwide cohort study’, *BMJ (Clinical research ed.)*, 344, p. e356. doi: 10.1136/bmj.e356.

Schofield, Z. V. *et al.* (2013) ‘Neutrophils - a key component of ischemia-reperfusion injury’, *Shock*, 40(6), pp. 463–70. doi: 10.1097/SHK.0000000000000044.

Schwartz, L. and Seeley, K. (2022) *Introduction to tangential flow filtration for laboratory and process development applications*. Available at: www.pall.com/contact (Accessed: 16 October 2019).

Shahjouei, S. *et al.* (2016) ‘Middle cerebral artery occlusion model of stroke in rodents: a step-by-step approach’, *Journal of Vascular and Interventional Neurology*, 8(5), pp. 1–8.

Sharma, R. R. *et al.* (2014) ‘Mesenchymal stem or stromal cells: a review of clinical applications and manufacturing practices’, *Transfusion*, 54(5), p. 1418. doi: 10.1111/TRF.12421.

Sheng, S. and Kong, F. (2012) ‘Separation of antigens and antibodies by immunoaffinity chromatography’, *Pharmaucetical Biology*, 50(8), pp. 1038–1044. doi: 10.3109/13880209.2011.653493.

Sinden, J. D. *et al.* (2017) ‘Human neural stem cell therapy for chronic ischemic stroke: charting progress from laboratory to patients’, *Stem Cells and Development*. doi: 10.1089/scd.2017.0009.

Skålén, K. *et al.* (2002) ‘Subendothelial retention of atherogenic lipoproteins in early atherosclerosis’, *Nature*, 417(6890), pp. 750–754. doi: 10.1038/nature00804.

Skotland, T. *et al.* (2019) ‘Exosomes and microvesicles: lipids as key components of their biogenesis and functions: exosomal lipid composition and the role of ether lipids and phosphoinositides in exosome biology’, *Journal of Lipid Research*, 60(1), p. 9. doi: 10.1194/JLR.R084343.

Smit, N. W. and Coronel, R. (2014) ‘Stem cells can form gap junctions with cardiac myocytes and exert pro-arrhythmic effects’, *Frontiers in Physiology*, 5. doi: 10.3389/fphys.2014.00419.

Smith, R. R. uckdesche., Marbán, E. and Marbán, L. (2013) ‘Enhancing retention and efficacy of cardiosphere-derived cells administered after myocardial infarction using a hyaluronan-gelatin hydrogel’, *Biomatter*. doi: 10.4161/biom.24490.

Smyth, T. *et al.* (2015) ‘Biodistribution and delivery efficiency of unmodified tumor-derived exosomes’, *Journal of Controlled Release*, 199, pp. 145–155. doi: 10.1016/j.jconrel.2014.12.013.

Sokolova, V. *et al.* (2011) ‘Characterisation of exosomes derived from human cells by nanoparticle tracking analysis and scanning electron microscopy’, *Colloids and surfaces. B, Biointerfaces*. Colloids Surf B Biointerfaces, 87(1), pp. 146–150. doi: 10.1016/J.COLSURFB.2011.05.013.

Stayton, P. *et al.* (1999) ‘Streptavidin-biotin binding energetics’, *Biomolecular Engineering*, 16(1–4), pp. 39–44. doi: 10.1016/S1050-3862(99)00042-X.

Steinbrecher, U. P. (1988) ‘Role of superoxide in endothelial-cell modification of low-density lipoproteins.’, *Biochimica et Biophysica Acta*, 959(1), pp. 20–30. doi: 10.1016/0005-2760(88)90145-2.

Stevanato, L. *et al.* (2009) ‘c-MycERTAM transgene silencing in a genetically modified human neural stem cell line implanted into MCAo rodent brain’, *BMC Neuroscience*. doi: 10.1186/1471-2202-10-86.

Stoddart, L. A. *et al.* (2015) ‘Application of BRET to monitor ligand binding to GPCRs’, *Nature Methods*, 12(7), p. 661. doi: 10.1038/NMETH.3398.

Stonesifer, C. *et al.* (2017) ‘Stem cell therapy for abrogating stroke-induced neuroinflammation and relevant secondary cell death mechanisms’, *Progress in Neurobiology*. doi: 10.1016/j.pneurobio.2017.07.004.

Stroemer, P. *et al.* (2009) ‘The neural stem cell line CTX0E03 promotes behavioral recovery and endogenous neurogenesis after experimental stroke in a dose-dependent fashion’, *Neurorehabilitation and Neural Repair*. doi: 10.1177/1545968309335978.

Tabas, I. and Lichtman, A. H. (2017) ‘Monocyte-macrophages and T cells in atherosclerosis’, *Immunity*, pp. 621–634. doi: 10.1016/j.immuni.2017.09.008.

Takahashi, Y. *et al.* (2013) ‘Visualization and in vivo tracking of the exosomes of murine melanoma B16-BL6 cells in mice after intravenous injection’, *Journal of biotechnology*. J Biotechnol, 165(2), pp. 77–84. doi: 10.1016/J.JBIOTEC.2013.03.013.

Takov, K. *et al.* (2020) ‘Small extracellular vesicles secreted from human amniotic fluid mesenchymal stromal cells possess cardioprotective and promigratory potential’, *Basic Research in Cardiology*. doi: 10.1007/s00395-020-0785-3.

Takov, K., Yellon, D. M. and Davidson, S. M. (2019) ‘Comparison of small extracellular vesicles isolated from plasma by ultracentrifugation or size-exclusion chromatography: yield, purity and functional potential’, *Journal of Extracellular Vesicles*. doi: 10.1080/20013078.2018.1560809.

Tang, J. *et al.* (2010) ‘Mesenchymal stem cells modified with stromal cell-derived factor 1 alpha improve cardiac remodeling via paracrine activation of hepatocyte growth factor in a rat model of myocardial infarction.’, *Molecules and Cells*, 29(1), pp. 9–19. doi: 10.1007/s10059-010-0001-7.

Tendera, M. *et al.* (2009) ‘Intracoronary infusion of bone marrow-derived selected CD34 +CXCR4+ cells and non-selected mononuclear cells in patients with acute STEMI and reduced left ventricular ejection fraction: results of randomized, multicentre myocardial regeneration by intraco’, *European Heart Journal*, 30(11), pp. 1313–1321. doi: 10.1093/eurheartj/ehp073.

Théry, C. *et al.* (2006) ‘Isolation and characterization of exosomes from cell culture supernatants and biological fluids’, *Current Protocols in Cell Biology*. doi: 10.1002/0471143030.cb0322s30.

Théry, C. *et al.* (2019) ‘Minimal information for studies of extracellular vesicles 2018 (MISEV2018): a position statement of the International Society for Extracellular Vesicles and update of the MISEV2014 guidelines’, *Journal of Extracellular Vesicles*. doi: 10.1080/20013078.2018.1535750.

Thomas, R. J. *et al.* (2009) ‘Automated, serum-free production of CTX0E03: a therapeutic clinical grade human neural stem cell line’, *Biotechnology Letters*. doi: 10.1007/s10529-009-9989-1.

Thygesen, K. *et al.* (2007) ‘Universal definition of myocardial infarction’, *European Heart Journal*, 28(20), pp. 2525–2538. doi: 10.1093/eurheartj/ehm355.

Thygesen, K. *et al.* (2012) ‘Third universal definition of myocardial infarction’, *European Heart Journal*, 33(20), pp. 2551–2567. doi: 10.1093/eurheartj/ehs184.

Tkach, M., Kowal, J. and Théry, C. (2018) ‘Why the need and how to approach the functional diversity of extracellular vesicles’, *Philosophical Transactions of the Royal Society: Biological Sciences*. doi: 10.1098/rstb.2016.0479.

Togliatto, G. *et al.* (2016) ‘Obesity reduces the pro-angiogenic potential of adipose tissue stem cell-derived extracellular vesicles (EVs) by impairing miR-126 content: Impact on clinical applications’, *International Journal of Obesity*, 40(1), pp. 102–111. doi: 10.1038/ijo.2015.123.

Tompa, P. (2012) ‘Intrinsically disordered proteins: a 10-year recap’, *Trends in Biochemical Sciences*, 37(12), pp. 509–516. doi: 10.1016/J.TIBS.2012.08.004.

Tóth, E. *et al.* (2021) ‘Formation of a protein corona on the surface of extracellular vesicles in blood plasma’, *Journal of Extracellular Vesicles*. Wiley-Blackwell, 10(11). doi: 10.1002/JEV2.12140.

Trenkenschuh, E. *et al.* (2022) ‘Enhancing the Stabilization Potential of Lyophilization for Extracellular Vesicles’, *Advanced Healthcare Materials*. John Wiley and Sons Inc, 11(5). doi: 10.1002/ADHM.202100538.

Tseliou, E. *et al.* (2015) ‘Fibroblasts rendered antifibrotic, antiapoptotic, and angiogenic by priming with cardiosphere-derived extracellular membrane vesicles’, *Journal of the American College of Cardiology*, 66(6), pp. 599–611. doi: 10.1016/j.jacc.2015.05.068.

U.S. National Library of Medicine (2022) *Needleman-Wunsch Global Align Nucleotide Sequences*. Available at: https://blast.ncbi.nlm.nih.gov/Blast.cgi?PAGE_TYPE=BlastSearch&PROG_DEF=blastn&BLAST_PROG_DEF=blastn&BLAST_SPEC=GlobalAln&LINK_LOC=BlastHomeLink (Accessed: 15 February 2022).

Veerman, R. E. *et al.* (2021) 'Molecular evaluation of five different isolation methods for extracellular vesicles reveals different clinical applicability and subcellular origin', *Journal of Extracellular Vesicles*, 10(9), p. e12128. doi: 10.1002/JEV2.12128.

Venslauskas, M. S. and Šatkauskas, S. (2015) 'Mechanisms of transfer of bioactive molecules through the cell membrane by electroporation', *European Biophysics Journal*, 44(5), pp. 277–289. doi: 10.1007/S00249-015-1025-X.

Vermeulen, L. *et al.* (2018) 'Endosomal size and membrane leakiness influence proton sponge-based rupture of endosomal vesicles', *ACS Nano*, 12(3), pp. 2332–2345. doi: 10.1021/ACSNANO.7B07583.

Vicencio, J. M. *et al.* (2015) 'Plasma exosomes protect the myocardium from ischemia-reperfusion injury', *Journal of the American College of Cardiology*. 2015/04/18, 65(15), pp. 1525–1536. doi: 10.1016/j.jacc.2015.02.026.

Virág, L. *et al.* (2003) 'Peroxynitrite-induced cytotoxicity: mechanism and opportunities for intervention', *Toxicology Letters*, 140–141, pp. 113–24. doi: 10.1016/s0378-4274(02)00508-8.

Virmani, R. *et al.* (2002) 'Vulnerable plaque: the pathology of unstable coronary lesions', *Journal of Interventional Cardiology*, 15(6), pp. 439–46. Available at: http://www.ncbi.nlm.nih.gov/pubmed/12476646 (Accessed: 13 October 2019).

Visnovitz, T. *et al.* (2019) 'An improved 96 well plate format lipid quantification assay for standardisation of experiments with extracellular vesicles', *Journal of Extracellular Vesicles*, 8(1). doi: 10.1080/20013078.2019.1565263.

Viswanathan, S. *et al.* (2019) 'Mesenchymal stem versus stromal cells: International Society for Cell & Gene Therapy (ISCT®) Mesenchymal Stromal Cell committee position statement on nomenclature', *Cytotherapy*, 21(10), pp. 1019–1024. doi: 10.1016/J.JCYT.2019.08.002.

Wang, X. *et al.* (2014) ‘Cardiomyocytes mediate anti-angiogenesis in type 2 diabetic rats through the exosomal transfer of miR-320 into endothelial cells’, *Journal of Molecular and Cellular Cardiology*, 74, pp. 139–150. doi: 10.1016/j.yjmcc.2014.05.001.

Wang, Y. *et al.* (2015) ‘Exosomes/microvesicles from induced pluripotent stem cells deliver cardioprotective miRNAs and prevent cardiomyocyte apoptosis in the ischemic myocardium’, *International Journal of Cardiology*, 192, pp. 61–69. doi: 10.1016/j.ijcard.2015.05.020.

Webber, J. and Clayton, A. (2013) ‘How pure are your vesicles?’, *Journal of Extracellular Vesicles*. doi: 10.3402/jev.v2i0.19861.

Wen, S. *et al.* (2014) ‘Characterization of constitutive promoters for piggyBac transposon-mediated stable transgene expression in Mesenchymal Stem Cells (MSCs)’, *PLoS ONE*, 9(4). doi: 10.1371/JOURNAL.PONE.0094397.

Williams, A. R. *et al.* (2013) ‘Enhanced effect of combining human cardiac stem cells and bone marrow mesenchymal stem cells to reduce infarct size and to restore cardiac function after myocardial infarction.’, *Circulation*, 127(2), pp. 213–23. doi: 10.1161/CIRCULATIONAHA.112.131110.

Witwer, K. W. *et al.* (2013) ‘Standardization of sample collection, isolation and analysis methods in extracellular vesicle research’, *Journal of extracellular vesicles*. J Extracell Vesicles, 2(1). doi: 10.3402/JEV.V2I0.20360.

Wöhrle, J. *et al.* (2010) ‘Results of intracoronary stem cell therapy after acute myocardial infarction.’, *The American Journal of Cardiology*, 105(6), pp. 804–12. doi: 10.1016/j.amjcard.2009.10.060.

Wright, A., Arthaud-Day, M. L. and Weiss, M. L. (2021) ‘Therapeutic use of mesenchymal stromal cells: the need for inclusive characterization guidelines to accommodate all tissue sources and species’, *Frontiers in Cell and Developmental Biology*, 9, p. 66. doi: 10.3389/FCELL.2021.632717/BIBTEX.

Wu, M. and Yuan, F. (2011) ‘Membrane binding of plasmid DNA and endocytic pathways are involved in electrotransfection of mammalian cells’, *PloS ONE*, 6(6). doi: 10.1371/JOURNAL.PONE.0020923.

Yang, P. C. (2018) ‘Induced pluripotent stem cell (iPSC)-derived exosomes for precision medicine in heart failure’, *Circulation Research*, pp. 661–663. doi: 10.1161/CIRCRESAHA.118.312657.

Yang, Q. *et al.* (2016) ‘Cellular and molecular mechanisms of endothelial ischemia/reperfusion injury: Perspectives and implications for postischemic myocardial protection’, *American Journal of Translational Research*, pp. 765–777.

Yao, S. *et al.* (2009) ‘Improvement of electroporation to deliver plasmid DNA into dental follicle cells’, *Biotechnology Journal*, 4(10), p. 1488. doi: 10.1002/BIOT.200900039.

Yellon, D. M. and Hausenloy, D. J. (2007) ‘Myocardial reperfusion injury’, *The New England Journal of Medicine*, 357(11), pp. 1121–1135. doi: 10.1056/NEJMra071667.

Yuan, Y. *et al.* (2018) ‘Stem cell-derived exosome in cardiovascular diseases: macro roles of micro particles’, *Frontiers in Pharmacology*. doi: 10.3389/fphar.2018.00547.

Zaman, S. and Kovoor, P. (2014) ‘Sudden cardiac death early after myocardial infarction pathogenesis, risk stratification, and primary prevention’, *Circulation*, pp. 2426–2435. doi: 10.1161/CIRCULATIONAHA.113.007497.

Zarovni, N. *et al.* (2015) ‘Integrated isolation and quantitative analysis of exosome shuttled proteins and nucleic acids using immunocapture approaches’, *Methods*, 87, pp. 46–58. doi: 10.1016/J.YMETH.2015.05.028.

Zhang, H. *et al.* (2018) ‘Identification of distinct nanoparticles and subsets of extracellular vesicles by asymmetric flow field-flow fractionation’, *Nature Cell Biology*. doi: 10.1038/s41556-018-0040-4.

Zhao, Y. *et al.* (2015) ‘Exosomes derived from human umbilical cord mesenchymal stem cells relieve acute myocardial ischemic injury’, *Stem Cells International*, 2015, p. 761643. doi: 10.1155/2015/761643.

Zorov, D. B., Juhaszova, M. and Sollott, S. J. (2006) ‘Mitochondrial ROS-induced ROS release: an update and review’, *Biochimica et Biophysica Acta - Bioenergetics*, pp. 509–517. doi: 10.1016/j.bbabio.2006.04.029.

Zwinkels, J. C., DeRose, P. C. and Leland, J. E. (2014) ‘Spectral fluorescence measurements’, *Experimental Methods in the Physical Sciences*, 46, pp. 221–290. doi: 10.1016/B978-0-12-386022-4.00007-8.

Supplementary material

Solutions, materials, instruments, cells, and software	Stock concentration, composition, or comments	Supplier and catalogue number
A23187, calcium ionophore	1mg; diluted later in DMSO	Sigma, C7522
Agar plate	15g bactoagar in 1l Lysogeny broth; autoclaved	N/A
Agarose, low melting point, UltraPure™	It was used for gels meant for DNA purification	Invitrogen, 16520050
ALFA elution peptide	ALFA Selector PE antibody	NanoTag Biotechnologies, N1520-L
Ampicillin sodium salt	Antibiotic	Glentham Life Sciences, GA7355
Anti-actin antibody (C-2)	Antibody against housekeeping protein	Santa Cruz Biotechnology, sc-8432
Anti-ALFA tag antibody, FluoTag-Q	C-terminal biotinylated antibody	NanoTag Biotechnologies, custom-made
Anti-ApoB primary antibody	Rabbit monoclonal antibody (H-300). Dilution: 1:200.	Santa Cruz Biotechnology, sc-25542
Anti-CD9 primary antibody	Mouse monoclonal antibody (M-L13). Dilution: 1:500.	BD Biosciences, 555370
Anti-CD63 primary antibody	Rabbit monoclonal antibody (H5C6). Dilution: 1:200.	BD Biosciences, 556019
Anti-CD81 primary antibody	Mouse monoclonal antibody (JS-81). Dilution: 1:500.	BD Biosciences, 555675

Anti-HSP70 primary antibody	Mouse monoclonal antibody (N27F3-4). Dilution: 1:100.	Santa Cruz Biotechnology, sc-66049
Anti-mouse secondary antibody	Goat anti-mouse polyclonal antibody (biotin). Dilution 1:2,000	Abcam, ab98691
Anti-rabbit secondary antibody	Goat anti-rabbit polyclonal antibody (biotin). Dilution 1:2,000.	Abcam, ab97073
Anti-SV40 T Ag (Pab 108) antibody	Mouse monoclonal antibody. Binds large and small T antigens.	Santa Cruz Biotechnology, sc-148
Basic fibroblast growth factor	Human	Invitrogen, 13256-029
BCA protein assay kit for low concentrations	Used for protein standard curve	Abcam, ab207002
BD Accuri C6 flow cytometer	N/A	BD Biosciences
Bovine serum albumin (BSA)	Blocking agent	Merck, A2153
Bicinchoninic acid assay (BCA) protein assay kit for low concentrations	For protein quantification in exosome samples	Abcam, ab207002
BlueJuice Gel Loading Buffer (10x)	60% glycerol, 60 mM EDTA, 10 mM Tris-HCl (pH 7.6), 0.03% bromphenol blue	ThermoFisher Scientific, 10816015
Bromodeoxyuridine (BrdU)	15mg. Synthetic nucleoside, analogue of thymidine. Used for inhibiting proliferating cells.	Lonza, CC-4519

PierceTM BSA Standard Pre-Diluted Set	For protein assay	ThermoFisher Scientific, 10531674
Cal-520, AM, fluorogenic calcium-sensitive dye	Lipophilic blocking groups of these dyes are cleaved by esterases. Resultant negatively charged dyes are fluorescent. Binding of Cal-520 to calcium greatly enhances its green fluorescence.	Abcam, ab171868
Calcein, AM (acetoxymethyl ester)		Sigma, 17783
CCCP, 2-[2-(3-Chlorophenyl) hydrazinylyidene] propanedinitrile	Inhibitor of oxidative phosphorylation. Diluted in DMSO.	Unknown
Cell culture dishes	Glass bottom	Greiner One, 627965
Claycomb Medium without L-glutamine	Composition as described previously (Claycomb *et al.*, 1998)	Sigma-Aldrich, 51800C
Clifton Ultrasonic Bath	35kHz	VWR International
Cobalt chloride, $CoCl_2$	≥98.0% purity, salt. Dissolved in recording buffer.	Sigma-Aldrich, 60818
Costar strip well plates	High protein binding wells	Cole-Parmer, 2580
Cyclosporin A (CsA)	Diluted in DMSO	Cell Guidance Systems, SM43
Cyclosporin H (CsH)	Diluted in DMSO	Sigma, SML1575-1MG
DELFIA assay buffer	Buffered protein and detergent solution	PerkinElmer, 1244-106

DELFIA enhancement solution	Acidic chelating detergent	PerkinElmer, 1244-104
DELFIA wash concentrate	Tris-HCl buffered salt solution with Tween20	PerkinElmer, 1244-114
Dexamethasone	N/A	Merck, D4902
Dimethyl sulfoxide (DMSO)	Diluent	Sigma-Aldrich, D8418
DMEM/F-12	It is a 1:1 mixture of DMEM and Ham's F-12 nutrient mix. It has high glucose and other DMEM nutrients (see DMEM for H9c2 cells), as well as zinc, hypoxanthine, putrescine, thymidine and other components from Ham's F-12 nutrient mix.	ThermoFisher Scientific, 11320033
DMEM with D-glucose, L-glutamine, and pyruvate (for H9c2 and HEK-293 cells)	110.3mM NaCl, 44.0mM $NaHCO_3$, 25mM glucose, 5.3mM KCl, 1.8mM $CaCl_2$, 1mM $C_3H_3NaO_3$, 0.9mM NaH_2PO_4, 0.8mM MgSO4, 0.25µM $Fe(NO_3)_3$ plus 15 amino acids, 8 vitamins and phenol red	ThermoFisher Scientific, 41966
DMEM with D-glucose, L-glutamine, and pyruvate (for MSCs)	The same as DMEM for H9c2 and HEK-293 cells. However, it has low level (1g/l) of glucose.	ThermoFisher Scientific, 11885084
DNA ladder, 1Kb Plus	100-15,000 base pairs, 18 chromatography-purified DNA fragments	ThermoFisher Scientific, 10787018

DOPC (1,2-Dioleoyl-sn-glycero-3-phosphocholine)	Used for lipid standard curve	Merck, P6354
Doxycycline hyclate	Antibiotic	Merck, D9891
Dynabeads M280	Magnetic beads 2.8µm in diameter; binding capacity: ~10µg biotinylated IgG per 1mg beads.	Invitrogen, 11205D
DynaMag-2 magnet stand	Suitable for 1.5ml Eppendorf tubes	ThermoFisher Scientific, 12321D
Electrophoresis Power Supply	Model 200/2.0	BIO-RAD
Epidermal growth factor (human)	N/A	Sigma-Aldrich, 11376454001
Eppendorf polypropylene graduated microtubes	Resistant to acids	ThermoFisher Scientific, 0030120086
Eu-labelled streptavidin	Used for labelling and detection of biotin-labelled antibodies	PerkinElmer, 1244-30
ExoScan	N/A	NanoView Biosciences
ExoView reader	N/A	NanoView Biosciences
ExoView tetraspanin kits	ExoView chips and antibody mixture	EV-TETRA-C, NanoView Biosciences
ExoViewer	N/A	NanoView Biosciences

FastDigest Green Buffer	It supports 100% activity of all FastDigest restriction enzymes	ThermoFisher Scientific, B72
Fiji	N/A	Open-source project
FlowJo	For analysis of data obtained with flow cytometers	BD Biosciences
Foetal bovine serum (FBS) for HL-1 cells	For cell media	Merck, TMS-016-B; ThermoFisher Scientific, F7524
Foetal bovine serum (FBS) for H9c2, HEK-293 cells and MSCs	For cell media	Merck, F9665
Foetal bovine serum (FBS) for neonatal cardiomyocytes	15ml; part of SingleQuots™ kit	Lonza, CC-4516
Fibronectin	1mg/ml	Sigma-Aldrich, F1141
FLUOstar OMEGA plate reader	For DELFIA	BMG Labtech
Formvar-carbon coated grids	3mm 75 or 300 mesh nickel	Agar Scientific, AGS138N6 or S138N3
G418, Geneticin	Antibiotic	ThermoFisher Sientific, 10131035
Gelatine from bovine skin	For HL-1 cells	Sigma-Aldrich, G9391
GelRed nucleic acid stain 10,000x	Absorbance: 302-312nm;	Merck, SCT123

	Emission: Ethidium Bromide or SYBR	
GeneJET gel extraction kit	The kit is used to purify DNA fragments from 25-20,000 base pairs in size with recovery rates up to 95%.	ThermoFisher Scientific, K0692
Gentamicin/Amphotericin-B	0.2ml; part of SingleQuots™ kit	Lonza, CC-4516
Glutamine	200mM	Sigma-Aldrich, G7513
Glutaraldehyde	Protein crosslinker	Sigma-Aldrich, G5882
Goat anti-mouse IgG, 5nm gold	Secondary antibody	BBI Solutions, EM.GMHL5
GoTaq DNA Polymerase	Taq DNA polymerase; part of GoTaq Colorless Master Mix	Promega, M7122
GXM-XDS401 inverted fluorescence biological microscope	Brightfield and fluorescent microscope	GT Vision
Horse serum	15ml; part of SingleQuots™ kit	Lonza, CC-4516
Human albumin	N/A	Grifols
Human insulin	N/A	Sigma-Aldrich, 91077C
Human transferrin	Mediates iron transportation to cells.	Sigma, T8158
Hydrogen peroxide (H2O2)	Stock is 30% (w/w) in water.	Sigma, H1009
IRdye 680LT infrared secondary antibody	Goat anti-mouse or anti-rabbit antibody.	LICOR

	Dilution 1:20,000.	
IRdye 800CW infrared secondary antibody	Goat anti-mouse or anti-rabbit antibody. Dilution 1:15,000.	LICOR
JEM-1400 transmission electron microscope and software	N/A	Joel Ltd.
Joel 1010 transmission electron microscope and software	N/A	Joel Ltd.
KflI	FastDigest restriction enzyme	ThermoFisher Scientific, FD2164
Laemmli	Reducing and denaturating blue-coloured agent which gives proteins total negative charge	Sigma, 38733
Laminin (mouse)	0.5-2.0mg/ml	ThermoFisher Scientific, 23017015
LAS AF software	Software for confocal microscope; software version is v.2.6.3.8173	Leica Microsystems
Leica TCS SP5 microscope	Confocal microscope	Leica Microsystems
LVis absorbance microplate	Allows low-volume protein quantification	BMG Labtech, LVis Plate
Lysis buffer (pH 7.4)	% IGEPAL (NP40), 30mM NaCl, 100mM Tris (pH6.8) in distilled water	N/A

Lysogeny broth	10g tryptone, 10g NaCl, 5g yeast extract, topped to 1l with distilled water; pH7; autoclaved	N/A
(2-)Mercaptoethanol	It reduces protein disulphide bonds.	Sigma-Aldrich, M6250
MitoParaquat (MitoPQ)	5mg; diluted later in DMSO	Abcam, ab146819
MitoSOX red mitochondrial superoxide indicator	50ug; diluted later in DMSO	ThermoFisher, M36008
MluI	FastDigest restriction enzyme	ThermoFisher Scientific, FD0564
Nano-Glo Dual-Luciferase Reporter Assay System	It is used to measure firefly and NanoLuc luminescence.	Promega, N1620
NanoSight CMOS camera	Complementary metal oxide semiconductor	C11440-50B, Hamamatsu Corporation
NanoSight laser unit	488nm (blue)	Malvern Panalytical
NanoSight LM10 NTA instrument	Used to determine size and quantity of nanoparticles	Malvern Panalytical
NanoSight software	v.3.1	Malvern Panalytical
NanoSight syringe pump	Used to push sample at constant speed	Malvern Panalytical
Neon™ Transfection System Pipette	Designed for use with Neon® Transfection System	ThermoFisher Scientific, MPP100
Neon™ Transfection System	Transfection of 10µl cell solution. The kit contains Resuspension Buffer R and tips for transfection.	ThermoFisher Scientific, MPK1025

Neon™ Transfection System Pipette Station	Designed for use with Neon™ Transfection System Pipette	ThermoFisher Scientific, MPS100
NheI	FastDigest restriction enzyme	ThermoFisher Scientific, FD0973
Nitrocellulose membrane Amersham Protran Premium	0.45µM pore size	GE Healthcare Life Sciences, 10600013
Norepinephrine bitartrate salt	For HL-1 cells	Sigma-Aldrich, A0937
Novex™ mini gels, 4-20% Tris-glycine, 15 WedgeWells	Polyacrylamide gels	ThermoFisher Scientific, XP04205BOX
Nuclease-free water	Used for molecular biology	ThermoFisher Scientific, AM9938
NuPAGE LDS sample buffer (4X)	It contains Coomassie G250 and phenol red tracking dyes. It is used to prepare samples for denaturation.	ThermoFisher Scientific, NP0007
Odyssey blocking buffer in TBS	Saline used for membrane blocking	LI-COR, 927-50000
Odyssey Infrared Imager and software	Software version is v.3.0.30	LI-COR
OMEGA Data Analysis	v.3.02R2	BMG Labtech
OMEGA Mars	v.8.10R2	BMG Labtech
Penicillin/Streptomycin	10^4U/ml of penicillin and 10^4µg/ml of streptomycin	Sigma-Aldrich, P4333
PHERAstar plate reader	N/A	BMG Labtech
PHERAstar plate reader software	v.4.00R4	BMG Labtech

Phosphate buffered saline (PBS; calcium and magnesium free), Dulbecco's	8g/l NaCl, 1.15g/l Na_2HPO_4, 0.2g/l $CaCl_2x2H_2O$, 0.2g/l $MgCl_2x6H_2O$	Sigma-Aldrich, D8537
Precision Plus Protein Dual Colour Standard	10 stained recombinant proteins (10–250 kD)	BIO-RAD, 161-0374
Progesterone	N/A	Sigma-Aldrich, P0130
Polyethylenimine (PEI), Alfa Aesar™	25kDa, linear	ThermoFisher Scientific, 11460630
PowerPac high current power supply	Used for electrophoresis	BIO-RAD
Putrescine dihydrochloride	A precursor of spermine, which is needed for cellular metabolism	Sigma-Aldrich, P7505
qEVoriginal column/35nm	~35nm pore size	SP5-GBP
QIAGEN Plasmid Maxi Kit	It can purify up to 500µg plasmid and uses 100-500 bacterial culture volume	Qiagen, 12162
QIAGEN Plasmid Mini Kit	It can purify up to 20µg plasmid and uses 3-10 bacterial culture volume	Qiagen, 12125
Quick CIP (calf intestinal alkaline phosphatase)	It is used for dephosphorylation of DNA or RNA ends.	New England BioLabs, M0525S
Rat cardiomyocyte basal medium	200ml	Lonza, CC-3275

Rat cardiac myocyte cells	4,000,000cells/vial; ≥85% purity; display beating at 24h in culture	Lonza, R-CM-561
Recording ischaemic buffer (pH 7.4)	156mM NaCl, 10mM HEPES, 10mM glucose, 3mM KCl, 2mM $MgSO_4$x7H O, 2mM $CaCl_2$, 1.25mM K_2HPO_4	N/A
10xRunning buffer	10g SDS, 30.3g Tris base, 144.2g glycine, 1l distilled water	N/A
Running buffer	100ml 10xRunning buffer, 900ml distilled water	N/A
Sodium selenite	N/A	Sigma-Aldrich, 214485
Spectrum hollow fiber filter	100kDa, hollow-fibre polyethersulfone (mPES)	Repligen, S02-E100-05-N
Stericup-GP sterile vacuum filtration system	0.22 µm pore size, polyethersulfone membrane	Millipore, SCGPU05RE
Supplemented Claycomb	1% penicillin/streptomycin, 10% FBS for HL-1 cells, 0.1mM norepinephrine, 2mM L-glutamine in Claycomb Medium without L-glutamine	N/A
Supplemented DMEM	1% penicillin/streptomycin, 10% FBS in DMEM with D-glucose	N/A
Syto60	Red fluorescent nucleic acid stain	ThermoFisher Scientific, S11342

T4 DNA ligase	5U/µl. T4 ligase facilitates formation of phosphodiester bond between juxtaposed 5'-phosphate and 3'-hydroxyl termini in double stranded DNA.	ThermoFisher Scientific, EL0011
10xTris buffered saline (TBS), pH 7.6	24.2g Tris base, 80g NaCl, 1l distilled water	N/A
Tris buffered saline (TBS)	100ml 10xTBS, 900ml distilled water	N/A
Tris-EDTA (TE) buffer	10mM Tris-Cl (pH8) and 1mM EDTA (pH8) in distilled water	N/A
Tetramethylrhodamine, methyl ester (TMRM)	Cell-permeant cationic red-orange, fluorescent dye which gets mainly sequestered in mitochondria.	ThermoFisher Scientific, T668
10xTransfer buffer	30.3g Tris base, 144.2g glycine, 1l distilled water	N/A
Transfer buffer	100ml 10xTransfer buffer, 200ml methanol, 700ml distilled water	N/A
Tris-acetate-EDTA (TAE) buffer	2M Tris base, 5.71% glacial acid, 0.05M EDTA, topped with deionized water to make 50x TAE buffer (pH8.5) → 1x TAE prepared in deionized water	N/A
Triton X-100	Mild detergent. Diluted in PBS.	Sigma-Aldrich, X100

TrypLE™ Express Enzyme	Recombinant trypsin	ThermoFisher Scientific, 12604013
Tween20	Detergent	Sigma, P2287
Uranyl-oxalate	Negative stain; pH7	Thomas Scientific, C993L46
Vanillin	N/A	Sigma-Aldrich, V1104
Vibra-Cell Ultrasonic Liquid Processor	Sonicator	VWR
Vivaspin 15R	30,000MWCO, 15ml volume, hydrosart	Sartorius, VS15RH22
Vivaspin 2	30,000MWCO, 2ml volume, hydrosart	Sartorius, VS02H21
W531 (pLenti PGK Neo DEST)	Plasmid which has PGK promoter	Addgene, 19067
XbaI	FastDigest restriction enzyme	ThermoFisher Scientific, FD0684

Supplementary table 1. The list of solutions, chemicals, bioactive molecules, instruments, and software used in this project.

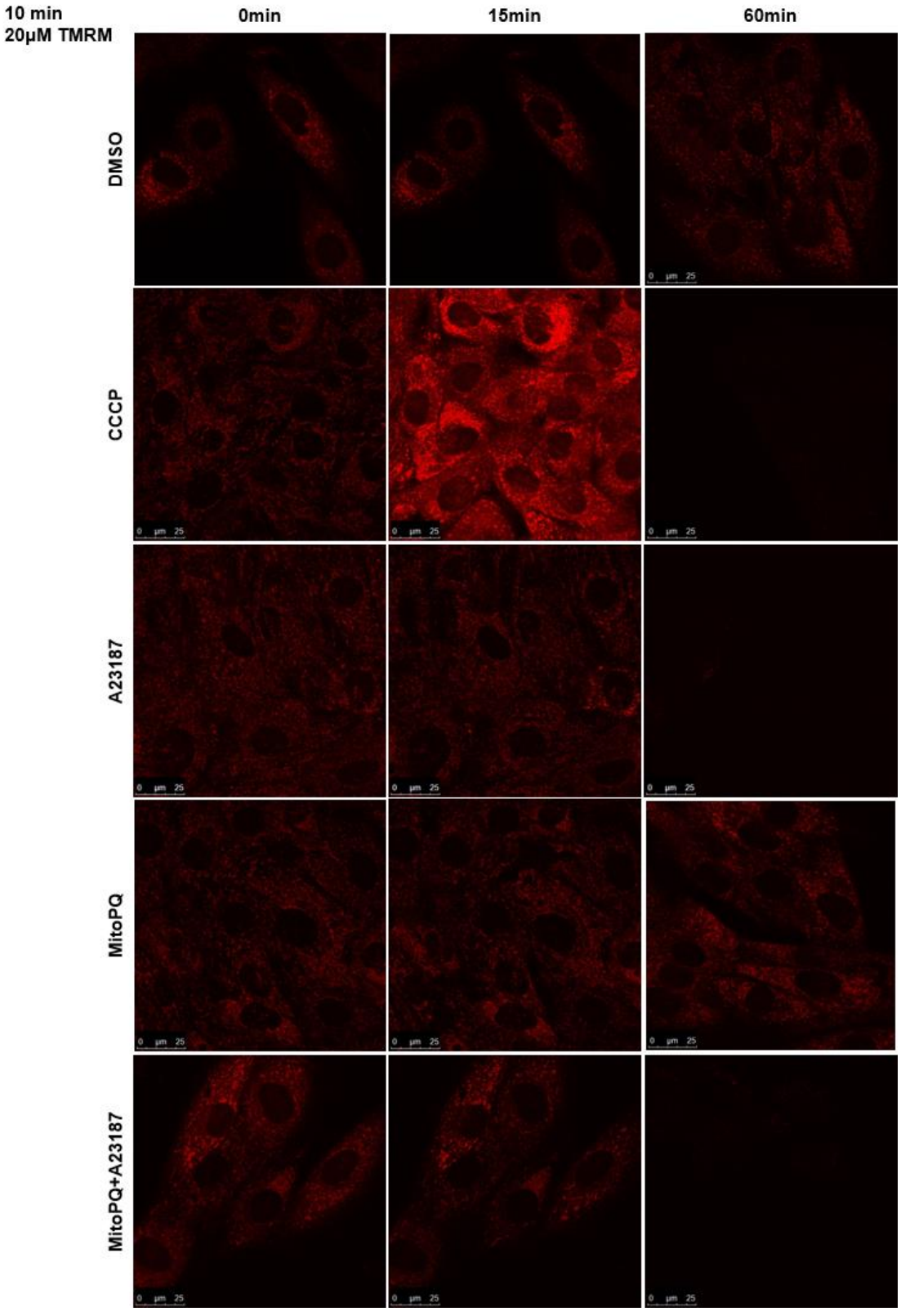
10 min
20μM TMRM
0min
15min
60min
DMSO
CCCP
A23187
MitoPQ
MitoPQ+A23187

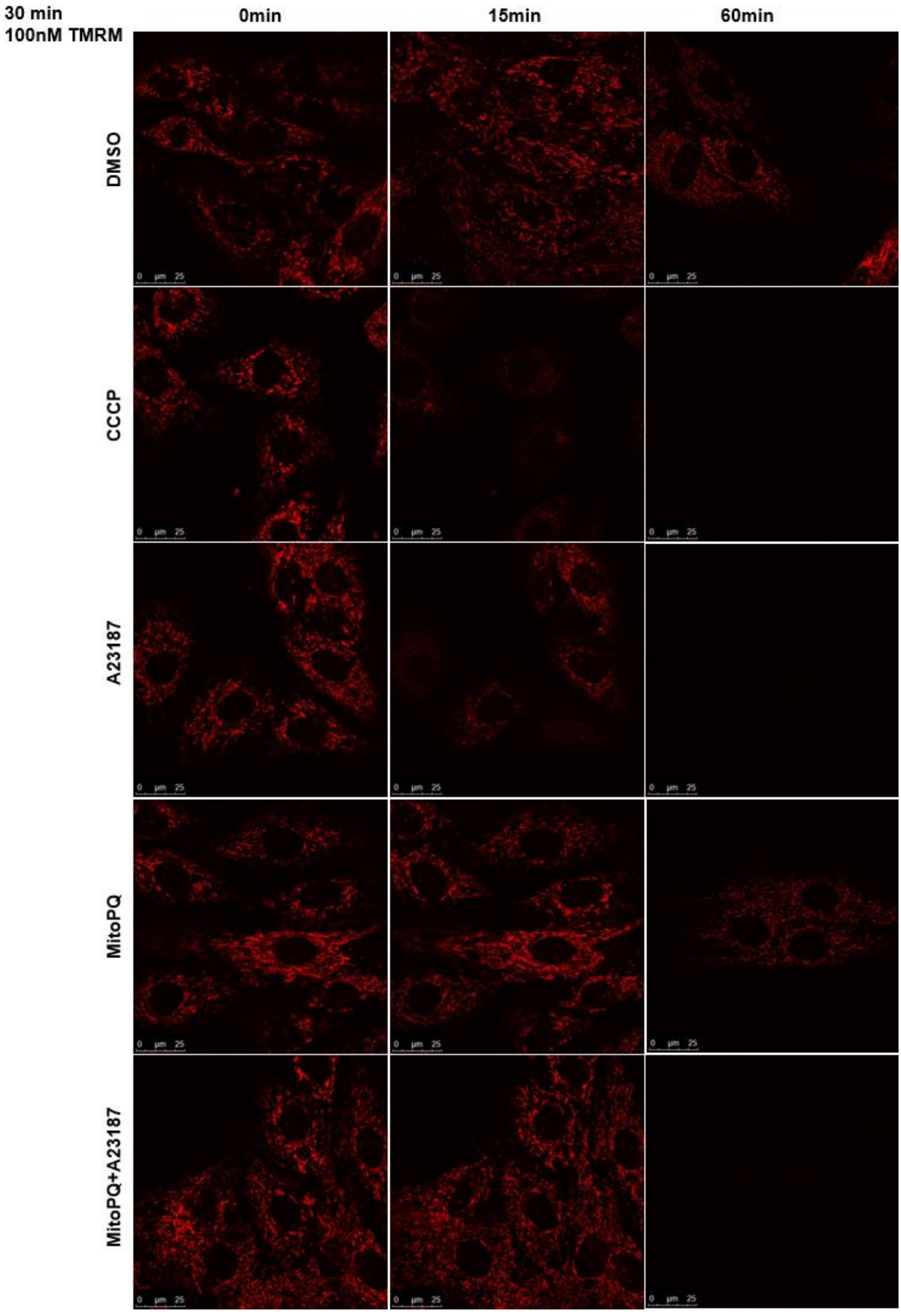
30 min
100nM TMRM
0min
15min
60min
DMSO
CCCP
A23187
MitoPQ
MitoPQ+A23187

Supplementary Figure 1. Effect of MitoPQ and A23187 on mPTP opening in H9c2 cells monitored with confocal microscope.

H9c2 cardiac myoblasts were treated with 20µM or 100nM TMRM for 10min or 30min, respectively. Then, cells were washed with PBS and imaged (0min reading). Immediately, dishes with H9c2 cells were treated with 10µM MitoPQ and/or A23187, or 1µM CCCP. DMSO was used as a negative control. Then, cells were imaged 15min and 60min after the drugs were added.

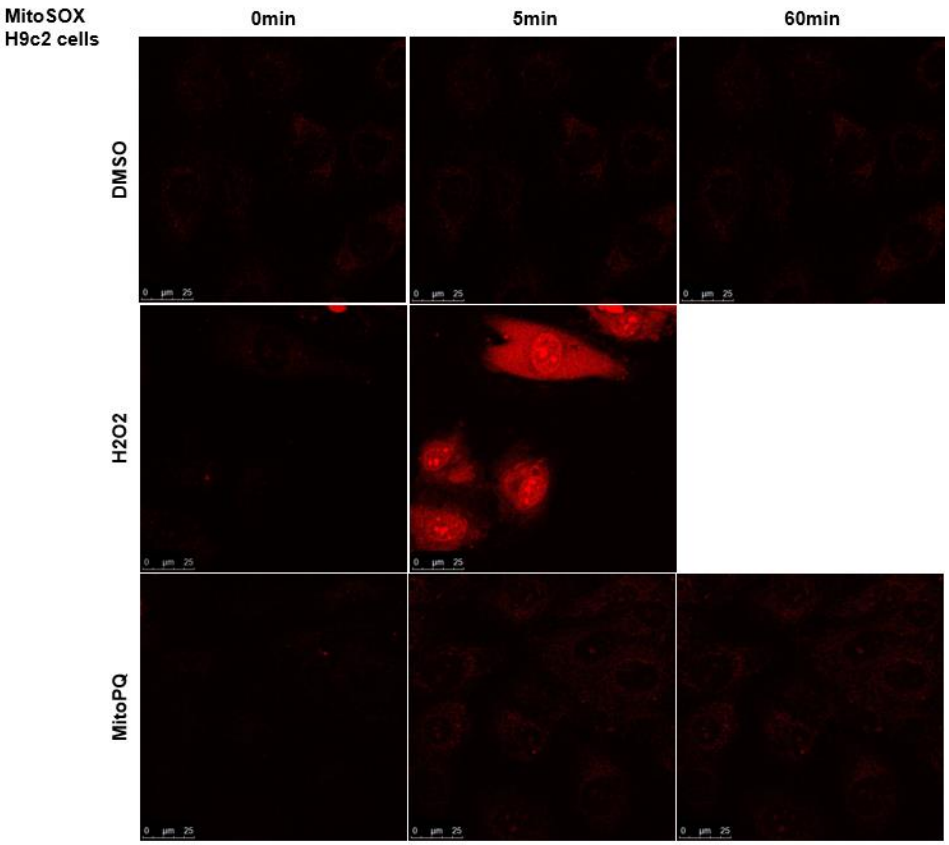
MitoSOX
H9c2 cells
0min
5min
60min
DMSO
H2O2
MitoPQ

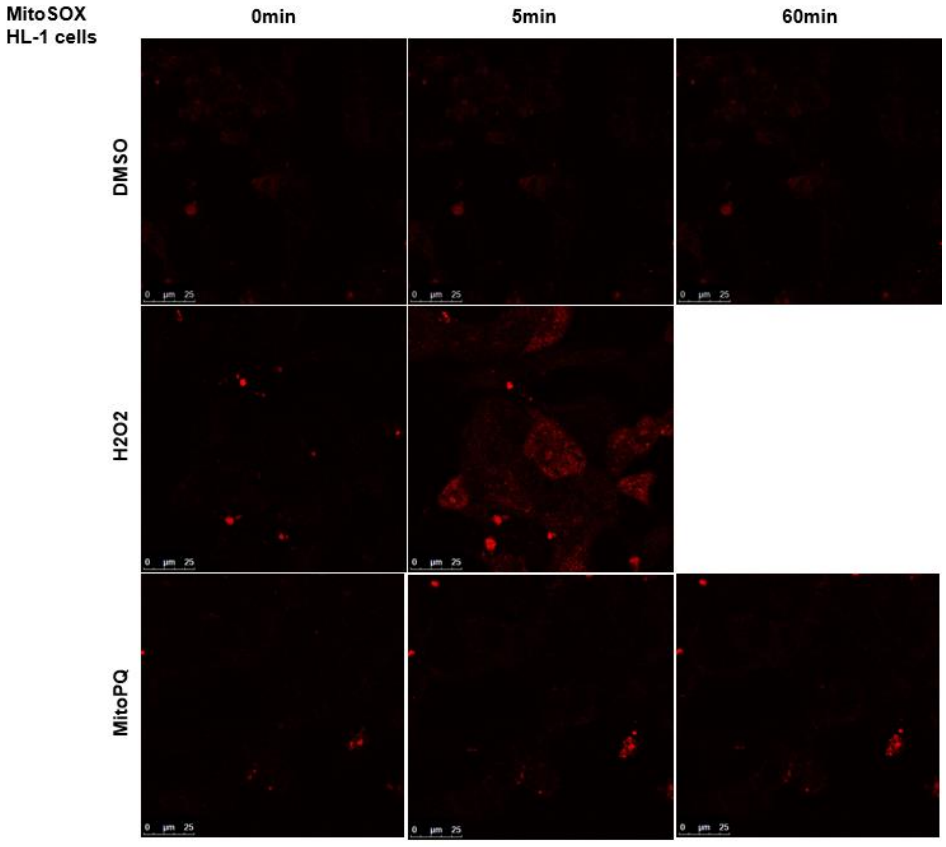
MitoSOX
HL-1 cells
0min
5min
60min
DMSO
H2O2
MitoPQ

Supplementary Figure 2. Effect of MitoPQ and A23187 on ROS levels in H9c2 and HL-1 cells monitored with confocal microscope.

H9c2 cardiac myoblasts and HL-1 cardiac muscle cells were treated with 1µM MitoSOX for 30min. Then, cells were washed with PBS and imaged (0min reading). Immediately, dishes with H9c2 cells were treated with 10µM MitoPQ. DMSO and 1M H_2O_2 were used as negative and positive controls. Then, cells were imaged 5min and 60min after the drugs were added.

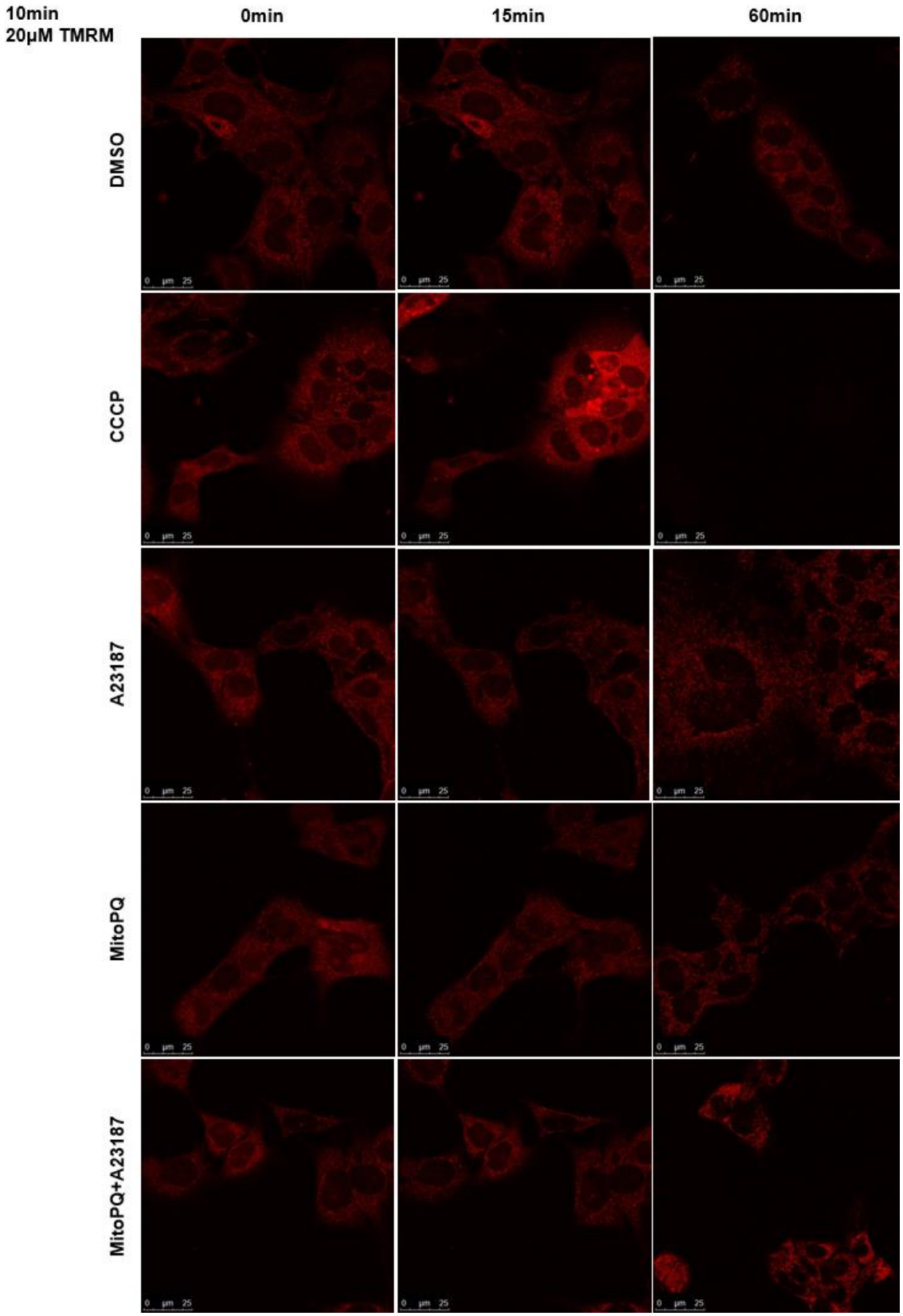
10min
20μM TMRM
0min
15min
60min
DMSO
CCCP
A23187
MitoPQ
MitoPQ+A23187

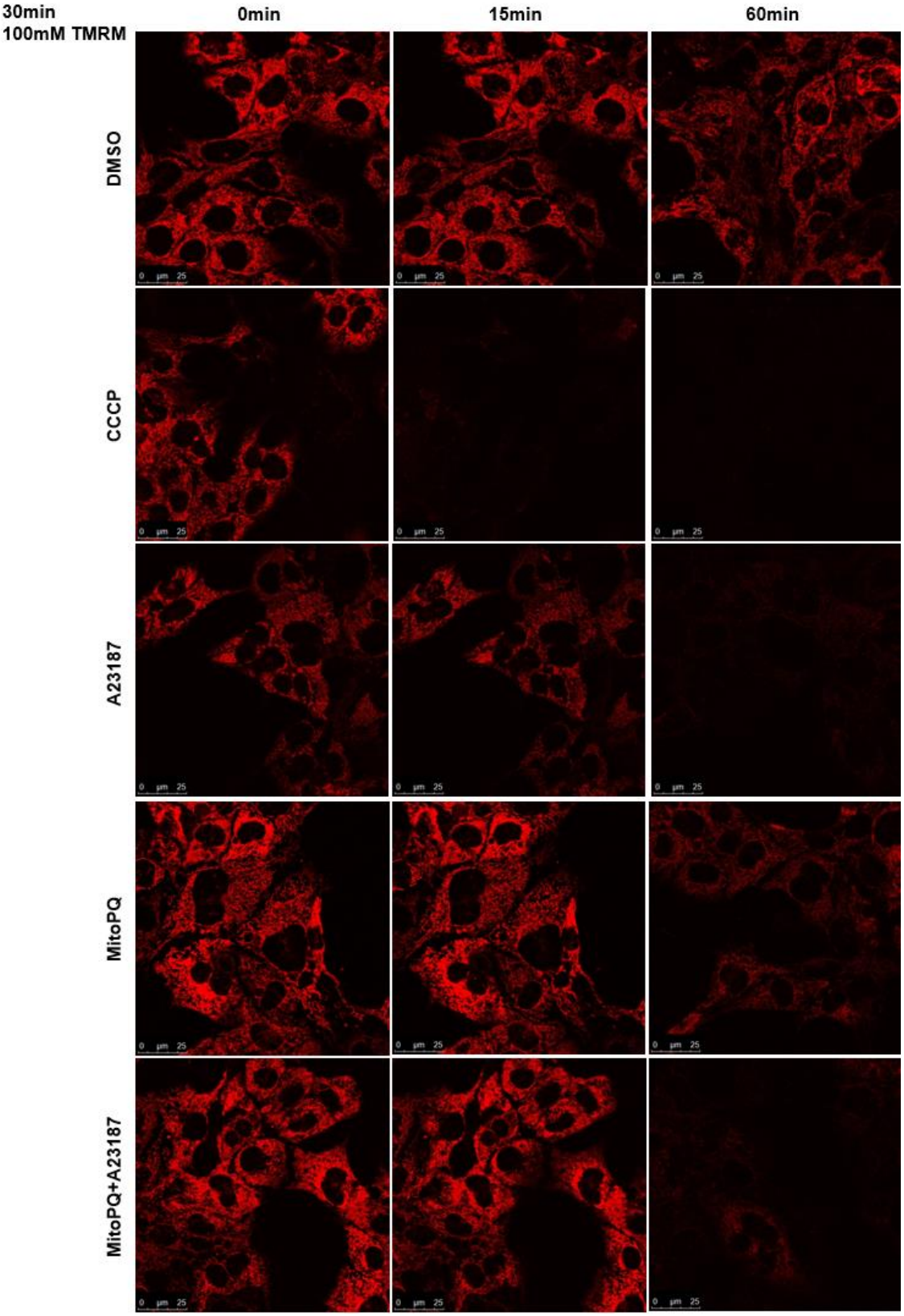
30min
100mM TMRM
0min
15min
60min
DMSO
CCCP
A23187
MitoPQ
MitoPQ+A23187

Supplementary Figure 3. Effect of MitoPQ and A23187 on mPTP opening in HL-1 cells monitored with confocal microscope.

HL-1 cardiac muscle cells were treated with 20µM or 100nM TMRM for 10min or 30min, respectively. Then, cells were washed with PBS and imaged (0min reading). Immediately, dishes with HL-1 cells were treated with 10µM MitoPQ and/or A23187, or 1µM CCCP. DMSO was used as a negative control. Then, cells were imaged 15min and 60min after the drugs were added.

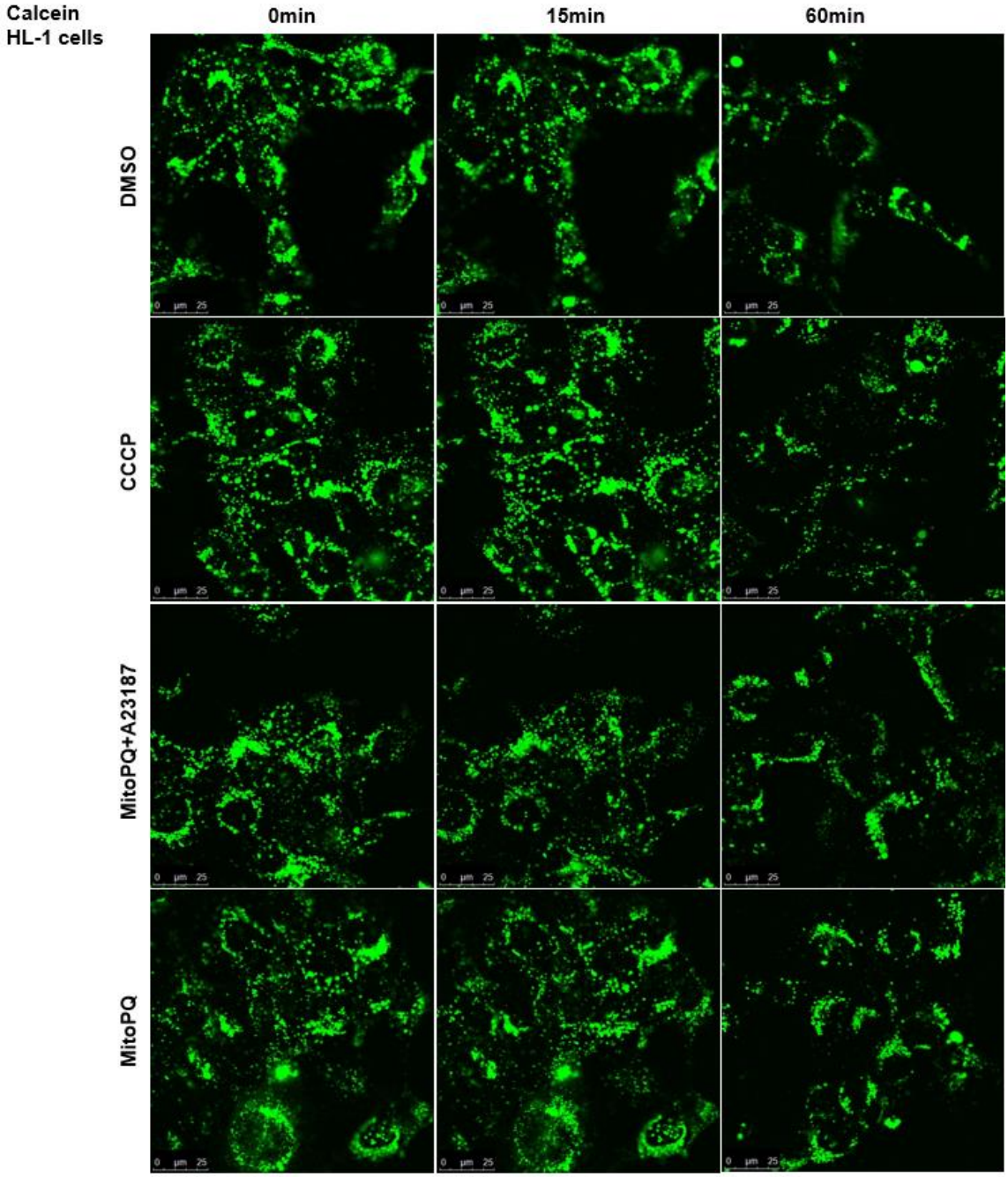
Calcein
HL-1 cells
0min
15min
60min
DMSO
CCCP
MitoPQ+A23187
MitoPQ

Supplementary Figure 4. H9c2 and HL-1 cells in calcein assay monitored with confocal microscope.

H9c2 cardiac myoblasts and HL-1 cardiac muscle cells were treated with 1μM calcein in 1M $CoCl_2$ for 15min. Then, de-esterification of calcein was allowed for further 20min. Then, cells were washed with PBS and imaged (0min reading). Immediately, dishes with H9c2 cells were treated with 10μM MitoPQ and/or A23187, or 1μM CCCP. DMSO was used as a negative control. Then, cells were imaged 15min and 60min after the drugs were added.

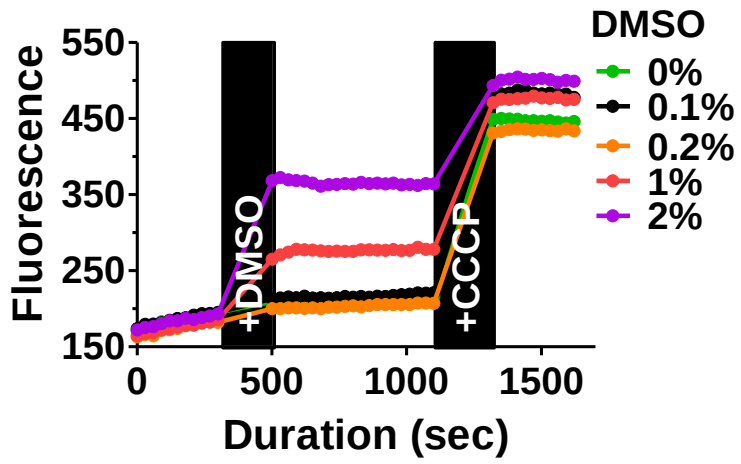

Supplementary Figure 5. Permeabilization of H9c2 cells with DMSO leads to TMRM leakage.

H9c2 cells were plated in 96 well plate (40,000 cells/well). Next day, they were treated with 20µM TMRM for 10min. After the cells were washed, the baseline recording was obtained. Next, various concentrations of DMSO were added to the cells and recording continued. Later, 5µM CCCP was added for 5min to obtain the maximal TMRM fluorescence.

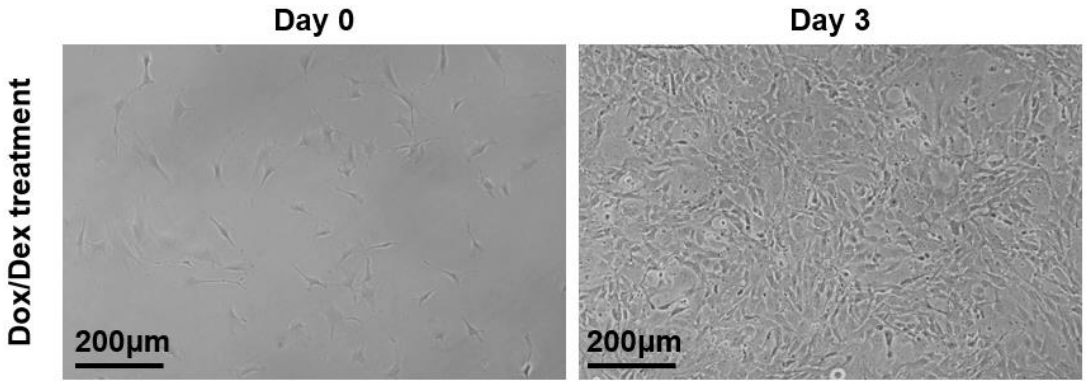

Supplementary Figure 6. Conditionally immortalized MSCs in the presence of dexamethasone and doxycycline.

MSCs were plated with DMEM, 10% FBS, 1% penicillin/streptomycin with 10-7M dexamethasone and 1µg/ml doxycycline on 10cm^2 dishes. For the next five days, cells were imaged and then harvested for Western blot.

Electroporation settings	Cell fluorescence	Cell death
900V, 40ms, 1 pulse	1	0
1,100V, 40ms, 1 pulse	2	0
1,300V, 40ms, 1 pulse	7	3
1,500V, 40ms, 1 pulse	6	8
1,700V, 40ms, 1 pulse	0	10
1,300V, 40ms, 2 pulses	5	9
900V, 40ms, 2 pulses	0	10
1,700V, 10ms, 1 pulse	0	10

Supplementary table 2. Various electroporation settings for MSC transfection.

MSCs at 10^7cells/ml were electroporated using Neon™ Transfection System and enhanced GFP-encoding plasmid. Next day, the number of dead cells and GFP fluorescence were evaluated on the scale of 10. Cells that were not transfected served as a negative control.

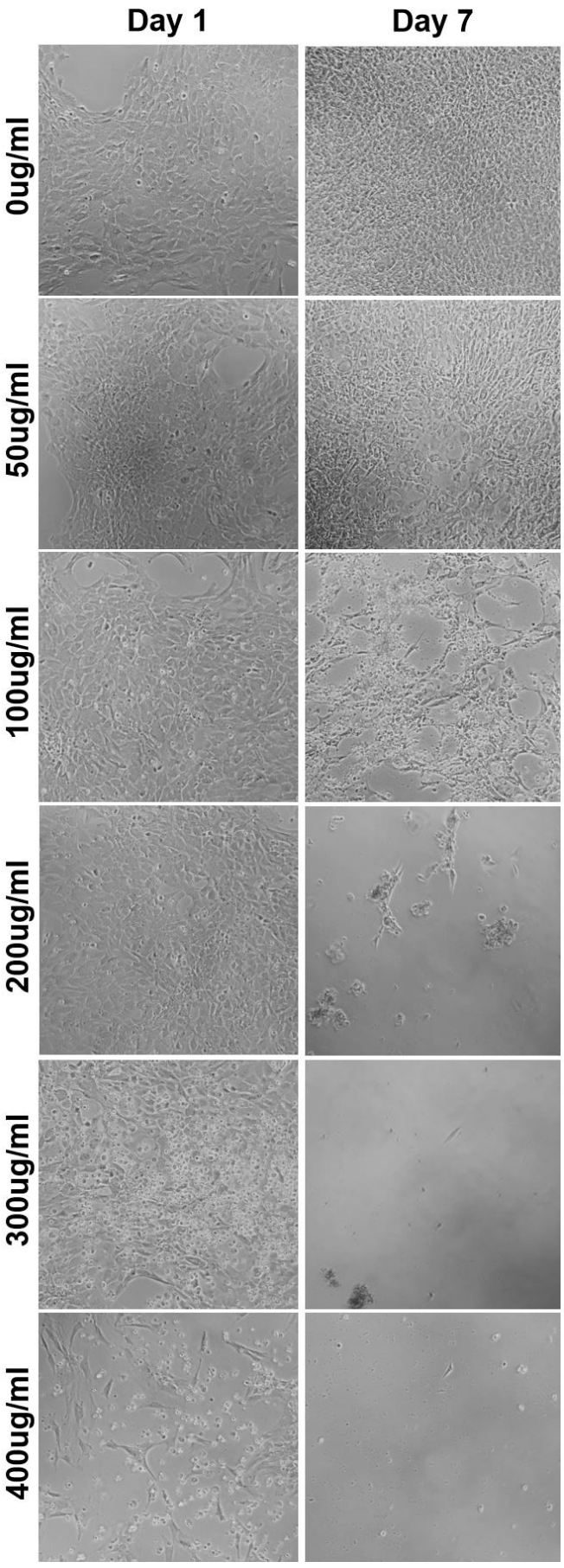
Day 1
Day 7
0ug/ml
50ug/ml
100ug/ml
200ug/ml
300ug/ml
400ug/ml

Supplementary Figure 7. MSCs a weeklong treatment with G418 antibiotic.

MSCs were plated at 60% confluency (Day -1). Next day, they were treated with G418 antibiotic of various concentrations (Day 0). Cells were imaged one or seven days after the treatment. Only some cell images are shown.

List of publications

Davidson, S.M. *et al*. (2022) ‘Methods for the identification and characterization of extracellular vesicles in cardiovascular studies - from exosomes to microvesicles’, *Cardiovascular Research*. doi: 10.1093/cvr/cvac031.

Katsur, M. *et al*. (2021) ‘Exosomes from neuronal stem cells may protect the heart from ischaemia/reperfusion injury via JAK1/2 and gp130’, *Journal of Cellular and Molecular Medicine*, 25(9), pp. 4455-4465. doi: 10.1111/jcmm.16515.

Buchanan, H. *et al*. (2020) ‘Synaptic loss, ER stress and neuro-inflammation emerge late in the lateral temporal cortex and associate with progressive tau pathology in Alzheimer's Disease’, *Molecular Neurobiology*, 57(8), pp. 3258-3272. doi: 10.1007/s12035-020-01950-1.

Posters

- UCL Doctoral School Poster Competition, 2021. ‘Roles of exosomes in the body and their purification from cell media’ (runner-up).
- UCL MRC DTP PhD Students Retreat, 2021. ‘Purification of exosomes which affect myriad of bodily processes.
- UCL Doctoral School Poster Competition, 2020. ‘Modelling cardiomyocyte mitochondrial injury to simulate myocardial infarction’.
- European Society of Cardiology, Basic Science Summer School, 2019. ‘Modelling cardiomyocyte mitochondrial injury to simulate myocardial infarction’
- UCL MRC DTP PhD Students Retreat, 2019. ‘Establishing cell model for evaluating cardioprotective potential of exosomes’.